DEPARTAMENTO DE FÍSICA DE MATERIALES

Universidad Autónoma de Madrid

DIRECT FEMTOSECOND LASER WRITING OF 3D PHOTONIC STRUCTURES IN RARE-EARTH DOPED LITHIUM NIOBATE

ESCRITURA DIRECTA MEDIANTE LÁSER DE FEMTOSEGUNDOS DE ESTRUCTURAS FOTÓNICAS 3D EN NIOBATO DE LITIO DOPADO CON IONES DE TIERRAS RARAS

Memoria que presenta

Airán Ródenas Seguí

Para optar al grado de

Doctor en Ciencias Físicas

Director: **Daniel Jaque García**

Noviembre de 2009

En memoria de

Sara Utray y Sardá

y José Seguí Poveda

Table of contents

Agradecimientos
Acknowledgements

"La física es al final experimental, y siempre se pueden producir sorpresas"

Peter Zoller

"Si hay algo en nosotros verdaderamente divino es la voluntad"

"Una severa autocrítica constituye el más precioso don del pensador"

Santiago Ramón y Cajal

"Amamos navegar en mares prohibidos"

Herman Melville, en *Moby-Dick*

Las citas aquí incluidas expresan en parte lo que me han enseñado varias personas a las que deseo expresar mi gratitud y reconocimiento.

En primer lugar al Director de esta tesis, al Profesor Daniel Jaque, por haberme transmitido el placer (y la ansiedad) que producen el aprendizaje y el descubrimiento. Por estar siempre disponible para echar una mano en el laboratorio (hasta tal punto que a veces deja de distinguirse quién es el estudiante), y por dar siempre sus consejos desde el primer al último día, aun cuando muchas veces (*todas!* dirá él) me he obstinado en mis ideas. Por permitirme muchas veces dirigir yo mismo mis investigaciones, por haberme ayudado a realizar diferentes estancias fuera de España sin las cuales yo, y esta tesis doctoral, no seríamos los mismos. Y por último, y no menos importante, por enseñarme a combatir la ineficacia del excesivo perfeccionismo, y la importancia de tener siempre bien claros los objetivos.

Quiero agradecer también la ayuda y la amistad del resto de componentes del Grupo de Espectroscopía Láser, con los cuales he compartido estos últimos cuatro años:

En primer lugar a la Profesora Luisa Bausá, por permitirme hacer aquella práctica de Láser de Estado Sólido en cuarto de carrera que disparó mi curiosidad por los láseres, y por haberme permitido formar parte del grupo un año después. Por dar siempre su apoyo y por mostrar siempre su interés y su optimismo en cualesquiera fueran las circunstancias.

Al Profesor José García Solé, por ofrecer su inestimable ayuda en cuantos problemas surgieran en cualquier tipo de experimento. Y sobre todo, por transmitir su entusiasmo por la investigación y la Universidad en todas sus facetas.

A la Doctora Mariola Ramírez, por toda su ayuda en el laboratorio, pero sobretodo fuera de él, en las *infernales*, y en todos los *garitos* a los que fuimos, que fueron menos de los que hubiera deseado. Por su sinceridad, y por todos sus valiosos consejos.

Al Doctor Pablo Molina, el letal *Brus Lee*, por estos años compartidos en el laboratorio desde que empezamos como dos auténticos pichones a aprender lo que es un láser (no sé si aun lo hemos entendido…), un congreso internacional, o una publicación. Por los todos buenos momentos.

A Emma Martín, *Emmi*, por su constante generosidad y su amistad. Por las cenas compartidas en los duros meses de invierno-verano de Melbourne. Y por supuesto, y aunque estas líneas no sean suficiente como agradecimiento, por la innumerable cantidad de veces que me ayudó con todos los papeles del Doctorado. Sin su ayuda no estaría escribiendo estas líneas ahora.

A Antonio Benayas, por ser la auténtica revolución del grupo. El mejor coordinador de eventos de ocio y congresos internacionales en Segovia. Por las innumerables discusiones y enfados con copa y cigarro en mano. Por estar siempre ahí para ayudar en cualquier clase de problema. Eres un fenómeno.

Y a las últimas incorporaciones del grupo con quienes he podido compartir pocos pero gratos momentos: Jesús Vicente y Laura Maestro.

También quiero agradecer al resto de compañeros del Departamento de Física de Materiales con quien he podido pasar muy buenos momentos: a Marta Quintanilla, Eugenio Cantelar, Pablo Díaz, Jorge Lamela, Fabrice Leardini, Jose Ramón y Juan Carlos Lagomacini.

A lo largo de estos años he podido tambien conocer y trabajar con investigadores de diferentes paises a los que quiero agradecer tambien por todo lo que me ayudaron en todo momento:

En Brasil, al profesor Tomaz Catunda (*I ai? Dio certo?...*) del Insituto de Física de Sao Carlos, que me enseñó cómo hacer grandes experimentos con los equipos más sencillos. A Carlos Jacinto, *Carlinhos*, de la Universidad Federal de Alagoas en Maceió, con quien compartí multitud de buenos ratos en la universidad, pero también en las fastuosas playas a las que me invitó a visitar con su magnífica familia y también al entonces estudiante André, un magnífico amigo.

En Argentina, La Plata, al Doctor Gustavo Torchia, no sólo por los buenos ratos en el CIOp, sino también y sobre todo por toda su ayuda a la hora de encontrar tanto un piso digno donde vivir como los mejores bares donde beber el mejor Malbec. Al Doctor Alberto Lencina, no sólo por dejarme habitar en su piso, sino sobre todo por las conversaciones en torno a la misteriosa naturaleza cuántica de la luz y las mujeres, por los mejores ratos con Fernet y asado, y por las fiestas en compañía de su increíble panda de amigos. Y por supuesto a Fabián, el mejor compañero de despacho y el mejor introductor del fantástico legado de Piazzola.

In Australia, Melbourne, first of all I ought to thank Professor Min Gu, for giving me the opportunity of being part of the Center of Micro-Photonics both in 2007 and 2009. My gratitude is enormous for all the help he gave during my stays and the experience and knowledge that I got from working there changed my perspectives and my confidence as a scientist. To Guangyong Zhou and Bahoua Jia, for helping me on every detail in the labs, and for sharing all their experience on the exciting subject of three-dimensional photonic crystals. Lastly, I also want to thank to Joel van

Embden and Elisa Nicoletti, for being the best friends one can imagine in that lost paradise of Australia.

Por último, deseo también agradecer a toda mi familia:

Mis padres Pablo y Francis; Sólo gracias a ellos soy quien soy, gracias por enseñarme que el placer y felicidad últimos residen simplemente en aprender. A mi prima Iris y mis tíos Isabel y Fernando, muchas gracias por todo el amor y apoyo estos últimos años, en esta tesis también hay mucho de ustedes, y aún daría para muchísimo más. Y por último, y en especial, a Sole, por ser el mayor y más importante descubrimiento que hice en mi vida. Por lo fantástica que eres en cada detalle. Porque me sorprendes cada día, y me haces comprender lo importante que es la vida. Gracias por confiar en mí.

Airán Ródenas Seguí

Madrid, 17 de noviembre de 2009

Chapter 1

Introduction and overview

All along this thesis work we will be dealing with laser pulses of around 100 fs which are focused inside crystalline materials to extremely small spots of around 1 µm in diameter. The combination of both ultrashort pulse duration and the tight focusing is the clue for all the effects and applications that are examined in this work.

To get an idea of how extremely short 100 fs is, one just has to know that it corresponds to about 10^{-13} seconds (i.e. 0.0000000000001 seconds). This means that the pulse duration would correspond to about 12 hours with respect to the age of the Universe (13.7×10^9 years [1]).

With respect to laser focal spot size, it is worth knowing that 1 µm (10^6 m = 0.000001 m) corresponds to about 1 eighth of a blood cell (8 µm), or 1 seventh of a chromosome (7 µm) [2]. Consequently, the reader will not be surprised if he notes that the method used for confining the laser pulses is extracted from biological sciences, i.e. the optical microscopy [3].

However, as we will see along this thesis, the singularity of using such extremely short laser pulses is that the interaction mechanism with matter is of nonlinear nature. This will turn out in that the size of the modification in the media will not be proportional to the size of the focused spot size, but smaller in some factor. As a result of this, tiny holes of around 90 nm diameter can be performed at the surface of a crystal, this being even smaller than the size of an influenza virus or

the HIV virus (130 nm), as seen on **Figure 1**. Sizes below 200 nm are typically outside the range of optical resolution, so that it gets clear that this technique allows reaching feature sizes which so far were only reachable by means of other techniques such as ion beam irradiation. Even though ion beam techniques still allow for even smaller resolutions of a few nanometres, the main distinctive advantage of using lasers is that the processing of the material can be done either at surface or inside the sample.

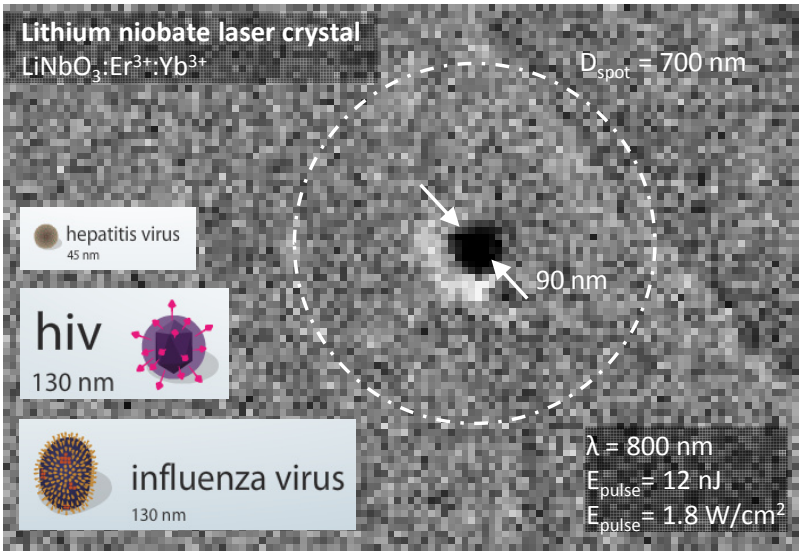

Figure 1. *Sub-micron surface hole ablated on the surface of a $LiNbO_3:Er^{3+}:Yb^{3+}$ sample. Comparable size viruses are also shown.*

The purpose of this thesis is to apply this femtosecond direct laser writing (DLW) technique to micro-fabricate photonic structures in laser materials such as rare-earth doped crystals. A photonic structure is an integrated device which allows controlling and manipulating light thanks to the dimensional confinement and optical properties of the material. The goal of integrated optics is to combine many different optical elements such as waveguide devices and photonic crystals on a single substrate. Such substrates can be designed to be used in a variety of applications in optical communications, instrumentation and sensing, in an analogue manner that electric circuits are used in integrated electronics.

One of the paradigmatic materials that is enabling integrated optics is the ferroelectric nonlinear crystal lithium niobate ($LiNbO_3$) [3], which offers incredible versatility and has allowed the development of new optical devices such as waveguide structures, electro-optical wavelength filters and polarization controllers, lasers, and very recently also photonic crystals. Benefiting from its good electro-optical, accustom-optical and nonlinear properties these devices can show remarkable properties such as nonlinear frequency conversion, ultrafast all-optical signal processing and single-photon generation.

Our goal is to investigate the accessibility of the DLW technique to create completely new devices that can be built using the 3 dimensions inside the material, thus enhancing the compactness and complexity of integrated devices. It is worth noting that the ultra-short pulse laser technique is the only one which has been demonstrated to offer the possibility of direct three-dimensionally micro-structuring inside transparent media, without altering the surface of the substrate.

Overall, this dissertation is divided in two parts. The first part of the thesis is concerned with the fundaments of direct ultra-short pulse laser microfabrication in $LiNbO_3$ (Chapters 2 and 3), and the second part covers some investigated applications which are integrated diffraction gratings in the laser crystal, optical buried waveguides, and three-dimensional photonic crystals (Chapters 4, 5 and 6).

Chapter 2 introduces Lithium Niobate and its structure, and material and optical properties of relevance for the investigations performed in this thesis.

Chapter 3 is a brief review of the fundamentals of direct laser microfabrication in dielectrics. The basic issues and operating parameters for using the technique are presented, and some examples based on experiments in $LiNbO_3$ are given, which are the basic knowledge from which the rest of works will be built. The ablation of micrometric and sub-micrometric surface holes, and the main aberration effects when writing submicron voxels inside the crystal is introduced.

Chapter 4 reports the results of laser action and non-collinear propagation based on the incorporation of one-dimensional and two-dimensional diffraction gratings onto a Nd^{3+} doped MgO:$LiNbO_3$ crystal. The polarization dependence of the diffraction efficiency and the laser gain and thresholds depending of each type of grating is presented.

Chapter 5 presents the spectroscopic analysis of the $LiNbO_3$ lattice changes present in two kinds of optical buried waveguides fabricated with low-repetition rate and high-repetition rate lasers. The index of refraction are estimated from micro-Raman and micro-Luminescence profiles, indicating that the mechanisms for waveguide formation are of stress induced piezo-optical nature, although in some cases a complete explanation requires from some other mechanism as the electro-optic effect.

Chapter 6 presents the results of three-dimensional (3D) photonic crystal inscription inside $LiNbO_3$ crystals. The near-infrared transmission spectra of different lattice structures are presented and the Bragg scattering effect on the intrinsic luminescence of the material is analyzed.

Chapter 7 summarizes the work contained within this dissertation.

A final **Appendix** is also included introducing the concept of photonic crystal, and reviewing the history of the concept and its practical realization. A comprehensive and updated review of published papers in the subject is given. The Appendix also discusses the different available fabrication techniques, the different kinds of 3D lattices and their characteristic dispersion properties, and some of their unique optical features and applications.

Introducción y contenido

A lo largo de esta tesis se habla a menudo de pulsos láser con una duración de en torno a 100 fs, que son enfocados en el interior de cristales a tamaños extremadamente pequeños de entorno a 1 µm de diámetro. Esta combinación de una duración del pulso extremadamente corta y su alto confinamiento espacial es el origen de los efectos físicos y aplicaciones que se examinan en esta tesis.

Para hacerse una idea de cuánto son 100 fs, basta con saber que corresponde con a 10^{-13} segundos (i.e. 0.0000000000001 segundos). Lo cual significa que frente a una segundo, este tiempo es equivalente a aproximadamente 12 horas frente a la edad del Universo ($13.7x10^{9}$ años [1]).

Con respecto al tamaño del foco donde toda la energía del pulso láser es confinada, 1 µm corresponde aproximadamente a la octava parte del tamaño de una célula sanguínea (8 µm), o la séptima parte de un cromosoma (7 µm) [2]. Por tanto, el lector no deberá sorprenderse si observa que el método empleado para confinar los pulsos láser en la escala micrométrica será el de microscopía óptica, donde la mayor parte de los objetivos de enfoque son diseñados para las ciencias biológicas [3].

Sin embargo, y como veremos a lo largo de esta tesis, lo singular de usar pulsos extremadamente cortos en el tiempo para micro-esculpir materiales reside en el hecho de que el mecanismo de interacción con el medio es fundamentalmente no lineal. Esto significa que el tamaño del área modificada no será proporcional al tamaño del foco laser, sino que será menor en un determinado factor. Como resultado de esta no linealidad veremos que, por ejemplo, es posible realizar agujeros de tan sólo 90 nm de diámetro en la superficie de un cristal. Estos tamaños son equivalentes a los de virus tales como la gripe o VIH [2], como se muestra en la **Figura 1**. Tamaños por debajo de los 200 nm están ya por debajo del límite de resolución óptica, lo cual implica que, debido a la alta no linealidad del proceso de inscripción esta técnica permite alcanzar una

resolución que hasta ahora pertenecía al ámbito de las técnicas de bombardeo mediante haces de iones. Aun así, y como veremos, las técnicas actuales de bombardeo iónico permiten alcanzar motivos superficiales de pocos nanómetros. ¿Por qué usar un láser entonces? La ventaja de usar un haz láser ultracorto en lugar de iones será que, como veremos, éste permite procesar el material tanto en su superficie como su interior, algo que hasta ahora era completamente imposible.

El propósito de este trabajo de tesis es aplicar la técnica de escritura mediante pulsos láser de femtosegundos para la obtención de estructuras fotónicas en materiales láser transparentes, tales como cristales de niobato de litio dopados con iones de tierras raras. Una estructura fotónica es un dispositivo integrado que permite controlar y manipular la luz gracias al confinamiento dimensional producido y las propiedades ópticas del material. El objetivo de la óptica integrada es combinar diferentes elementos ópticos tales como guías de onda o cristales fotónicos, en un solo substrato. Estos substratos podrán ser diseñados para ser usados en una muy amplia variedad de aplicaciones, en una manera análoga a como los circuitos eléctricos conforman la electrónica integrada. Las aplicaciones inmediatas de la tecnología fotónica cubren el área de las telecomunicaciones ópticas, la instrumentación, o sistemas de detección ultrasensibles y ultra-rápidos para medicina o biotecnología.

Uno de los materiales paradigmáticos que ha permitido desarrollar la tecnología de óptica integrada es el cristal no lineal ferroeléctrico de niobato de litio ($LiNbO_3$) [3], debido a que ofrece una increíble versatilidad funcional que ha permitido el desarrollo de nuevos dispositivos fotónicos tales como guías de onda, filtros de frecuencias electro-ópticos, controladores de la polarización, láseres, y también recientemente cristales fotónicos. Estos dispositivos aprovechan las propiedades funcionales del material, tales como sus propiedades electro-ópticas, acusto-ópticas y no lineales, de manera que los dispositivos pueden ofrecer funciones relevantes tales como la conversión de frecuencias no lineal, el procesado ultra-rápido óptico de señales, y la generación de *single-photons*.

Nuestro objetivo es por tanto investigar la posibilidad de usar la técnica de escritura mediante pulsos láser de femtosegundos para desarrollar dispositivos completamente nuevos que aprovechen las tres dimensiones dentro del material, para de esta manera aumentar la compacidad

y complejidad de los dispositivos integrados. Es necesario mencionar que la técnica láser mediante pulsos ultracortos es la única que se ha demostrado que posibilita la escritura tridimensional en el interior de un material sin dañar en ningún grado su superficie.

Esta tesis está básicamente dividida en dos partes. En la primera parte se discuten los fundamentos físicos del micro-estructurado mediante pulses láser ultracortos en cristales de $LiNbO_3$ (Chapters 2 y 3). La segunda parte presenta los resultados de investigación en torno a las aplicaciones, tales como elementos de difracción integrados en el medio láser, guías de onda, y cristales fotónicos tridimensionales (Chapters 4, 5 y 6).

El **Capítulo 2** (**Chapter 2**) es una introducción al niobato de litio y su estructura. Algunas de sus propiedades físicas y ópticas que serán de interés en el resto de capítulos son analizadas.

El **Capítulo 3** (**Chapter 3**) es un breve resumen en torno a los fundamentos de la escritura mediante pulsos ultracortos en niobato de litio. Se describen los conceptos básicos y parámetros relevantes de la técnica, y se presentan algunos ejemplos experimentales realizados en niobato de litio. Estos experimentos constituyen el conocimiento previo mediante el cual el resto de trabajos serán realizados. Se demuestra la ablación de estructuras micrométricas y sub-micrométricas superficiales, y también se investigan las principales aberraciones ópticas que pueden tener lugar al inscribir voxels sub-micrométricos en el interior del cristal.

El **Capítulo 4** (**Chapter 4**) presenta los resultados concernientes a la acción laser y propagación no-colineal de la radiacción fundamental generada en cristales láser de Nd^{3+}:MgO:$LiNbO_3$, mediante la creación de redes de difracción integradas de una y dos dimensiones. Se presenta la dependencia de la eficiencia de difracción así como las propiedades laser para cada tipo de red superficial.

El **Capítulo 5** (**Chapter 5**) presenta los resultados del análisis espectroscópico de micro-Raman y micro-Luminiscencia de los cambios producidos en la red cristalina del niobato de litio en dos tipos de guía de onda fabricados mediante pulsos de femtosegundos: Guías fabricadas en el régimen no-

térmico mediante bajas frecuencias de pulso,y guía fabricadas en el régimen térmico mediante altas repeticiones de pulsos. Los cambios de índice de refracción son estimados en primera aproximación mediante los perfiles de micro-Raman y micro-Luminiscencia, indicando que el origen principal del guiado es debido a un cambio de índice de tipo piezo-óptico, probablemente producido por la generación de campos de stress inducidos en el foco láser.

El **Capítulo 6** (**Chapter 6**) presenta los resultados de la escritura tridimensional de cristales fotónicos en cristales niobato de litio dopado con tierras raras. Se presentan los espectros de transmitancia en el infrarojo cercano de estructuras con diferentes parámetros de red, así como sus efectos en la luminiscencia del material.

El **Capítulo 7** (**Chapter 7**) resume el trabajo presentado en esta tesis.

El Apéndice final (**Appendix**) es un texto introductorio sobre cristales fotónicos, desde el concepto hasta los principales aspectos de su fabricación e historia. Se presenta así mismo una lista actualizada de las principales publicaciones en el campo de cristales fotónicos tridimensionales. Y se discuten las principales técnicas disponibles para su fabricación en dielectricos, las diferentes tipos de redes y sus diferentes propiedades dispersivas, así como sus principales aplicaciones.

References

[1] G. Hinshaw et al., *Five-Year Wilkinson Microwave Anisotropy Probe Observations: Data Processing, Sky Maps, and Basic Results*, Astrophysical Journal Supplement Series **180**, 225 (2009)

[2] http://learn.genetics.utah.edu/

[3] http://microscope.olympus.com/uis2/

[4] W. Sohler et al., *Integrated optical devices in lithium niobate*, OPN January 2008, 24-31, www.osa-opn.org

Chapter 2

Lithium Niobate

In this chapter a brief overview of the structure, material and optical properties of $LiNbO_3$ and the different micro-structuring techniques of $LiNbO_3$ is given.

2.1. Introduction

Lithium niobate has been one of the most extensively studied materials in the last decades mainly due to its unique combination of ferroelectric and optical properties. Today, more than 400 papers are being published every year [1]. A very good review of its physical and chemical properties was already made by Räuber in 1978 [2].

$LiNbO_3$ was first described in 1928 by Zachariasen [3], but it was not until 1949 that Mathias and Remeika discovered its ferroelectric properties studying single crystals grown from a flux [4]. However, systematic research on $LiNbO_3$ truly started in 1965, when both Fedulov [5] and Ballman [6] reported the successful growth of single crystals by the Czochralski technique, and then Nassau et al. [7, 8] and Abrahams et al. [9-11] published a five paper series on its physical properties in 1966.

Between 1965 and 1967 most of the basic experiments on acoustic wave propagation, electro-optic modulation, and bulk nonlinear laser optics - second harmonic generation (SHG) and optical parametric oscillation (OPA) - were performed. Between 1967 and 1980 extensive work was then devoted to improving the quality and homogeneity of grown samples, and to applications in photorefractive holographic storage, optical waveguides, and surface acoustic wave (SAWs) devices [2]. Published papers from these first years of research mainly concern on the growth, physical properties and functionality of $LiNbO_3$, and papers in the specific area of Optics only span a 5% of the records [1].

Around 1980 the industrial production of $LiNbO_3$ wafers was strongly increased, reaching word supply values. In 1984 the first $LiNbO_3$ waveguide modulator was commercialized, and in 1992 the first 100 mm long commercial quality waveguide was demonstrated. In 1996 periodically poled $LiNbO_3$ (PPLN) OPO's were commercially introduced, in 2002 15-cm diameter $LiNbO_3$ samples were available, and in 2006 the annual production of $LiNbO_3$ had reached hundreds of tons [12]. However, most of the commercially supplied samples were (and mostly still are) all undoped

$LiNbO_3$, while already by the mid 80's the scientific research in $LiNbO_3$ was directing towards optical applications of doped $LiNbO_3$ [1].

In the period 1990-2009 the percentage of published papers on $LiNbO_3$ in the area of Optics reached the 40% of total records [1], being much of these works based on ion doped samples such as magnesium ions or rare earth ions such as neodymium or erbium ions, used for nonlinear optical and laser applications [13-16].

As we will also see in the last section a renewed interest has also appeared in the last years to find new techniques for the synthesis of nanostructured crystalline $LiNbO_3$ (such as inversed opal films, nanotubes, or nanowires) without the need of complex Czochralski based crystal growing techniques. Although still extensive research has to be done before these methods reach the high crystalline quality which is already available by means of the Czochralski technique.

2.2. Structure and material properties

2.2.1 Crystal structure

As all ferroelectric materials, $LiNbO_3$ is a non-centrosymmetric, piezoelectric material [17]. The structure of $LiNbO_3$ corresponds to the trigonal space group (*R3c*), in the ferroelectric phase the point group is $3m$ (C_{3v}). At around 1100-1200°C the crystal undergoes its phase transition to the paraelectric non-polar phase, with point group $\bar{3}m$ (D_{3d}) [2, 18].

As all ferroelectric materials, $LiNbO_3$ shows a spontaneous polarization which can be reversed by applying a sufficiently large electric field, so that the atoms experience a small relative shift and the crystal is turned into its electric twin. Samples typically exhibit different spatial regions were the polarization direction is reversed. These regions are usually called ferroelectric *domains*, and the polarization direction is always defined by its unique crystallographic *c*-axis.

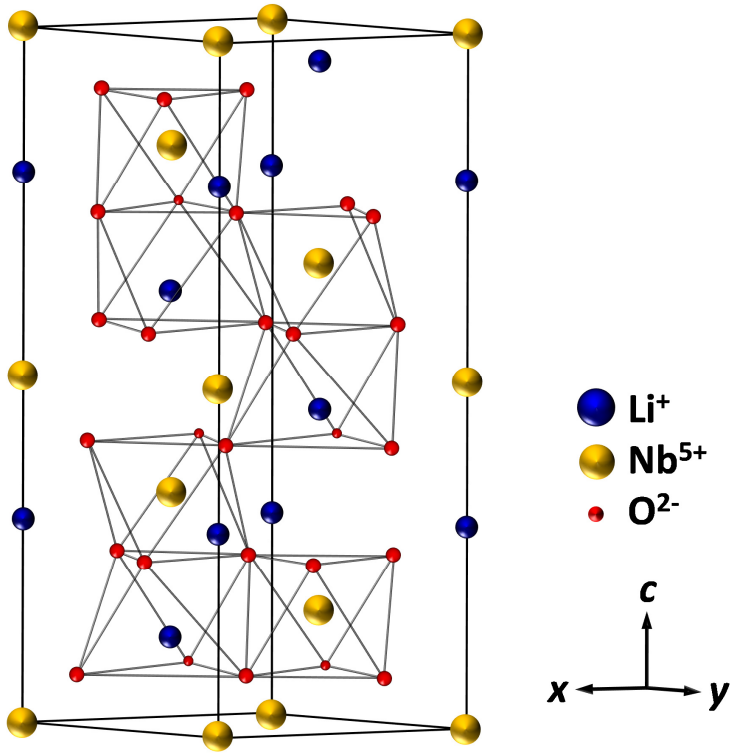

Fig. 2.1. *Schematic diagram of the crystallographic structure of $LiNbO_3$ single crystal in one unit cell. Oxygen ions are shown in red, defining the different stacked octahedra; lithium ions are shown in blue, above the close packed O ion plane separating them from the vacant octahedron; and niobium ions are in yellow colour, inside their octahedron. The cation sequence along the optical c-axis is Li, vacancy, Nb, Li, vacancy, etc.*

The lattice structure of undoped $LiNbO_3$ comes defined by its oxygen octahedron, BO_6, in which six oxygen ions (O) surround a Li or Nb ion (B). In the most symmetric phase, i.e. in the high-temperature paraelectric non-polar phase, the time-averaged mean position of the cation B corresponds to the geometric centre of the oxygen octahedron, while at the ferroelectric phase this cation appears displaced from the centre position. The oxygen octahedral units O_6 are joined by connecting their faces, which results in a matrix of distorted octahedra connected by their faces along the polar *c*-axis. The sequence of ions filling the O octahedra along the *c*-axis is Li^+, vacancy, Nb^{5+}, Li^+, vacancy, Nb^{5+}, etc., as it is shown in **Figure 2.1**. The displacements that Li^+ and Nb^{5+} ions undergo during the phase transition are slightly different. Nb^{5+} ions move from the centre position inside the octahedron to an asymmetric position along the *c*-axis within the same octahedron, and

Li^+ ions move from one octahedron to the adjacent vacant octahedron through the close-packed O ions plane.

The Li/Nb ratio is an important feature of the crystal, and it is usually defined with respect to the Li content as C=[Li]/([Li]+[Nb]). The congruent melting composition is C=0.486 or, as usually indicated, 48.6 mol% Li_2O. The stoichiometric composition is C=0.5. This ratio is a relevant parameter as several important properties of $LiNbO_3$ depend on the composition, such as the Curie point, the relative birefringence value, the phase-matching temperatures for SHG, the coercive field, the electro-optic coefficients, the strain and local electric fields adjacent to domain walls, the nonlinear optical coefficients, and others [2, 19].

2.2.2 Crystal physical properties

The physical properties of a crystal are defined by relations between measurable quantities. While some properties can be determined without referring to any direction in the crystal, others have to be specified to the direction along which they are measured. Thus, for a few properties such as the density, all crystals are considered *isotropic*, while for others, such as for example the thermal conductivity or the dielectric function, the crystals are said to be *anisotropic*.

Important useful properties of $LiNbO_3$ that are normally considered as isotropic are its *volume mass density*, $\rho \approx 4640$ (kg/cm^2), its *specific heat capacity*, $c_p \approx 714$ (J/kg·K), or its *thermal conductivity*, $\kappa \approx 2.67$ (W/m·K) [20].

On the contrary, direction dependent properties have to be specified by a tensor of a given rank, with the number of independent coefficients being given by the symmetry of $LiNbO_3$.

For the point group *3m* (C_{3v}) of $LiNbO_3$ a different number of independent components is given depending on the tensor rank*, as shown in **Table 2.1**.

Rank of tensor	# of independent coef.	Examples of properties
1	1	pyroelectricity
2	2	dielectric function thermal expansion
3	4	piezoelectricity electro-optic effect nonlinear optic effect
4	**6** **or** **8**	**elasticity** **elasto-optical properties** **piezo-optic effect**
6	14	third order elasticity

Table 2.1. *Number of independent coefficients for tensorial physical properties in point symmetry 3m* [17]

Extensive analysis on all the important properties included in **Table 2.1** have been given in previous review works and are thus not included here, for the sake of brevity [2, 18-20]. However, we will give special attention to the piezo-optic properties of $LiNbO_3$, as they will become necessary in following chapters, in relation with the fabricated photonic structures.

2.2.2.1 The piezo-optic effect

The piezo-optic effect gives the relation between an applied stress and the corresponding change in the refractive index. As the notion of *stress* will be extensively used in following chapters, it needs to be defined.

* The rank of a tensor equals the number of subscripts by which it is described. In this sense, a tensor of zero rank is a scalar, a tensor of first rank is a vector, a tensor of second rank is a two-dimensional matrix, and so on [17].

A body in which one part exerts a force on neighbouring parts is said to be in a state of *stress*. The force exerted on a volume element by its surrounding is proportional to the area of the surface element, and the force per unit area is called the *stress*.

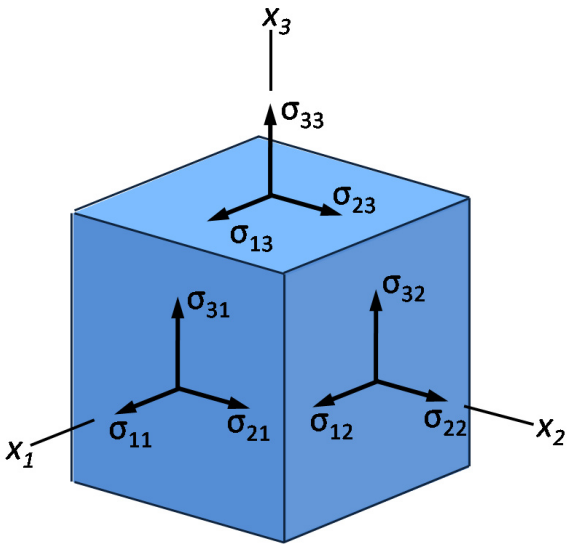

Fig. 2.2. *The forces on the faces of a unit cube in a homogeneously stressed body* [17]

The forces exerted towards the positive ends of the main axes will be considered as positive, and the forces exerted across the opposite faces of the cube will be considered to be equal and opposite to those shown in **Fig. 2.2**. Elements σ_{11}, σ_{22} and σ_{33} are the *normal components* of stress, and σ_{12}, σ_{21}, σ_{23}, etc. are the *shear components*. As indicated, a positive value for each normal component then indicates a *tensile stress*, and a negative value implies a *compressive stress*. The stress is then a nine element second rank tensor, σ_{ij}, although it is important to point out that it is different from the previous second rank tensors mentioned in **Table 2.1**, in the sense that it is not a physical property of the crystal, i.e. it is not a *matter tensor*.

It can be shown that the stress tensor is a symmetrical tensor, so that it can be referred to its principal axes and only three coefficients are needed to specify it. The stress tensor can have any orientation in the crystal, like an electric field, and so it is called a *field tensor* [17].

As previously mentioned, the refractive index can be altered by introducing a stress field to the crystal. The change of refraction index caused by stress in absence of external electric fields is usually called the piezo-optic effect[†]. The refractive index of an anisotropic crystal comes defined by the *dielectric tensor* so that $n_{ij}=V\varepsilon_{ij}$, and it can be represented by an ellipsoid known as the *optical indicatrix*, defined by the different elements $b_{ij}=[\varepsilon^{-1}]_{ij}$ [21].

The distortion of the indicatrix, neglecting higher-order terms other than the first one in the stress field, is given by:

$$\Delta b_{ij} = \pi_{ijkl}\sigma_{kl} \tag{2.1}$$

where π_{ijkl} is the fourth rank tensor giving the piezo-optic effect, and σ_{kl} is the second rank stress tensor. Usually the effect is also expressed in terms of the strain instead of the stress, which gives a measure of the change in length along a certain direction with respect to the original length. In this case there exists the alternative expression:

$$\Delta b_{ij} = p_{ijkl}s_{kl} \tag{2.2}$$

where p_{ijkl} is the fourth rank tensor giving the elasto-optic effect, and s_{kl} is the second rank strain tensor. The interrelation between the piezo-optic and elasto-optic coefficients is given by the elasticity of the crystal, in the form:

$$p_{ijkl} = \pi_{ijmn}c_{mnkl} \tag{2.3}$$

where c_{mnkl} is the fourth rank elastic stiffness tensor.

[†] Similarly, a change in the refractive index as a result of a strain is known as the *photo-elastic effect*.

Table 2.2

Form of the elastic (c_{ij}), piezo-optic (π_{ij}) and elasto-optic (p_{ij}) matrices

Trigonal symmetry - Classes *32*, *3m* and $\bar{3}m$

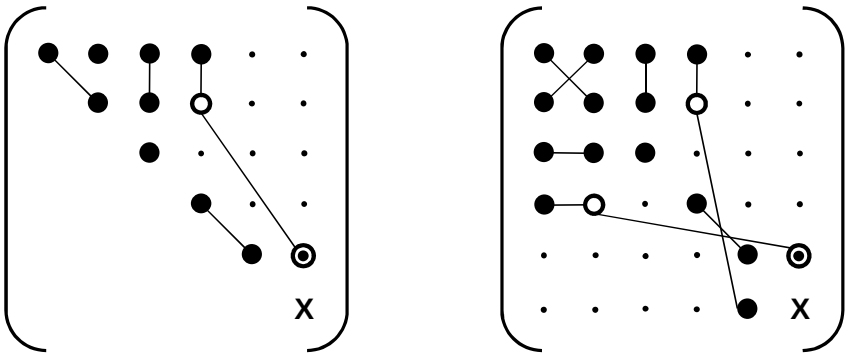

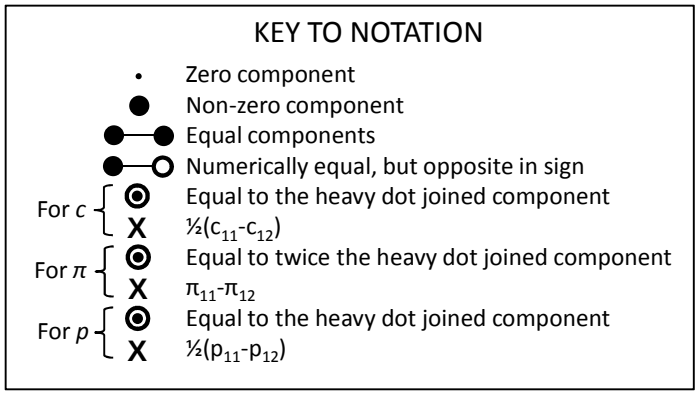

As previously indicated, these three tensors can be contracted by taking into account both the trigonal symmetry classes $3m$ and $\bar{3}m$, to 6 X 6 matrices. The general tensor forms resulting from symmetry considerations are summarized in **Table 2.2** [17]. It is worth noting that the elastic stiffness matrix is symmetrical along its diagonal, while this is in general not true for the elasto-optic and piezo-optic matrices, thus, in **Table 2.2** the left hand matrix form corresponds to the elastic stiffnes tensor, and the right hand form to the elasto-optic and piezo-optic tensors.

In **Table 2.3** the different values for the independent coefficients of the elastic stiffness, piezo-optic and elasto-optic effects are given. It is important to note that the direct measurement of the piezo-optic coefficient is rather complicated, and thus they are normally calculated from the elastic

stiffness and the elasto-optic coefficients by using **Eq. 2.3**. Usual values for the elastic stiffness and elasto-optic tensor are given in **Table 2.3** [22, 23], and the corresponding calculated piezo-optic coefficients are also indicated.

Elastic	c_{11}	c_{12}	c_{13}	c_{14}	c_{33}	c_{44}	-	-	($x10^{11}$ Nm^{-2})
$LiNbO_3$	2.031	0.53	0.742	0.085	2.413	0.646	-	-	[22]
Elasto-optic	p_{11}	p_{12}	p_{13}	p_{14}	p_{31}	p_{33}	p_{41}	p_{44}	-
$LiNbO_3$	-0.026	0.090	0.133	-0.150	0.179	0.071	-0.302	0.292	[23]
Piezo-optic	π_{11}	π_{12}	π_{13}	π_{14}	π_{31}	π_{33}	π_{41}	π_{44}	($x10^{-11}$ m^2N^{-1})
$LiNbO_3^{calc}$	-0.030	0.022	0.058	-0.225	0.075	-0.016	-0.230	0.512	Eq. 2.3

Table 2.3. *Elastic (c_{ij}), elasto-optic (p_{ij}), and piezo-optic (π_{ij}) coefficients of $LiNbO_3$.*

To obtain the changes in the refractive index it is then straightforward using the matrix equation:

$$\Delta n_i = -\frac{n_i^3}{2}\pi_{ij}\sigma_j ; (i, j = 1,...,6) \tag{2.4}$$

Let's consider the simple case that a hydrostatic pressure, P=3 kbar, is applied to the crystal. As it was previously indicated a hydrostatic compressive stress implies a negative value for the symmetric tensor, so that the stress tensor will be of the from $\sigma_{ij}=-P\cdot\delta_{ij}$. In such a case, using **eq. 2.4**, and **Tables 2.2** and **2.3** for Mg:$LiNbO_3$ crystals, the index changes will be given by:

$$\begin{aligned}
\Delta n_x &\cong \frac{n_o^3}{2}(\pi_{11}+\pi_{12}+\pi_{13})P = \frac{n_o^3}{2}(\pi_{11}+\pi_{12}+\pi_{13})P = \frac{n_o^3}{2}0.05P = 0.025 n_o^3 P \\
\Delta n_y &\cong \frac{n_o^3}{2}(\pi_{21}+\pi_{22}+\pi_{23})P = \frac{n_o^3}{2}(\pi_{12}+\pi_{11}+\pi_{13})P = 0.025 n_o^3 P \\
\Delta n_z &\cong \frac{n_e^3}{2}(\pi_{31}+\pi_{32}+\pi_{33})P = \frac{n_e^3}{2}(2\pi_{31}+\pi_{33})P = \frac{n_e^3}{2}(0.134)P = 0.067 n_e^3 P \\
\Delta n_4 &= \Delta n_5 = \Delta n_6 = 0
\end{aligned} \tag{2.5}$$

this indicating that both the refractive indices of $LiNbO_3$ increase with increasing hydrostatic pressure. Supposing that we measure the refractive index at a wavelength of λ=589.3nm, then the corresponding index increments can be estimated (taking the reported values for the refractive indices of n_o=2.2986 and n_e=2.2100 at that wavelength [24]) as:

$$\Delta n_o = (2.2986)^3 \cdot 0.025 (\text{x}10^{-3}\ \text{kbar}) \cdot 3\ (\text{kbar}) = 0.91\ \text{x}10^{-3}$$

$$\Delta n_e = (2.21)^3 \cdot 0.067 (\text{x}10^{-3}\ \text{kbar}) \cdot 3\ (\text{kbar}) = 2.17\ \text{x}10^{-3}$$

which matches extremely well with measured values of $\Delta n_o = 0.95\text{x}10^{-3}$ and $\Delta n_e = 2.12\text{x}10^{-3}$ for an applied hydrostatic pressure of 3 kbar [24].

2.3. Optical properties

$LiNbO_3$ is a uniaxial anisotropic crystal with negative birefringence ($n_e < n_o$). As previously said, its basic optical properties were immediately characterized after it was first grown by the Czochralski technique in 1965 [5, 6].

The dielectric properties in the visible and IR (see **Figure 2.3**) and its optical phonons were, for instance, extensively studied by Barker and Loudon in 1967 [25]. Since then, research on its optical properties has been directed towards specifying issues like the important influence that stoichiometry changes (due to changes in the Li/Nb ratio) or ion doping (with ions like Mg^{2+} or Zn^{2+} to avoid photorefractive damage) have on the refraction index [26, 27, 28], or on its nonlinear

refraction and absorption under laser excitation in the nanosecond (ns) [29], picoseconds (ps) [30], or femtosecond (fs) pulse duration range [31, 32]. Recent interests also include the characterization of its dielectric response in the far-IR region (300µm – i.e. 1THz) where it shows a giant birefringence ($\Delta n = n_o - n_e = 1.61$) [33], and it use to characterize nonlinear periodic poled $LiNbO_3$ (PPLN) structures [34], to give only some examples.

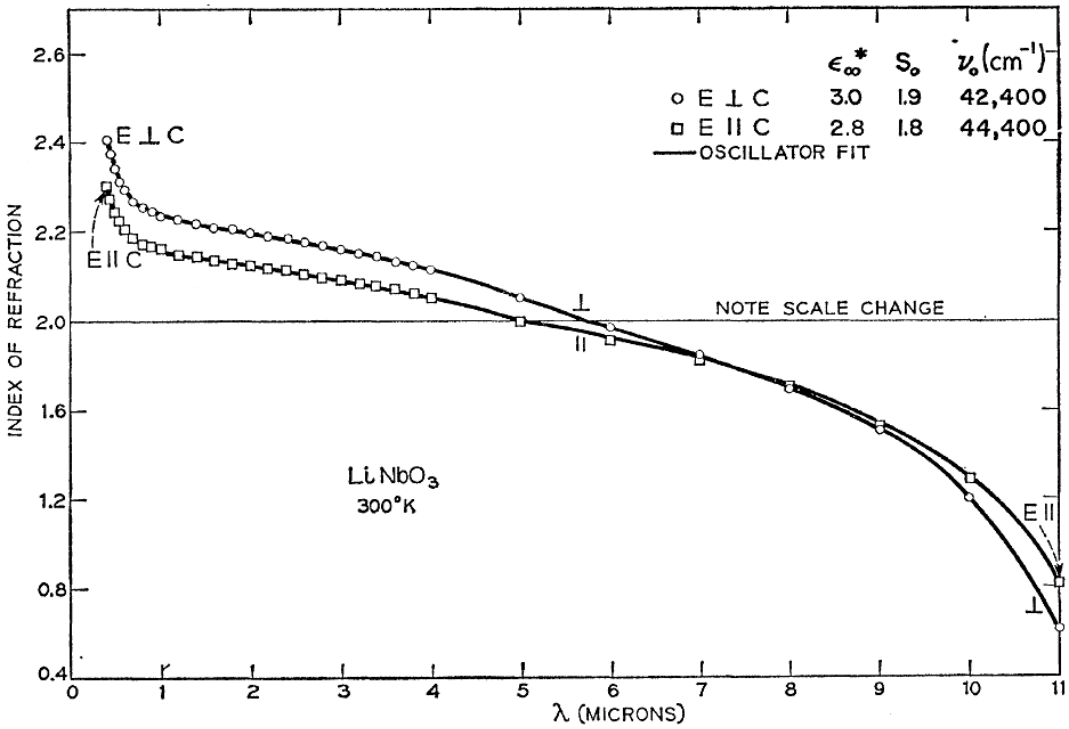

Fig 2.3. *Index of refraction of $LiNbO_3$ in the visible to IR range* [25]

Lithium niobate is also nonlinear material which allows for the harmonic generation and parametric conversion of optical frequencies, and if doped with laser ions like rare-earth ions it can show interesting laser applications as a ferroelectric non-linear laser material [14-16, 20]. In the following chapters some of these properties, such as the luminescence properties of Nd^{3+} and Er^{3+}:Yb^{3+} codoped crystals (**Chapter 5** and **6**, respectively), the laser emission of Nd^{3+}:MgO:$LiNbO_3$ (**Chapter 4**), and some of the Raman properties of $LiNbO_3$ (**Chapter 5**) will be analyzed in some detail in the context of $LiNbO_3$ microstructuring by femtosecond laser pulses irradiation.

2.4. Micro-structuring techniques

2.4.1 Ion beam techniques

During the last decades, focused ion beams have became a very useful and versatile tool in the microelectronics industry, and from that knowledge it has also been applied to crystals such as $LiNbO_3$. The method has led to several very different techniques with different applications, such as ion beam deposition, ion beam etching/milling, ion implantation, swift ion irradiation, crystal ion slicing, and focused ion beam (FIB), or ion beam-enhanced etching [35]. The energy ranges which are applied depend much on the type of technique, ranging from 10-100 eV in ion beam deposition to MeV in the rest. The main modification effect when irradiating crystal samples is the damaging of lattice structure and/or modification of the refraction index, by means of causing nuclear and/or electronic damage. Usually consist on several subsequent processing steps like wet etching or thermal treatment to remove sacrificial volumes or layers. Typical ionic species used are Ar, H, He, C, N, O, F, Si, Cl, Ni, Cu, Sn, Gd, U, Ga, Ti, or others.

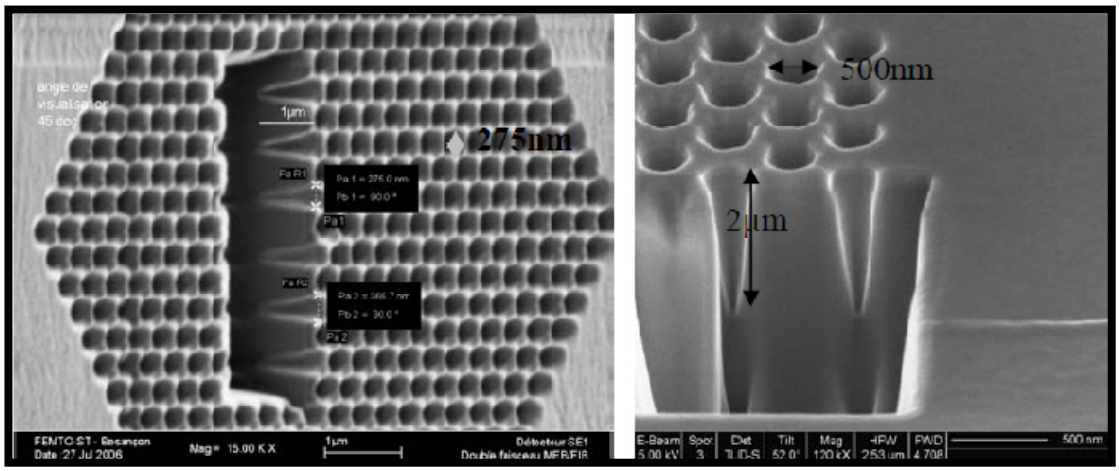

Fig 2.4. *SEM images of FIB cross-sections in $LiNbO_3$ 2D photonic crystals, by N. Courjal et al.* [47]

The main advantages of these ion beam techniques is that they are in a mature stage now, and allow micro-fabricating high quality devices, like very smooth thin films [36-43], waveguides [44], or two-dimensional crystals [45], to mention some examples, with spatial resolutions down to the

nanometre scale [46]. The main disadvantage is that they are intrinsically limited to surface two dimensional patterning, so that a direct three-dimensional (3D) structuring of bulk material without affecting its surface is not possible.

2.4.2 Laser writing techniques

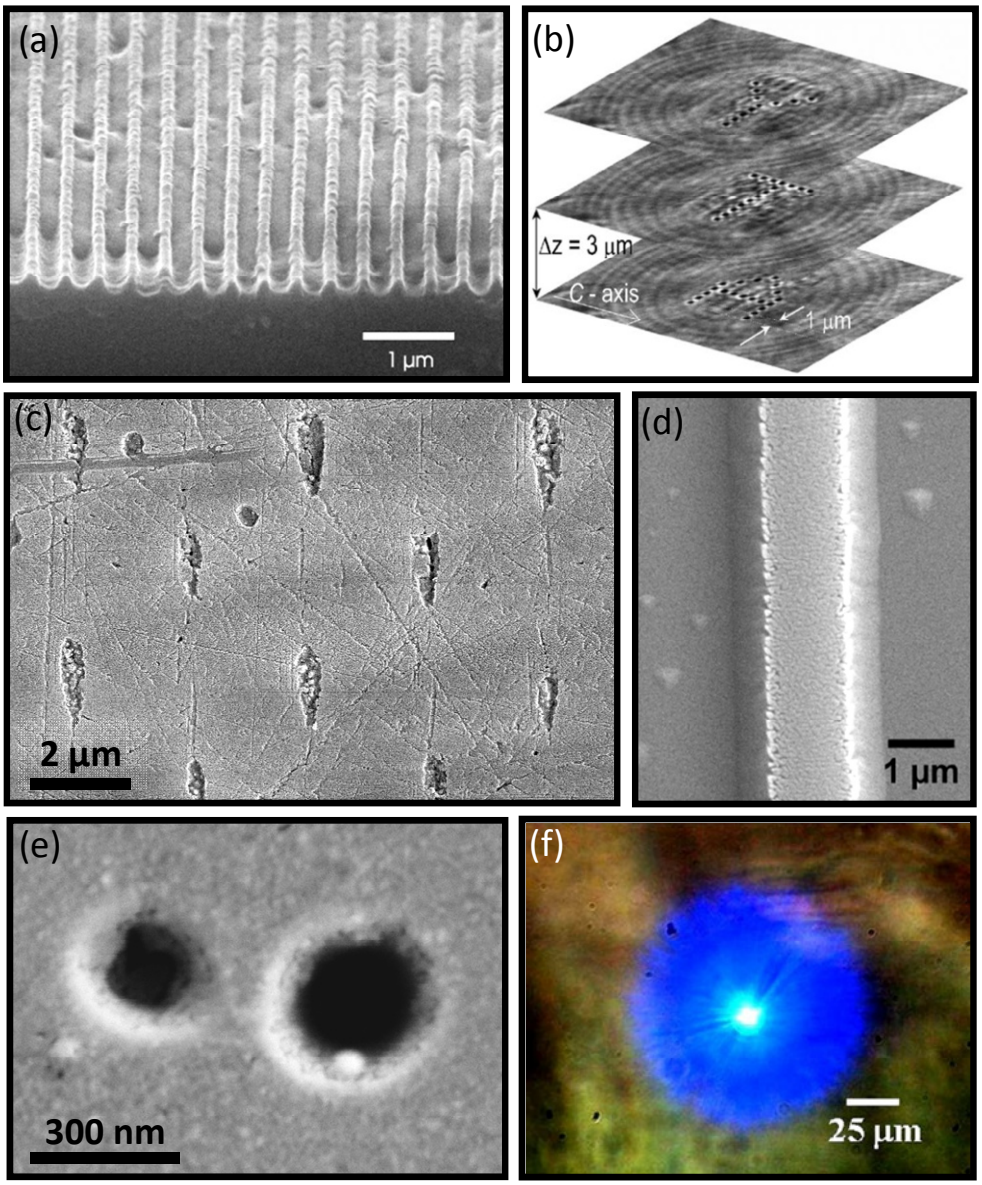

Fig 2.5. *Laser writing applications related to $LiNbO_3$:* **(a)** *Submicron surface relief gratings* [48]*,* **(b)** *3D optical data storage* [56]*,* **(c)** *3D fcc structure photonic crystals* [50]*,* **(d)** *direct ferroelectric domain inversion* [55]*,* **(e)** *surface nanoholes* [63]*,* **(f)** *frequency doubling emission from crystalline $LiNbO_3$ directly grown inside silicate glass* [59].

The application of laser writing in $LiNbO_3$ is manifold: it is generally used to fast generate new or improved functional surface devices such as submicron surface gratings [48], or 3D devices such as waveguides or photonic crystals [49, 50], but it is also used for a wider range of applications such as optical purification of samples [51], etching enhancement [52] or frustration [53], domain inversion [54, 55], optical 3D rewritable bit data storage [56-58], or even for the growth of crystalline $LiNbO_3$ from inside silicate glasses [59]. **Figure 2.5** shows some examples of such applications.

Although the laser-induced breakdown in optically transparent materials has been studied extensively since the laser was invented in the 60's, studies on the laser micro-processing of $LiNbO_3$ truly started in the 80's, mostly based on the use of UV ns pulses [60]. The advent of ultra-short fs pulse laser systems later in the 90's (thanks to new laser techniques such as the chirped pulse amplification (CPA) [61]) changed the prospects, mainly as a result of the finding that the plasma generated during the breakdown could be confined at the threshold regions, thus providing precise control of the processed areas and smaller and faster structures [62]. This finding boosted research on the subject for medical laser applications but it also proved useful for solid-state microelectronics and photonics.

Although current laser patterned structures do not achieve the resolution and smoothness of ion beam fabricated ones, the advantages of ultrafast laser processing $LiNbO_3$ are the fundamental 3D spatial control of the technique, allowing to process bulk material without affecting its surface, and the wide range of different material modifications which can be performed depending on parameters such as the photon energy, pulse duration time, repetition rate, polarization, focusing optics, and so on. The current smaller features achieved in $LiNbO_3$ by direct laser writing reach the $\lambda/10$ limit performed at a wavelength of 0.8 µm, thus giving features 80 nm wide [63]. However, due to new availability of deep-UV ultrashort pulse laser sources [64] the hope is that resolutions down to 20 nm could be achievable by using direct focusing or alternatively by using customizable diffractive optical masks [65].

2.4.3 Chemical etching

Chemical wet etching of $LiNbO_3$ has been mainly investigated in the context of ion beam processing or periodic domain poling [66], so that it is used to reveal volumes whose external face presents a different etchability mainly as a result of lattice changes such as amorphization or different optical axis orientation. The main etching agents used so far in $LiNbO_3$ are: $HF:H_2O$ mixtures in different concentrations [67, 68], $HF:HNO_3$ in mainly (1:2) mixture [69-71], and $HF:H_2SO_4$ in (1:2) mixtures [72]. The *+c* face normally presents a much higher resistance to HF solutions than the *-c* face. Enhancements of the etching process have been reported by means of low-temperature (175-275^{o}C) annealing after processing with ion beams [67], or by ultrasonic baths and/or heating during the wet etching process [72].

With respect to laser processing only a few works have reported the wet etching of $LiNbO_3$, which has been mainly performed with $HF:H_2O$ (1:2) and $HF:HNO_3$ (1:2) mixtures allowing for a complete and precise removal of amorphous volumes after both UV (355 nm) CW irradiation [52], UV (248 nm) 500 fs [53], and IR (800 nm) fs pulse writing [50].

2.4.4 New synthesis techniques of nano-structured $LiNbO_3$

As explained along this chapter, $LiNbO_3$ is one of the most versatile optical materials due to its adequate combination of non-linear and ferroelectric properties, which has led to a deep investigation of its properties over more than 40 decades. All along this introductory chapter references have been given referring to bulk sample devices, however, it is worth mentioning some alternative synthesis approaches which have been recently explored in the context of nanostructure material research.

During the last decade considerable interest has been given to the fundamental application of the $LiNbO_3$ properties into nano-structured materials such as photonic crystals and other nano-structures, due to their potential application in nano-photonic devices. The interest relies on the fact that an enhanced behaviour relative to their bulk counterparts is expected, emerging from the dimensional confinement of light interactions in the media.

As it has been shown, most of the fabrication techniques rely on the growth of samples and subsequent micro-structuring approaches for obtaining thin films or micro-structured devices from them. To avoid further processing of $LiNbO_3$ to achieve nano-scale dimensions, some new approaches have recently been addressed which could allow the synthesis of crystalline nanosized or nanoporous $LiNbO_3$ crystals.

Recent achievements include the synthesis of $LiNbO_3$ inverse opal films with tailored structural properties, which could prove useful for photonic applications [73], the growth of $LiNbO_3$ crystalline nanoparticles keeping the the crystal lattice space group 3m, and showing control over the growth length along the polar axis [74], and the growth of free-standing, well formed $LiNbO_3$ nanowires showing second harmonic responses which could be used as highly orientationally sensitive devices to detect signals bellow the diffraction limit [75].

References

[1] See for example published works with the words "lithium niobate OR LiNbO3" in the title, in the Web of Science® database, of ISI Web of Knowledge℠, published by Thomson Reuters.

[2] A. Räuber, *Chemistry and physics of lithium niobate*, Current Topics in Materials Science **1**, 481-601, Kaldis, North-Holland, Amsterdam (1978)

[3] W. H. Zachariasen, Skr. Norske Vid.-Ada., Oslo, Mat. Naturv. **4** (1928)

[4] B. T. Matthias and J. P. Remeika, *Ferroelectricity in the Ilmenite structure*, Phys. Rev. **76**, 1886 (1949)

[5] S. A. Fedulov, Z. I. Saphiro, P. B. Ladyzhin, *Growth of crystals of $LiNbO_3$, $LiTaO_3$ and $NaNbO_3$ by Czochralski method*, Sov. Phys. Crystallogr. **10**, 2, 218 (1965)

[6] A. A. Ballman, *Growth of piezoelectric and ferroelectric materials by the Czochralski technique*, J. Am. Ceram. Soc. **48**, 2, 112 (1965)

[7] K. Nassau, H. J. Levinstein, and G. M. Loiacono, *Ferroelectric lithium niobate. 1. Growth, domain structure, dislocations and etching*, J. Phys. Chem. Solids **27**, 983 (1966)

[8] K. Nassau, H. J. Levinstein, and G. M. Loiacono, *Ferroelectric lithium niobate. 2. Preparation of single domain crystals*, J. Phys. Chem. Solids **27**, 989 (1966)

[9] S. C. Abrahams, J. M. Reddy, and J. L. Bernstein, *Ferroelectric lithium niobate. 3. Single crystal X-ray diffraction study at 24°C*, J. Phys. Chem. Solids **27**, 997 (1966)

[10] S. C. Abrahams, J. M. Reddy, and J. L. Bernstein, *Ferroelectric lithium niobate. 4. Single crystal neutron diffraction study at 24°C*, J. Phys. Chem. Solids **27**, 1013 (1966)

[11] S. C. Abrahams, J. M. Reddy, and J. L. Bernstein, *Ferroelectric lithium niobate. 5. Polycrystal X-ray diffraction study between 24° and 1200°C*, J. Phys. Chem. Solids **27**, 1019 (1966)

[12] Crystal Technology, Inc., http://www.crystaltechnology.com/

[13] Y. Furukawa, K. Kitamura, S. Takekawa, K. Niwa, and H. Hatano, *Stoichiometric Mg:$LiNbO_3$ as an effective material for nonlinear optics*, Opt. Lett. **23**, 24 (1998)

[14] J. O. Tocho, J. A. Sanz García, F. Jaque, and J. García Solé, *Fluorescence bands of Nd^{3+} sites in $LiNbO_3$:Nd,Mg laser system*, J. Appl. Phys. **70**, 10, 5582 (1991)

[15] C.-H. Huang, L. McCaughan, and D. M. Gill, *Evaluation of Absorption and Emission Cross Section of Er-Doped $LiNbO_3$ for Application to Integrated Optic Amplifiers*, J. Lightwave Tech. **12**, 5, 803 (1994)

[16] E. Cantelar, M. Quintanilla, P. L. Pernas, G. A. Torchia, G. Lifante, and F. Cussó, *Polarized emission and absorption cross-section calculation in $LiNbO_3:Tm^{3+}$*, J. Lum. **128**, 988-991 (2008)

[17] J. F. Nye, *Physical Properties of Crystals*, Oxford University Press, New York, 1985

[18] P. Molina, PhD Thesis, Universidad Autónoma de Madrid, Madrid, 2009

[19] V. Gopalan, K. L. Schepler, V. Dielorf, and I. Biaggio, *Ferroelectric Materials*, in *The Handbook of Photonics*, CRC Press 2007.

[20] K. K. Wong, *Properties of Lithium Niobate*, IEE, London, UK, 2002

[21] J. M. Cabrera, F. Agulló López, F. J. López, *Óptica electromagnética. Vol. II: Materiales y aplicaciones*, Addison-Wesley / Universidad Autónoma de Madrid, Madrid, 2000

[22] R. V. Damle, *Elastic constants of lithium niobate,* J. Phys. D, Appl. Phys. **25**, 1091-1095 (1992)

[23] A. Yariv, and P. Yeh, *Optical Waves in Crystals*, J. Wiley & Sons, New York, 1990

[24] K. Vedam, and T. A. Davis, *Piezo- and Thermo-optic behavior of $LiNbO_3$*, Appl. Phys. Lett. **12**, 4, 138-140 (1968)

[25] A. S. Barker Jr., and R. Loudon, *Dielectric properties and Optical Phonons in $LiNbO_3$*, Phys. Rev. **158**, 2 (1967)

[26] U. Schlarb, K. Betzler, *Influence of the defect structure on the refractive indices of undoped and Mg-doped lithiumniobate*, Phys. Rev. B **50**, 751-757 (1994)

[27] G. Lifante, E. Cantelar, J. A. Muñoz, R. Nevado, J. A. Sanz-García, F. Cussó, *Zn-diffused $LiNbO_3:Er^{3+}/Yb^{3+}$ as a waveguide laser material*, Opt. Mat. **13**, 181-186 (1999)

[28] G. K. Kitaeva, I. I. Naumova, A. A. Mikhailovsky, P. S. Losevsky, and A. N. Penin, *Visible and infrared dispersion of the refractive indices in periodically poled and single domain Nd:Mg:$LiNbO_3$ crystals*, Appl. Phys. B **66**, 201-205 (1998)

[29] R. K. Choubey, R. Trivedi, M. Das, P. K. Sen, P. Sen, S. Kar, K. S. Bartwal, and R. A. Ganeev, *Growth and study of nonlinear refraction and absorption in Mg doped $LiNbO_3$*, J. Crystal Growth **311**, 2597-2601 (2009)

[30] H. Li, F. Zhou, X. Zhang, W. Ji, *Picosecond Z-scan study of bound electronic Kerr effect in $LiNbO_3$ crystal associated with two-photon absorption*, Appl. Phys. B **64**, 659-662 (1997)

[31] H. P. Li, C. H. Kam, Y. L. Lam, W. Ji, *Femtosecond Z-scan measurements of nonlinear refraction in nonlinear optical crystals*, Opt. Mat. **15**, 237-242 (2001)

[32] J. N. B. Reddy, S. Elizabeth, H. L. Bhat, N. Venkatram, D. N. Rao, *Influence of non-stoichiometric defects on nonlinear absorption and refraction in Nd:Zn codoped lithium niobate*, Opt. Mat. **31**, 1022-1026 (2009)

[33] D. Di, G. Ma, J. Ge, S. Hu, and N. Dai, *Terahertz pulse shaping vie birefringence in lithium niobate crystal*, Appl. Phys. B **94**, 623-628 (2009)

[34] W. M. Liu, A. N. Tuchak, Y. H. Yan, G. Kh. Kitaeva, and S. H. Tang, *Characterization of domain structure of periodically poled Mg:$LiNbO_3$ through multifrequency terahertz generation*, Opt. Lett. **34**, 13, 2027 (2009)

[35] F. Chen, *Photonic guiding structures in lithium niobate crystals produced by energetic ion beams*, Appl. Phys. Reviews – Focused Review, J. Appl. Phys. **106**, 081101 (2009)

[36] L. C. Feldman, J. W. Mayer, and S. T. Picraux, *Materials Analysis by Ion Channeling*, Academic, New York, 1982

[37] J. Davidson, and I. Reid, *Novel ion-assisted antireflection coatings for lithium-niobate devices*, Electron. Lett. **25**, 9, 557-558 (1989)

[38] M. Levy, R. M. Osgood Jr., R. Liu, L. E. Cross, G. S. Cargill III, A. Kumar, and H. Bakhru, TITULO, Appl. Phys. Lett. **73**, 2293 (1998)

[39] M. Levy, and A. M. Radojevic, in *Wafer bonding: Applications and Technology*, edited by M. Alexe and U. Gosele, Springer-Verlag, Berlin, Heidelberg, 2004

[40] P. Raibei, and P. Günter, *Optical and electro-optical properties of submicrometer lithium niobate slab waveguides prepared by crystal ion slicing and wafer bonding*, Appl. Phys. Lett. **85**, 4603 (2004)

[41] P. Raibei, and W. H. Steier, *Lithium niobate ridge waveguides and modulators fabricated using smart guide*, Appl. Phys. Lett. **86**, 161115 (2005)

[42] D. W. Ward, E. R. Statz, K. A. Nelson, R. M. Roth, and R. M. Osgood, *Terahertz wave generation and propagation in thin-film lithium niobate produced by crystal ion slicing*, Appl. Phys. Lett. **86**, 022908 (2005)

[43] Y. C. Yu, C. H. Chen, H. Niu, J. Y. Hsu, and T. N. Yang, TITULO, Nucl. Instrum. Methods Phys. Rev. B **256**, 558 (2007)

[44] T. Ruiz, A. Méndez, M. Carrascosa, J. Carnicero, A. García-Cabañez, J. Olivares, F. Agulló-López, A. García-Navarro, and G. García, *Tailoring of refractive index profiles in $LiNbO_3$ optical waveguides by low-fluence swift-ion irradiation*, J. Phys. D: Appl. Phys. **40**, 4454-4459 (2007)

[45] F. Lacour, N. Courjal, M.-P. Bernal, A. Sabac, C. Bainier, M. Spajer, *Nanostructuring lithium niobate substrates by focused ion beam milling*, Opt. Mat. **27**, 1421-1425 (2005)

[46] A. García-Navarro, A. Méndez, J. Olivares, G. García, F. Agull-López, M. Zayat, D. Levy, L. Vazquez, *Morphology of ion tracks and nanopores in $LiNbO_3$ produced by swift-ion-beam irradiation*, Nucl. Instrum. Methods Phys. Res. B **249**, 172-176 (2006)

[47] N. Courjal, M.-P. Bernal, M. Spajer, G. Ulliac, R. Salut, J. Dahlah, and S. Benchabane, *FIB milling for lithium niobate photonic crystals*, Proceedings of the First International Workshop on FIB for Photonics, Eindhoven, the Netherlands, 13-14 June 2008, edited by R. M. de Ridder, F. Ay, and L. J. Kauppinen.

[48] K. Chen, J. Ihlemann, P. Simon, I. Baumann, and W. Sohler, *Generation of submicron surface gratings on $LiNbO_3$ by ultrashort UV laser pulses*, Appl. Phys. A **65**, 517-518 (1997)

[49] L. Gui, B. Xu, and T. C. Chong, *Microstructure in lithium niobate by use of focused femtosecond laser pulses*, IEEE Photon. Technol. Lett. **16**, 5, 1337 (2004)

[50] A. Ródenas, G. Zhou, D. Jaque, and M. Gu, *Rare-earth spontaneous emission control in three-dimensional lithium niobate photonic crystals*, Adv. Mater. **21**, 34, 3526 (2009)

[51] M. Kösters, B. Sturman, P. Werheit, D. Haertle, and K. Buse, *Optical cleaning of congruent lithium niobate crystals*, Nat. Photon. **3**, 510-513 (2009)

[52] F. K. Christensen, M. Müllenborn, *Sub-band-gap laser micromachining of lithium niobate*, Appl. Phys. Lett. **66**, 21, 2772 (1995)

[53] S. Mailis, P. T. Brown, C. L. Sones, I. Zergioti, R. W. Eason, *Etch frustration in congruent lithium niobate single crystals induced by femtosecond ultraviolet laser irradiation*, Appl. Phys. A **74**, 135-137 (2002)

[54] C. L. Sones, C. E. Valdivia, J. G. Scott, S. Mailis, R. W. Eason, D. A. Scrymgeour, V. Gopalan, T. Jungk, E. Soergiel, *Ultraviolet laser-induced sub-micron periodic domain formation in congruent undoped lithium niobate crystals*, Appl. Phys. B **80**, 341-344 (2005)

[55] A. C. Muir, C. L. Sones, S. Mailis, R. W. Eason, T. Jungk, Á. Hoffmann, and E. Soergel, *Direct-writing of inverted domains in lithium niobate using a continuous wave ultra violet laser*, Opt. Express **16**, 4, 2336 (2008)

[56] S. Juodkazis, M. Sudzius, V. Mizeikis, H. Misawa, E. G. Gamaly, Y. W. Liu, O. A. Louchev, K. Kitamura, *Three-dimensional recording by tightly focused femtosecond pulses in $LiNbO_3$*, Appl. Phys. Lett. **89**, 6, 062903 (2006)

[57] E. G. Gamaly, S. Juodkazis, V. Mizeikis, H. Misawa, A. V. Rode, W. Z. Krolikowski, and K. Kitamura, *Three-dimensional write-read-erase memory bits by femtosecond laser pulses in photorefractive $LiNbO_3$ crystals*, Curr. Appl. Phys. **8**, 416-419 (2008)

[58] S. Juodkazis, V. Mizeikis, M. Sudzlus, H. Misawa, K. Kitamura, S. Takekawa, E. G. Gamaly, W. Z. Krolikowski, and A. V. Rode, *Laser induced memory bits in photorefractive $LiNbO_3$ and $LiTaO_3$*, Appl. Phys. A **93**, 1, 129-133 (2008)

[59] LNB growth laser glass

[60] M. Eyett, and D. Bäuerle, *Influence of the beam spot size on ablation rates in pulsed-laser processing*, Appl. Phys. Lett. **51**, 24, 2054 (1987)

[61] D. Strickland, and G. Mourou, *Compression of amplified chirped optical pulses*, Opt. Commun. **56**, 219 (1985)

[62] D. Du, X.Liu, G. Korn, J. Squier, and G. Mourou, *Laser-induced breakdown by impact ionization in SiO_2 with pulse widths from 7 ns to 150 fs*, Appl. Phys. Lett. **64**, 23 (1994)

[63] A. Ródenas, J. Lamela, D. Jaque, G. Lifante, F. Jaque, A. García-Martín, G. Zhou, and M. Gu, *Near-field imaging of femtosecond laser ablated sub-λ/4 holes in lithium niobate*, Appl. Phys. Lett. **95**, 181103 (2009)

[64] T. Nagy, P. Simon, *Generation of 200-μJ, sub-25-fs deep-UV pulses using a noble-gas-filled hollow fiber*, Opt. Lett. **34**, 15, 2300 (2009)

[65] J. Ihlemann, J. H. Klein-Wiele, J. Bekesi, and P. Simon, *UV Ultrafast Laser Processing using Phase Masks*, J. Phys.: Conf. Ser. **59**, 449-452 (2007)

[66] P. Molina, M. O. Ramírez,J. V. García-Santizo, S. Álvarez-García, R. Pazik, W. Strek, P. J. Derén, and L. E. Bausá, *Micrometric spatial control of rare earth ion emission in $LiNbO_3$: A two-dimensional multicolor array*, Appl. Phys. Lett. **95**, 051103 (2009)

[67] A. Ofan, O. Gaathon, L. Vanamurthy, S. Bakhru, H. Bakhru, K. Evans-Lutterodt, and R. M. Osgood Jr., *Origin of highly spatially selective etching in deeply implanted complex oxides*, Appl. Phys. Lett. **93**, 181906 (2008)

[68] M. Bianconi, F. Bergamini, G. G. Bentini, A. Cerutti, M. Chiarini, P. De Nicola, G. Pennestrì, *Modification of the etching properties of x-cut Lithium Niobate by ion implantation*, Nucl. Instr. Met. Phys. Res. B **226**, 1238-1241 (2008)

[69] F. Laurell, J. Webjörn, G. Arvidsson, and J. Holmberg, *Wet etching of proton-exchanged lithium niobate - A novel processing technique*, J. Lightwave Tech. **10**, 11 (1992)

[70] H. Hu, R. Ricken, W. Sohler, and R. B. Wehrspohn, *Lithium niobate ridge waveguides fabricated by wet etching*, IEEE Photon. Tech. Lett. **19**, 6, 417 (2007)

[71] M. L. Crespillo, M. Otto, A. Munoz-Martin, J. Olivares, F. Agulló-López, M. Seibt, M. Toulemonde, and C. Trautmann, *Optimization of nanopores obtained by chemical etching on swift-ion irradiated lithium niobate*, Nucl. Instr. and Meth. B **267**, 6, 1035-1038 (2009)

[72] Z. D. Gao, Q. J. Wang, Y. Zhang, and S. N. Zhu, *Etching study of poled lithium tantalite crystal using wet etching technique with ultrasonic assistance*, Opt. Mat. **30**, 847-850 (2008)

[73] D. Wang, F. Caruso, *Lithium Niobate Inverse Opals Prepared by Templating Colloidal Crystals of Polyelectrolyte-Coated Spheres*, Adv. Mater. **15**, 3, 205 (2003)

[74] B. D. Wood, V. Mocanu, and B. D. Gates, *Solution-Phase Synthesis of Crystalline Lithium Niobate Nanostructures*, Adv. Mater. **20**, 4552-4556 (2008)

[75] R. Grange, J.-W. Choi, C.-L. Hsieh, Y. Pu, A. Magrez, R. Smajda, L. Forró, and D. Psaltis, *Lithium niobate nanowires synthesis, optical properties, and manipulation*, Appl. Phys. Lett. **95**, 143105 (2009)

Chapter 3

Femtosecond laser writing in $LiNbO_3$

In this chapter the subject of direct femtosecond laser writing into $LiNbO_3$ is introduced. First, a theoretical introduction to the focal intensity distribution of a Gaussian beam and its nonlinear propagation effects and main optical aberrations which are usually encountered are overviewed. The different nonlinear ionization mechanisms responsible for the permanent modification of crystals are also briefly overviewed, together with the effects the repetition rate and scan speed or pulse overlapping have on the microfabrication process. Secondly, experimental results depicting some of the different effects previously explained are shown.

3.1. Introduction

The laser microstructuring of a dielectric is the process in which the energy of a laser beam is transferred to the material causing some kind of structural changes within the focal volume.

The mechanisms by which the modification of a solid takes place can be usually divided into two cases: In the low energy density case the laser fluence is well below the damage threshold but it is sufficient to trigger a particular change in the material optical and structural properties. In the high energy density case *optical breakdown* occurs, which is the process in which the absorbed laser energy causes the ionization of a large number of electrons, and these subsequently transfer its energy to the lattice causing bond breaking and converting the absorbing volume into a high density plasma.

Independently of whether the laser inscription is performed at the surface or inside a crystal, plasma expansion always induces strong pressures on the surroundings which can be much greater than the material strength, and cause the appearance of stress fields and piezo-optic refractive index changes of different sign. Ionized regions can also relax and re-solidify in an amorphous phase, so that the index of refraction of these zones will be significantly lower than that of the crystalline ones.

In the following sections the non-linear laser-solid interaction when a laser pulse is tightly focused inside a transparent dielectric is very described. In **Section 3.2** the fundamental issues concerning the laser inscription process are briefly overviewed, and comparison is then made with $LiNbO_3$ ablation and bulk direct write experiments in **Section 3.3**.

3.2. Microstructuring of dielectrics

As mentioned, to explain the laser microstructuring phenomena in crystals it is necessary to revise the basic material and optical issues regarding the laser focal shape and intensity distribution, the role of pulse duration and repetition rate with respect to the induced modifications effects, the

differences when focusing at the surface interface or in bulk volume, the optical distortion effects which can be induced by the material nonlinearity or by the aberrations of the focusing optics, and finally the typical photo-response mechanisms of ferroelectric materials such as $LiNbO_3$. In the following sections these issues are briefly explained.

3.2.1. Laser intensity distribution in the focal region

The electric field in the focus of an ideal Gaussian beam, $E(r,z,t)$, reads [1]:

$$E(r,z,t) = E_0(t)\frac{1}{\left(1+\frac{z^2}{z_0^2}\right)^{\frac{1}{2}}} exp\left\{-\frac{r^2}{r_0^2\left(1+\frac{z^2}{z_0^2}\right)}\right\} \times exp\left\{-ikz - ik\frac{r^2}{2z\left(1+\frac{z^2}{z_0^2}\right)} + itan^{-1}\left(\frac{z_0^2}{z^2}\right)\right\} \quad (3.1)$$

where r_0 is the beam waist minimum (radius) at $z=0$, and z_0 is the Rayleigh length. Supposing the beam is not distorted by nonlinear effects in the material, the lateral and axial extents of the focal volume at $1/e^2$ intensity level to be:

$$r_0 = 0.61\lambda/NA \quad (3.2)$$

$$L = 2z_0 = 2\pi r_0^2 n_0/\lambda \quad (3.3)$$

where n_0 is the real part of the refraction index, λ is the laser wavelength, and NA the numerical aperture lens. The cylindrical focal volume (where the electric field decreases e-fold along the radius and by a factor of two along the z-axis is then, in a first order approximation:

$$V_{foc} \cong 2\pi r_0^2 z_0 = 2.7 n_0 \lambda^3/NA^4 \quad (3.4)$$

and the focal spot area is:

$$S_{foc} \cong 1.17\lambda^2/NA^2 \quad (3.5)$$

Supposing these approximations, the typical laser intensity values for direct laser micro-fabricating inside a solid can be calculated. Using a tight focusing microscope objective of NA=1.4, a laser wavelength of 0.8 μm, and a refractive index of 2.2, the focal volume parameters will be: volume *V*=0.8 μm^3, focal spot diameter *d*=0.7 μm, and the axial extension *L*=2 μm.

These focal dimensions imply that if a 120 fs pulse of energy 100 nJ is focused inside the crystal, the total intensity inside the sample will be almost of the order of petawatts per cm^2:

$$I = \frac{(1-R)E_{pulse}}{\tau_{pulse} S_{foc}} = 1.9 \times 10^{14}\ W/cm^2 = 0.19\ PW/cm^2 \quad (3.6)$$

where R is the sample reflectivity, $R=(n_0\text{-}1/n_0+1)^2$ for normal incidence.

In real experiments however, the focal shape can be strongly distorted if the laser is focused inside a nonlinear material. The origin of these distortions can always be in the focusing system optical aberrations, but also, and very importantly, they can be produced by the material nonlinear response to the laser field.

3.2.2. Distortions of the focal region

At first instance the direct laser writing (DLW) technique only requires choosing of an adequate lens and to move the focal spot through the sample, in order to direct write the desired design. However, depending on the laser power and NA of the writing optics, the material can happen to change its behaviour, playing an active role and switching the interaction process from an externally focused to an internal self-focused one. What is more, depending only on the optics used, the light distribution inside the medium can departure from the expected Gaussian shape as a result of geometrical optical aberrations. Although these two issues belong to different branches of Optics (geometrical optics and nonlinear optics) they are typically encountered when micro-fabricating inside a nonlinear crystal such as $LiNbO_3$, and so they are next overviewed.

3.2.2.1. Self-focusing and filamentation

The self-focusing of light is the process by which an intense beam modifies its own propagation path as a result of the intensity dependent index of refraction of the transparent medium [2]. The converging effect due to a laser induced positive index increase is illustrated in **Figure 3.1 (a)**. As an approximation, this behaviour is usually taken into account by considering the intensity dependence of the refraction index and absorption coefficient in the form:

$$n = n_0 + n_2 I \tag{3.7}$$

$$\alpha = \alpha_0 + \beta I \tag{3.8}$$

where n_2 and β are the nonlinear refraction-index and absorption coefficients, respectively. The nonlinear refraction and absorption of $LiNbO_3$ laser crystals is usually measured by Z-scan techniques [3, 4]. The main mechanisms by which the nonlinear refraction is entailed are the electronic Kerr (also called Kerr electro-optic effect or quadratic electro-optic effect) [2], and the pump induced thermal lens [5] and excited state population lens effects [6]. However, when the irradiation is performed with short laser pulses, in the nanosecond (ns) to femtosecond (fs) range, thermal and population effects can be disregarded (unless high intensities and very high repetition rates are used (~MHz) which can entail heat accumulation), and the main nonlinear effect is of Kerr electronic type.

The main nonlinear refractive index and absorption coefficients reported in literature for short pulse in $LiNbO_3$ crystals are listed in **Table 3.1**. As it can be seen, the multiphoton absorption process is a two photon (2PA) or three photon (3PA) absorption process depending on the wavelength used (visible or NIR), and independently on the pulse duration in the 1 ns to 150 fs studied range. It is however very remarkable that the multiphoton nonlinear absorption coefficient β is 2 orders of magnitude lower in the ps range with respect to the ns range, and 3 orders of magnitude for the fs regime. With respect to the nonlinear refraction, the Kerr self-focusing effect is always positive, with the only exception of undoped congruent $LiNbO_3$ in the ns regime, for which it is negative, most probably due to the photorefractive effect. The nonlinear refraction index n_2 is of

the same order of magnitude for ps and fs pulses, and 3 orders of magnitude lower than in the ns regime.

	Nanosecond			Picosecond	Femtosecond				
Set-up, Ref., MPA	**6 ns, @1064 nm, 10 Hz, Ref.[7], 3PA**			**25 ps, @532 nm, 10 Hz, Ref.[8], 2PA**	**150 fs, @780 nm, 76 MHz, Ref.[9], 3PA**	**110 fs, @800 nm, 1 kHz, Ref.[10], 3PA**				
Sample	CLN	MgO:LN 5 mol%	MgO:LN 7 mol%	CLN	MgO:LN 6 mol%	SLN	CLN	Zn:LN 1 mol%	Zn:LN 2.5 mol%	Nd:Zn:LN 1.5-2.5 mol%
n_2 (cm/TW)	-2.1	1.51	1.26	5.3 $x10^{-3}$	2 $x10^{-3}$	1.446 $x10^{-3}$	1.132 $x10^{-3}$	1.006 $x10^{-3}$	0.880 $x10^{-3}$	0.956 $x10^{-3}$
β (cm/GW)	27.8	27.4	28.0	2.5 $x10^{-1}$	-	6.7 $x10^{-2}$	9.4 $x10^{-2}$	6.5 $x10^{-2}$	7.5 $x10^{-2}$	8.1 $x10^{-2}$

Table 3.1. *Z-scan parameters, multiphoton absorption process (MPA), and nonlinear refractive index and absorption parameters for different stoichiometric and congruently doped $LiNbO_3$ samples.*

However, it is important noticing that the values obtained by these Z-scan experiments are applicable up to ~25 GW/cm^2, which is the damage threshold typically observed in such experiments [11], while for DLW microfabrication the usual intensities at the focus spot are of about 10^2 GW/cm^2 (see **Ec. 3.6**). Due to this difference in the laser intensity, and as we will see in **Section 3.2.3**, the absorption and ionization mechanisms which can be induced when DLW microfabricating in $LiNbO_3$ can differ from a simple multiphoton absorption process. Nevertheless, these different n_2 values are important in order to differentiate between the different Kerr effect nonlinear regimes which are entailed by the laser beam. In this sense, the optical Kerr effect can originate from at least two contributions, an ultrafast pure electronic response with time constants below 1 fs, and a slower response due to inelastic Raman scattering and nuclear motion [12]. The optical Kerr coefficient is thus clearly dependent on the pulse duration, as seen by the values in **Table 3.1**.

The complexity of short pulse nonlinear propagation is further increased by the generation of plasma volumes in the crystal due to ionization of the medium. The ionization of the medium summed to the nonlinear self-focusing processes implies that the laser propagation cannot be easily predicted, and complex calculations on the propagation and interaction mechanisms have to be performed. In general, the generation of a plasma involves a local reduction in the refraction index [13], making the beam to diffract and diverge (see **Figure 3.1 (b)**).

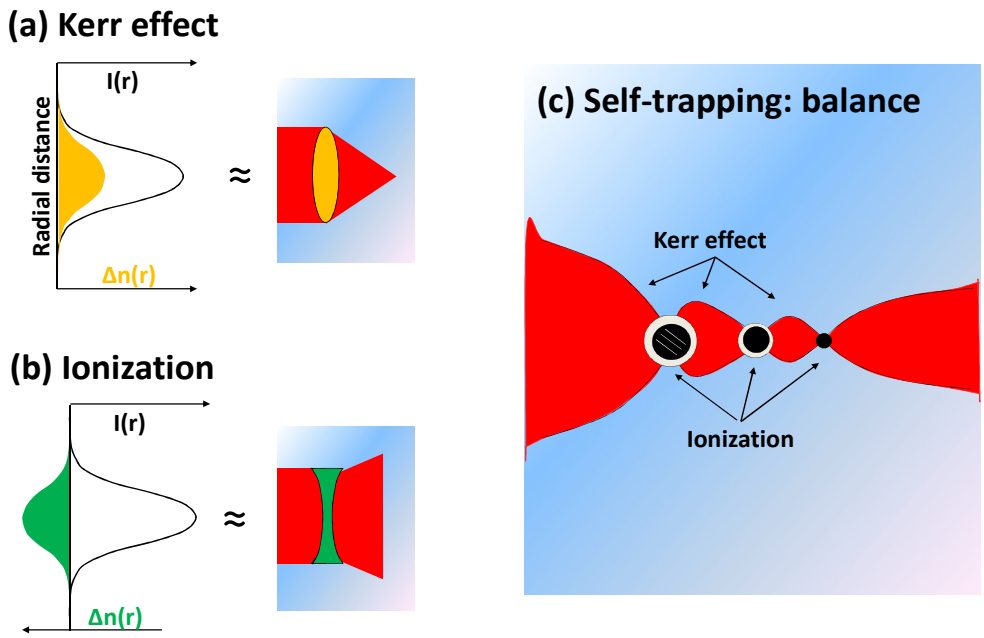

Fig. 3.1. *Schematic representation of the self-focusing Kerr effect due to positive nonlinear* n_2 **(a)**, *divergence of the beam at ionized regions* **(b)**, *and the particular case of self-trapping in the core of the beam, where a spontaneous filament emerges supported by the balance between Kerr-induced self-focusing and plasma-induced de-focusing* **(c)**.

A different self-action effect to the self-focusing is the self-trapping of light, which is illustrated in **Figure 3.1 (c)**. In this process the laser beam can propagate with a quasi-constant diameter as a consequence of the balance between self-focusing and diffraction effects, such as those occurring when the transparent media is locally ionized. The process is also usually called *filamentation* [14], or sometimes *self-channeling* [15, 16], due to the fact that the quasi-continuous self-guided beam can happen to propagate for a few, to many Rayleigh lengths. It is known that the core of the filament contains only a small fraction of the total beam power, limited by the so called *'intensity*

clamping effect', while the remaining excess stays in the filament periphery, without apparent trapping. **Fig. 3.1 (c)** depicts the focusing-defocusing balance of the beam core.

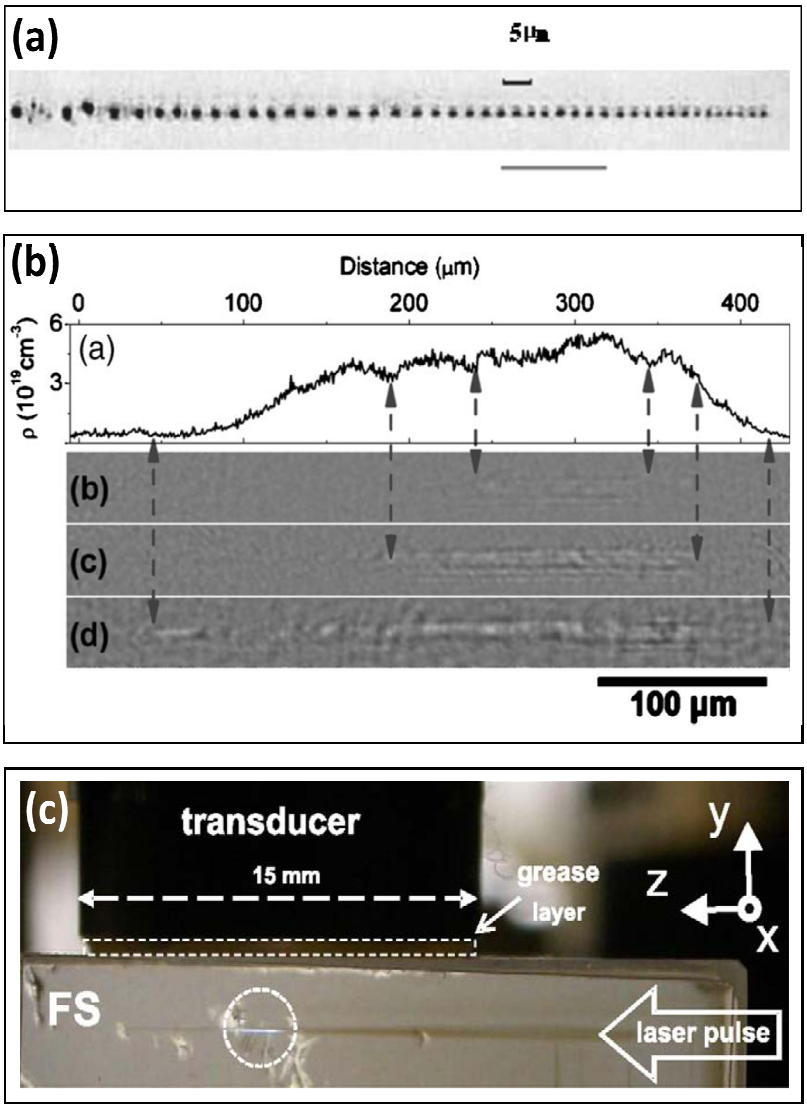

Fig. 3.2. *Examples of self-trapped filaments created in bulk transparent samples:* **(a)** *Quasi-periodic voxel structure with a length of several hundred micrometers inside CaF_2 crystals written with 250 pulses with 30 μJ single pulse energy, at a wavelength of 800 nm, 120 fs duration, 1 kHz frequency and focused with 0.9 NA objective at 950 μm depth* [17]. **(b)** *Filament structures written in fused silica glass after single-shot accumulation of 1, 10, and 100 pulses -(b), (c), (d), respectively on the inset- at a wavelength of 248 nm, 450 fs and focused with 0.4 NA at 900 μm depth; (a) shows the calculated time-integrated maximum electron density along the plasma string from pump-probe experiments* [18]. **(c)** *Side-view of the plasma channel (dashed circle), and optical damage tracks (damage traces) in fused silica after single pulse irradiation with 20 μJ, 800 nm wavelength, 150 fs, 1 kHz frequency and focused with a 0.035 NA lens* [19].

Figure 3.2 shows some results on fs pulse induced self-channels in CaF_2 crystals (**Fig 3.2(a)**) and fused silica glasses (**Fig. (b)** and **(c)**), which are among the most used transparent materials for filamentation investigations in solids.

Despite the huge amount of theoretical and experimental studies devoted to the subject, the physics underlying the spontaneous formation of filaments in transparent dielectrics is still under debate. The most common description considers the filament as a self-guided beam whose dynamic equilibrium is supported by the balance between self-focusing of the Kerr nonlinear medium and defocusing at plasma regions (where the plasma is induced by the laser ionization of the medium) and diffraction. However, other models have been proposed, in which *filamentation* occurs without *self-channelling*. In this case the role of non-trapped light is essential, and filamentation appears mainly due to multiphoton ionization-induced nonlinear losses, rather than electron plasma induced changes in the refractive index [16].

Independently of the exact underlying mechanisms, the self-trapping or filamentation of pulses is known to occur at a threshold power condition, given by the critical value:

$$P_{cr} = \frac{\pi(0.61)^2\lambda_0^2}{8n_0n_2} \approx 0.15\frac{\lambda_0^2}{n_0n_2} = 0.44\ MW|_{LiNbO_3} \tag{3.9}$$

which is of about 0.44 MW for doped $LiNbO_3$ samples and 150 fs laser pulses (see **Table 3.1** for n_2 values). When the power of the laser beam greatly exceeds this P_{cr} value then self-focusing occurs, and filamentation will happen if the exact balance conditions are produced.

3.2.2.2. Numerical aperture and spherical aberration

Another important subject when DLW is the distortion of the focal intensity distribution due to optical aberrations of the focusing lenses. At the interface between air and glass spherical aberration is known to occur, for example, causing a variation of the focus position as a function of the incidence angle.

Figure 3.3 (a) shows this geometrical effect, which modifies the linear focus known for index-matching conditions, producing an elongation due to the different incident angles, characterized by the distance between the paraxial focus and the marginal focus. Moreover, as a result of this distortion not only longitudinal spreading of the light distribution occurs, but also radial spreading takes place.

Spherical aberration is the effect by which rays originating from one object point before the lens intersect at different points for different angles on the other side of the lens [20]. The effect is originated by the index mismatch at the dielectric interface, and both different scalar [21, 22] and vectorial [23, 24] theories of diffraction have been employed to describe it.

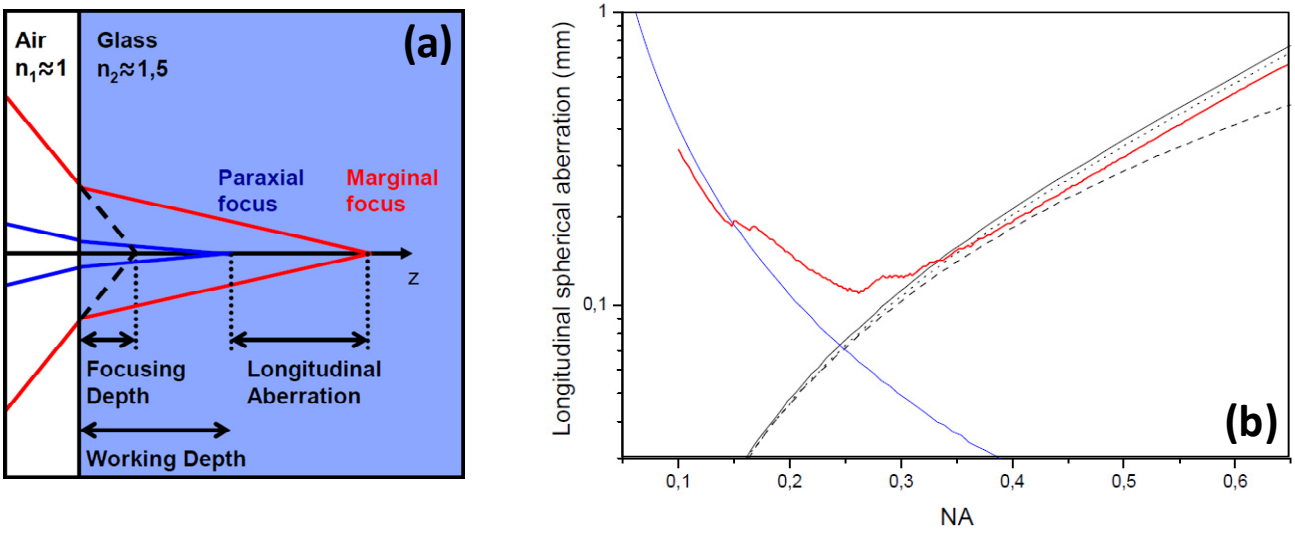

Fig. 3.3. (a) *Focusing geometry showing the linear focusing depth (focus in air, i.e. in index-matching conditions), the paraxial focus or working depth, and the marginal focus, or longitudinal spherical aberration LSA. The best focus is located at an intermediate point between the marginal and paraxial focuses.* **(b)** *Longitudinal spherical aberration as a function of NA for a fixed depth of 3 mm in fused silica as deduced from different approaches: red is the vectorial approach, solid line and dots are different scalar approaches, dashed is using Seidel theory, and blue is the confocal parameter* $l_{confocal}$ [25].

The most visible effect of spherical aberration is the characteristic elongation of the focal volume along the longitudinal direction, shown in **Fig. 3.3 (a)**. The basic resulting effect is that the deeper the focusing, the more elongated the focal volume becomes.

In most theoretical studies a longitudinal spherical aberration parameter (LSA) is defined in order to characterize the effect, which is the distance between the paraxial and marginal focuses. In the particular case of low NA, for example, the longitudinal spreading of light is mainly due to diffraction effects, and the LSA parameter is simply described by a confocal parameter $l_{confocal}$:

$$l_{confocal} = 4n_2 \frac{\lambda}{NA^2} \tag{3.10}$$

However, this formula works only for the low NA limit (NA≤0.15). While other models give a better prediction for the high NA regime. The dependence of LSA with NA, for the different models, is shown in **Figure 3.3 (b)**, as extracted from the work of Huot et al [25]. It can be seen that while the $l_{confocal}$ parameter is correct for low NA, other scalar approaches underestimate the LSA for low NA, the vectorial approach giving the full description. The general conclusion is that for high enough NA, and depending on the focusing depth, spherical aberration governs.

Further theoretical details of this effect are out of the scope of this work, but an experimental characterization of the high-NA focusing in different crystals is presented on **Section 3.3.2.2**.

3.2.2.3. Birefringence induced aberration

It is very interesting to consider the special case of high-NA (NA≥0.6) focusing in high index media such as crystals. In this case the spherical aberration is very strong, but an additional aberration effect can appear if the crystal shows birefringence: supposing a uniaxial crystal and a laser beam propagating along the symmetry axis, the radially and tangentially polarized beams will focus at different points along the longitudinal axis. This polarization broadening can be so strong, that for certain conditions the two spots separate completely.

This effect was predicted and calculated in 2001 by Stallinga while working at the Philips Research Laboratories using a Debye approach to vector diffraction theory [26]. **Figure 3.4** shows the vector diagram at the interface. The two propagation media 1 and 2 are separated by an interface at *z=-d*. The exit pupil of the optical system is at *z=-R*, and the focal plane is at *z=0*. Medium 1 is isotropic, and medium 2 is uniaxial birefringent with the optical axis $\hat{a}$ along the z axis.

The associated wavevectors are $\hat{k}_1$ and $\hat{k}_2$, and the polarization vectors are $\hat{p}_1$and $\hat{p}_2$ (parallel to the incidence plane), and $\hat{s}_1$ and $\hat{s}_2$ (perpendicular to the plane of incidence and optical axis). Thus, there are two polarization field components: the radially polarized, and the tangentially polarized one.

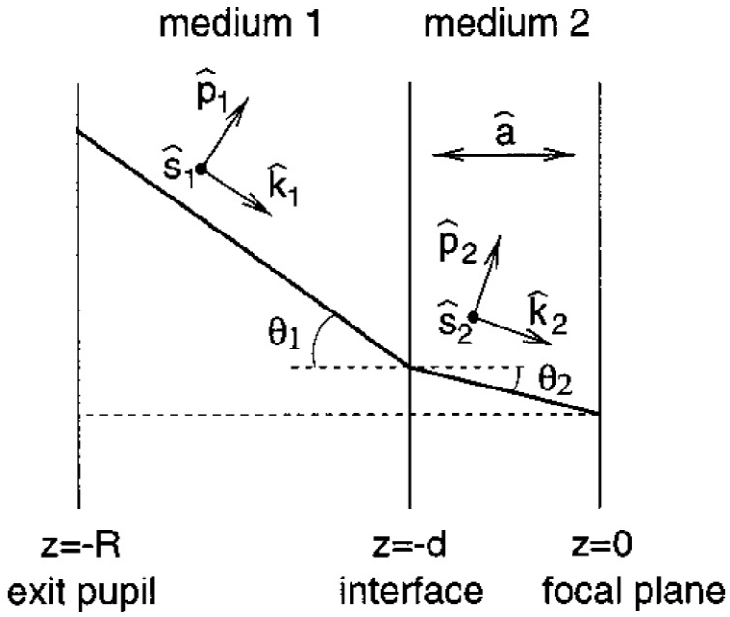

Fig. 3.4. *Vector diagram presented by Stallinga in his work from 2001 [26]. The two propagation media 1 and 2 are separated by an interface at z=-d. The exit pupil of the optical system is at z=-R, and the focal plane is at z=0. Medium 1 is isotropic, and Medium 2 is uniaxial birefringent with the optical axis â along the z axis. The associated wavevectors are $\hat{k}_1$ and $\hat{k}_2$, and the polarization vectors are $\hat{p}_1$and $\hat{p}_2$ (parallel to the incidence plane), and $\hat{s}_1$ and $\hat{s}_2$ (perpendicular to the plane of incidence and optical axis).*

The final effect is that the focal spot of the radially polarized field in the exit pupil will be defocused with respect to the tangential polarization focus spot. The distance between the two polarized spots depends on the value of birefringence and NA used.

The focal point must be on the optical axis because of rotational axis, so that the intensity distribution in the meridional plane for different values of axial birefringence can be calculated, and it is shown in **Figure 3.5** as extracted from [26]. In this calculation the input polarization was

circular, and the writing parameters are NA=0.85, λ=400nm, n_1=1, n_2=1.5, and d=150µm. The focal spot broadening can be seen to deform as the birefringence is increased causing a focal splitting.

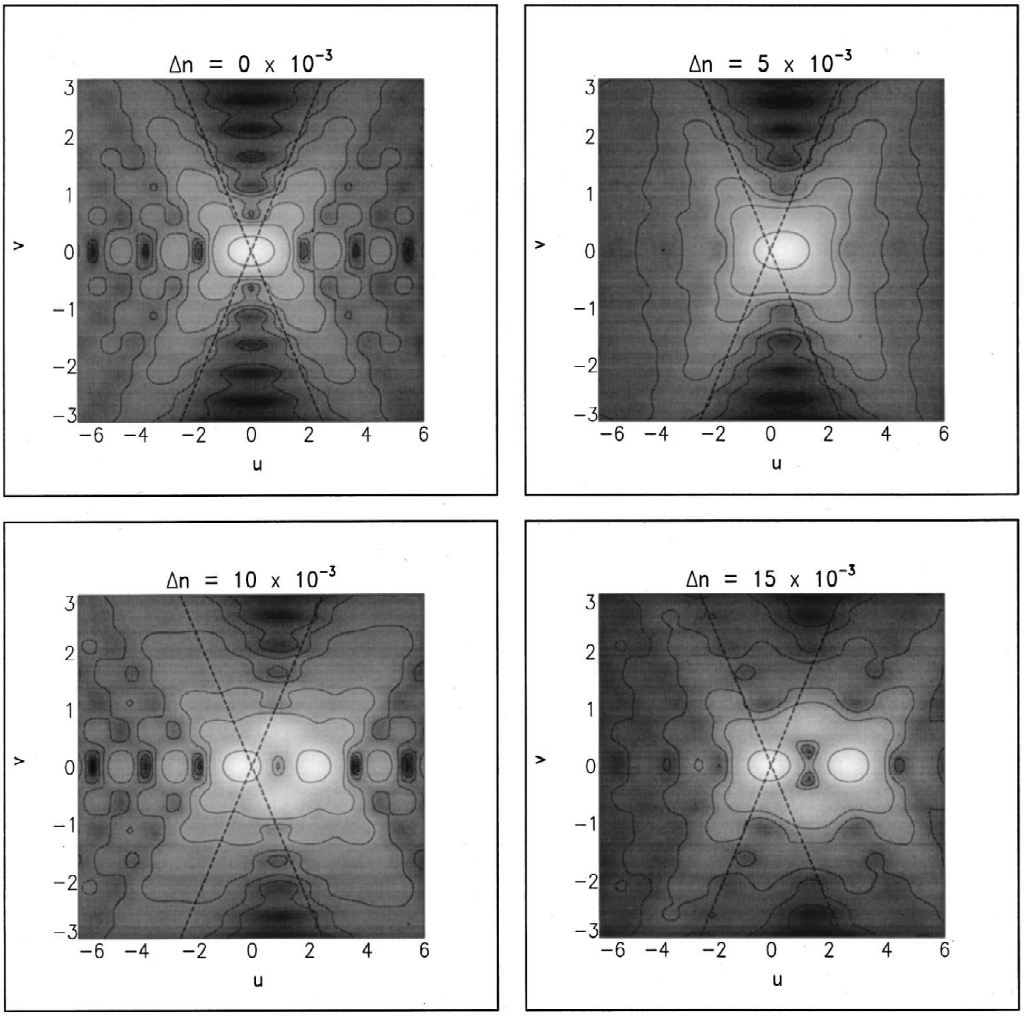

Fig. 3.5. *Intensity distribution calculation in the meridional plane for different birefringence values, as extracted from [26]. The intensity increases from black to white. Full lines are isophotes for intensities 0.50, 0.10, 0.05, 0.02, 0.01, 0.005,and 0.001; The input polarization was circular, and the writing parameters are NA=0.85, λ=400nm, n_1=1, n_2=1.5, and d=150µm. The focal spot broadening can be seen to deform as the birefringence is increased causing a focal splitting.*

This effect can be observed in rare-earth doped $LiNbO_3$ crystals, which present a birefringence of about ~$80x10^{-3}$ at the NIR wavelength of 800 nm. Experimental results with linear input polarization and immersion oil NA=1.45 optics are presented in the **Section 3.3.2** of this chapter.

3.2.3. Photo-ionization mechanisms in crystals

The direct laser-induced optical breakdown of dielectrics by fs laser pulses is very precise when the laser fluence is near the threshold. Focused pulses from a high-power fs laser can damage virtually any material when the induced electric field is high enough to produce optical breakdown. However, despite numerous works on the subject the deterministic nature of the interaction process is yet not well understood.

In the traditional view of the ablation mechanism, optical breakdown is believed to be produced by *avalanche ionization*, in which the seed un-bound free-electrons in the focal region are accelerated by the laser electric field to create a cascade of free electrons through impacts or collisions, and the seed electrons are conversely obtained by *multiphoton absorption* (MPA). This ablation mechanism was anticipated by Bloembergen in 1974 [27]. The MPA process has been generally believed to be the main ionization process responsible for providing seed fre-electrons, through the absorption of several photons by bound electrons, so that its energy would be enough to bridge the bandgap ($E_g \approx 3.9$ eV in $LiNbO_3$). This nonlinear absorption process is depicted in **Figure 3.6**, where a simplified energy diagram is shown. Once the electrons are in the conduction band, they serve as seed for further ionization via *avalanche* (or *impact*) *ionization*. As already said, the avalanche process occurs when electrons in the conduction band absorb sufficient energy to ionize another electron via direct collision, and then these two electrons can continue the process of absorption and impact ionization, creating more free carriers in an cascade mechanism which makes the density of free electrons to grow exponentially.

However, seeds can also be considered to come from other processes such as electron *tunnelling*. In a famous work, Keldysh showed that both multiphoton and tunnelling processes could be described within the same framework, giving a parameter (the *Keldysh parameter*) that can 'select' between both processes simply depending on the laser intensity and frequency, and on the energy band gap and refraction index of the dielectric material [28]. *Tunnelling ionization* is the process by which the electric field of the laser suppresses the Coulomb well that binds the valence

electrons to its atom. If the laser electric field is strong enough, the Coulomb well is distorted enough for the bound electron to tunnel and become a free electron in the conduction band.

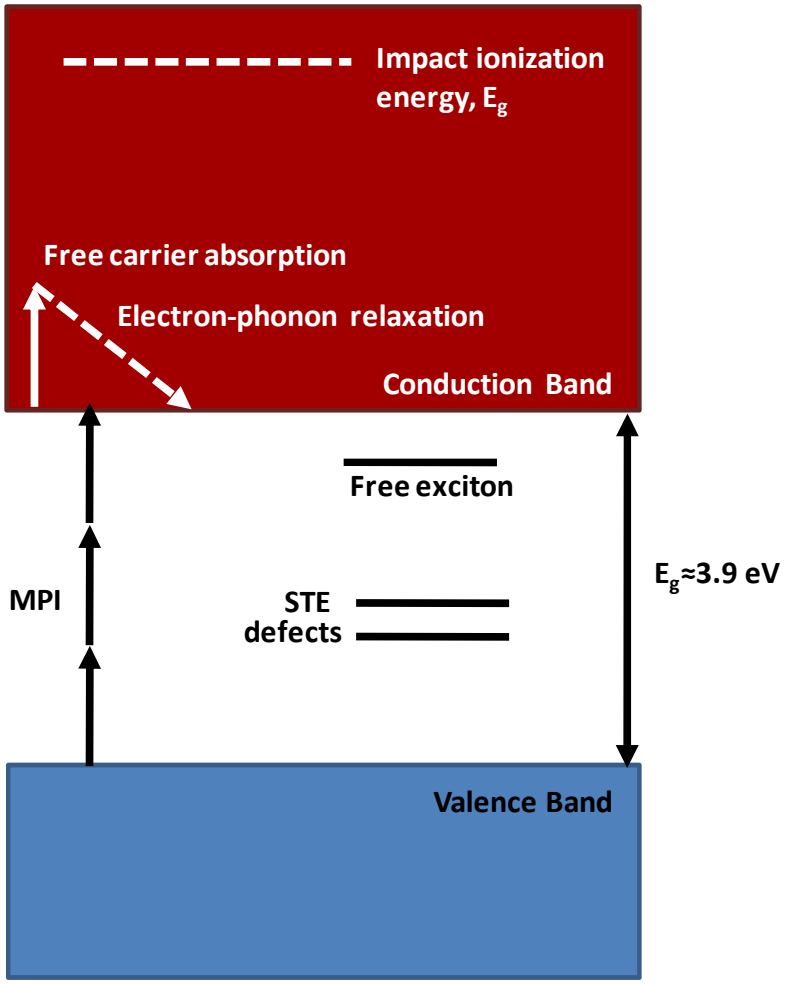

Fig. 3.6. *Energy band diagram and absorption process in $LiNbO_3$. 800 nm light (1.55 eV) is assumed. Free electrons are initially generated through multiphoton ionization (MPI) for the defect free material. Once free electrons are excited impact ionization may also promote electrons from the valence band to the conduction band via transfer from highly energetic electrons whose energy is higher than that of the bandgap. Free excitons, self-trapped excitons (STE's) and defects may also play a role in the ionization mechanism.*

Hence, the three basic ionization mechanisms which have been normally considered to be responsible for free-electron plasma creation are strong-field ionization -*multiphoton ionization* (MPI) or *tunnelling ionization*- and subsequent *avalanche ionization* (AI) [1, 29].

In this framework, and considering usual fabrication parameters (150 fs pulse duration, 100 nJ pulse energy, 800 nm wavelength, and high NA optics) the ionisation process inside dielectrics is traditionally mainly described by MPI and AI processes, being the relative contribution of both mechanisms different at different wavelengths, pulse durations, laser intensity, and for different materials [1].

Conversely, Joglekar et al. have recently (2004) stated that contrary to common belief [27, 30-32], MPI does not play a significant role in the damage process at the intensity threshold, and what is more that the Keldysh theory has to be rejected [33]. The main finding is that the dominant mechanism is a Zener ionization (tunnelling) followed by a combination of saturated avalanche ionization processes. The final conclusion of their work is that the minimum feature size achievable ultimately depends on the valence electron density, which is normally sufficiently high in value and uniform along the sample to give the deterministic behaviour characteristic of damage threshold.

The main conclusions of Joglekar et al. with respect to direct laser writing in dielectrics close to threshold levels were: (1) damage does not strongly depend on local impurities or defect states within the material, (2) the damage threshold scales with the energy band gap of materials and it is almost independent on the laser polarization, so that the ionization cannot be driven by a MPI process, but rather by a tunnelling Zener process, (3) the Keldysh theory fails to describe the optical breakdown processes in transparent solids, (4) the damage process is ultimately given by the valence electron density, and all valence electrons are ionized in the region of material damage.

3.2.4. Femtosecond laser ablation

The physical processes underlying fs pulse laser ablation are extremely complex due to the combination of the different photo-ionization processes and the propagation of incident laser pulses in a changing interface and material. An approximate description of the main properties of ablation can however be given taking into account a scalar approximation to the beam propagation, and basic photo-ionization processes such as avalanche and multiphoton ionization [34]. From such an approximation basic interaction processes and effects can be well predicted, such as diffraction

of subsequent pulses on the previously ablated hole, saturation of the ablation depth with pulse number, and amorphized zones surrounding the ablated volume.

The ablation rate can normally be simply fitted with a logarithmic curve with the laser power. Supposing a Gaussian beam the single pulse ablation rates are normally well described by the law [35]:

$$D^2 = 2\omega_0^2 ln\left(\frac{F_{peak}}{F_{th}}\right) \tag{3.11}$$

where D is the crater diameter, ω_0 is the beam radius at $1/e^2$ intensity, F_{peak} is the peak laser fluence, and F_{th} is the threshold fluence at which the ablation is supposed to be zero (i.e. D=0).

The peak laser fluence, F_{peak}, is related to the total pulse energy E_{pulse} as given in **Eq. 3.12**. As most results in the literature are traditionally reported in terms of the average laser fluence F_{av}, supposing a Gaussian beam its value is half the peak value:

$$F_{peak} = \frac{2E_{pulse}}{\pi\omega_0^2} = 2F_{av} \tag{3.12}$$

From **Eq. 3.12** it gets clear that the ablation rate can also be expressed in terms of the laser pulse energy, instead of fluence. As the energy can be more easily measured than the fluence, it is normally very convenient to report the E_{th} value as well:

$$D^2 = 2\omega_0^2 ln\left(\frac{E_{pulse}}{E_{th}}\right) \tag{3.13}$$

The slope of the squared diameter ablation curve is thus independent of the choosing of fluence or energy as control parameter, and it is directly related to the laser beam radius at $1/e^2$ intensity. This expression works very well for single pulse experiments, in the multipulse ablation regime, however, the diameters of craters are no longer directly related to the simple Gaussian beam exposure, and different processes such as beam diffraction at the previous ablated holes can or accumulation of ablated material can alter crater shapes from the predicted in **Eq. 3.13**. In such

cases it is very useful to determine the fluence and energy thresholds, but the constants giving the slope of the logarithmic curve are no longer simple to interpretate.

Another relationship which is normally used for determining ablation thresholds is the Beer's Law [36]:

$$h_{pulse} = \alpha_{eff}^{-1} ln\left(\frac{E_{pulse}}{E_{th}}\right) \tag{3.14}$$

where h_{pulse} is the ablation depth, and α_{eff} is the *effective absorption coefficient*, or the inverse of the *effective optical penetration depth,* α_{eff}^{-1}. This formula is again more useful in single pulse experiments. If multipulse ablation is performed the ablated depth is normally divided by the pulse number, so that it gives the average ablation rate per pulse.

In **Section 3.3** experimental results are presented in different multipulse configurations verifying the validity of these formulae in rare earth doped $LiNbO_3$.

3.2.5. Repetition rate and scan speed

There is a fundamental difference between writing with high-repetition (~10 MHz) and low-repetition rate (~1 kHz) fs laser systems. In low-repetition rate systems the time interval between emitted pulses is of about 1 ms, which is a time three orders of magnitude longer than the characteristic 1 μs heat diffusion time out of the focal volume. On the other hand, in high-repetition rate oscillators the time between pulses is of about 12 ns, so that there is not enough time for the energy deposited by each pulse to diffuse out of the focal volume. These differences are schematically shown in **Figure 3.7**. This means that the accumulated heat will anneal the focal volumes and its surroundings, and it will induce thermal damage on regions outside the focal volume if the energy is too high. The effective cooling time depends on the spot size and the thermal diffusivity D_{th} of the material in the form:

$$\tau_{eff} = \frac{d_{spot}^2}{D_{th}} \tag{3.15}$$

Values for τ_{eff} in $LiNbO_3$ normally range from 0.5-100 μs depending on the focal spot size 1-10 μm, respectively. From the thermal diffusivity time it is then easy to determine if heat accumulation will occur by comparing it with the time between pulses.

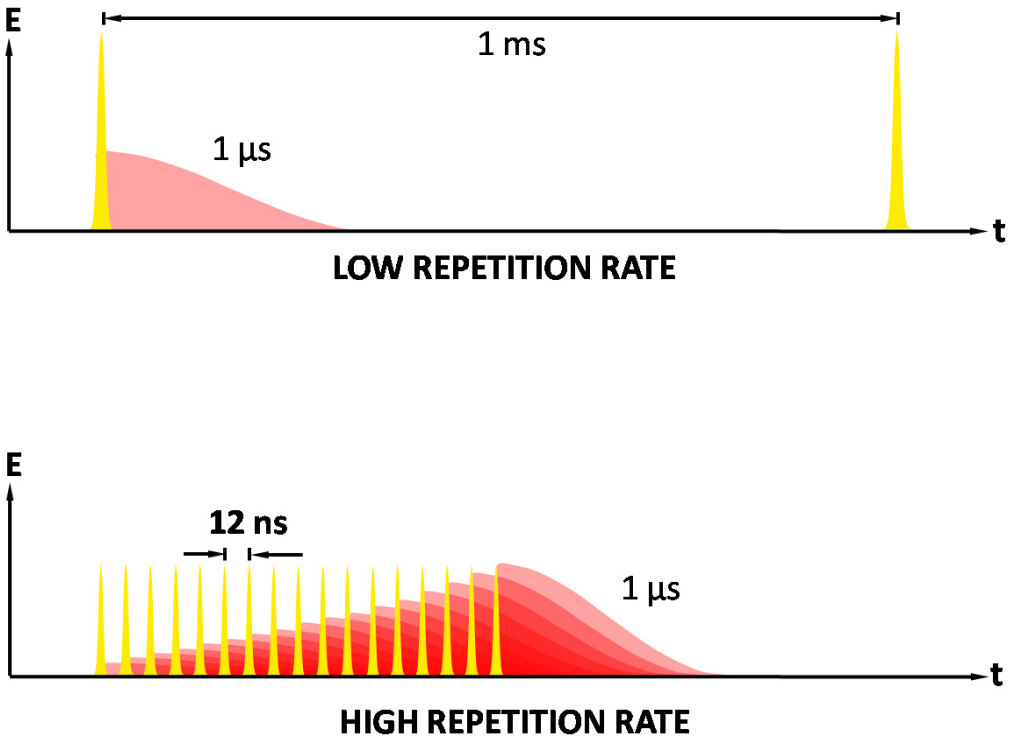

Fig. 3.7. *Schematic diagram of the heat accumulation process depending on the repetition rate of the fs laser system.*

A second important issue to determine is the number of pulses accumulating at one point in the sample, especially in the case that the inscription is performed by scanning the laser beam. In this case the scan speed, v_{DLW}, and the laser repetition rate f_{laser}, give the separation between the different focal points in the sample:

$$L_{pulses} = \frac{v_{DLW}}{f_{laser}} \tag{3.16}$$

From the separation distance between pulses and the focal spot diameter the number of pulses overlapping in a spot diameter can then be estimated as:

$$N_{overlap} = \frac{d_{spot}}{D_{pulses}} \tag{3.17}$$

In the next section examples are given of the effect of scan speed when writing inside $LiNbO_3$. In **Chapter 5** a more detailed analysis of the thermal accumulation and diffusion processes is also given, in the context of buried waveguide fabrication.

3.3. Experimental results

Here we show different results concerning the surface ablation and bulk inscription in $LiNbO_3$.

3.3.1. Surface ablation

Results are here presented in two sections, first low-NA surface ablation experiments are described and important parameters of the interaction process are obtained. Secondly, high-NA experiments are shown are ablation parameters are compared.

3.3.1.1. Low NA

Figure 3.8 shows different surface grooves performed on a x-cut Nd^{3+}(0.5%):MgO(4%):$LiNbO_3$ sample. The writing set-up consisted on a 800 nm wavelength femtosecond amplifier giving 120 fs pulse duration pulses a t a repetition rate of 1kHz. The objective lens was a 10X (NA 0.3), but the laser beam was spatially filtered with a 3 mm aperture pinhole so that the effective NA was reduced to about NA 0.08, giving a focal spot of 6 µm in radius. The nonlinear ionization process is clearly depicted by the fact that the ablated features are much smaller than the focal spot diameter. The line grooves were performed with energies ranging from 0.5 µJ to 4.97 µJ, and at scan speeds of 25 and 50 µm/s, giving equivalent overlapping pulses of 485 and 242 per spot, respectively. The ablated holes were performed with pulse energies of 2 and 4 µJ and 150 pulses per spot.

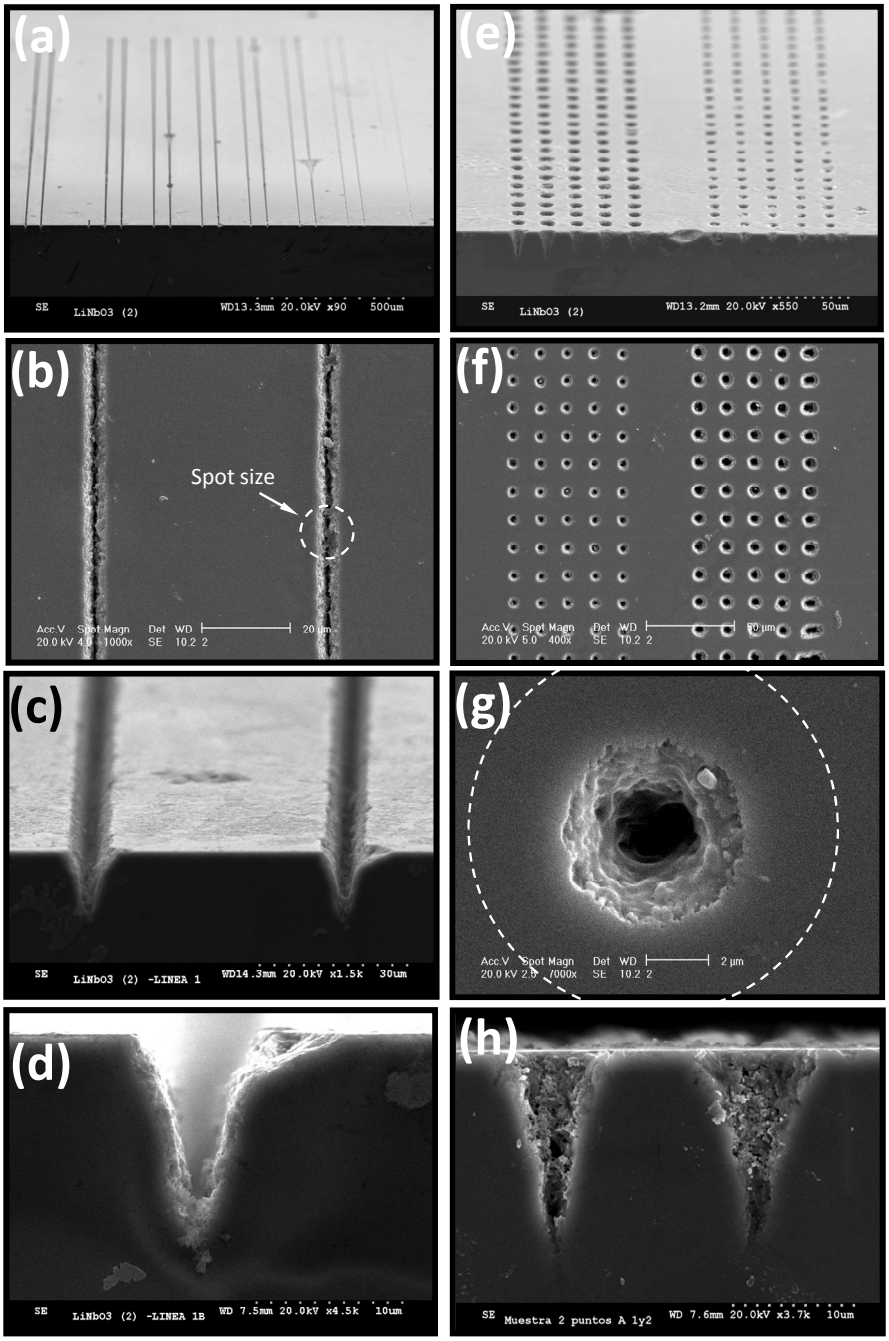

Fig. 3.8. *Surface ablation relief features in Nd^{3+}:MgO:$LiNbO_3$ as seen by SEM microscopy:* **(a)-(d)** *show details of surface relief grooves from different angles. Each pair of lines shows the ablated grooves at scans speeds of 25 µm/s and 50 µm/s (left and right, respectively)* **(e)-(h)** *show details of ablated holes from different angles. All images were taken after the sample lateral face was polished and cleaned with acetone and ethanol in a 5 min. ultrasonic bath. The 12 µm diameter spot size is marked to depict how the nonlinear ionization process allows performing features much smaller than the beam size.*

From different pictures as that in **Fig. 3.8 (d)** the ablated depths per pulse were measured and plotted against the laser pulse energy and average fluence. These results are shown in **Figure 3.9**.

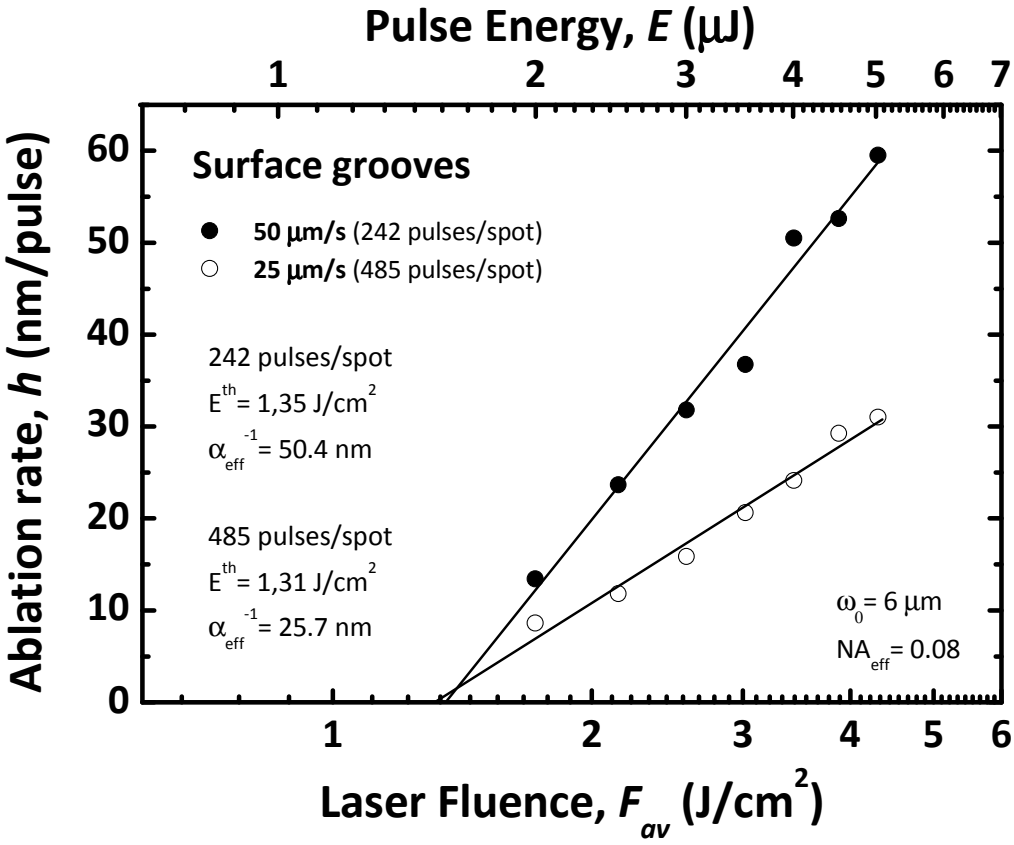

Fig. 3.9. *Surface ablation groove depths as a function of laser pulse energy and average fluence*

The resulting fluence thresholds are 1.31 J/cm^2 and 1.35 J/cm^2 for grooves performed at the scan speeds of 25 μm/s (485 pulse/spot) and 50 μm/s (242 pulses/spot). This difference is expected due to the known saturation of ablated channels with pulse number and the effect of threshold lowering due to the creation of pre-ablation induced defects (incubation effect) [29, 34]. The fluence threshold parameter is a value expected to be independent of the focusing optics, supposing that the ablation process is performed in similar ambient conditions and laser parameters. Typical reported values for single pulse ablation in undoped congruent $LiNbO_3$ vary

from 1.8 to 2.5 J/cm^2 [37-39]. Thus, the ablation with hundreds of pulses in a scan mode gives a fluence threshold reduced by more than a 30% of that of single pulse regime.

3.3.1.2. High NA

For high-NA experiments both x-cut and z-cut, and undoped and rare-earth doped samples of congruent $LiNbO_3$ were used. The laser parameters were the same as for low-NA experiments, but in this case ablation was performed without scanning so that nanoholes were created. The objective used was an oil immersion 100X (NA 1.4). The expected focal beam diameter is of 700 nm. Holes were performed by multipulse ablation at an intermediate dose of 50 pulses in all cases.

Figure 3.10 shows results on an undoped z-cut $LiNbO_3$ sample. In Fig. 3.10(a) holes with different doses were performed. In Fig. 3.10 (b)-(g) different structures such as 2D paterns, hexagons, triangles and pairs of holes with different separations were performed. The aim of these structures is to investigate the induce near-field transmission effect by means of Near-Field Scanning Microscopy (NSOM) (results not shown here).

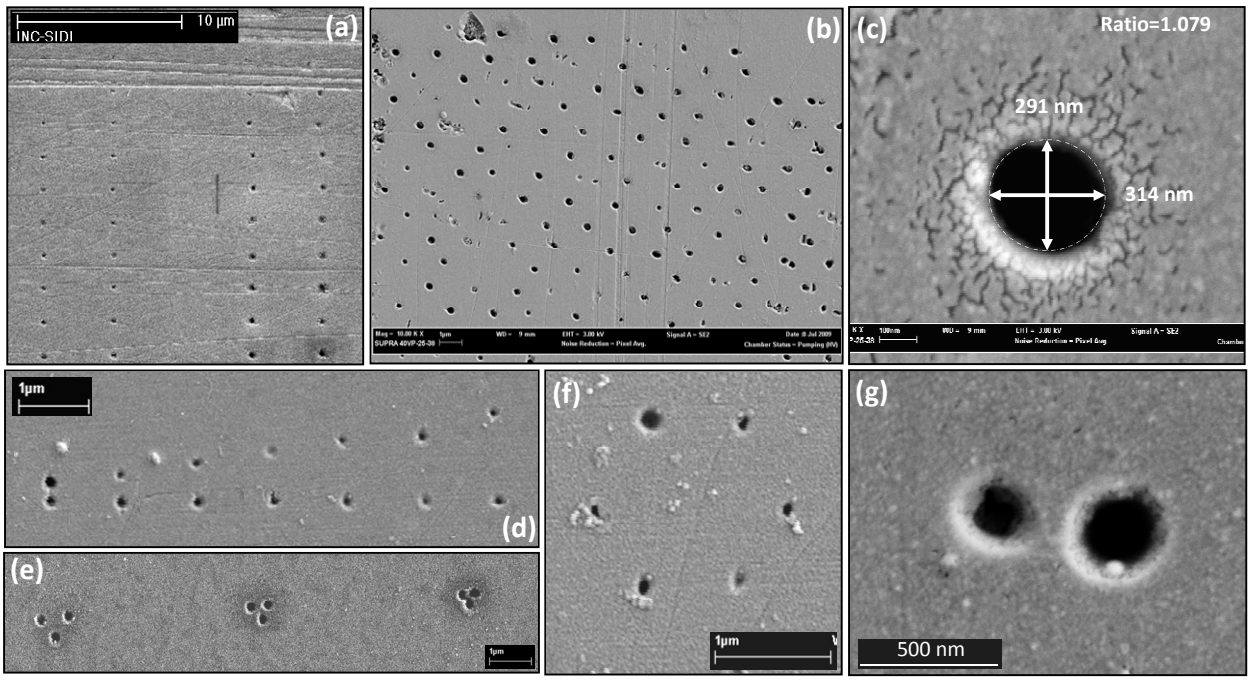

Fig. 3.10. *Different sub-micron holes performed in z-cut $LiNbO_3$*

Sub-micron holes were also performed in different samples, such as x-cut Er^{3+}:Yb^{3+}:$LiNbO_3$, showing very similar results in terms of shape and size dependence with pulse energy. Due to the fact that holes are performed at very low energy levels, laser instabilities were found to be the main source of indetermination in the hole sizes. **Figure 3.11** shows a 2D nano-hole pattern performed in x-cut Er^{3+}:Yb^{3+}:$LiNbO_3$. It can be seen how the laser fluctuations produce a rather high dispersion in the hole diameter. In this sense, a laser fluctuation of ±0.5 nJ at the ablation threshold can result in the appearance or not of a hole, so that some missing holes are also present in the 2D structures.

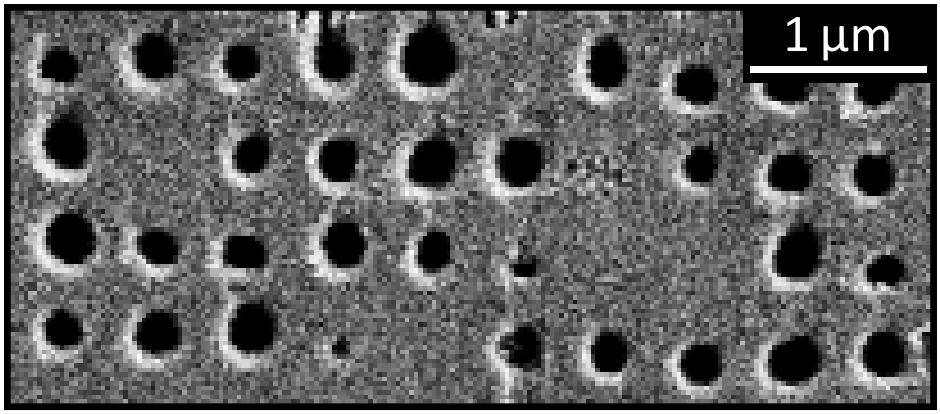

Fig. 3.11. *2D nano-hole pattern performed in x-cut Er^{3+}:Yb^{3+}:$LiNbO_3$*

To reduce the dispersion in the hole size measurement several holes were always done at the same dose and their diameter was averaged. This process was always done systematically so that 4 or 8 holes with the same pulse energy were fabricated. By measuring these average holes diameter an ablation curve was performed in the case of x-cut Er^{3+}:Yb^{3+}:$LiNbO_3$, which is shown in **Figure 3.12**.

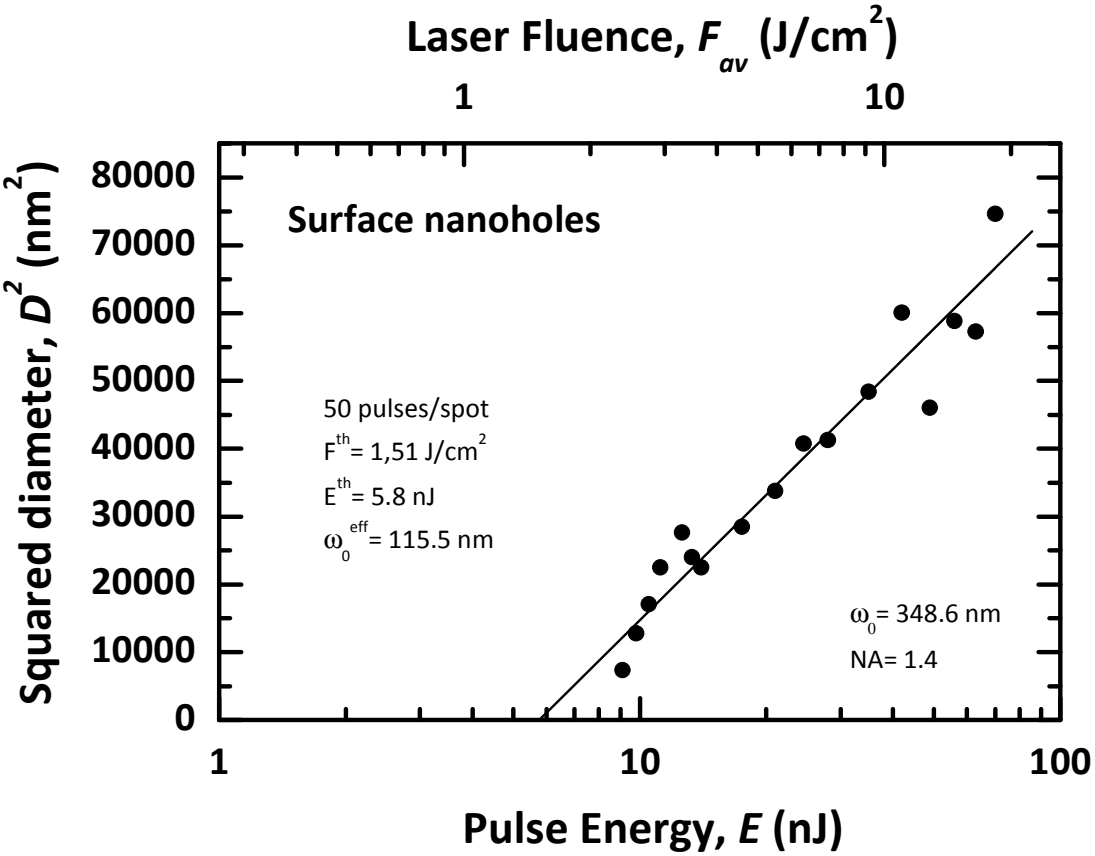

Fig. 3.12. *Ablation curve for x-cut Er^{3+}:Yb^{3+}:$LiNbO_3$*

The obtained fluence threshold for 50 pulses is 1.51 J/cm^2, which is a value very close to that obtained from the previous measurements with low-NA optics (1.35 J/cm^2), as seen on the previous section. The fact that the fluence threshold well agrees with low-NA experiments is also somewhat surprising, due to the fact that these experiments are performed in oil-immersion, which could modify the plasma expansion dynamics at the interface with respect to those in air.

Nevertheless, the hole diameters range from 80 nm to 250 nm, this meaning that the obtained hole sizes are of about λ/4 to almost λ/10. In this sense, it appears to be extremely interesting to perform this experiments by using lower wavelengths from the NIR to visible, in order to determine the lower limit in feature sizes achievable by this technique.

The second fitting parameter is the effective spot radius, which in this case gives a value 3 times lower than the theoretical one (115.5 nm). This difference is expected due to the fact that the ablation experiment is performed in a multipulse regime and thus different interactions effects from subsequent pulses are being mixed in the equation.

3.3.2. Three-dimensional writing: High-NA induced optical aberrations

For 3D writing the optical set-up was the same as that for high-NA ablation. In this case experiments were performed for both x-cut and z-cut Er^{3+}:Yb^{3+}:$LiNbO_3$ sample surfaces.

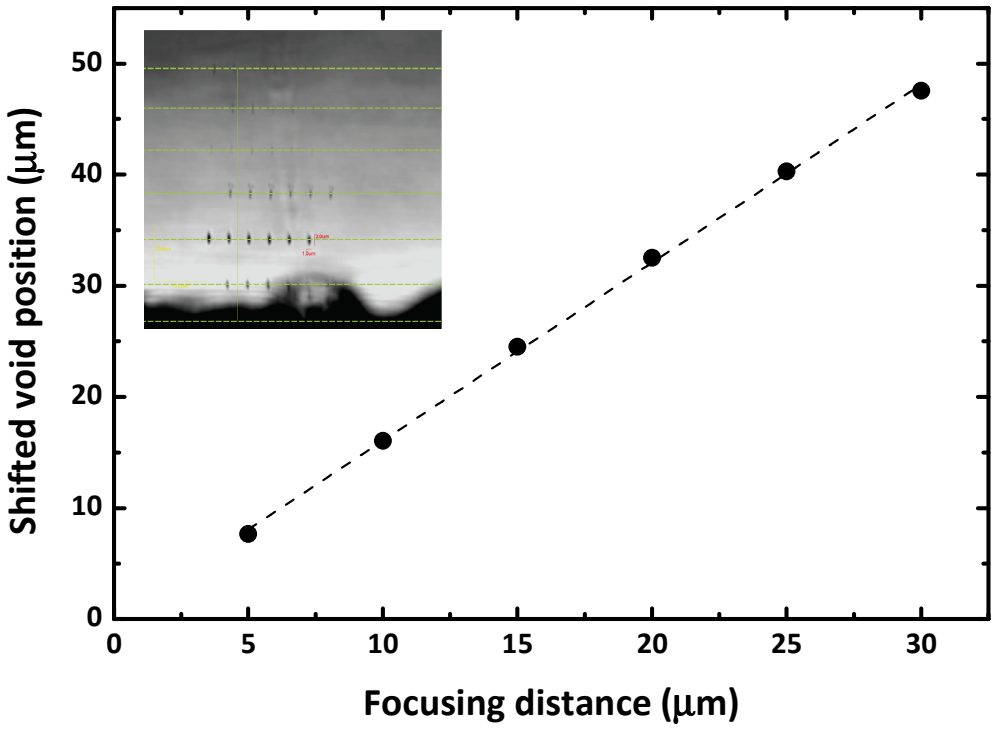

Fig. 3.13. *Experimental focus shift induced by the NA 1.4objective, and linear fit of data. Inset shows an image of an array of voxels written at different depths, from the measurements are performed.*

For x-cut samples the expected aberration is spherical aberration, which can be observed as a shift in the focus position inside the sample, and an elongation of the focal spot. To correct the

focus shift a simple experiment was done by writing voxels with a moderate energy at different depths inside the sample. Voxels were written close to the sample lateral face, so that voxels could be afterwards characterized by transmission optical microscopy. By measuring the different voxel distances to surface, a linear relationship was observed which allows calibration the amount of focal shift occurring for every depth inside the sample. Results are shown in Figure **3.13**. From the slope of the fitting line a focal shift of 1.6 times the linear focal depth was obtained. This means that for every 1 μm that the focus position is moved deeper in the sample the aberrated focus will move 1.6 μm.

In the case of z-cut samples strong birefringence induced aberration was observed. Experiments were in this case made with a NA 1.45 TIRFM 60X microscope objective. Results are shown in **Figure 3.14**, in which different voxels written at different depths and with different energies are summarized. As the modification inside the crystal follows the intensity distribution, the characteristic birefringence aberration previously described in **Section 3.2.2.3** (**Fig. 3.5**) describes very well the main observed features. For low energies only the peak lobes of the intensity distribution modify the crystal, producing changes in the refraction index that can be seen from transmission optical microscopy. The focal spot appears to split into two separated spots at the linear focus depth of 15 μm. The separation between the two lobes increases with depth. If high energy is used then the full intensity distribution between the two main spots produces also an index changes and so the transmission contrast allows visualizing the very strongly aberrated focal intensity distribution.

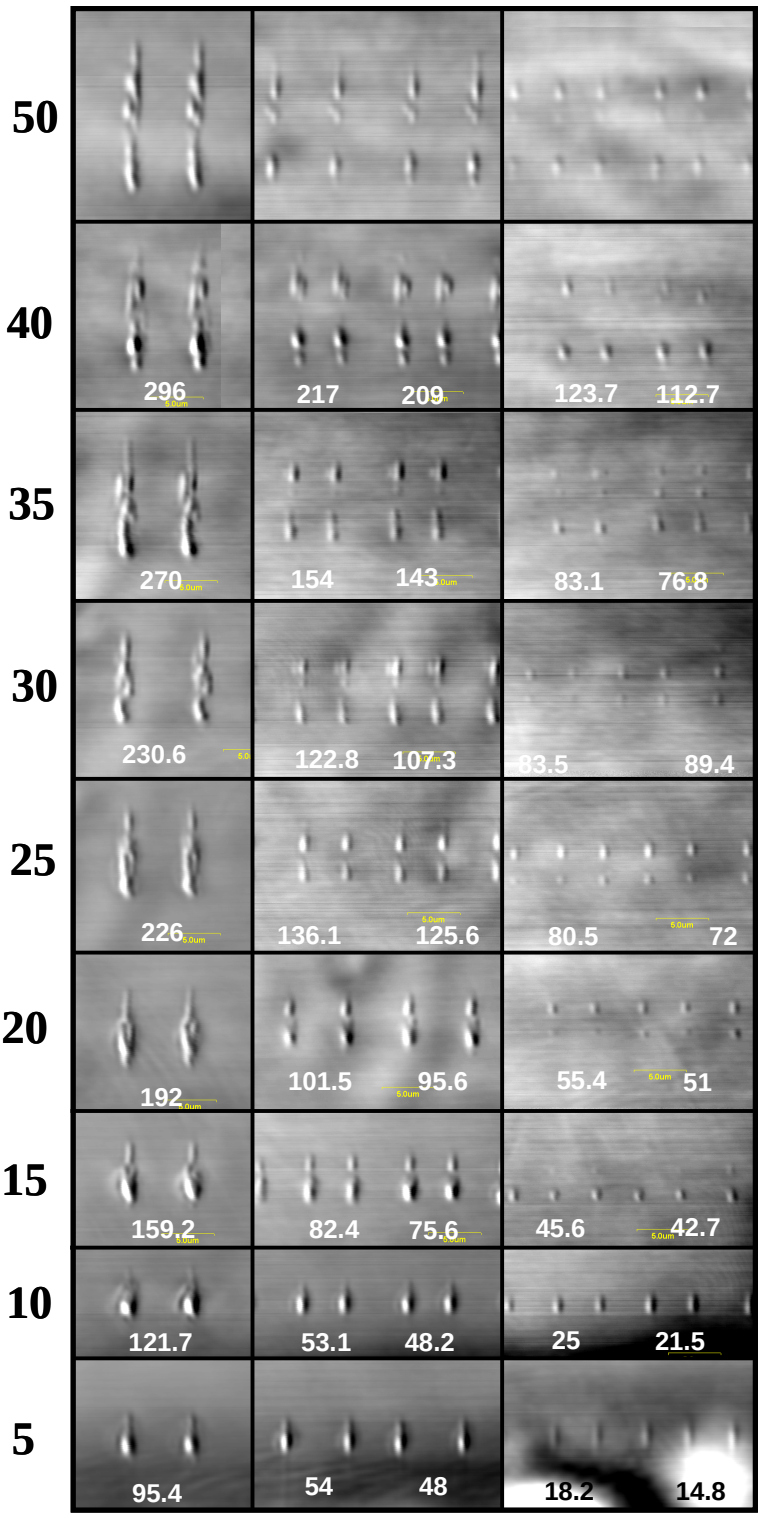

Fig. 3.14. *Confocal optical transmission images of a $LiNbO_3:Er^{3+}:Yb^{3+}$ processed with the usual set-up of 120 fs pulses of 800 nm wavelength at 1 KHz repetition rate and 50 ms exposure time. Units are µm for the focal depth along the z-axis, and nJ for the laser energies, at left and insets, respectively. Laser comes from the bottom.*

References

[1] E. Gamaly, B. Luther-Davis, and A. Rode, *Laser-matter interaction confined inside the bulk of a transparent solid*, Chapter 2, *3D Laser Microfabrication*, edited by H. Misawa and S. Juodkazis, Wiley-VCH, Federal Republic of Germany, 2006

[2] R. W. Boyd, *Nonlinear Optics*, Academic Press, New York, 1992

[3] M. Sheik-Bahae, A. A. Said, T. H. Wei, D. J. Hagan, and E. W. Van Stryland, *Sensitive measurement of optical nonlinearities using a single beam*, IEEE J. Quantum Electron. **26**, 760 (1990)

[4] L. Pálfalvi, B. C. Tóth, G. Almasi, J. A. Fülöp, and J. Hebling, *A general Z-scan theory*, Appl. Phys. B **97**, 679-685 (2009)

[5] J. Shen, R. D Lowe, and R. D. Snook, *A model for cw laser induced mode-mismatched dual-beam thermal lens spectrometry,* Chemical Physics **165**, 385-396(1992)

[6] O. L. Antipov, O. N. Eremeykin, A. P. Savikin, V. A. Vorob'ev, D. V. Bredikhin, and M. S. Kuznetsov, *Electronic changes of refractive index in intensively pumped Nd:YAG laser crystals*, IEEE J. Quantum Elect. **39**, 7, 910-918 (2003)

[7] R. K. Choubey, R. Trivedi, M. Das, P. K. Sen, P. Sen, S. Kar, K. S. Bartwal, and R. A. Ganeev, *Growth and study of nonlinear refraction and absorption in Mg doped $LiNbO_3$ single crystals*, J. Cryst. Growth **311**, 2597-2601 (2009)

[8] H. Li, F. Zhou, X. Zhang, W. Ji, *Picosecond Z-scan study of bound electronic Kerr effect in $LiNbO_3$ crystal associated with two-photon absorption*, Appl. Phys. B **64**, 659-662 (1997)

[9] H. P. Li, C. H. Kam, Y. L. Lam, and W. Ji, *Femtosecond Z-scan measurements of nonlinear refraction in nonlinear optical crystals*, Opt. Mater. **15**, 237-242 (2001)

[10] J. N. Babu Reddy, S. Elizabeth, H. L. Bhat, N. Venkatraman, and D. N. Rao, *Influence of non-stoichiometric defects on nonlinear absorption and refraction in Nd:Zn co-doped lithium niobate*, Opt. Mater. **31**, 1022-1026 (2009)

[11] H. Li, F. Zhou, X. Zhang, W. Ji, *Bound electronic Kerr effect and self-focusing induced damage in second-harmonic-generation crystals*, Opt. Comm. **144**, 75-81 (1997)

[12] R. H. Stolen, and W. J. Tomlison, *Effect of the Raman part of the nonlinear refractive index on propagation of ultrashort optical pulses in fibers*, J. Opt. Soc. Am. B **9**, 4, 565-573 (1992)

[13] M. D. Fleit, J. A. Fleck, *Effect of refraction on spot-size dependence of laser-induced breakdown*, Appl. Phys. Lett. **24**, 4, 169-172 (1974)

[14] A. Couairon, and A. Mysyrowicz, *Femtosecond filamentation in transparent media*, Phys. Rep. **441**, 47-189 (2007)

[15] www.filamentation.org, a recently launched (April 2009) internet resource dedicated to nonlinear laser propagation, developed and maintained by the Stelios Tzortzakis and the UNIS Group located at the IESL-FORTH in Greece.

[16] E. Gaizauskas, *Filamentation versus optical breakdown in bulk transparent media*, Chapter 6, *3D Laser Microfabrication*, edited by H. Misawa and S. Juodkazis, Wiley-VCH, Federal Republic of Germany, 2006

[17] X. Hu, Y. Dai, L. Yang, J. Song, C. Zhu, and J. Qiu, *Self-formation of quasiperiodic void structure in CaF_2 induced by femtosecond laser irradiation*, J. Appl. Phys. **101**, 023112 (2007)

[18] D. G. Papazoglou, I. Zergioti, and S. Tzortzakis, *Plasma strings from ultraviolet laser filaments drive permanent structural modifications in fused silica*, Opt. Lett. **32**, 14, 2055 (2007)

[19] V. Mizeikis, S. Juodkazis, T. Balciunas, S. I. Kudryashov, V. D. Zvorykin, A. A. Ionin, and H. Misawa, *Optical and ultrasonic monitoring of femtosecond laser filamentation in fused silica*, Appl. Surf. Science **255**, 9721-9723 (2009)

[20] M. Born and E. Wolf, *Principles of Optics*, Cambridge University Press, Cambridge, 7th (expanded) edition, 1999

[21] M. J. Booth, and T. Wilson, *Refractive index mismatch induced aberrations in single-photon and two-photon microscopy and the use of aberration correction*, J. Biomed. Opt. **6**, 266-272 (2001)

[22] M. J. Booth, M. A. A. Neil, and T. Wilson, *Aberration correction for confocal imaging in refractive-index-mismatched-media*, J. Microsc. **192**, 90-98 (1998)

[23] P. Török, P. Vagra, and G. Németh, *Analytical solution of the diffraction integrals and interpretation of wavefront distortion when light is focused through a planar interface between materials of mismatched refractive indices*, J. Opt. Soc. Am. A **12**, 2660-2671 (1995)

[24] J. S. H. Wiersma, T. D. Visser, P. Török, *Annular focusing through a dielectric interface: scanning and confining the intensity*, Pure Appl. Opt. **7**, 1237-1248 (1998)

[25] N. Huot, R. Stoian, A. Mermillod-Blondin, C. Mauclair, and E. Audouard, *Analysis of the effects of spherical aberration on ultrafast laser-induced refractive index variation in glass*, Opt. Express **15**, 19, 12395 (2007)

[26] S. Stalinga, *Axial birefringence in high-numerical-aperture optical systems and the light distribution close to focus*, J. Opt. Soc. Am. A **18**, 11, 2846 (2001)

[27] N. Bloembergen, *Laser-induced electric breakdown in solids*, IEEE J. Quantum Electron. **QE-10**, 375-386 (1974)

[28] L. V. Keldysh, Zh. Eksp. Teor. Fiz. **47**, 1945 (1964) [Sov. Phys. JETP **20**, 1307 (1965)]

[29] J. R. Vázquez de Aldana, C. Méndez, and L. Roso, *Saturation of ablation channels micro-machined in fused silica with many femtosecond laser pulses*, Opt. Express **14**, 3, 1329 (2006)

[30] B. Stuart, M. Feit, A. Rubenchick, B. Shore, and M. Perry, *Laser-induced Damage in Dielectrics with Nanosecond to Subpicosecond Pulses*, Phys. Rev. Lett. **74**, 2248-2251 (1995)

[31] M. Lenzner, S. Krüger, S. Sartania, Z. Cheng, C. Spielmann, G. Mourou, W. Kautek, and F. Krausz, *Femtosecond Optical Breakdown in Dielectrics*, Phys. Rev. Lett. **80**, 4076-4079 (1998)

[32] A. Tien, S. Backus, H. Kapteyn, M. Murnane, and G. Mourou, *Short-Pulse Laser Damage in Transparent Materials as a Function of Pulse Duration*, Phys. Rev. Lett. **82**, 3883-3886 (1999)

[33] A. P. Joglekar, H.-H. Liu, E. Meyhöfer, G. Mourou, and A. J. Hunt, *Optics at critical intensity: Applications to nanomorfing*, PNAS **101**, 16, 5856-5861 (2004)

[34] J. R. Vázquez de Aldana, C. Méndez, L. Roso, and P. Moreno, *Propagation of ablation channels with multiple femtosecond laser pulses in dielectrics: numerical simulations and experiments*, J. Phys. D: Appl. Phys. **38**, 2764-2768 (2005)

[35] A. Ben-Yakar, and R. L. Byer, *Femtosecond laser ablation properties of borosilicate glass*, J. Appl. Phys. **96**, 9 (2004)

[36] J. Krüger, and W. Kautek, *The femtosecond* pulse *laser*: a *new tool for micromachining*, Laser Phys. **9**, 30 (1999)

[37] D. C. Deshpande, A. P. Malshe, E. A. Stach, V. Radmilovic, D. Alexander, D.Doerr, D. Hirt, *Investigations of femtosecond laser assisted nano and microscale modifications in lithium niobate*, J. Appl. Phys. **97**, 074316 (2005)

[38] A. García-Navarro, F. Agulló-López, J. Olivares, J. Lamela, and F. Jaque, *Femtosecond laser and ion-shift damage in lithium niobate: A comparative analysis*, J. Appl. Phys. **103**, 093540 (2008)

[39] J. Lamela, G. Lifante, T. P. J. Han, F. Jaque, A. García-Navarro, J. Olivares, and F. Agulló-López, *Morphology of ablation craters generated by fs laser pulses in $LiNbO_3$*, Appl. Surf. Sci. **255**, 3918-3922 (2009)

Chapter 4

Laser gain and non-collinear propagation through diffraction gratings in Nd^{3+}:MgO:$LiNbO_3$

In this chapter we study the direct femtosecond laser microfabrication of one dimensional (1D) and two dimensional (2D) integrated surface relief diffraction gratings in Nd^{3+}:MgO codoped $LiNbO_3$ laser crystals. The polarization dependence of the diffracting efficiency in each case is characterized, and continuous wave laser oscillation at 1.06 μm wavelength is demonstrated through the gratings. The intra-cavity non-collinear laser propagation at 1.06 μm is characterized, and the laser gain and thresholds through each kind of grating is reported.

4.1. Introduction

In the last decade the ultrashort pulse laser processing of all kinds of solid media has been proved to be a powerful technique with applications in nanotechnology, photonics, biotechnology, medicine and many other areas [1-4]. For integrated optical applications, probably the most simple and straightforward demonstration would be that of inscribing a diffractive microstructure in a transparent dielectric media of interest such as an optical fibre or a nonlinear material.

Indeed, the microfabrication of both volume and surface gratings with exceptional precision and design flexibility has been demonstrated by means of either femtosecond (fs) laser holographic or direct laser writing (DLW) methods in glasses or in frequency doubling crystals [5-9]. Demonstrated applications are beam shaping [7], or the control of non-collinear nonlinear processes such as second-harmonic generation (SHG) [9, 10], or sum-frequency generation (SFG) [11], all of them applications which are of enormous importance for the production of coherent laser radiation in wide spectral ranges [12].

Due to the three-dimensional (3D) flexibility of the DLW microfabrication technique, the integration of diffractive devices in an optically functional material appears as an advantageous feature with respect to traditional bulk optical elements, since the monolithic design of these micro-devices allows for an optimized performance which can be robust and repeatable against ambient conditions, moreover than miniaturized.

Due to these advantages, the idea of incorporating a diffracting microstructure inside a nonlinear and laser active material such as Nd^{3+}:MgO:$LiNbO_3$ appears as an important step towards more complex designs based on DLW 3D optical circuits inside optical functional materials. In this chapter we investigate the simple idea of introducing a diffracting element inside the laser media itself, and we analyze the extent to which this incorporation can alter the laser capabilities of the media. These measurements are the first demonstration that such a non-collinear propagation of the laser radiation generated inside the active media can be very effectively produced by simply direct laser inscribing the desired grating.

4.2. Direct femtosecond pulse laser writing of surface relief diffraction gratings

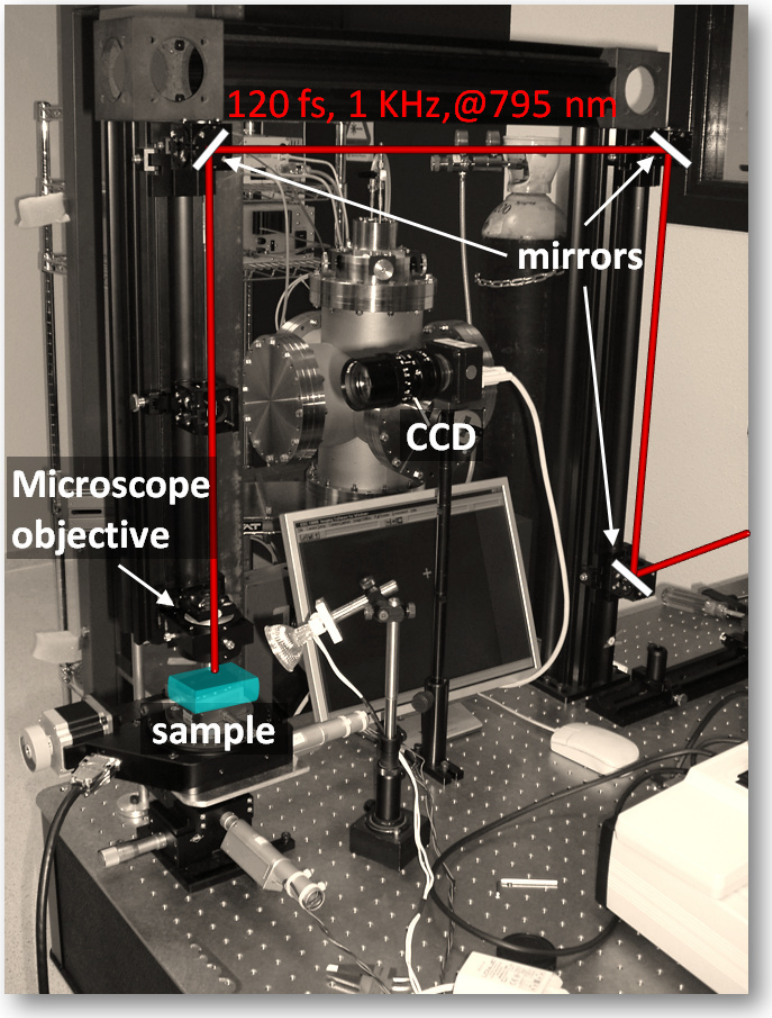

Figure 4.1. *DLW micromachining set up at the Fotón Charro in 2006, at the Universidad de Salamanca*

The DLW microfabrication was done at the laser centre Fotón Charro, at the Universidad de Salamanca, see **Figure 4.1**. The writing system consisted on a Ti:Sapphire regenerative amplifier (Spitfire, Spectra Physics) operating at 795 nm wavelength, 1 KHz repetition rate, and with a pulse duration of 120 fs. The micro-structuring was made by using transversal writing, i.e. with the incident laser beam focused perpendicular to the patterned grating. A fixed 3 mm aperture was used to control the beam width, and the irradiation fluence was controlled by using a set of neutral

filters positioned just before the microscope objective. The laser was focused on the surface of the Nd^{3+}:MgO:$LiNbO_3$ crystal by using a 10X microscope objective (NA = 0.30), getting an irradiation spot of about 5 μm in diameter.

The sample was a Nd^{3+}:MgO codoped $LiNbO_3$ crystal grown by the Czochralsky method with Nd^{3+} and MgO concentrations of 0.5 and 4 at.%, respectively. After cutting and polishing to optical grade, the sample was mounted on a XYZ positioning stage in order to produce a micrometric translation on the three axes with an uncertainty below 1 μm. All of the processing was performed in air under normal conditions of temperature and pressure. With this set up different lines and holes could be easily fabricated by multipulse surface ablation.

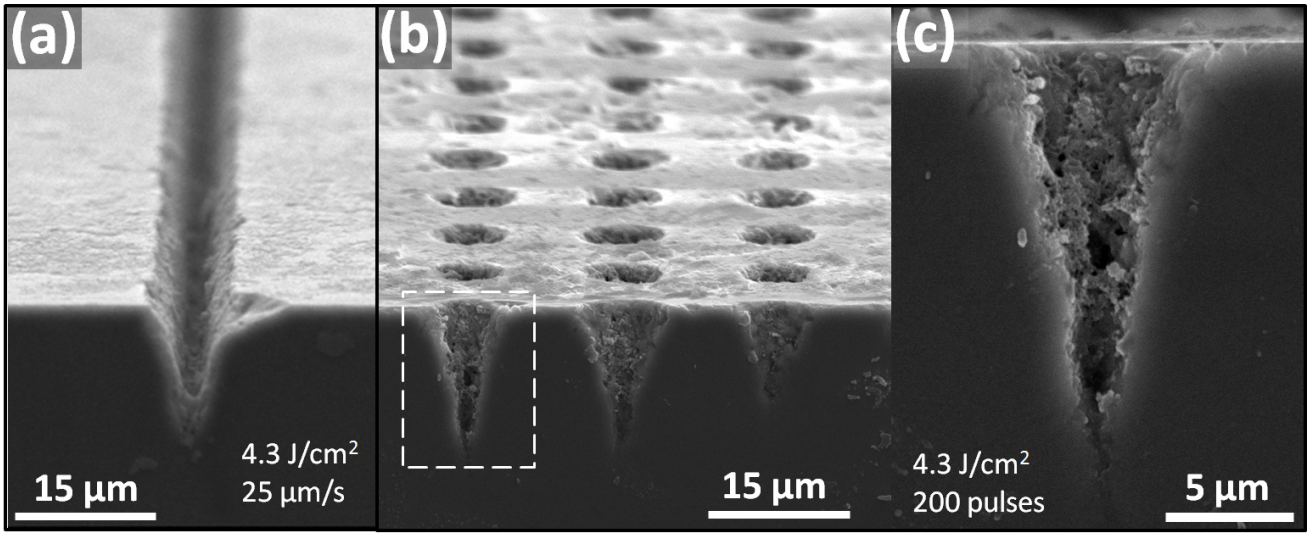

Figure 4.2. *Femtosecond laser pulse surface writing in Nd^{3+}:MgO:$LiNbO_3$.* ***(a)*** *Line groove written with a laser fluence of 4.3 J/cm^2 and speed of 25 μm/s.* ***(b)*** *Hole array with same fluence and 200 laser pulses per spot.* ***(c)*** *Hole cross-section of the area marked white in (b).*

Examples of the as fabricated hole and line sizes which were obtained with this setup are given in **Figure 4.2**; where a line groove written with a laser fluence of 4.3 J/cm^2 and scan speed of 25 μm/s **(a)**, a hole array with same fluence and 200 laser pulses per spot **(b)**, and a hole cross-section after polishing **(c)**, are shown (for more details on the fluence dependence, morphology and size of these structures see **Chapter 3**).

Following this procedure, two different kind of patterns were written at the surface of the Nd^{3+}:MgO:$LiNbO_3$ crystal. The irradiation fluence was set to 2 J/cm^2, being this slightly above the multipulse $LiNbO_3$ femtosecond laser ablation threshold for this configuration (~1.35 J/cm^2, see **Chapter 3** for more details).

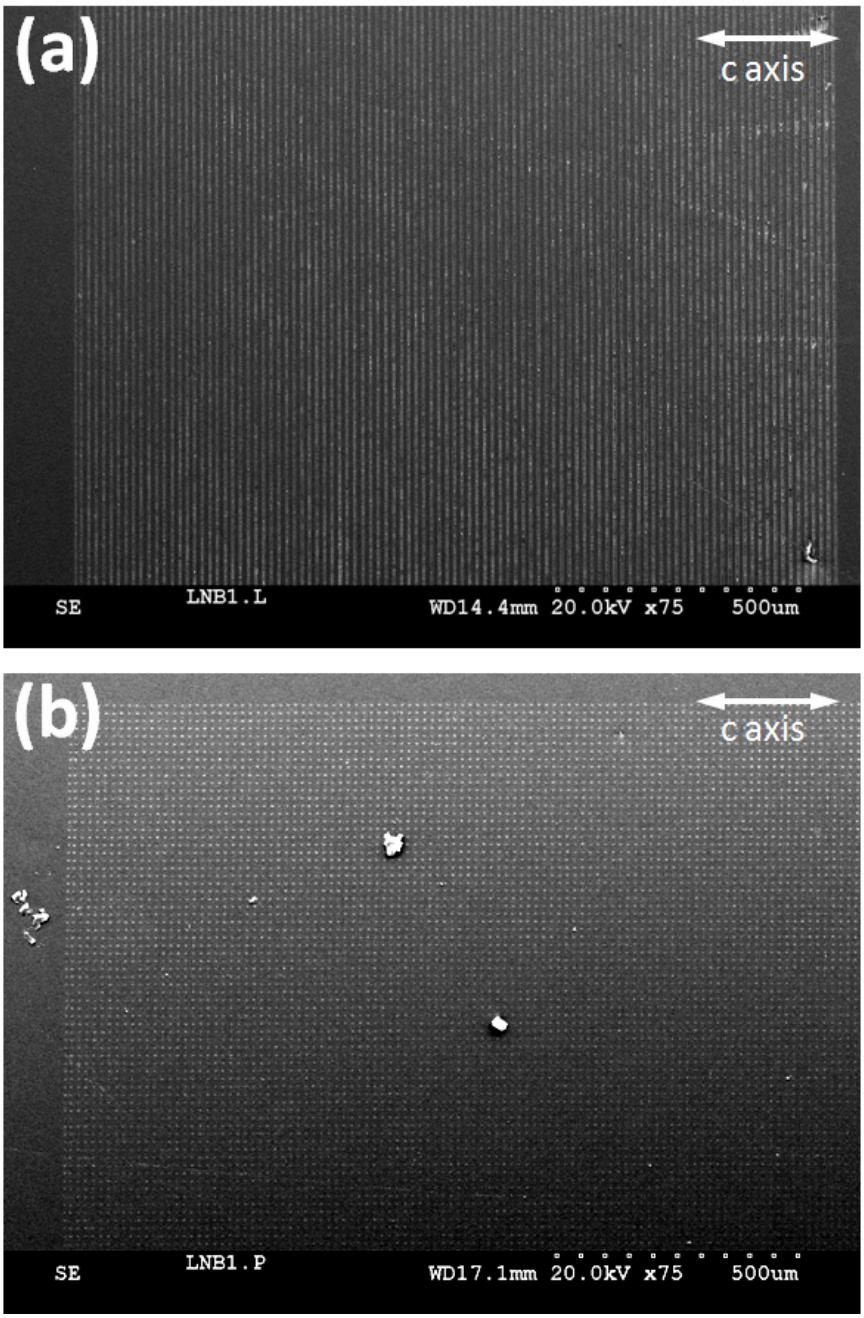

Figure 4.3. *SEM images of the fabricated 1D (a) and 2D (b) surface relief diffraction gratings. The orientation of the lithium niobate optical c-axis is indicated.*

The first pattern consists of a periodical array of line grooves with a separation of 15 μm as measured from centre to centre. The writing speed was set to 50 μm/s. The second pattern corresponds to a 2D square array of holes with a hole-hole separation of 15 μm. In this case the number of pulses per spot was set to 200. **Figure 4.3** shows SEM images of the as-fabricated 1D and 2D surface patterns. The orientation of the optical *c*-axis is indicated in both images. In the 1D case the optical axis was arbitrarily set perpendicular to the line grooves. After irradiation all samples were slightly polished about 500 nm in order to remove any ablation debris and surface imperfections, and afterwards immersed in an acetone ultra-sound bath, and then cleaned with ethanol.

From further SEM analysis we estimated the grating line and hole widths to be 2.4 ±0.3 μm and 2.1 ±0.2 μm, respectively*, so that the groove widths are much higher than the laser wavelengths. To obtain de mean feature depth, one of the lateral faces was polished to optical grade until holes reached the surface. The obtained mean ablation depths were ~6.5 μm and ~5.8 μm for dots and lines, respectively.

4.3. Optical characterization

The diffracting elements were first studied by coupling a 10 mW linearly polarized He-Ne laser emission at 0.6328 μm wavelength, along the normal direction. The different order diffraction intensities were measured using a calibrated thermopile mounted on a translation stage. The diffraction efficiency, η_{diff} , is here defined as the corresponding n-order diffraction intensity divided by the zero order intensity.

The obtained 1D and 2D far-field diffraction patterns are first shown in **Figures 4.4 (a)** and **(b)**, respectively. Efficiency results are displayed in **Figure 4.5 (a)** and **(b)** for the 1D and 2D diffracting

* Errors indicate the statistical size disorder of the structures as obtained from SEM analysis.

gratings respectively, and for the two relevant polarizations of the He-Ne beam; electric field parallel and perpendicular to the optical *c*-axis.

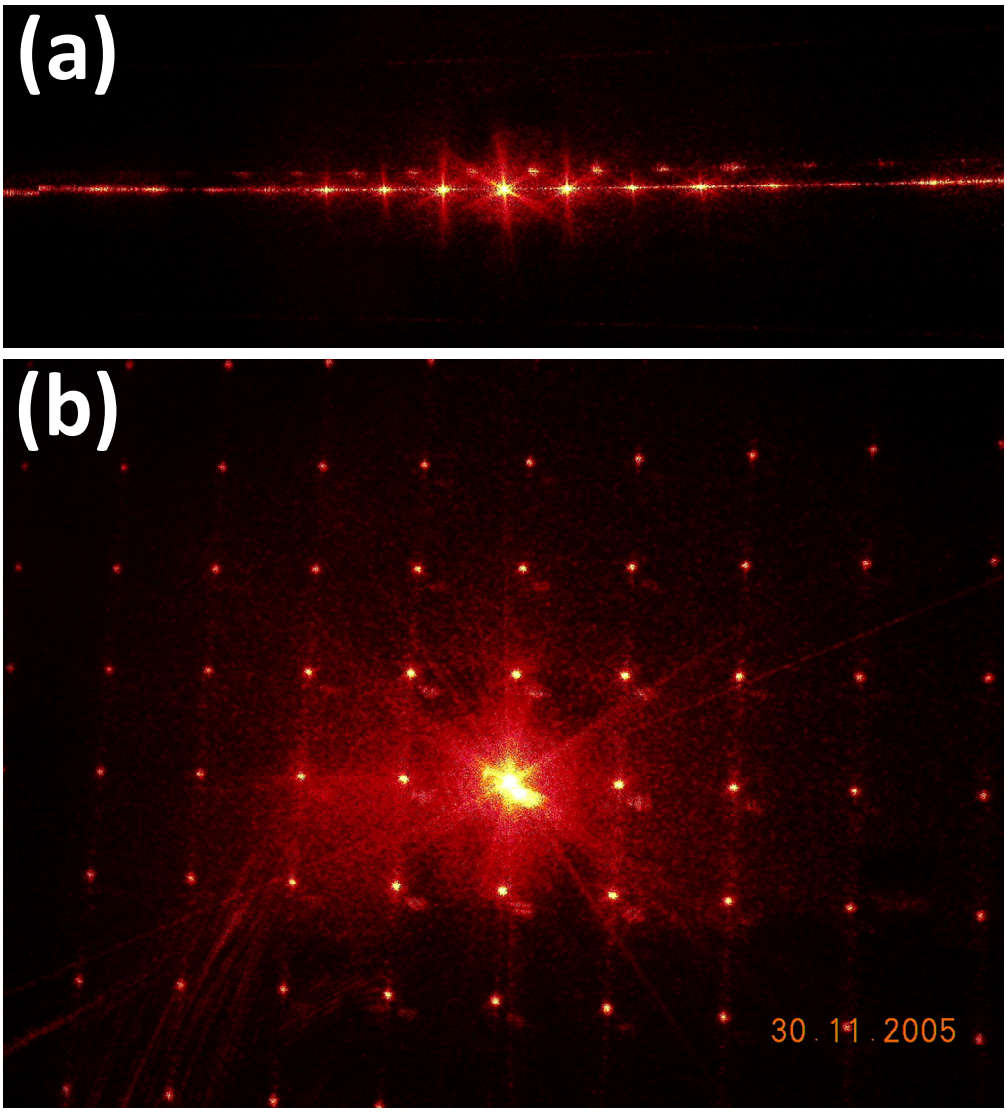

Figure 4.4. *1D and 2D He-Ne diffraction far field patterns*

For both types of diffraction gratings it was found that when the electric field of the He-Ne beam was ordinary polarized, the first order diffraction efficiency was about 2.8 and 2.6 times higher than when it was extraordinary polarized, for the 1D and 2D gratings, respectively. This very similar drop in the diffraction efficiency for both kinds of gratings can be partly explained by taking

into account that, as a general rule, the diffraction efficiency is enhanced when the refractive index contrast is increased. In our case, when the electric field of the laser radiation is parallel to the diffraction grooves it is perpendicular to the optical axis of the $LiNbO_3$ crystal, in such a way that it is ordinary polarized. In this case, the refractive index change will be determined by $\Delta n_{paralell} = n_o - 1$, where n_o is the ordinary refractive index of $LiNbO_3$ at the wavelength corresponding to the diffracted beam, and 1 stands for the refractive index of the air inside the ablated volumes (grooves or dots for the 1D or 2D gratings, respectively). Since $LiNbO_3$ is a negative birefringent crystal we have that $n_o > n_e$, and the index contrast will be higher for ordinary polarized beams. In the particular case of a 0.6328 μm wavelength He-Ne beam, this difference in index contrast is as high as ~0.084.

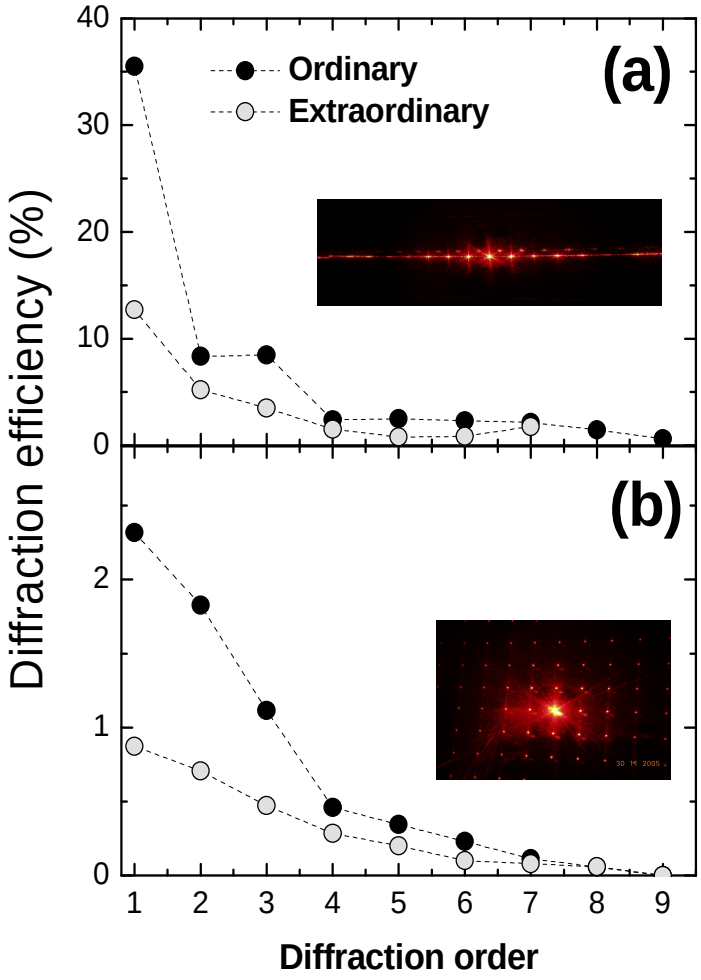

Figure 4.5. *Diffraction efficiency as a function of the diffraction order for the 1D and 2D case **(a)** and **(b)**, respectively.*

In the case of 2D gratings, the diffraction efficiency is also known to vary significantly with the polarization direction, but this difference is usually important for values of $\lambda/d \geq 0.15$, being λ the diffracted light wavelength and d the separation between grooves [13]. As in our case this factor has a value 1.06 µm / 15 µm = 0.07, it can be stated that it is improbable that this effect is the cause of our observed differences, rather than the previously explained birefringent effect.

4.4. Intra-cavity experiments

The laser performance of the micro-patterned Nd^{3+}:MgO:$LiNbO_3$ sample was investigated by placing it inside a quasi-hemispherical cavity, which is schematically drawn in **Figure 4.6**. As an input mirror (IM) we used a flat dichroic mirror of high transmittance at pump wavelength (0.81 µm) and high reflectance at laser wavelength (1.06 µm, corresponding to the ${}^4F_{3/2} \rightarrow {}^4I_{11/2}$ laser channel).

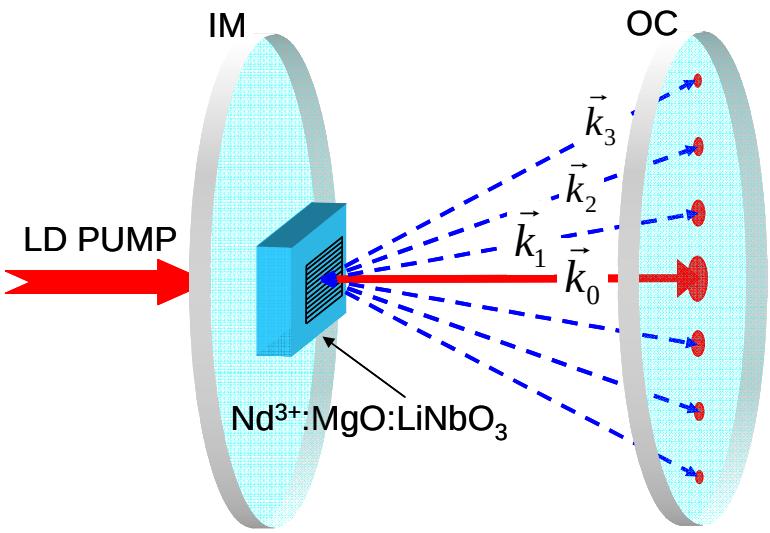

Figure 4.6. *Laser cavity used in the experiments.*

The output coupler (OC) was a 10 cm radius of curvature mirror with a transmittance of 1% for the laser radiation. End-pumping was performed by using a 100 µm fiber coupled diode laser operating at ~810 nm, corresponding to the ${}^4I_{9/2} \rightarrow {}^4F_{5/2}$ transition peak. The fibre output was

collimated and focused using two lenses, giving a minimum pump beam radius at the laser crystal of 90 μm. Cavity length was set to 9 cm, leading to a laser beam waist of ~100 μm. The Nd^{3+}:MgO:$LiNbO_3$ crystal was placed with the opposite face to the patterned one as close as possible to the IM, thus ensuring that pump radiation is not initially diffracted. The output laser power was then measured with a calibrated power meter.

When pump was achieved through the 1D or 2D periodic array, continuous wave stable laser oscillation at 1.06 μm could be easily obtained. **Figure 4.7** shows an infrared digital picture revealing the spatial distribution of the 1.06 μm laser radiation at the output coupler (**4.7 (a)** and **(b)** for the 1D and 2D patterns, respectively).

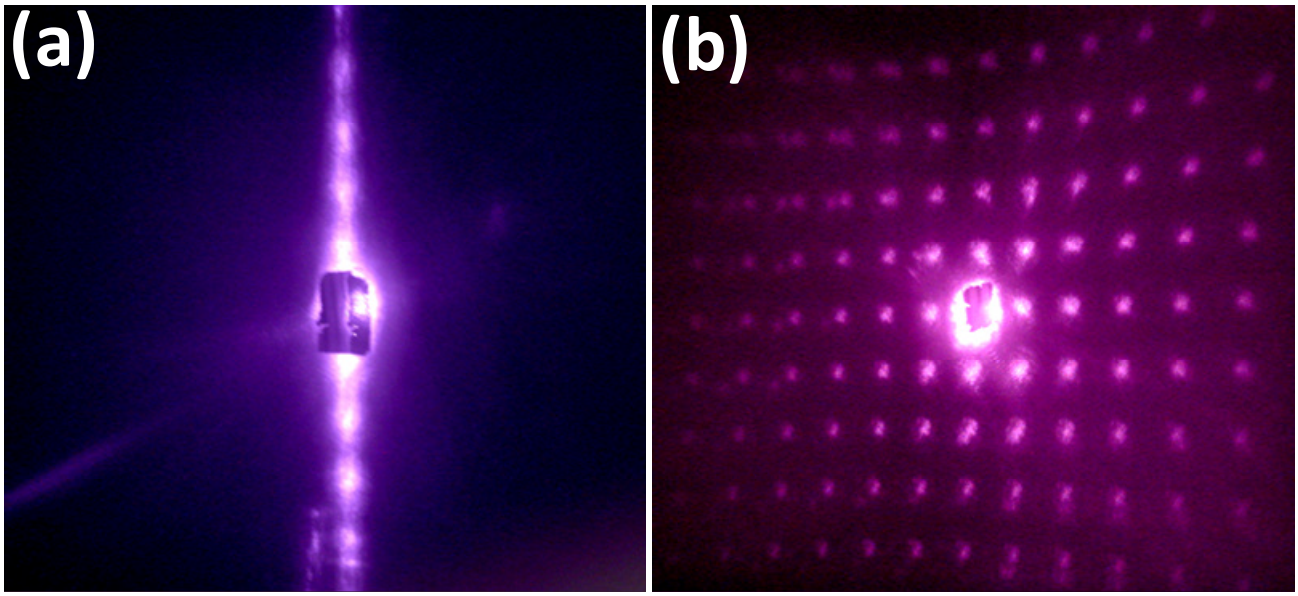

Figure 4.7. *Spatial distribution of 1.06 μm wavelength laser radiation at the output coupler;* ***(a)*** *and* ***(b)*** *correspond to laser oscillation thorough the 1D and 2D patterns, respectively. Both pictures were obtained with the output mirror partially covered in order to allow laser oscillation.*

It was found that the non-collinear laser light propagation was obtained by increasing, in both 1D or 2D arrays, the propagation angle by an amount equal to 4.5^{o} for the first order. This being in

accordance with the theoretical diffraction angle θ_{diff} = 4.05 ^{o} obtained from the well known condition:

$$d \sin \theta_{diff} = n\lambda \qquad (4.1)$$

with d = 15 μm the distance between diffraction grooves or dots, $n = 1$, 2, 3,... for the first, second and higher diffraction orders, respectively, and λ the diffracted wavelength (1.06 μm).

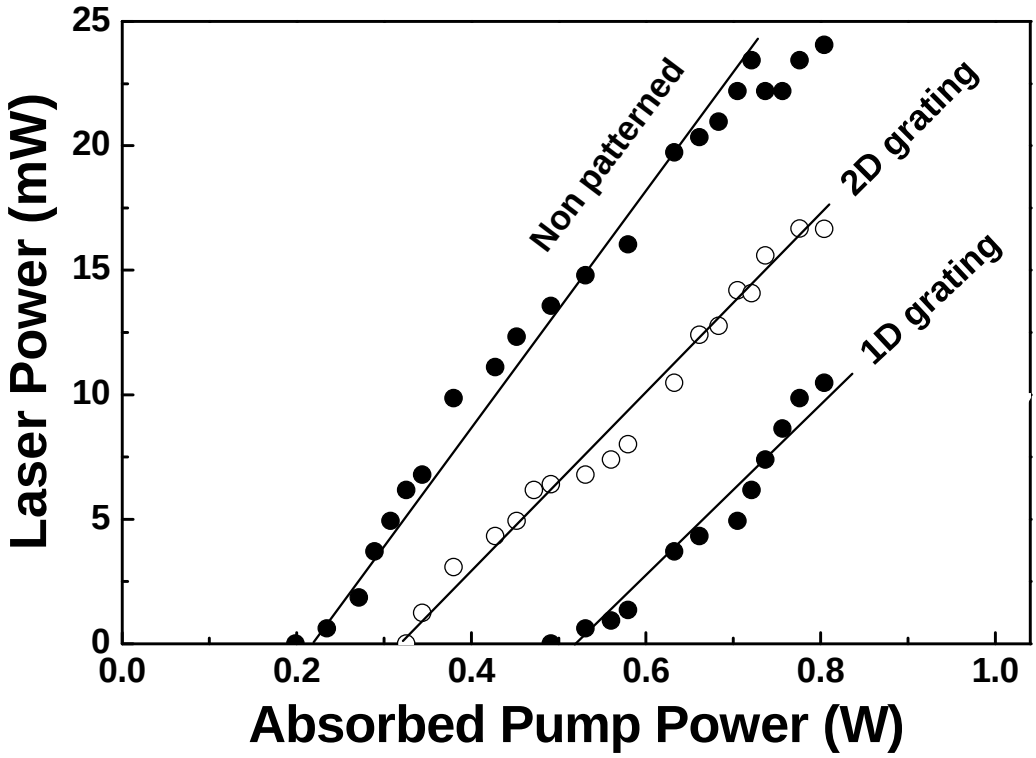

Figure 4.8. *Laser curves obtained from the Nd:$LiNbO_3$ crystal through an non patterned area and from the 1D and 2D diffraction elements.*

Figure 4.8 shows the output laser power at 1.06 μm as obtained when the laser action was achieved along a non-patterned area of the Nd^{3+}:MgO:$LiNbO_3$ crystal, and when laser oscillation was achieved through the 1D and 2D diffracting elements. For all the cases the infrared laser radiation was found to be extraordinary polarized (i.e. with its electric field parallel to the optical *c*-axis). This can be explained in terms of the higher emission cross section of Nd^{3+} ions in $LiNbO_3$ crystals for this particular polarization, and also by the fact that optical losses due to diffraction are

higher for the ordinary polarized emission. In our sample, the diffraction efficiency is lower for an extraordinary fundamental radiation (see **Fig. 4.5**) so that if higher laser intensities at the different diffracted orders are desired, ordinary laser oscillation polarized is required in order to access to higher diffraction efficiencies. This could be achieved by using additional intra-cavity optical components such as Brewster plates.

When laser action was achieved through any of the diffracting elements, a clear increment in the laser threshold was observed with respect to that at a non patterned area, while the changes in the slope efficiency are found to be rather small. The threshold increments can be attributed to an increment in the intra-cavity optical losses associated to the non diffracted beam (the zero order oscillating radiation). Consequently, the fraction of incident light which is diffracted into the different orders can be considered as an additional source of optical losses. Since the 2D grating has a lower efficiency (see **Fig. 4.5**), the diffraction induced optical losses are expected to be lower than those induced by the 1D diffraction element. This being in reasonable agreement with the lower laser thresholds obtained for the 2D grating with respect to those found for the 1D case.

4.5. Conclusions

The fs pulse DLW method for micro-fabricating surface relief gratings in Nd^{3+}:MgO:$LiNbO_3$ laser crystals has been investigated, and a comparative study has been performed for two specific cases of one-dimensional and two-dimensional surface relief gratings. It has been concluded that the technique allows for an ultrafast fabrication of high quality gratings in rare-earth doped $LiNbO_3$ crystals. Although the gratings were not optimized in terms of groove size and period for any specific application, it was qualitatively found that the slope efficiency of the laser cavity was not significantly altered when laser oscillation was produced along them. On the other hand, due to the fact that the non-collinear propagation introduces losses to both the pump and fundamental laser oscillation the laser thresholds are observed to be significantly altered, depending on the diffraction efficiency of the selected gratings.

References

[1] S. Nolte, G. Kamlage, F. Korte, T. Bauer, T. Wagner, A. Ostendorf, C. Fallnich, and H. Welling, *Microstructuring with femtosecond lasers*, Adv. Eng. Mater. **2**, 1-2 (2000)

[2] S. Nolte, M. Will, J. Burghoff, and A. Tünnermann, *Ultrafast laser processing: new options for three-dimensional photonic structures*, J. Modern Opt. **51**, 16-18, 2533-2542 (2004)

[3] R. R. Gattass, and E. Mazur, *Femtosecond laser micromachining in transparent materials*, Nat. Photon. **2**, 219-225 (2008)

[4] G. Della Valle, R. Osellame, and P. Laporta, *Micromachining of photonic devices by femtosecond laser pulses*, J. Opt. A: Pure Appl. Opt. **11**, 013001 (2009)

[5] L. Sudrie, M. Franco, B. Prade, and A. Mysyrowicz, *Writing of permanent birefringent microlayers in bulk fused silica with femtosecond laser pulses*, Opt. Commun. **171**, 279-284 (1999)

[6] K. Kawamura, T. Ogawa, N. Sarukura, M. Hirano, and H. Hosono, *Fabrication of surface relief gratings on transparent dielectric materials by two-beam holographic method using infrared femtosecond laser pulses*, Appl. Phys. B **71**, 119-121 (2000)

[7] X. Wang, H. Guo, H. Yang, H. Jiang, and Q. Gong, *Fabrication of beam shapers in the bulk of fused silica by femtosecond laser pulses*, Appl. Opt. **43**, 4571-4574 (2004)

[8] N. Takeshima, Y. Narita, S. Tanaka, Y. Kuroiwa, and K. Hirao, *Fabrication of high-efficiency diffraction gratings in glass*, Opt. Lett. **30**, 4 (2005)

[9] Y. Li, P. Lu, N. Dai, X. Wang, Y. Wang, B. Yu, and H. Long, *Surface relief diffraction gratings written on β-BaB_2O_4 crystal by femtosecond pulses*, Appl. Phys. B **88**, 227-230 (2007)

[10] C. Méndez, J. R. Vázquez de Aldana, G. A. Torchia, and L. Roso, *Integrated-grating-induced control of second-harmonic beams in frequency-doubling crystals*, Opt. Lett. **30**, 2763-2765 (2005)

[11] C. Romero, J. R. Vázquez de Aldana, C. Méndez, and L. Roso, *Non-collinear sum-frequency generation of femtosecond pulses in a micro-structured β-BaB_2O_4 crystal*, Opt. Express **16**, 22, 18109-18117 (2008)

[12] R. W. Boyd, *Nonlinear Optics*, Elsevier Science, 2003

[13] See for example, Optical and Laser devices Description in: http://www.shimadzu.com/

Chapter 5

Direct femtosecond laser writing of optical waveguides in lithium niobate

In this chapter we study the direct femtosecond pulse laser fabrication of optical waveguides in lithium niobate. An overview on the subject is presented and the effects of different fabrication parameters are discussed. Waveguides fabricated in both the thermal and non-thermal regime are analyzed by means of μ-Raman and rare-earth ion μ-luminescence experiments, and the main lattice changes are investigated. For the waveguide fabricated in the thermal-regime a tensile stress field is found which well explains the observed guiding, while for the waveguide fabricated at the non-thermal regime the Raman measured biaxial shear stress field explains only partially the observed guiding, and second contributing index-change mechanisms are discussed.

5.1. Introduction

Since the advent of the ultrashort pulse lasers [1, 2], the concept of ultrafast laser processing transparent materials started being developed with the aim of achieving a three dimensional (3D) integration of optical devices into the micron scale [3-5], and also in the search for new optical data storage/retrieval applications [6, 7]. Since then (mid 90's), the technique has been proven to be a unique method for microstructuring all kinds of materials, with special attention to those of interest in the field of photonics and optoelectronics, for which miniaturization is a fundamental issue. The continuous growth in popularity of the technique has led to a very wide range of photonic devices, such as waveguide lasers [8], frequency conversers [9], wavelength splitters [10], micro-diffracting elements [11], microfluidic laser resonators [12], photonic crystals [13-17], improved LEDs [18], MEMS [19], optical vibration sensors [20], and an ever growing list of devices in almost any kind of new or old materials.

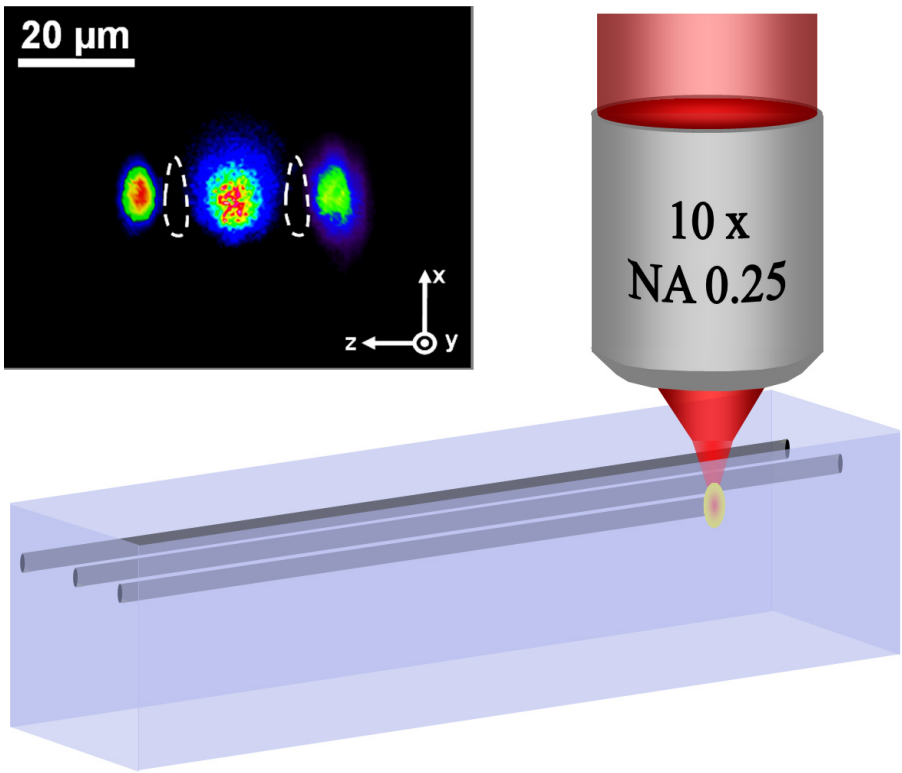

Figure 5.1. *Illustration scheme for DLW buried waveguides in a transparent material by use of ultrashort laser pulses and example of a fabricated waveguide in a lithium niobate crystal: measured near-field intensity distribution of propagating modes at 632.8 nm wavelength, at both sides of two written channels [32].*

In the particular approach for writing 3D waveguide arrays inside a transparent crystal, the light-guiding regions are in general created by scanning the ultrashort-pulse laser focus inside the material (see scheme on **Figure 5.1**). The laser pulse durations normally range between 80 femtoseconds (fs) to a few picoseconds (ps) of commercially available systems. Due to the extreme simplicity of this fabrication approach, the DLW technique features outstanding advantages as a single-step and ultrafast process for generating 3D optical circuits in processing times of even only seconds, depending on the device complexity.

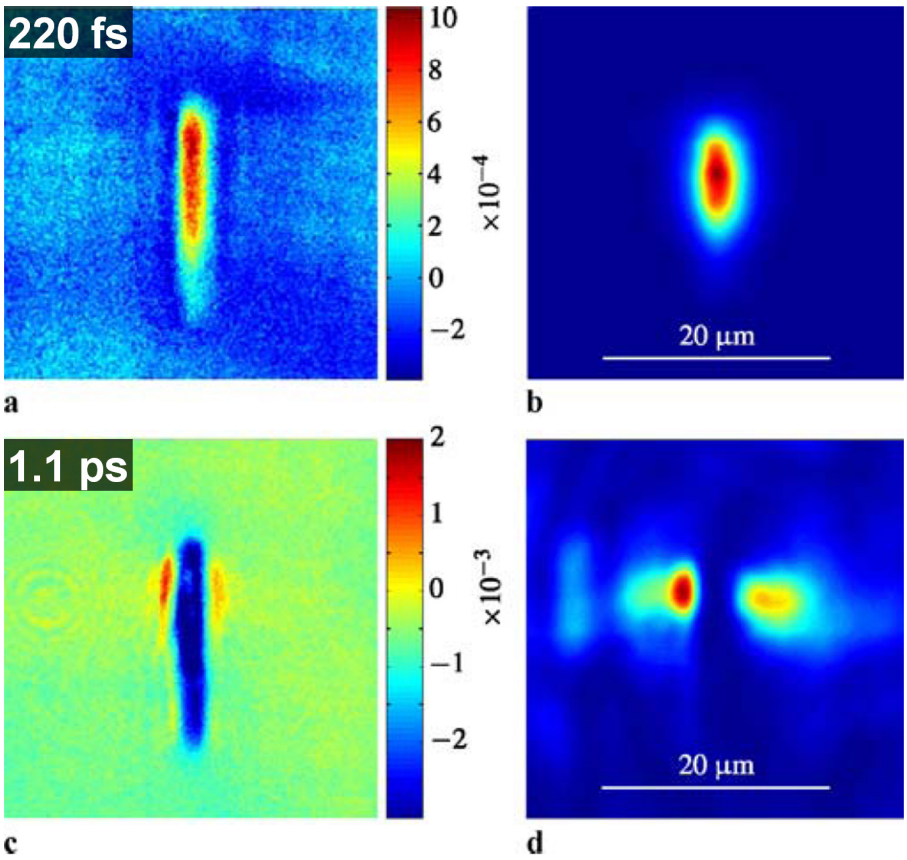

Figure 5.2. *Examples of laser induced extraordinary refractive-index changes -(a) and (c)-, and guided optical modes at 633 nm -(b) and (d)- in x-cut $LiNbO_3$, both performed with the same laser pulse energy (0.2 μJ), but different temporal pulse widths of 220 fs and 1.1 ps, as indicated. Figures extracted from Ref. [27].*

The exact waveguide formation mechanism not only depends on the material, but also, and very critically, it depends on the ultrashort-pulse laser irradiation conditions. From a phenomenological description, the approaches for DLW waveguides can be divided into those in which the refractive-index increase appears located at the laser focal volumes (see an example on

Figure 5.2(a)), usually called Type-I waveguides, and those in which the refractive index decreases at the laser focus, while indirectly increases on its surroundings, usually called Type-II (see **Figure 5.2(c)**)[*]. Both such effects can arise from diverse interaction mechanisms, with a different origin depending on the material properties, and on the laser parameters (such as the pulse temporal length, wavelength, pulse repetition rate, energy, type of polarization, scan speed, and focal spot size).

In addition, depending on the pulse duration and energy applied, the material can happen to change its behaviour playing an active role in the pulse propagation dynamics, switching the interaction process from an externally focused, to an internal *self-focusing* dominated one. This process can further increase the 3D fabrication possibilities if adequately tailored[†]. **Figure 5.2** exemplifies how two channels written with identical pulse energy, but different pulse duration, can produce such different results.

The DLW fabrication of waveguides in transparent materials was first demonstrated in glasses [5], later extended to crystals [21], and since then several studies have been carried on $LiNbO_3$ [9, 22-32]. The most distinctive issue between these studies in $LiNbO_3$ is that early works were mainly performed with low-repetition rate (1-5 kHz) fs lasers, and the investigations were focused on the optimization of scanning speed, pulse energy, polarization, and temporal pulse width, for tailoring the best waveguide properties [22, 24, 25]. Soon after that, high-repetition rate (600 KHz - 1 MHz) ultrashort pulse lasers were also applied over a broader multi-dimensional parameter space for optimizing optical losses, mode symmetry, and processing speeds [23, 28, 29][‡]. Within these studies, symmetric waveguides with low 0.6 dB/cm propagation losses at the 1300-nm telecom band were obtained, which matched the previous results of waveguides formed at the low repetition rate, but with the advantage of a 50-fold faster fabrication speed of 46 mm/s [23].

[*] A specific nomenclature has risen in the literature regarding these two types of waveguides. Waveguides in which a refractive-index increase appears at the writing laser focal volume have been referred to as Type I, and others as Type II. This straightforward and useful nomenclature can be however inefficient since it can blend into a same category waveguides formed by very different physical mechanisms (for instance by different effects such as the photorefractive, electrooptic, or the piezooptic effect).

[†] See **Chapter 3** for a general study on laser microstructuration of $LiNbO_3$ crystals.

[‡] A more detailed review of the different fabrication parameters which have been investigated in $LiNbO_3$ is given on section 5.2.2.

It is important to note that although the use of higher frequencies speeds up the fabrication process, it can also introduce thermal accumulation and heat flow processes into the set of modifying mechanisms. Due to this, it is still not clear which laser parameters give the lowest propagation losses while at the same time maintain the nonlinear properties of the $LiNbO_3$ lattice unchanged. What is more, it is also not yet clear which waveguides are the most durable and temperature resistant. All these issues –device functionality and reliability- are of enormous importance in most applications, and especially in those like high-power devices, satellite technologies, or in astrophotonics, for which the ultrafast DLW technique has already been anticipated as the best potential fabrication technology [33].

Fulfilling all these technical requirements in a $LiNbO_3$-based device continues being a very challenging task, and the main reason is that $LiNbO_3$ presents a rather complex crystalline structure into which the extreme interaction of ultrashort-pulse lasers can generate a broad range of effects[§]. Thus, the observed index changes can be a product of different sorts of intense laser interaction processes which induce strong lattice alterations which have been observed in $LiNbO_3$ crystals and other dielectrics: generation of high defect densities, space charge electric fields, lattice stress, changes in the local stoichiometry, ionic rearrangements, or localized amorphization of different degrees [17, 23, 24, 26, 27, 30-32, 34-38, 45-47, 49, 51, 53, 79, 81].

Despite the widespread interest in laser-writing optical waveguides in crystals, and specifically in $LiNbO_3$, still little is known about the exact physical mechanisms which are responsible, in each case, for the formation of high refractive index regions. In other words, little is still known about the exact lattice changes which produce the observed refractive-index increments, and about how the ultrashort laser pulses produce those lattice modifications. As previously mentioned, functionality and reliability are the main aspects to look after when designing any new device, and thus, a precise understanding from the material science point of view is needed. In this sense, a clear association between the $LiNbO_3$ lattice changes and the fabricated waveguide characteristics would provide a deeper understanding of the fabrication process, which would lead to an optimization of the waveguide properties. What is more, such an understanding of the underlying physical mechanisms

[§] See **Chapter 2** for details on the properties of $LiNbO_3$ crystal.

could also show the way to new possible fabrication schemes or applications which, otherwise, would maybe not be recognized.

In the following sections we describe the fabrication and microstructural characterization of DLW $LiNbO_3$ waveguides produced by two mainly different methods, which produce surface or deep buried waveguides. Particular attention has been put to the fabrication of buried waveguides, as these can lead to 3D waveguide circuits and devices inside the material.

5.2. Review on DLW fabrication of waveguides

5.2.1 Surface waveguides

In the case of surface writing, increased refractive-index channels can be produced below or at the laterals of an ablated groove. These guiding regions can appear as a result of the induced strain field entailed by the ultrashort-pulse laser microexplosion process and are, in this sense, clear fingerprints of the high pressures induced in the surroundings of laser generated micro-plasma[**]. Although this surface waveguide fabrication method has not been investigated yet in detail in $LiNbO_3$ crystals, it has been recently reported by the authors in other crystalline materials such as ceramic Nd^{3+}:YAG[††]. We provide here evidence that such a process can also be tailored in rare-earth ion doped $LiNbO_3$ for the creation of close to surface waveguides.

Figure 5.3 shows an image of two waveguides created at the surface of a Pr^{3+}:$LiNbO_3$ sample, as seen on an optical microscope transmission image of the waveguide cross-section. As writing laser a 120 fs, 1 kHz, Ti:Sapphire laser oscillator operating at 796 nm wavelength was used. The peak laser fluence was varied between 2-5 J/cm^2, and the laser focusing was performed by means of a 10X microscope objective of numerical aperture 0.30, giving a focal spot of around ~3.2 μm in diameter. In order to scan lines a computer controlled XYZ positioning stage was used, at a set speed of 26

[**] See Chapter 3 for an analysis of the induced micro-stress under fs laser ablation in $LiNbO_3$.
[††] Results on surface and bulk DLW of photonic structures in Nd:YAG ceramics were first presented at COLA 2007 International Conference on Laser Ablation [46].

µm/s. All the process was performed in air under normal atmospheric and room temperature conditions.

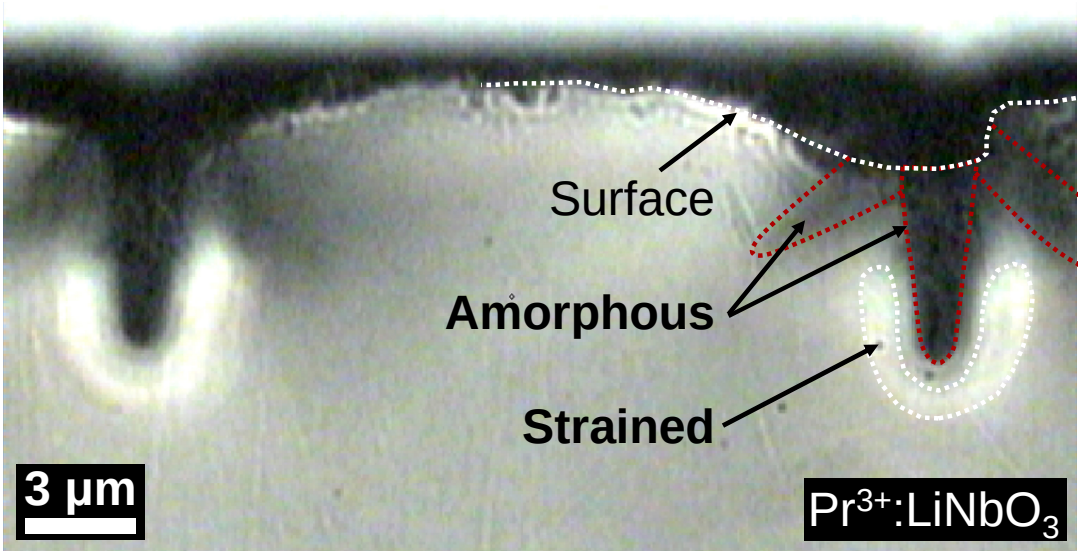

Figure 5.3. *Optical microscope image of two written tracks under which strain fields produce waveguiding tracks. Peak laser fluence was set to ~4 J/cm^2.*

Three main distinct zones can be distinguished in **Fig. 5.3**, namely an ablation area (not clear in this cross section of the sample due to the imperfect polishing process which produces broadening of the ablated channel lateral sides), an main amorphous channel appearing below the ablated volume (dark region), and a crystalline strained area surrounding it (bright region). The amorphous track is known to reproduce the laser focal distribution where the peak fluence is slightly below the ablation threshold, but is still high enough to produce a high density of free electrons, which subsequently can comprise plasma or a high defect density area. Two lateral amorphous channels can also be observed, which are known to be produced by the diffraction of pulses in the previously written channel (due to the fact that in this writing conditions several pulses interact with the same sample area). The strained region is known to consist on mainly defect-free crystalline $LiNbO_3$, which is assumed to be produced by the high pressures entailed by the plasma formation and the ablation microexplosion process. These areas have been analyzed in detail by µ-Raman and µ-Luminescence confocal microscopy, and a maximum compressive stress of around ~2 GPa was

obtained at the strained region [32], which can explain the observed refractive index increments through the piezooptic effect (see **Chapter 3** for further details).

As mentioned, the irradiation conditions for these tracks are those of multipulse ablation, where around 125 laser pulses are focused on the same focal spot area (under these parameters each laser pulse in the scanned line would irradiate at a point only ~26 nm distant from the next). This multipulse scanning regime is known to lead to multiple accumulation processes such as lattice defect incubation, and of a saturation of the laser ablated depth due to diffraction of the incoming pulses in the created track [32, 49, 50]. In our experimental conditions, the depth of the amorphous track was observed to be very critical with laser pulse energy. In this sense, it was found that if the laser pulse energy was controlled different kind of ablation and amorphous tracks would be obtained, in such a way that waveguide modes with different shapes could be obtained below the different ablated grooves. **Figure 5.4** shows the measured waveguide mode as seen by end-coupling experiments using a He-Ne laser (632.8 nm), in a lower energy surface relief groove performed on an Nd^{3+}:$LiNbO_3$ sample. This waveguiding mode was observed in the immediate region below the surface relief groove.

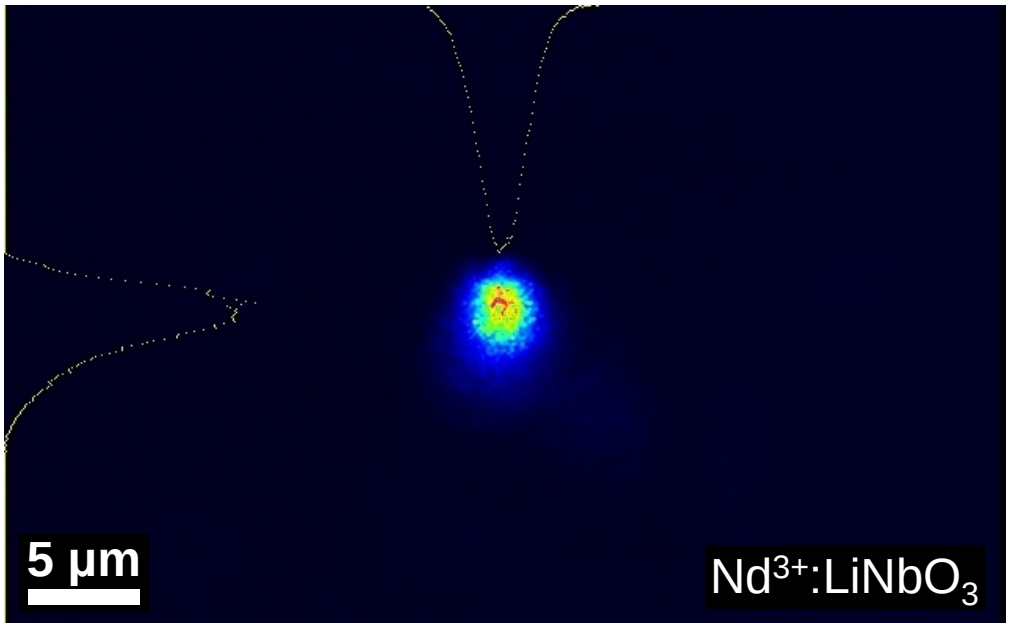

Figure 5.4. *Near-field intensity distribution of the vertically polarized waveguide mode at 632.8 nm, and immediately below the performed surface relief groove [48].*

It should be mentioned that despite the results here shown, the fs laser pulse surface processing of laser crystals is still mostly unexplored as a way to produce new surface waveguiding and photonic devices. It can be easily predicted that if the ablation process is done on a previously ion indiffused or proton exchanged sample (to create refractive-index confinement in the vertical dimension), and a further third step of wet etching was performed in order to remove the amorphous volumes, then high-quality ridge waveguides could be expected. These waveguides would also have the additional advantage of an easy incorporation of electrodes on the previously ablated volumes surrounding the waveguiding channels. Thanks to the high spatial precision of the DLW technique, waveguides with widths down to the 1 μm size can be expected, which would imply an extremely high light confinement, by means of the step index-contrast in the lateral dimension. Such a strong light confinement would imply higher propagation nonlinear effects, a more efficient electrooptic use of the available electric field between electrodes, and also a highly efficient light amplification and laser action if the crystal was doped with laser ions like Nd^{3+}, Yb^{3+} or Er^{3+} rare-earth ions.

Despite the interest on this and other related approaches of the surface DLW technique, neither of them was investigated during this thesis period of time, mainly because of a lack of time. Instead, the focus was rather put on the fabrication of deeply buried waveguides, which would allow the inscription of 3D circuits inside the material. The next section tackles this issue.

5.2.2 Deep buried waveguides

In this section we first provide a brief description of the DLW process in $LiNbO_3$, we summarize the different works published up to date by different authors, and describe the diverse interaction regimes which can be induced depending on the different choosing of DLW parameters.

In the case of buried optical waveguides in $LiNbO_3$, extensive research has been already conducted by groups all over the world since the first demonstration by Gui et al. in 2004. The ultimate goal of these research works is developing the technique for obtaining functional high

quality 3D optical circuits on $LiNbO_3$, and other related crystalline materials. The set up for writing buried waveguides is that depicted in **Fig. 5.1**. Despite its apparent simplicity, the different DLW set ups span an eight dimensional parameter space of: pulse temporal width, repetition rate, energy, wavelength, polarization, focusing numerical aperture (NA), scan speed, and sample orientation. It is also worth mentioning that this parameter space can be further extended if the shape of the laser beam is engineered, by using extra focusing lenses (for instance, an extra cylindrical lens would led to a more astigmatic beam with elliptical cross section, instead of spherical), although in our study we will not consider such case.

The two first important parameters to look at are the laser pulse temporal-width, and the repetition rate, as they will determine the type of light-matter interaction regime which will be made in the crystal. As previously said, investigations have already been performed in the pulse temporal range from ~100 fs to ~1 ps, and for repetition rates ranging from the kHz to MHz regime. Once these parameters are set, the NA of the focusing lens and the pulse energy are important control parameters which will further determine the morphology, size and degree of material modification which will be performed inside the sample. Last but not least, other parameters such as the scan speed, the crystal axis orientation, and the laser wavelength and polarization need also to be carefully looked after, in order to properly control and optimize the waveguide properties.

This classification is only a starting guide route into the DLW process, and in some cases certain specific parameters (such as for instance the laser polarization, or the sample orientation) will be critical for entailing (or hindering) some specific interaction processes or unexpected features. As a general rule, however, it is important to be aware that it is always the whole combination of parameters (within this 8D parameter space) what can determine the kind of modification and waveguide properties which will be induced inside the crystal. Still, one can always found, or at least one would desire to have, a specific experimental set up under which the variation of parameters such as the laser polarization or the scan direction in the sample, would not produce any significant variation in the performed modifications. This is especially important if one wants to fabricate arbitrary spatial designs into the sample, were different writing directions and different

polarizations of the pulses with respect to the sample axis would always take place (for example if curved waveguides are performed).

Do to the extreme difficulty of performing a complete comprehensive study over the whole parameter space, still today no convincing solution or optimum fabrication conditions have been found, in terms of waveguide quality and functionality. In order to throw some light into this 'fabrication puzzle', **Table 5.1** summarizes the set ups of the different works published on fs DLW of waveguides in $LiNbO_3$, up to the first half of the year 2009.

With this list of fabrication parameters we can now analyze and compare the different conditions in which the different waveguides were performed. This collection and organization of the published data is not only intended to provide a panoramic view over the existent literature, but also to make clear what has been previously investigated, and obtain the trends which have been used by the different researchers.

Table 5.1. Experimental thermal accumulation conditions

Date	Author	f	τ	Speed	λ (nm)	Polarization	NA	Focus (μm)	Crystal axis	# lines	E (μJ) (Δn type)	Merit	Ref.
2004, 7 Jan	L. Gui	1 kHz	150 fs	50 μm/s	775	Circular	0.4	500	Z-cut	1	10 (?)	1st waveguide & Y-splitter	24
2006, 9 Feb	R. R. Thomson	5 kHz	520 fs	2 - 20 μm/s	800	Linear	0.4	250	Z-cut	1	0.2 (I) / 0.4 (II)	Discover Δn-type I& II	25
2006, 3 Jul	J. Burghoff	1 kHz	40 fs (?)	100 μm/s	800	Linear	0.65	200	Z-cut / X-cut	1	(I) ≤ 0.5 < (II) (18: x-cut)	SHG @1.064 μm	9
2006, 2 Aug	A. Nejadmalayeri	1 kHz	1 ps	0.6 - 0.9 mm/s	800	Circular	0.5	70	Z-cut	1	0.7 (II & III?)	Prop. Losses 0.7–1.0 dB/cm @1.3–1.5 μm	23
2006, 7 Sept	Y. L. Lee	1 kHz	130 fs	10 μm/s	781	?	0.4	20	Z-cut PPLN	6	0.4 (I)	SHG-QPM @1.5 μm; $3x10^{-4}$ % $W^{-1}cm^{-2}$	40
2006, 10 Oct	J. Burghoff	1 kHz	40 fs - 1.1 ps	100 μm/s	800	Linear (pp)	0.65	100-130	Z-cut / X-cut	1	0.2 – 1 (I & II)	Structural characteriz. @1 kHz DLW	27
2007, 28 Feb	J. Burghoff	1 kHz	40 fs (?)	100 μm/s	800	?	0.65	200	Z-cut / X-cut	1	I ≤ 0.5 < III(1.5) & II(6)	Morphology study & SHG (no new)	38
2007, 2 Mar	H. T. Bookey	600 kHz	350 fs	4 mm/s	1040	Linear (pp)	0.6/0.3eff	150	Z-cut	20	0.37 (I)	Prop. Losses 0.6 dB/cm @1.5 μm	28
2007, 21 May	R. Osellame	600 kHz	350 fs	6 mm/s	1030	Linear (pp)	0.6/0.3eff	250	Z-cut PPLN	20	0.27 (I)	SHG-QPM @1.5 μm; 6.5 % $W^{-1}cm^{-2}$	29
2007, 4 Jun	J. Burghoff	1 kHz	100 fs - 1.2 ps	100 μm/s - 1 mm/s	800	?	0.65	50-150	X-cut / Z-cut	1	0.2-0.3 (I & II)	Δn mechanism discussion; types I & II	26
2007, 29 Jun	H. Chen	25 MHz	100 fs	200 μm/s	800	Linear	0.65	200	Z-cut	1	0.075 (I?)	1x4 waveguide array coupling @0.63 μm	41
2007, 10 Jul	A. Nejadmalayeri	700 kHz	600 fs	46 mm/s	1045	Circular	0.55	110	Z-cut	1	0.5 (II & III)	0.6 dB/cm @1.3 μm. + thermal effects study	23
2007, 24 Sept	J. Thomas	1 kHz	2.5 ps	0.8 mm/s	800	Circular	0.65	50	Z-cut PPLN	1	0.4 (II)	SHG-QPM @1.064 μm; 58% efficiency	42
2007, 28 Nov	W. Yang	250 kHz	150 fs	200 μm/s	800	Linear	0.55	150	-Z-cut	1	2 - 2.4 (I & II)	Non-reciprocal light pressure and heat flow	34
2008, 22 May	S. Zhang	1 kHz	50 fs	400 μm/s	800	?	0.4	200	Z-cut PPLN	1	10 (II)	SHG-QPM @1.5μm; 4.8 % $W^{-1}cm^{-2}$	43
2008, 9 Aug	A. Ródenas	700 kHz	600 fs	46 mm/s	1045	Circular	0.55	110	Z-cut	1	0.5 (II & III)	1st Raman study of DLW waveguide Ref. 24	30
2008, 25 Aug	M. Heinrich	1 kHz	2.5 ps	0.8 mm/s	800	Circular	0.65	150	X-cut	1	0.9 (II)	Planar array coupling @0.63 μm (Type II)	44
2009, 4 Feb	B. McMillen	250 kHz	150 fs	1 mm/s	770	?	0.68	150	Z-cut $LiTaO_3$	?	0.3 (III?) / 1 (?)	$LiTaO_3$ DLW waveguide Raman study	45
2009, ?	A. Ródenas	1 kHz	120 fs	50 μm/s	796	Linear	0.3	500	X-cut	1	1 (II)	Raman study Type II waveguides	31

As previously mentioned, the first key parameters are the laser pulse duration and the repetition rate. As most of the studies have only been performed in the short window of ~100 fs to 1 ps, the duration of the pulses can be thought to be bellow the electron-phonon lattice coupling time and thus significant heating due to a single pulse irradiation can be disregarded. Thus, the first important differentiation between different waveguides can be made between those performed at the low repetition rates (KHz), and those at high repetition rates (MHz), for which fundamentally different thermal regimes apply. This differentiation is important since it can determine, in combination with the rest of parameters, whether the modification process is done in the thermal or non-thermal regime. A simple calculation can be made to clarify and determine this effect, taking into account the different DLW parameters:

The focal spot diameter of a supposedly Gaussian beam at $1/e^2$ its peak intensity is:

$$d_{spot} = 1.22\lambda / NA \tag{5.1}$$

and the spatial separation between two consecutive pulses in a scan is:

$$L_{pulses} = v_{DLW} / f_{laser} \tag{5.2}$$

where v_{DLW} is the scanning speed, and f_{laser} is the laser frequency (i.e. repetition rate). Knowing the separation and the size of spots we can calculate the number of pulses which overlap in a spot diameter as:

$$N_{pulses} = d_{spot} / L_{pulses} \tag{5.3}$$

The number of pulses overlapping on a same sample volume gives us an idea on the accumulation of any kind of effects the laser pulse can cause; for example the amount of induced lattice defects such as cracks, or the possible heat accumulation within the spot volume. But yet, this number does not explain whether the heating processes would be relevant or not on the whole interaction process.

To know if heat is being built up by the subsequent pulses, or kept constant, we can simply look at the thermal diffusivity of the material, D_{th}, which could be experimentally measured, or also calculated from the known specific heat capacity, c_p, the thermal conductivity, κ, and volume mass density, ρ, of $LiNbO_3$ as:

$$D_{th} = \kappa/(\rho c_p) \tag{5.4}$$

By introducing then the corresponding values for $LiNbO_3$ (see **Chapter 2** for details on $LiNbO_3$ properties) we can obtain a value of $D_{th} \approx 8 \times 10^{-7}$ m^2/s, and we can then use this value for the thermal diffusion at the laser focal volumes[‡‡]. From this, the effective cooling time for the spot volume, τ_{eff}, can be calculated as [51]:

$$\tau_{eff} = d_{laser}^2 / D_{th} \tag{5.5}$$

Values for τ_{eff} normally range from 0.5-100 µs for focal spot diameters of about 1-10 µm (i.e. for high or low NA respectively, for a 0.8 µm wavelength). By comparing this heat diffusion time with the time interval between pulses we can then determine whether during the DLW process there is thermal accumulation or not. It is useful to define the critical frequency at which this thermal regime would start as:

$$f_{cr} = 1/\tau_{eff} \tag{5.6}$$

Which ranges from 8 to 1600 kHz, and from this critical frequency we can now normalize the laser pulse frequency used, which can be used to differentiate and compare the results of the different sets of DLW parameters used in $LiNbO_3$ (see **Table 5.1**). That is, a normalized frequency, f_n:

$$f_n = f_{laser} / f_{cr} \tag{5.7}$$

[‡‡] As the reader would have noticed, we are then assuming here that the thermal diffusivity values of the laser excited volumes are the same as that of the material in normal conditions, i.e. that this diffusivity value does not change with temperature. We allow this approximation here as the only purpose of this analysis is obtaining a general idea on how the fabrication parameters can control the kind of modification process, and as we will see further on, experimental results fit well with this simple approximation.

which tells us how high or low is the laser pulse repetition rate we are using with respect to heat accumulation. Whenever the normalized frequency is below or above 1, the fabrication process will be regarded to be outside, or inside, the thermal regime, respectively.

To classify the basic waveguide fabrication conditions we need also to choose a second key parameter apart from the normalized frequency. As previously said, the NA of the writing optics and the laser pulse energy are also two important parameters to control. While the NA values normally used for waveguide writing are low, in most cases NA < 0.7, the experimental pulse energy values which have been reported for waveguide writing fluctuate between a more than 2 orders of magnitude difference (0.07 - 18 μJ). Due to this much higher dispersion in the investigated values we chose then the laser pulse energy as a second parameter.

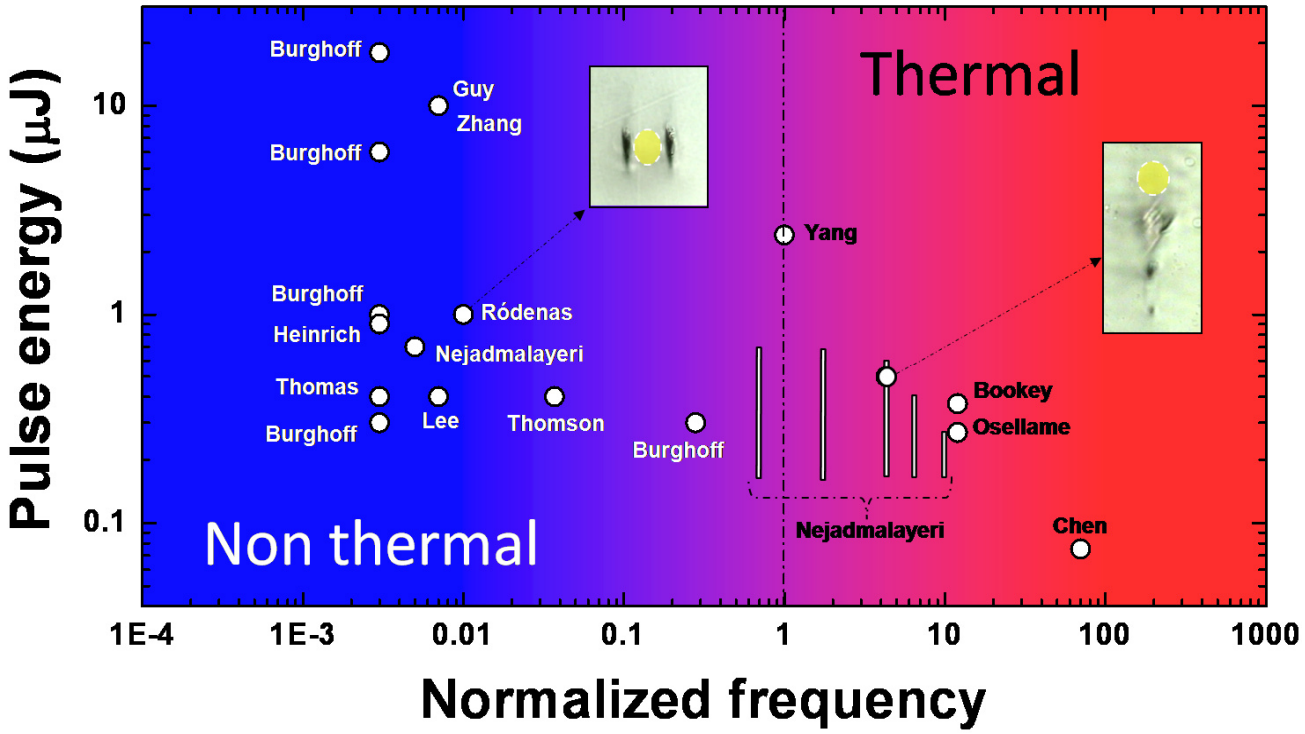

Figure 5.5. *Fabrication map showing the laser pulse energy versus normalized frequency. Depicting the different thermal regimes of each work and the mean energy values normally used for waveguide writing.*

By using data from **Table 5.1**, together with **Eqs. 5.1** to **5.7**, a map can be built up now over the published experimental DLW parameters for fabricating buried optical waveguides in $LiNbO_3$ crystals. This map is shown in **Figure 5.5**, representing the laser pulse energy versus normalized frequency in each case.

As it can be seen, most of the reported works have been done in the non-thermal regime, or rather *low-thermal* regime, where no heat accumulation occurs during the line scans. It can also be seen that the normalized frequency values reported in literature vary for more than 4 orders of magnitude. The '*coolest*' waveguides (lower normalized frequencies) have been fabricated, mainly by Burghoff et al., at frequencies almost 3 orders of magnitude lower than that at the approximate limit for thermal accumulation. The fact that waveguides fabricated at the same laser repetition rate (1 kHz), such as those of Burghoff et al. and Ródenas et al, show quite different normalized frequencies is due to the use of different NA optics, which change the fabrication thermal conditions by simply changing the laser spot size, and thus changing the effective cooling time. At the same time, the '*hottest*' $LiNbO_3$ waveguides (higher thermal regime) have been fabricated at frequency values more than 1 order of magnitude above the limit, and were extensively studied by Nejadmalayeri et al. [23].

It is important to note that this fabrication 2D map gives only a partial aspect of the laser interaction modification process, mainly the mechanisms related to the heat increase and accumulation during the writing process inside the sample, and the range of laser pulse energies used on that. However, there are other important aspects which could be studied, for instance, a plot of scan speed versus propagation losses, or numerical aperture (NA) versus propagation losses, would also be important. To study the relation between these and other parameters, the rest of the laser writing set up parameters would have to be fixed. Such a study has only been reported so far, to the authors' knowledge, by Nejadmalayeri et al. in 2007 [23], in a notable work where a mapping of the propagation losses of TE polarized modes, for waveguides written with different energies and scan speeds, and for two different repetition rates of 250 kHz and 700 kHz, was performed. These plots are shown in **Figure 5.6**, and although they only cover certain fractions of the thermal regime

and its limits (see **Fig. 5.5**), they corroborate the assumption previously made of a critical frequency (see **Eq. 5.7**) above which heat accumulation effects start to appear[§§].

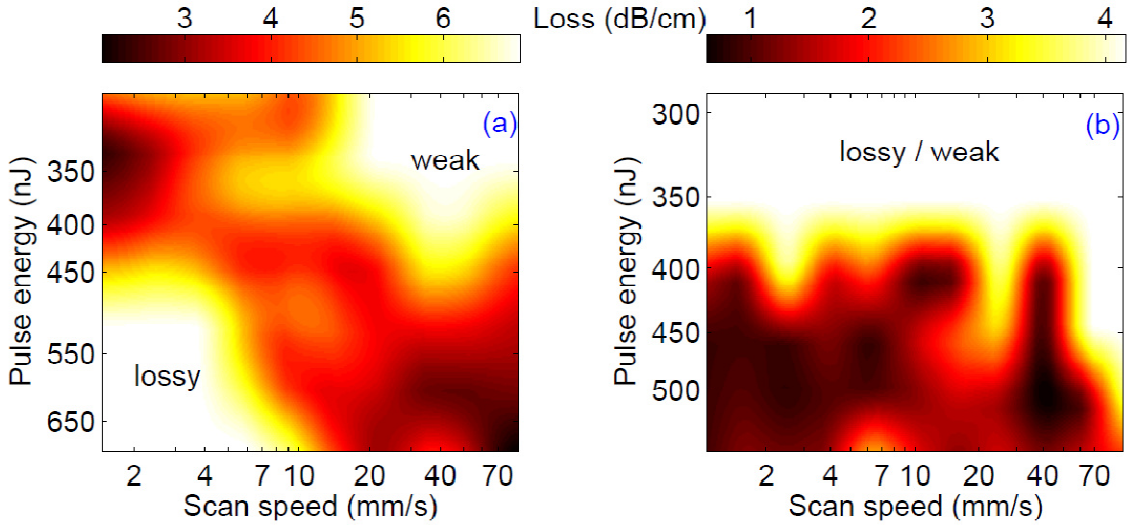

Figure 5.6. *Propagation losses of waveguides fabricated with different laser pulse energies and scan speeds for the two high laser frequencies of 250 kHz (a) and 700 kHz (b). Figure extracted from [23].*

In their specific whole set up (see **Table 5.1**), these 250 kHz and 700 kHz frequencies translate into normalized frequency values of 1.7 and 4.7 (see **Fig. 5.5**). The information provided by the propagation losses mapping in **Fig. 5.6** is of great importance to understand the basic mechanisms in ultrafast laser writing buried waveguides in $LiNbO_3$ crystals. A qualitatively different behavior in the induced changes and morphology was observed when waveguides were fabricated at a normalized frequency of 1.7 or at higher 4.7. Although the following conclusions are only valid for the specific settings of circular polarization, NA (0.55), pulse duration (600 fs), laser wavelength (1045 nm), and sample orientation (z-cut), the following trends were observed in $LiNbO_3$:

[§§] It is fair mentioning here that the first experimental studies on fs laser writing of transparent dielectrics in the thermal regime were done by Schaffer et al. in 2000 [54], in a work where they first demonstrated that heat accumulation and melting could be performed inside glass using a high repetition rate oscillator (25 MHz). Also four years after that work, Juodkazis et al. provided a qualitative description of the thermal stress induced by the heat accumulation, setting an analytical expression with a 2D model, and demonstrating that crack-free irreversible damage can be induced inside glass by using 12 ps pulses of 355 nm wavelength at 80 MHz repetition rate. The main mechanism was described as a laser induced "dielectric breakdown without crack formation in a softened material around the irradiated volume", and the width of the scanned lines was shown to depend on the scanning speed as $\sqrt{1/v}$, as expected for a diffusion controlled process [51].

At a normalized frequency of f_n ~5 (700 kHz, see **Fig. 5.6 (b)**) there can exist a critical laser pulse energy threshold (~360 nJ) below which, independently of the scan speed studied, waveguiding cannot appear, and above which low loss propagation (≤ 0.7 dB/cm) can appear on a wide energy range, from 400 - 550 nJ. This simple behavior must be related to the thermal heating and annealing of the irradiated volumes while the focus is scanned. The thermal region is defined by the condition that the heat affected zone (HAZ) cools slower than the time which passes between subsequent pulses arrive (see **Eqs. 5.1** to **5.7**). Due to this, a continued heating process could be causing thermal relaxation of the lattice so that shock-wave pressure induced damage, as well as defect induced damage, would be strongly reduced by the annealing processes. The efficiency of this laser driven annealing process however only depends on the time arrival between pulses, and the scanning speed would have little effect on the annealing strength at these speed ranges (< 80 mm/s). The laser pulse energy, on the contrary, is responsible both for the temperature increase of the irradiated volume, for the extension of the HAZ, and density and extension of the different kinds of lattice defects formed. It is therefore straightforward to conclude that -in this frequency and scan speed range- it is the increasing amount of deposited energy per pulse the factor which would drive a refractive-index increment process in the surroundings of the damaged focal volume capable of producing low-loss waveguiding. This waveguiding would occur when neither the annealing process would erase the induced index change, nor the accumulated not-annealed defects would induce lineal losses of propagating light, by acting as scattering centers. Further on increasing the pulse energy, it is also expectable that the amount of induced defects would start introducing excessive losses at a certain value, as it is seen to occur at ~550 nJ for a speed of 7 mm/s in **Fig. 5.6 (b)**.

At a normalized frequency of f_n ~2 (250 kHz, see **Fig. 5.6 (a)**) however, a significantly different trend is observed. In this case low propagation losses of about ~2 dB/cm were only observed for certain specific combinations of energy and scan speeds, constituting a diagonal frequency window where increasing the pulse energy demands increasing the scanning speed. No threshold pulse energy was therefore observed, and the underlying mechanisms responsible for the different minima in the losses would have to be explained in a different manner. As this frequency corresponds to a normalized frequency of around 2, it is clear that for this intermediate frequency

the annealing process and any shock-induced strain or defects must be on a critical balance, where the previously observed independency on the scanning speed is no longer valid, and the percentage of pulse overlapping becomes now important. In this case the amount of induced defects would be critical for controlling the optical losses, and thus too much energy deposited on a low speed scan would yield lossy waveguides, and too low energy deposited while scanning too fast would only yield a weak waveguiding. Although the pulse overlapping here (in the scan speed range from 1-70 mm/s for their specific set up) only varies from a 99.8% to 87.9% (i.e. merely a 10%), this behaviors are observed in **Fig. 5.6 (a)**.

A question can also rise concerning why the waveguides fabricated at f_n ~5 show much lower (≤ 0.7 dB/cm) losses than that at the lower f_n ~2 (~2 dB/cm). We can only speculate here that this occurs due to the fact the intermediate frequencies allow the production of more lattice defects than waveguides fabricated at higher frequencies, where the annealing process is stronger. However, this is the case if the same scan speeds and pulse energy are considered. The fact that no other published work reports on waveguiding at these laser pulse frequencies, could also be an indication that this regime is not favorable for low-loss waveguide fabrication. However, such a hypothesis can also be wrong if applied in general, and would only account for the experimental conditions applied on Nejadmalayeri et al. work [23].

With respect to applied task of waveguide fabrication, the above analysis depicts clearly how the laser pulse repetition rate is a parameter that can completely modify the range of processes which get involved in the waveguide formation, due to the heat increase, accumulation, diffusion, and to the annealing processes[***].

However, even if all these ultrafast optical and thermodynamic processes which modify the material are understood, it is still not clear which are the exact crystal lattice change mechanisms

[***] In this sense it appears clear that further waveguide fabrication experiments should be performed on a configuration where the laser-induced defect volumes were more confined and reduced, and the size and value of increased refractive-index zones enhanced. This could be the case if higher NA optics were used, as in the first works in glasses by Schaffer et al. [54]. Although Burghoff et al. have systematically used medium NA of 0.65 in all their experiments, the laser confinement of these objectives is still well below that of oil immersion objectives of NA ≥ 0.9. In this sense, it can be expected that if a complete study over scanning speeds, repetition rates and pulses energy was performed, new micrometer cross-section size, low-loss waveguide fabrication frequency windows could appear, by using such optics.

which take place after the relaxation of the material, and which are responsible for the increased refractive-index zones. Understanding this process is the purpose of the research work presented in the following sections.

The lowest propagation loss waveguides found by Nejadmalayeri et al. (0.6 dB/cm @1300 nm) matched the previously lowest ones reported [22, 28], but with the significant advancement of a more than one order of magnitude higher fabrication speed, as they were fabricated at much higher repetition rates. Due to the practical importance of these waveguides, these are the ones studied in the next section (shown on the right inset of **Fig. 5.5**). In their work, Nejadmalayeri et al. point out that the observed low-loss TE polarized guiding could be "attributed to the stress induced increase of the ordinary refractive-index", while for orthogonal polarization (TM), guiding was observed at different zones at the sides of the damaged focal volumes, but with propagation losses too high for any quantitative analysis.

The question proposed in the next section is to investigate whether this hypothesis for the observed refractive index increments is correct or not, and which is the exact lattice modification which responds to the observed behavior. In addition, we also want to investigate the case of waveguides written in non-thermal conditions where no annealing processes take place, as the information obtained from such a comparison would be valuable for a further understanding of the laser interaction process and final waveguide formation mechanism. This approach has not been hitherto investigated until this work.

With this goal, two relevant kinds of waveguides covering both the thermal and non-thermal regimes are analyzed. The cross sections of these two types of waveguides were shown on the insets of **Fig. 5.5**. The respective waveguiding areas in each case are shown by yellow filled circles. In the first case, a waveguide fabricated in the low-thermal regime (1 kHz, f_n~0.01) on a Nd^{3+}:MgO codoped $LiNbO_3$ sample is investigated [31]. This type of waveguide was also previously reported on Nd:YAG crystalline laser ceramics (i.e. fabricated under the same exact conditions), which lead to the highest laser efficiency so far reported in a laser-written waveguide [52]. In the second case, we

analyze the previously mentioned waveguide fabricated in the high-thermal regime (0.7 MHz, f_n~5) on a non-doped $LiNbO_3$ sample [30].

5.3. Crystal lattice changes in buried $LiNbO_3$ waveguides

In this chapter we describe the fabrication and compare the micro-spectroscopy changes of two different kinds of waveguides: one fabricated at the thermal regime and other in the non-thermal one. To thoroughly compare both types of waveguides, these steps are followed:

i) Waveguides general description
ii) Fabrication parameters
iii) Morphology
iv) Confocal μ-Raman and μ-Luminescence analysis
v) Discussion

5.3.1. Waveguides general features

Low-repetition rate DLW in a Nd^{3+}:MgO:$LiNbO_3$ sample: The two-line approach.

This waveguide was fabricated on a *x*-cut Nd:MgO:$LiNbO_3$ sample grown from the melt by the Czochralski technique with Nd^{3+} and MgO concentrations of 0.3 at.% and 5 at.%, respectively. **Figure 5.7 (a)** and **(b)** show a microscope transmission image of the two-line waveguide end-face, and the three different propagation modes which can be excited at 632.8 nm wavelength, respectively. **Fig. 5.7 (b)** is in fact a composed image done with three pictures taken after longitudinally translating the sample, so that both the laterals and central mode can be excited at each respective position. No evanescent coupling was observed, and guiding was observed for the three independent channels, for both TE and TM polarizations. The optical losses of these waveguides were not measured at the time when this manuscript was written, but they can be expected to be similar to that fabricated by Burghoff et al. in similar conditions [9], and which yielded propagation losses of 1.5 dB/cm.

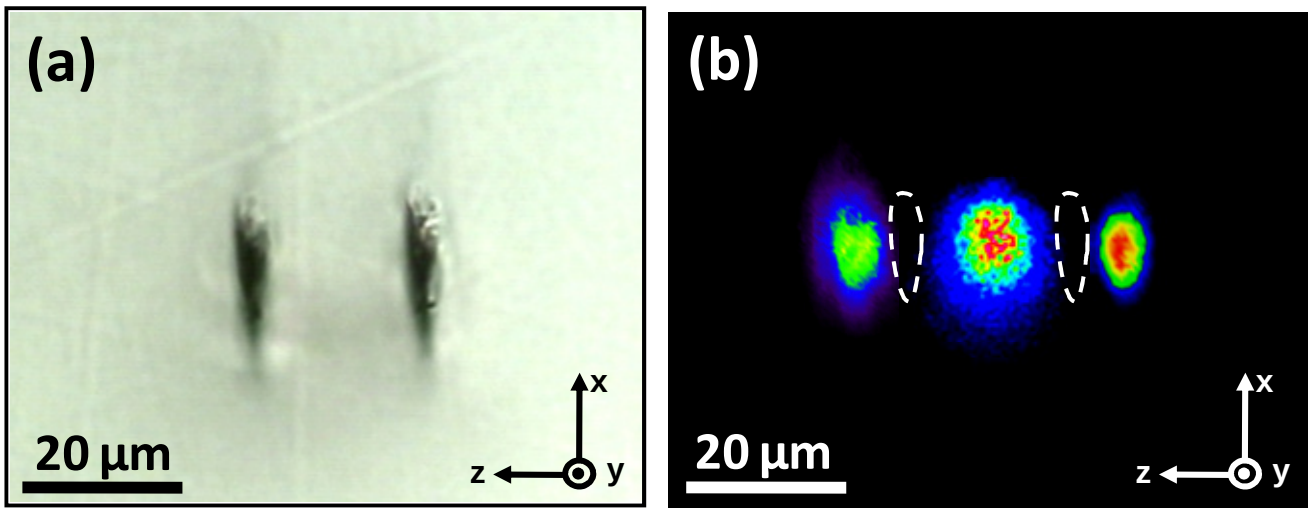

Figure 5.7 (a) *Microscope transmission image of a double-line type waveguide written on a Nd^{3+} doped $LiNbO_3$ sample.* **(b)** *Composition of the near-field intensity distributions of the three possible propagation modes at 632.8 nm wavelength.*

This kind of waveguide relies on the laser inscription of two close lying parallel tracks of slightly amorphized $LiNbO_3$, which configure a very resistant and versatile type of deep buried waveguide. Between the different types of waveguides which have been already fabricated in the low-thermal regime, this two-line technique is probably the most fruitful one, as it is the only one which has been extensively studied in different works and by different authors, and in only a few years it has led to different specific breakthroughs, such as to second harmonic generation (SHG) by birefringent frequency doubling [9], to SHG by quasi-phase matching (QPM) in a periodic poled $LiNbO_3$ sample (PPLN) [42, 43], to demonstrations of evanescent coupling in 2D waveguide arrays [44], and also to highly efficient laser action in Nd:YAG crystalline ceramics [52].

High-repetition rate DLW in undoped $LiNbO_3$: Low-loss waveguide ultrafast fabrication

This waveguide was fabricated on a congruent *z*-cut sample (Crystal Technology 99-60011-01) by Amir et al., and as previously indicated, these waveguides showed low propagation losses of 0.6 dB/cm at 1300 nm wavelength [23].

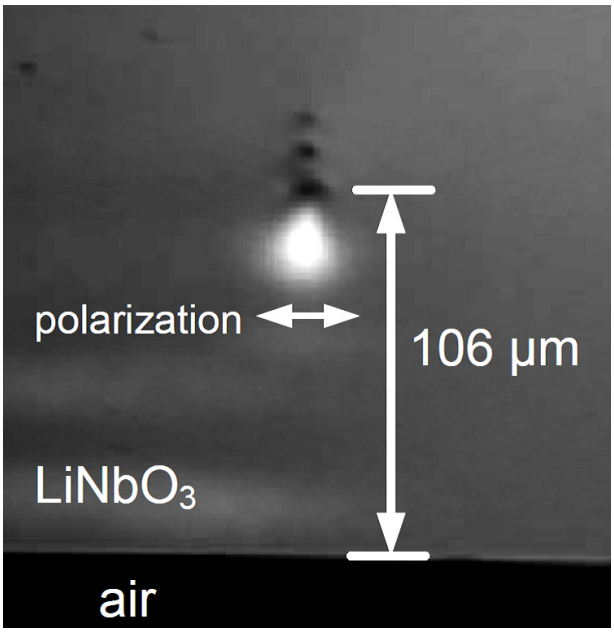

Figure 5.8. *Microscope transmission image of the waveguide cross section showing the 1300 nm TE polarized propagation mode close laying the first to surface damage volume. Figure extracted from [23].*

5.3.2. Fabrication parameters

The parameters used for the fabrication at both the thermal and non-thermal regimes are listed in the **Table 5.2**:

Regime	f(kHz)	τ(fs)	v(µm/s)	λ(nm)	Pol.	NA	h(µm)	Axis	E(µJ)	f_n
Non-thermal	**1**	120	50	800	Linear	0.3	500	x-cut	1	**0.01**
Thermal	**700**	600	46000	1045	Circular	0.55	110	z-cut	0.5	**4.7**

Table 5.2. *Set up parameters for the fabrication of the different waveguides.*

As previously indicated, the fabrication differences between these two waveguides can be summarized by the normalized frequencies of 0.01 and 4.7 for the non-thermal and thermal cases, respectively, and by the different pulse durations used.

The normalized frequency gives the ratio between the laser pulse frequency used for fabrication and threshold frequency for which thermal accumulation occurs, which only depends on

the thermal diffusivity of the sample and on the focal spot size. With respect to the pulse duration, it is 5 times higher for the high-repetition rate waveguide, this meaning that the non-linear interaction phenomena will not be exactly the same. However, double-line type II waveguides in the low-repetition rate have been fabricated under different pulse duration (40 fs [9], 120 fs [31], and 1 ps [26]) with very small differences in the morphology of the written tracks, so that for pulse duration below 1 ps and in a first order approximation, large differences are not to be expected with respect to the performed modifications. Due to this, we expect that the main differences between these two waveguides will be produced by the different repetition rates used, i.e. by the different thermal regimes in which they have been fabricated.

Under fs and ps pulse laser Z-scans experiments, results indicate that the main non-linear refraction effect is positive and of Kerr electronic type origin [55], and thus it can cause the self-focusing of pulses if the laser power is above a threshold power P_{cr}. The laser pulse power can be estimated to be ~7 MW for the non-thermal case, and ~0.7 MW for the thermal one, by taking into account the sample pulse durations, laser pulse energy and the energy loss due to the reflectivity of the sample. From this it can be estimated that this laser power is ~20P_{cr} for the non-thermal case, i.e. well above the threshold, and ~2P_{cr} for the thermal one, i.e. close to the threshold. P_{cr} is the threshold power for self-focusing (estimated by $\lambda^2/2\pi n_0 n_2$, where n_0=2.2 and $n_2 \approx 2\text{x}10^{-15}$ cm^2/W are the linear and nonlinear refractive indexes of $LiNbO_3$, respectively, and λ the specific wavelength used in each case). This means that, in a first order approximation, any self-focusing effect should be clearer in the non-thermal waveguide case, due to the higher power applied and shorter pulse duration, and in the thermal-regime waveguide modifications should follow the filament or self-trapped behavior (see **Chapter 3** for more details). On the other hand, the number of overlapping pulses is almost the same for both waveguides, of a very high value of ~98%.

Apart from this, due to the fact that the laser polarization, and the samples orientation and compositions are significantly different, comparison between these two waveguides is not straightforward, but it is nevertheless an interesting issue as the physical and optical properties of each kind of fabricated waveguide are expected to be different on the base that different laser interaction mechanisms have been involved in their creation.

5.3.3. Morphology study

Figure 5.9 shows the microscope transmission images of the corresponding cross section of both waveguides, displayed at the same magnification for an easy comparison of their different features apparent at the microscope. It is important to remark the different axial orientation of the samples in each case. While one has been written along the *x*-axis, the other has been fabricated along the optical *c*-axis. However, in both cases the optical *c*-axis is contained on the waveguide's cross section. The main increased refractive-index areas, corresponding to the waveguide volume, are marked with white dashed lines. The observed guiding polarizations (TE or TM) are also indicated.

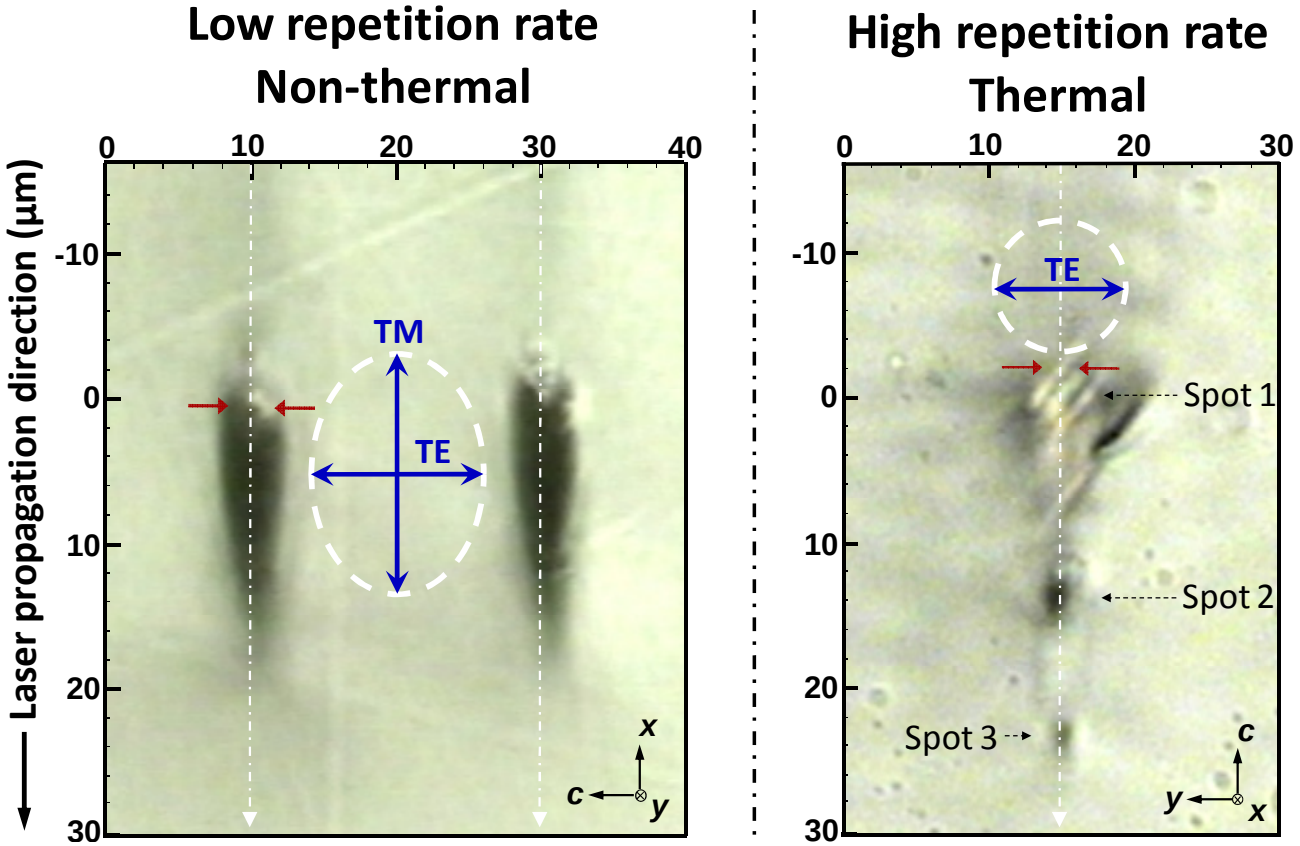

Figure 5.9. *Microscope transmission images of the cross section of both waveguides at same scale. The main increased refractive-index areas and the different polarized guiding configurations are indicated. The observed small bubbles in the image of the right correspond to air bubbles in the interface between immersion oil of the high NA objective and the sample.*

The theoretically estimated focal diameter, following **Eq. 5.1**, is indicated by blue arrows in order to compare. As it can be seen by a first inspection, in the case of the low-repetition rate waveguide, which is written in absence of thermal accumulation, the apparent diameter size of the laser induced damage channels matches well with the laser focus diameter (d_{spot}=3.2 μm). However, in the case of the waveguide written in the thermal regime, the diameter size of the laser induced cracks is almost the double of the focal spot diameter (d_{spot}=2.3 μm), as it would be expected for a modification process where heat accumulation and diffusion processes play a dominant role. Indeed, it is known that in the case of low-frequency direct fs pulse laser irradiation the damaged zones normally extend in regions which can be much smaller than the laser focal spot, while for high-frequency irradiation where thermal effects are present, the modified volumes can extend to regions far from the laser focal spot.

With respect to the longitudinal size (along the laser propagation path) the axial length of the focal volume can be roughly estimated as twice the aberration free Rayleigh length (z_0), which yields around ~46 μm for the non-thermal waveguides, and ~17 μm for the thermal case (estimated as $2z_0=2\pi(d_{spot}/2)^2 n_o/\lambda$). On the other hand, the main extension of observed dark regions is of ~18 μm and ~6 μm for the non-thermal and thermal waveguides, respectively; which is around 2.6 times smaller than the estimated focal volume lengths in both cases.

From this, it can be concluded that damaged regions in the non-thermal region have a much smaller extension than the focal volume probably due to the nonlinearity of the excitation process. On the other hand, for waveguides written in thermal regime the longitudinal extension is much smaller than expected, and a refocusing behavior is observed due to the fact that three different main damage channels are observed. This very different morphology with respect to the expected extension for the focal region indicates that some additional effects must be taking place, apart from the simple Kerr effect, which in fact is expected to be small in this case. The fact that the waveguide is written on the thermal regime indicates that maybe the thermo-optic effects could be modifying the propagation conditions at the focal regions, but also due to the fact that the sample is undoped some other nonlinear effects such as the photorefractive effect could also be causing a distortion of the laser pulse propagation dynamics. As a deeper understanding of this refocusing

effect would need from further experimental investigations and numerical calculations, which are out of the scope and focus of this work, we cannot give here any further conclusion regarding the observed refocused behavior in the thermal regime waveguides.

Another feature of the waveguide written in the thermal regime is that it shows a wider damage region, even though the laser beam waist was smaller, and also visible lattice defects are seen in the form of crystalline cracks, which appear aligned along the cleavage direction of the $LiNbO_3$, following the crystalline planes at ~55^o with respect to the horizontal *y* axis[†††]. This lattice cracks are not observed in the non-thermal waveguide.

5.3.4. Confocal μ-Raman and μ-Luminescence analysis

In order to investigate the kind of $LiNbO_3$ lattice modifications present on each of waveguide, μ-Raman and μ-Luminescence spectra (in the case of Nd^{3+} ions doped sample) were taken.

An introduction on the Raman and luminescence properties of undoped and Nd^{3+} doped $LiNbO_3$ can be found on **Chapter 2** of this thesis. However, for the sake of comprehensiveness, the basic Raman properties of $LiNbO_3$, which are of interest for the following analysis, are here revised.

As previously said, the cross section planes of the two analyzed waveguides correspond to crystalline planes containing the optical *c*-axis. This means that if Raman is measured in back-scattering configuration keeping the polarization direction constant with respect to the optical axis, the corresponding Raman symmetry will be the same one for both waveguides. Following the standard Porto notation [56], the measuring configuration was that of *y(zz)y* and *x(zz)x*, for the low-repetition rate and high-repetition rate laser fabricated waveguides, respectively. This notation simply means that the incident (laser) and back-scattered (Raman signal) light paths will always be perpendicular to the sample face (i.e. axis *y* (*x*) for the non-thermal (thermal) waveguides, as it can be seen from **Fig. 5.9**), and that the polarization of both signals will always be along the *z* direction, i.e. parallel to the optical *c*-axis. This configuration not only allows for a direct comparison between

[†††] See **Chapter 2** for further details concerning the lattice structure of $LiNbO_3$

the Raman spectra of both waveguides, but it also considerably simplifies the number of Raman modes which will be excited, allowing for a more accurate spectral analysis due to the fact that the different Raman modes will be much more spectrally isolated from each other. The *y(zz)y* and *x(zz)x* Raman spectra of $LiNbO_3$ crystals are both constituted by the same four transverse optical A_1(TO) Raman modes [57-59], as shown in **Figure 5.10**.

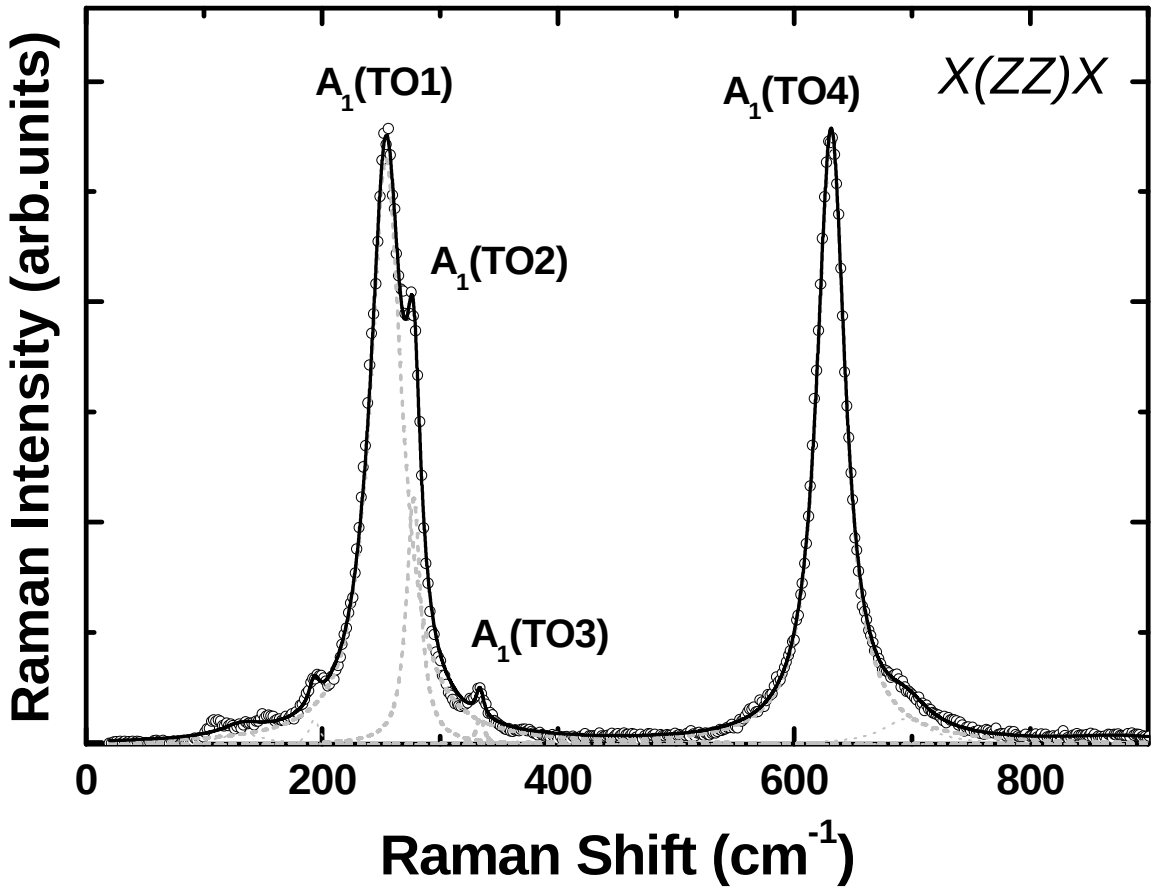

Figure 5.10. *Typical μ-Raman spectra obtained in x(zz)x configuration in a Nd^{3+}:MgO:$LiNbO_3$ sample. The four Raman transverse optical modes are indicated. The figure shows experimental data as open circles, total fitting curve as black continuous line, and the Lorentzian fit of each of the corresponding modes as grey dotted lines. Minor extra bands and peaks are also included in the fitting for a correct deconvolution of the ATO modes.*

According to previous works [58-62], these four modes can be associated to specific lattice sites motions:

$A_1(TO_1)$: Vibrations along the *c*-axis of B sites (Nb ions or Nb vacancies) against the O sub-lattice, leaving A sites (Li ions, Li vacancies, and Nb antisites) relatively static.

$A_1(TO_2)$: Antiphase vibrations between the A and B sites along the *c*-axis, with O ions static.

$A_1(TO_3)$: Rigid rotations of the whole O ion octahedron along the *c*-axis.

$A_1(TO_4)$: Stretching vibrations of the O ion octahedron along the *xy* plane.

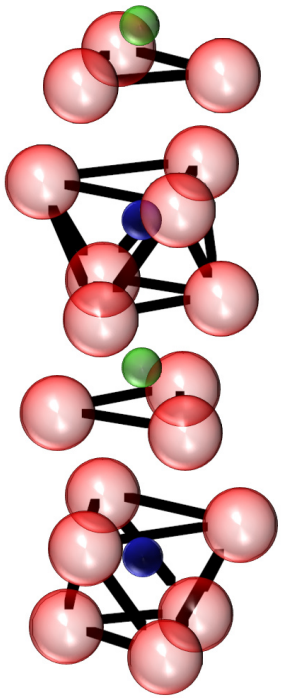

Figure 5.11. *Schematic diagram of the unit cell of the $LiNbO_3$ crystal. Red spheres represent oxygen ions, green spheres A sites (i.e. Li ions, Li vancancies, Nb antisites), and blue spheres represent B sites (i.e. Nb ions or Nb vacancies). The optical c axis comes defined by the aligned ionic configuration -Nb-Li-V-Nb-Li-V…*

Low-repetition rate DLW in a Nd^{3+}:MgO:$LiNbO_3$ sample: The two-line approach.

In order to analyze both the waveguide and the written lines a confocal μ-Raman scan was performed along the perpendicular direction to the written lines and across the waveguide mode. The scan was performed using a high NA 1.4 100X UPlanSApo oil-immersion microscope objective focused at 10 μm below the polished sample face. The excitation laser pump power was 10 mW, and the single 488 nm wavelength emission line of an Argon laser was used. The spatial resolution of this set up is then well below 0.5 μm. A spectrum was taken at every 0.5 μm spatial step, and the total scan length was 100 μm. Total measuring time was 10 h.

Figure 5.12 shows the results obtained for the intensity and FWHM variations of the four ATO modes available, in a scan across the two damage tracks and waveguide volume. Fitting of the data was performed using Labspec© software, and each Raman mode was well fitted to a damped harmonic oscillator of Lorentzian shape. To simplify the fitting task, spectra were separately analyzed for the different spectral regions from 0-450 cm^{-1} (low frequencies) and 450-900 cm^{-1} (high frequencies), corresponding to the $A(TO_{1-3})$ and $A(TO_4)$, respectively (see **Fig. 5.10**). Each set of data for the 4 different modes is overlapped in **Fig. 5.12** in order to clarify the slight differences between each one, but also to show that the overall behavior of the intensity and damping of the phonon modes is mainly the same. The FWHM variations of the $A(TO_3)$ mode are not included as no clear information could be obtained out of the noise level of the analysis.

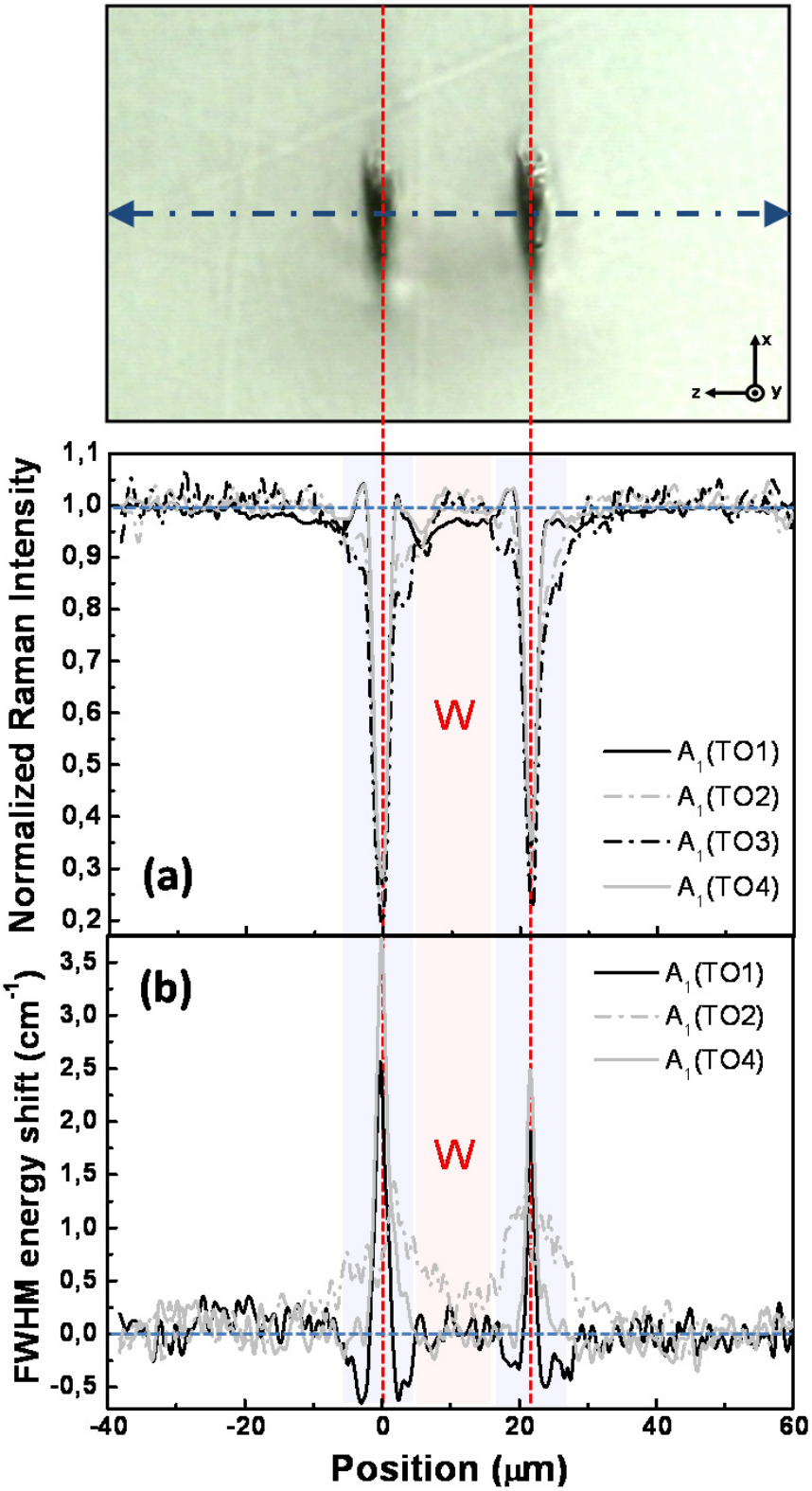

Figure 5.12. *Spatial dependence of the integrated Raman intensity* **(a)** *and of the FWHM (damping) of the different Raman modes as crossing both written lines and waveguide* **(b)**. *See technical details on the text.*

It appears clear that a sharp reduction in the integrated Raman intensity is produced at the written lines (of up to an 80% of the signal at non irradiated volumes), this being accompanied by a relevant spectral broadening of all the Raman modes. At the waveguide mode volume, however, no such features are observed. The coordinate positions where all of the observed Raman modes decrease in intensity and increase in damping (FWHM), are indicated by the vertical red discontinuous lines, which appear at the coordinates (0, 21.9) μm. These two points will be hereafter considered as the nuclei of the damage lines.

It is worth mentioning here that when analyzing intensity changes, the observed strong decrease in intensity is both a consequence of the direct laser induced lattice damage but also a byproduct of the in-depth focusing inside the sample (10 μm deep), which was performed in order to optimize the Raman signal at the waveguide position, and also to avoid any laser induced heating of the oil immersion interface between the objective lens and sample. No substantial decrease in the spatial resolution is expected due to this deep focusing as the experiment is performed using high NA and confocal aperture, but the decrease in the Raman signal was found to be dependent on the focusing depth at the damaged zones, as these act as scattering centers for both the excitation laser and Raman signal coming from inside the sample. Thus, the obtained values for the intensity decrease at damaged zones cannot be compared to those of other Raman analysis performed with different focusing conditions.

The combination of an intensity decrease and a damping increase of the phonon modes indicate that a large density of extended defects has been induced at the damaged zones. These defects cause a local disordering of the Nd^{3+}:MgO:$LiNbO_3$ lattice, which is seen by the clear spectral broadening (the damping increase) of the observed modes. These two facts mean that a slight degree of amorphization has been induced at the focal volume of the laser, i.e. at the deep written lines. These changes are also analogous to those observed in He^+ ion implanted $LiNbO_3$, in which a decrease of the Raman modes intensity and increase in its damping was also found at the nuclear stopping region [62, 66].

Fig. 5.12 (b) also shows that the spatial changes in the damping are slightly different between the three A(TO_1), A(TO_2) and A(TO_4) modes. While the A(TO_4) mode -grey continuous line in **Fig. 5.12**- features a very sharp increase in damping of +3.75 cm^{-1} only at the center of the damaged lines, with a mean extension diameter of ~1.4 μm -calculated as the mean FWHM of a Gaussian fit for both the two peaks in Fig. **5.12 (b)**-, the damping of the A(TO_1) mode also matches this diameter of ~1.4 μm (maximum damping increase of +2.6 cm^{-1}), but in this case it also shows a decrease in the damping on its surroundings, which extends to about ~6 μm from the center of the defect line (decrease in the damping values to about -0.7 cm^{-1}). And reciprocally the A(TO_2) mode shows a medium increase in its damping (+1.4 cm^{-1}), but which is not confined to the damaged dark region, but it also extends far from the central defect lines in a somehow mirrored trend to the A(TO_1) damping decrease. In this sense, the increase in the damping of the A(TO_2) mode approximately coincides with the decrease of the A(TO_1). The overall diameter of this extended region where the damping of the modes fluctuates is highlighted in **Fig. 5.12** as blue regions, extending over ~12 μm.

This correlated behavior between both modes is not observed in any other region of the sample, than at the laterals of both defect lines and, furthermore, the intensity in its modulation is much higher than the average dispersion or noise of the measurements. Thus, it can be disregarded that this result is an artifact due to the fitting process (deconvolution) of the Raman modes. The correlation is not perfect however, for instance, at ~18 μm (left part of the right line) the damping of the A(TO_2) is observed to increase while the value for the A(TO_1) mode has remained relatively unchanged.

A clear experimental observation can be already extracted: The A(TO_4) features a continuous increase in damping extending for about ~1.4 μm at each defect line. The A(TO_1) also shows a region of about ~1.4 μm in extension where its damping increases, and an outer shell with a decreased damping extending to about ~6 μm; the total modulation extending about ~12 μm. Finally, the A(TO_2) mode only shows increments in its damping, for the same total extension of about ~12 μm.

A clear conclusion is then extracted, at this stage, from **Fig. 5.12**:

There appears to be a damage core of about ~1.4 μm in extension (in the transversal plane to the defect lines) where the $LiNbO_3$ lattice presents an overall disorder in all its lattice sites, i.e. overall increase in the damping of all modes, and where a general decrease in the mode intensities is observed. Thus, it can be assessed as an amorphous core or nucleus, which appears dark at microscope image. Surrounding this amorphous core, a modulation in the disorder associated to the Nb sites (B sites) and Li sites (A sites) is present, in complete absence of disorder in the O ions octahedron. The intensity of the different modes varies in this region: The A(TO_1) and A(TO_4) do not show any clear decrease in intensity, while the A(TO_2) and A(TO_3) appear to decrease about a 10% of its value at non-irradiated volumes.

Apart from the damping and intensity of each phonon mode, its vibration energy was also obtained. **Figure 5.13** shows the results obtained for the Raman shift variations of the four ATO modes, as obtained from the fitting analysis. These variations are shown in separate graphs for ease of visualization. The different plots are vertically aligned so that the position scale is the same for the four modes, and so the exact Raman shifts at each position can be precisely correlated between the four plots.

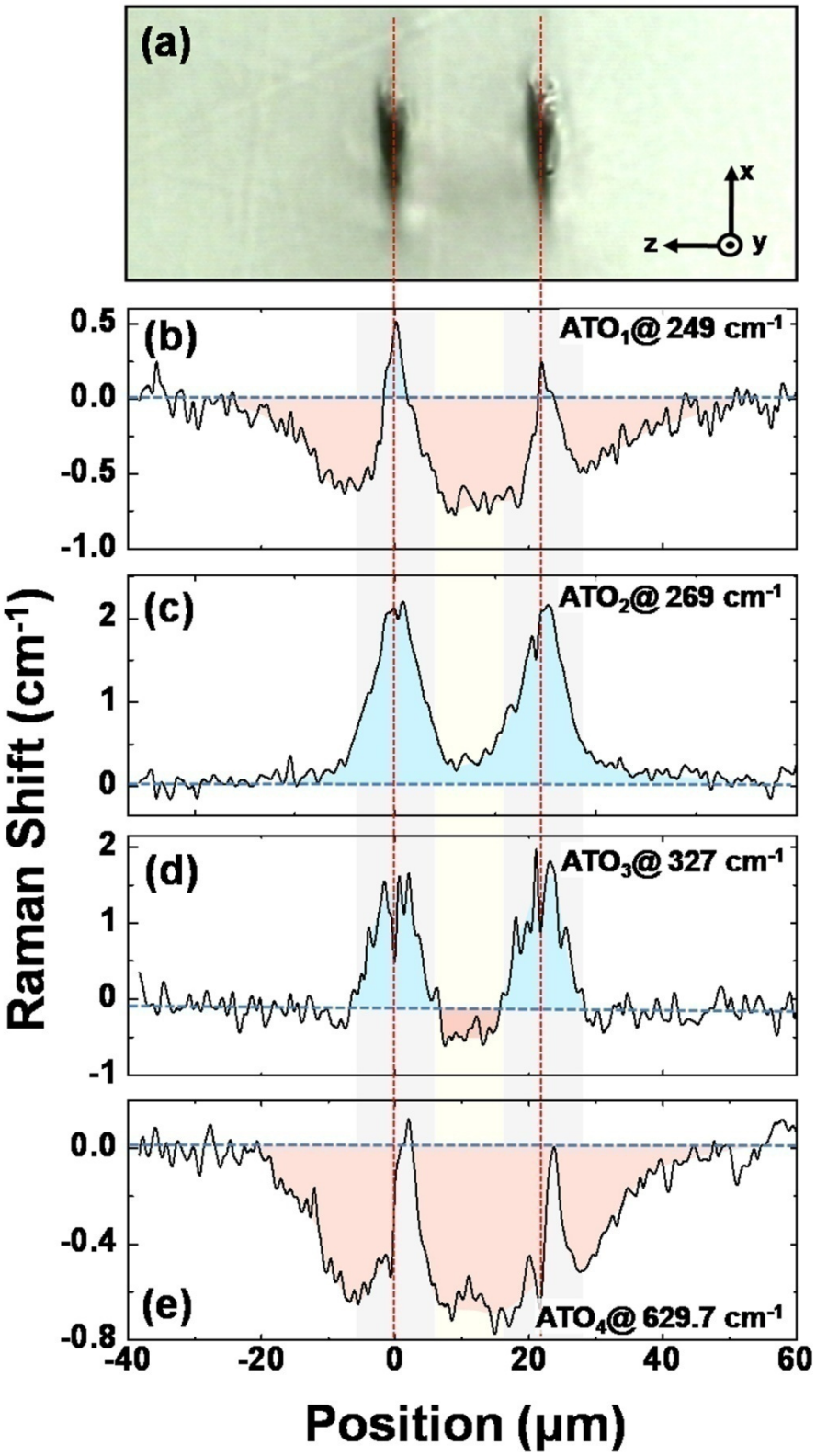

Figure 5.13. *Spatial dependence of the Raman shifts. See technical details on the text.*

The vertical red discontinuous lines indicate the central part of the defect lines at the previously determined central coordinates (0, 21.9) μm (previously determined from the sharp intensity and damping peaks of the plots in **Fig. 5.12**). It is worth saying that all data in **Figs. 5.12** and **5.13** are part of the same experiment and analysis. That is, all the values for intensity, FWHM and energy shifts, were always obtained from the fitting of one single Raman spectrum at each particular position in the sample, and can thus be correlated by its spatial coordinate.

The trends observed in **Fig. 5.13** are somehow more complex than those observed in **Fig. 5.12**, because in this case it is clear that the energy shift of the phonon modes is present at both the waveguide and the damage zones. In this case both blue-shifts and red-shifts of the phonon frequencies have been highlighted as blue and red regions, respectively. The damage and waveguide zones are also marked as darker and brighter zones, respectively, with the spatial extensions extracted from the analysis of **Fig. 5.12**.

The observed general trend is that the $A(TO_1)$ and $A(TO_4)$ phonon modes are red-shifted around the damage lines, while the $A(TO_2)$ and $A(TO_3)$ are blue-shifted.

Damage lines: At the damage lines, which correspond to the direct fs laser written volumes, again two regions can be distinguished, corresponding to a nucleus and a transition region surrounding the former.

Nucleus: At the nucleus volume, a general blue-shift of the $A(TO_1)$, $A(TO_2)$ and $A(TO_3)$ modes is observed. However, only the $A(TO_1)$ clearly delimits this very confined region. The mean width of this apparent nuclei volume well matches the previously obtained value of ~1.4 μm. Thus, the nucleus region mainly shows lattice distortions involving ionic displacements or rotations along the *c*-axis (strong blue-shifts of the $A(TO_2)$ and $A(TO_3)$ modes), which appear extremely clear for the $A(TO_2)$ mode as the amount of blue-shift is of about ~2.15 cm^{-1}. This strong blue-shift can be interpreted in a first order approximation as an axial compression of the $LiNbO_3$ unit cell along the optical axis, which in this case coincides with the perpendicular axis to the damage lines, and which means that a slight reduction in the distance between A sites and B sites has been induced. The

mean blue-shift also observed for the A(TO_1) mode (~0.38 cm^{-1}) can be reasonably interpreted as a shortening of the distances between the B sites (Nb ions or Nb vacancies) and the O sub-lattice, which is consistent with a compression along the optical axis which brings the B sites closer to the O ion sub-lattice. The A(TO_4) shows a rather different behavior to the rest, as its frequency remains non-shifted, and its modulation also appears slightly altered on the right hand side of the damage, i.e. only along one direction of the optical axis. This shift is observed in the original data and it does not correspond to a plotting error. The fact that the behaviour of the A(TO_4) mode remains quite static at the core of the damaged lines, also reinforces the interpretation that the main lattice distortion at the damage core is that of a compression along the *c*-axis without almost no distorting the O ion octahedron positions along the *xy* plane of the $LiNbO_3$ lattice.

Surroundings to damage core: Surrounding this region both the A(TO_2) and A(TO_3) modes feature a clear extended blue-shift, which in the case of the A(TO_2) extends all along the space between defect lines and to about ~20 μm at the sides of the lines, and in the A(TO_3) mode a transition region to a change to red-shifts occurs at about ~6 μm from the center, centered at the waveguide mode volume. On the other hand, the A(TO_1) and A(TO_4) both consistently appear red-shifted also extending to about ~20 μm at the sides of the damage lines. The strain fields in these regions are then quite the same as those in the core (compression along the *c*-axis), but in these regions the O ion octahedron also appears to be slightly distorted, as the A(TO_1) and A(TO_4) modes both show intermediate red-shifts, which can be interpreted as an enlargement of the distances defining the octahedron in the *xy*-plane.

Summarizing, the dark damaged lines appear then characterized by a nucleus of ~1.4 μm where an anisotropic compression along the *c*-axis has been induced, and surrounded by a transition region extending to ~5.3 μm at each side of the core, where both the compression along the *c*-axis and a dilatation of the *xy*-plane defined by the O octahedral, coexist.

Waveguide: At the laterals of the damaged lines a volume of increased refractive-index is known to occur due to the observed guiding modes shown in **Fig. 5.7 (b)**. At these regions the A(TO_1), A(TO_3) and A(TO_4) modes are clearly red-shifted, while only the A(TO_2) mode is still slightly

blue-shifted (~0.3 cm^{-1}). This behavior is quite the same as that in the surroundings of the damaged core, but in this case the dilatation of the O octahedron is much dominant, given the clear red-shifts of the $A(TO_1)$ mode (~-0.69 cm^{-1}), $A(TO_3)$ mode (~-0.5 cm^{-1}), and the $A(TO_4)$ mode (~-0.69 cm^{-1}).

In order to summarize, and to correlate all the different lattice changes observed by this Raman analysis with the waveguide morphology observed, a short overall description of the Raman features is given in the **Table 5.3**:

	Damage Core				**Surrounding**				**Waveguide**			
Mode	**$A(TO_1)$**	**$A(TO_2)$**	**$A(TO_3)$**	**$A(TO_4)$**	**$A(TO_1)$**	**$A(TO_2)$**	**$A(TO_3)$**	**$A(TO_4)$**	**$A(TO_1)$**	**$A(TO_2)$**	**$A(TO_3)$**	**$A(TO_4)$**
Intensity	**0.3**	**0.25**	**0.2**	**0.31**	1	0.91	0.87	1	0.97	1.02	1	0.99
FWHM	**2.22**	**0.87**	-	**3.75**	**-0.5**	**0.87**	-	0.14	0	0.31	-	0
Energy Shift	0.38	**2.15**	1.36	-0.2	**-0.43**	**1**	0.75	**-0.43**	-0.69	0.3	-0.5	**-0.69**

Table 5.3. *Raman modes changes at the different zones in the waveguide*

In **Table 5.3** all the main Raman values for each modified zone are summarized. The important values which best describe the main lattice distortions (those which show the highest and clearer variations, as previously discussed) are highlighted.

From this table it appears clear that the two main Raman modes whose information can be regarded as independent form the others are the $A(TO_2)$, which gives information about the A-B sites, and the $A(TO_4)$, which gives information about the O ions subsystem. The behavior of the $A(TO_3)$, which is supposed to be only dependent on the rotational mobility of the whole O octahedron along the *c*-axis, is however observed to follow intermediate trends to that of the formers, and thus its variations are more difficult to interpret. The behavior of the $A(TO_1)$, which was previously assigned to vibrations of the B sites with respect to the O octahedron, is also well confirmed, as it is observed to follow an intermediate behavior between the $A(TO_4)$ and $A(TO_2)$, although with a much stronger dependence to the changes in the O octahedron, mainly due to the fact that the Li concentration is much lower.

Due to these correlations, a clear conclusion is obtained, that any changes in the $A(TO_2)$ mode can be related to changes in the A sites, as far as the $A(TO_1)$ does not follow them, as this would imply that the behavior could be also related to changes in the B sites. This conclusion for the

correlation between A_1(TO) Raman modes and the different lattice sites is in agreement with that obtained in previous works by Fontana et al., where the Raman changes in MgO doped $LiNbO_3$ were studied as the Mg concentration was varied [67, 68].

From these observations, and the values in **Table 5.3**, the main lattice alterations observed in the waveguide structure are summarized in the next **Table 5.4**:

REGION	Extension	Defects	Disorder	Compression	Dilatation
Damaged core	~1.4 µm	amorphous	general	Strong and along *c*-axis	No
Surrounding	~5.3 µm	A sites	A sites	Strong along *c*-axis	Intermediate along the *xy*-plane
Waveguide	~10 µm	no	no	Weak and along *c*-axis	Strong and along the *xy*-plane

Table 5.4. *Review of the anisotropic lattice changes induced in the waveguide. The extension of damaged core and waveguide is the total lateral extension of these zones, and for the surrounding the lateral extension is indicated.*

A clear picture has then been obtained of the lattice micro-modifications performed in the two-line waveguide. Concerning the damaged zones, the extension approximately matches that observed in the transmission microscope characterization given previously (see **section 5.3.3**, **Fig. 5.10 (a)**). And with respect to the waveguide, the obtained extension for the main anisotropic dilatation of the $LiNbO_3$ well matches the extension of the main propagation mode observed at 632 nm wavelength of ~10 µm (see **Fig. 5.7 (b)**). Thus, the increased refractive index responsible for waveguiding seems to be due to the anisotropic dilatation of the $LiNbO_3$ lattice along the direction parallel to the damage lines, which in this case corresponds to the *xy*-plane defined by the O ions.

As all the refractive-index changes produced in the waveguide must be due to these specific local changes of the lattice structure, some corresponding changes in the spectral properties of the Nd^{3+} ions should also be observed. In order to analyze the effects in the spectroscopic properties of the Nd^{3+} ions, the experimental optical set up was the same as for confocal µ-Raman, with the exception that the notch filter was removed. The analysis of all collected spectra was also

performed with Labspec© software, and the plotting of all data was performed with the help of WSxM© software [69].

Due to the high luminescence quantum efficiency of Nd^{3+} ions (η=0.94 for the emitting state $^4F_{3/2}$ in Nd^{3+}:MgO:$LiNbO_3$ codoped samples) [70], a mapping of the emission spectra could be easily performed, well extending over all the modified zones. As for Raman experiments, a 10 mW continuous wave 488 nm wavelength laser was used. In this case the laser radiation excites the Nd^{3+} ions from their $^4I_{9/2}$ ground state, up to the $^2G_{3/2}$ excited state, and then the subsequent $^4F_{3/2} \rightarrow {}^4I_{9/2}$ emission band from the Nd^{3+} ions is selectively collected. The hydrostatic pressure dependence of the transition energies of this emission band has been previously studied [71], and it was found that the peak energies shows a clear dependence with the changing strength of the crystalline field as a result of increasing the pressure. It was found that as the pressure increases the emission peaks shift towards lower energies [71]. As the waveguiding regions have been observed to consist on anisotropically dilated regions, and the damage regions on compressed volumes, it is expected that the emission spectra of the Nd^{3+} ions should correspondingly show some different kind of changes, in response to the different kinds of lattice alterations on each region.

To perform the luminescence study both the polarized and non-polarized emission spectra were analyzed. While the non-polarized emission gives information on the different transition energies, bandwidths and intensities, the polarized spectra can also give information on how the dipolar character of the transitions has been altered due to the lattice distortions, by looking at the relative intensity changes between the different polarizations of the emission spectra. **Figure 5.14 (a)** and **(b)** show examples of both the polarized and non-polarized μ-luminescence spectra as obtained at room temperature at a non-irradiated region of the sample. The well known $^4F_{3/2} \rightarrow {}^4I_{9/2}$ emission band corresponds to 10 sub-Stark levels transitions, that is, to 10 emission peaks corresponding to electronic transitions between the two-fold degenerate $^4F_{3/2}$ state (R_1 and R_2 levels), and the 5-fold degenerate $^4I_{9/2}$ state ($Z_{1\text{-}5}$ levels), as shown in the inset where a partial energy diagram showing the levels studied here is depicted [72-74].

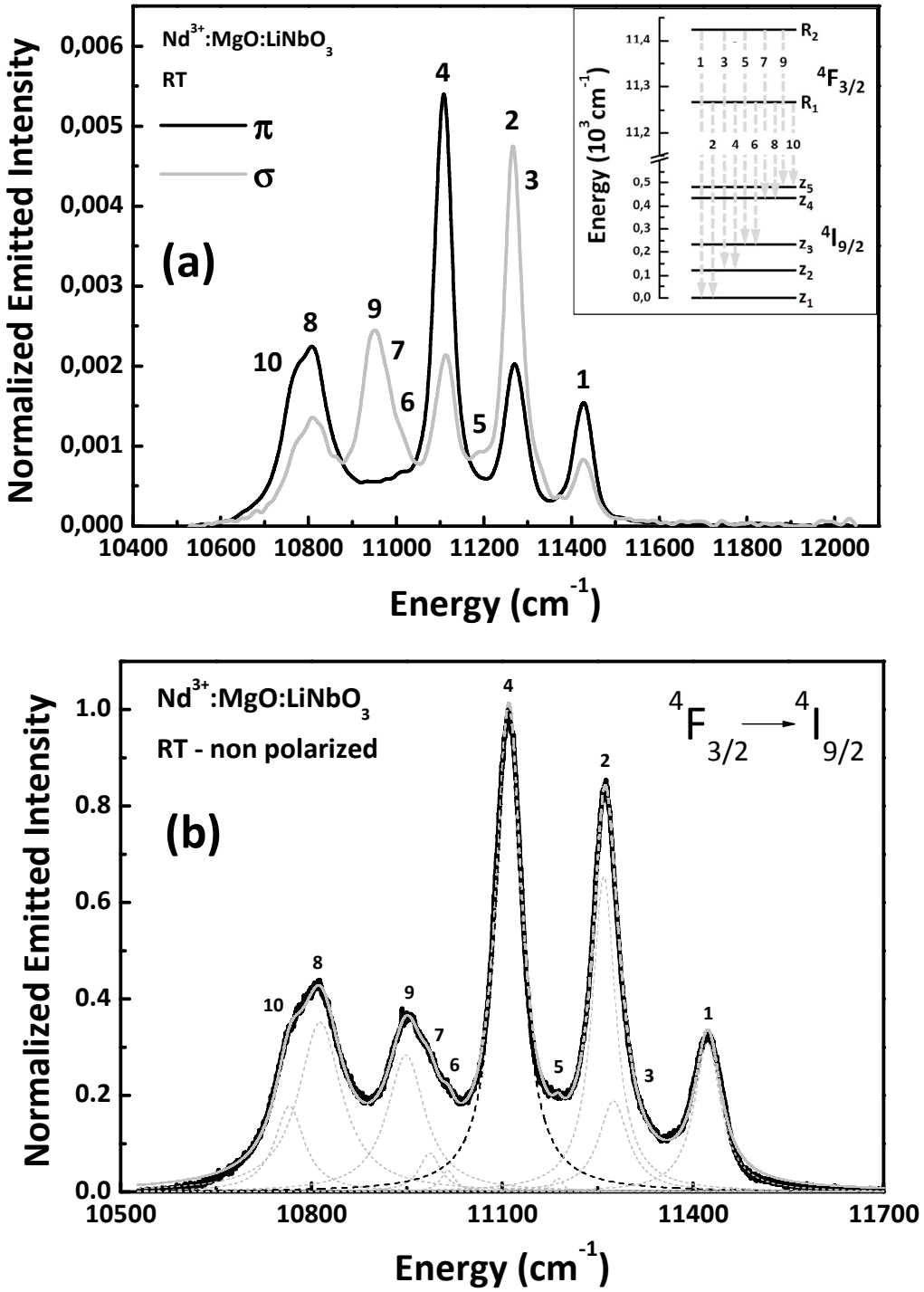

Figure 5.14. ***(a)*** *Polarized μ-luminescence spectra corresponding to the $^4F_{3/2} \rightarrow {}^4I_{9/2}$ emission band of Nd^{3+} ions obtained from a Nd^{3+}(0.3 mol %):MgO(5 mol %):$LiNbO_3$ crystal sample at room temperature. Inset shows an energy level diagram of the corresponding electronic transitions. The scale of the energies has been re-scaled to clarify the different Stark levels energy positions.* ***(b)*** *Typical μ-luminescence spectrum corresponding to the non polarized emission at room temperature, and its corresponding deconvolution with Lorentzian peaks. The central peak at 11114 cm^{-1} is used for the spectral analysis of the waveguide properties.*

The non-polarized emission was used to perform a 2D mapping of the luminescent properties extending over all the modified regions. For this, a 50X NA 0.75 objective was used focused at surface. For the $\sigma(\vec{E} \perp c)$ and $\pi(\vec{E} \| c)$ polarized emission spectra only one scan along the same direction as that for the previous Raman experiments was done. For this case a high resolution NA 1.4 100X UPlanSApo oil-immersion microscope objective was also used, and in this case the objective was again focused 10 μm deep into the sample, as in the previous μ-Raman experiments. The use of higher NA optics, and polarization of the measured spectra, is intended to improve the spatial resolution and at the same time search for any further information coming from the different dipolar character of the transitions, which is due to the specific lattice symmetry of the Nd^{3+} ion local sites.

As it can be seen from **Fig. 5.14 (a)** and **(b)**, the only well isolated peaks are those corresponding to the $R_2 \rightarrow Z_1$ and $R_1 \rightarrow Z_2$ transitions, i.e. the peaks corresponding to transitions 1 and 4 as shown in the figure. As the peak 4 is much more intense than peak 1, it was chosen for probing all the luminescence changes in these experiments. From the mapping and analysis of these μ-luminescence spectra a 2D plot of the intensity, peak linewidth, and energy shift was performed, which is shown in **Figure 5.15**. From this figure it appears clear that the luminescent properties of the Nd^{3+} ions are clearly inhomogeneously distributed along the different regions of the DLW buried waveguide.

Firstly, the normalized fluorescence intensity (**Fig. 5.15 (a)**) is observed to be significantly reduced at the two defect lines, as it is expected at the core of the damage zone. However, this decrease in intensity (at dark regions in **Fig. 5.15 (a)**) is of only around a ~20% with respect to that at non irradiated regions (bright regions in **Fig. 5.15 (a)**). This means that the degree of amorphization or the density of induced lattice defects is not high, due to the fact that the luminescence is not quenched.

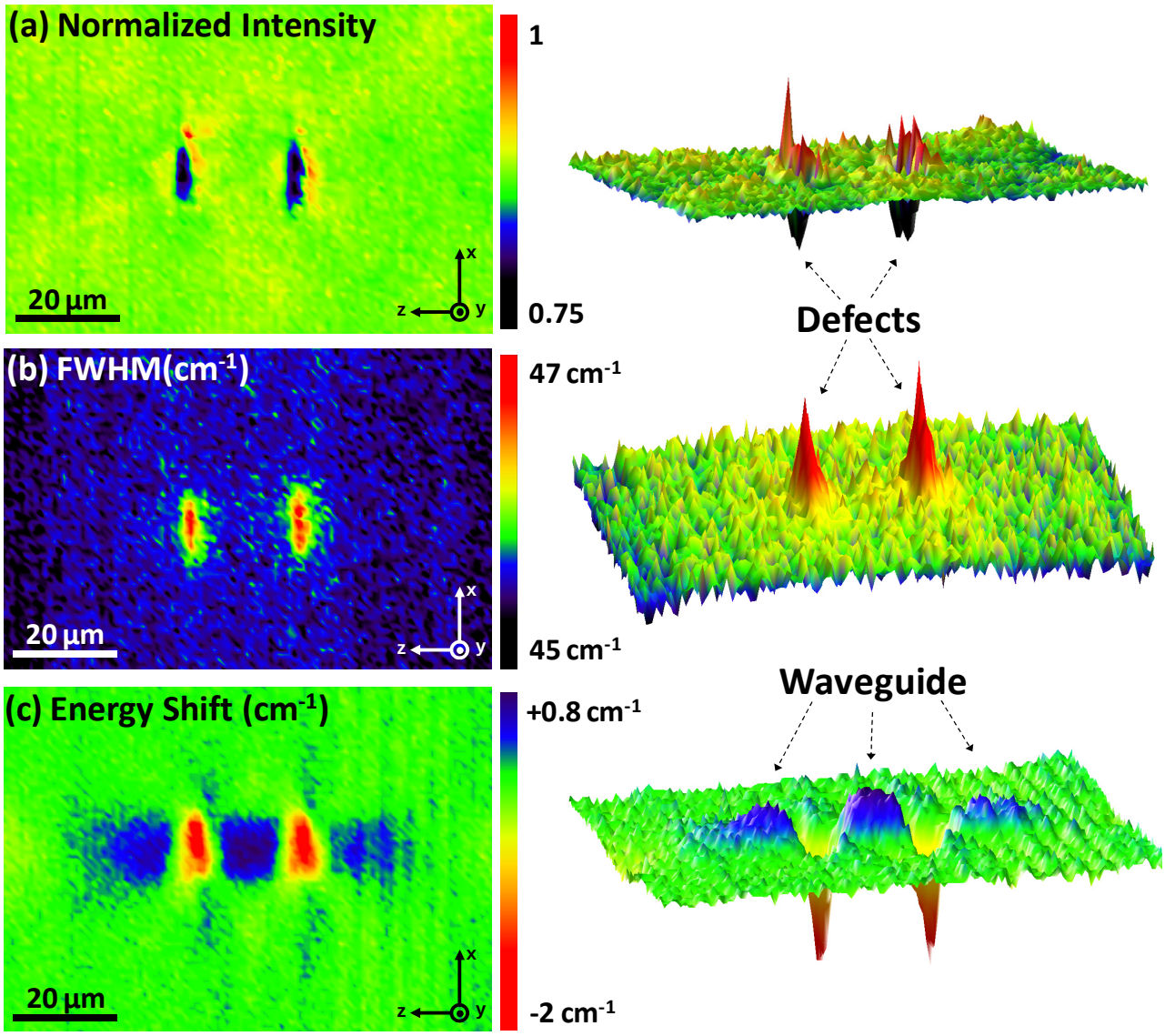

Figure 5.15. *Spatial distribution of the intensity* **(a)**, *FWHM* **(b)**, *and energy shift* **(c)** *of the main luminescence peak within the non polarized* $^4F_{3/2} \rightarrow {}^4I_{9/2}$ *emission band of* Nd^{3+} *ions, located at around 11114* cm^{-1}. *Three-dimensional plots are also shown, which allow visualizing the magnitude of spectral changes relative to the noise level in the measurements.*

At the sides of the central defect regions, a surrounding region of slightly enhanced emission is also observed (brighter zones of the image in **Fig. 5.15 (a)**), which also appears somehow slightly more distributed around the right hand side of the defect lines. This enhancement in the luminescence efficiency is of about a ~10% for the analyzed emission line, and coincides spatially with the previous surrounding region identified by Raman scattering, where a slight reordering of

Nb sites (B sites) is suggested by the observed decrease in damping of the $A(TO_1)$ mode (see **Fig. 5.12** or **Table 5.3**). As Nd^{3+} ions occupy the Li sites, one nice explanation for this slight emission intensity enhancements would be that the Nd^{3+} ions could have diffused out of the damaged region, incorporating into Li sites and moving the Nb antisites (Nb ions in Li sites) into their corresponding sites, i.e. into B sites, well explain also the observed Raman mode decrease in bandwidth (decrease in damping). This kind of ion diffusion has in fact been observed very recently in fs laser irradiated Eu^{3+} doped silicate glasses [75]. However, neither time-resolved measurements were here performed along these micrometric regions (in order to asses any change in the luminescence lifetimes as a result of the changing distances between Nd^{3+} ion pairs), nor any compositional study (such as EDX) was performed. Due to this, a more simple explanation should also be considered, that these regions, which also appear slightly brighter at the microscope, could correspond to regions in which the refraction index has been increased locally, thus producing an enhancement in the collected luminescence as a result of the better coupling between the pumping laser focal volume and the emitted luminescence.

Along with the luminescence intensity decrease at the centre of the defect lines, a slight increase in the FWHM is also observed (**Fig. 5.15 (b)**), very well localized at the same volume where the intensity is observed to decrease. This increase in the linewidth is however of only around a ~4% for the analyzed emission line, confirming that the degree of amorphization is rather low at the written lines. Both the luminescence intensity reduction and the broadening of the emission peak confirm that at the tracks a significant amount of lattice defects and structural disorder have been induced, although the degree to which these lattice defects affect the luminescence properties is not high. However, at the waveguiding zones, where the refractive index has been increased, neither of these features is observed and the luminescent properties of the laser ions are then completely well preserved. This fact is of tremendous importance since the first application of this waveguides would be that of integrated laser systems.

As previously said, the spectral energy position of the emission lines is known to be very sensitive to changes not only associated with disorder or damage, but also and very importantly, to alterations of the crystal field symmetry and strength around the location of Nd^{3+} ions, that is, at

their mainly octahedral sites. In this case (see **Fig. 5.15 (c)**), the changes in the crystalline field appear characterized by the strongly marked red-shift of the emission peak (-2 cm^{-1}) at the damaged volumes, and by the blue-shifts at each side of them (+0.8 cm^{-1}), matching with the waveguiding high refractive-index regions, as shown in the figure.

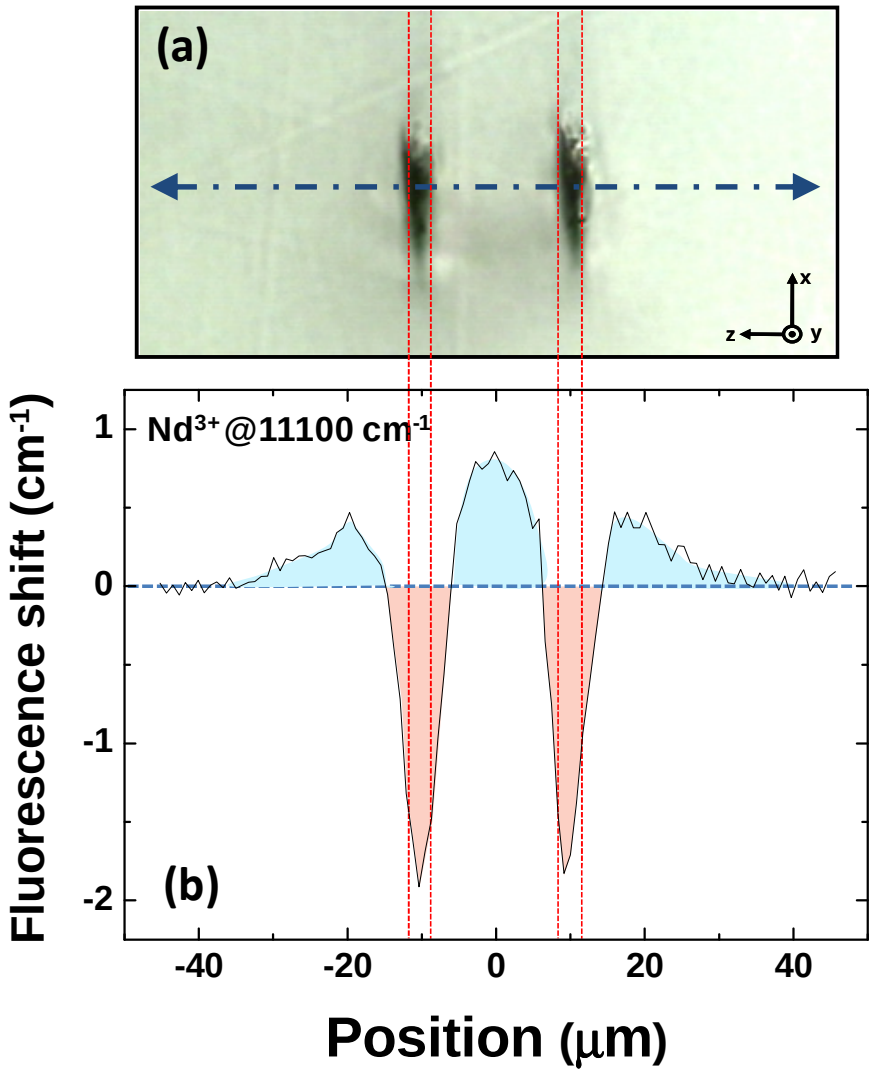

Figure 5.15. *Spectral energy shift distribution of the main luminescence peak within the non polarized* $^4F_{3/2} \rightarrow {}^4I_{9/2}$ *emission band of* Nd^{3+} *ions, located at around 11114* cm^{-1}*, across the two written lines and waveguiding volumes.*

For an easier visualization of this effect, a cross section of the energy shift plot in **Fig. 5.15 (c)** is presented on **Figure 5.16**. As it can be seen, a clear red-shift of the emission peak has been induced at the damaged volumes, while a blue-shift of the emission peak is induced on their surroundings,

which has its maximum at the waveguiding volumes. As it was explained on **Chapter 3**, red/blue-shifts of the Nd^{3+} lines in our MgO:$LiNbO_3$ samples can be unequivocally related to local increments/reductions in the crystalline field acting over the luminescent ions. This crystal field effect was in fact clearly confirmed by performing high-pressure hydrostatic luminescence studies with our samples, observing how the emission bands and the lifetimes of the $^4F_{3/2}$ excited state are strongly influenced by changes in the strength of the crystal field acting on the rare-earth Nd^{3+} ions [71, 32].

At the light of these works, and in a first order approximation, from the observed spectral shifts of **Fig. 5.16** it can be concluded that the crystal field strength has increased at the damaged volumes (compressed regions), and decreased at the waveguiding volumes (anisotropically dilated regions). Thus, in this particular case, it is reasonable to link the mechanism at the origin of the refractive-index increase with the observed reduction in the strength of the crystalline field.

To further corroborate that the refractive index changes at the waveguiding volumes are related to changes in the crystal field, the neodymium ions emission along the spatial line scan was analyzed for both σ and π polarizations. Since any kind of anisotropic lattice distortion should induce a slight change in the crystalline field symmetry, this change in the symmetry should have to be observed as a change in the relative intensities between both $\sigma\left(\vec{E} \perp c\right)$ and $\pi\left(\vec{E} \| c\right)$ polarized emission cross sections. To verify this, the polarized emission cross section of the emission peak 4 (see **Fig. 5.14 (a)**) was probed along the waveguide and damage lines. The integrated area of the polarized emission peak was then normalized to its value at normal non-irradiated values, and the ratio between the σ and π polarized normalized emissions was obtained for each point in the sample, as shown in **Fig. 5.17**.

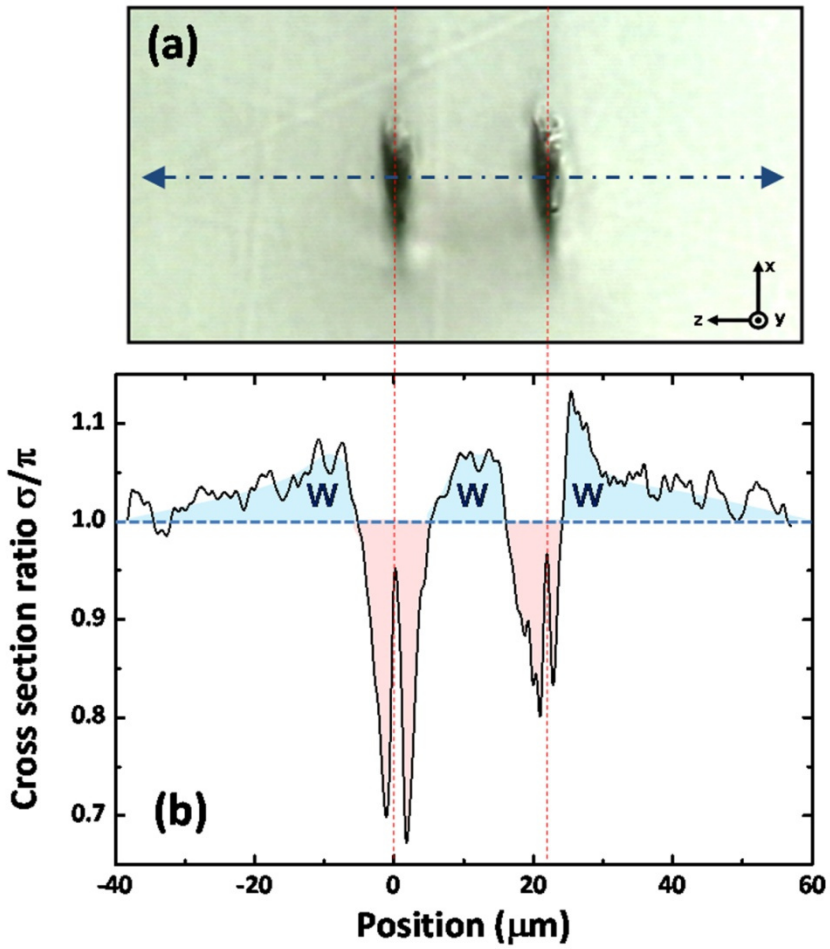

Figure 5.17. *Variations of the polarization ratio of the central emission peak 4 at 11114 cm^{-1} of the $^4F_{3/2} \rightarrow {}^4I_{9/2}$ emission band of Nd^{3+} ions, scanned across the waveguiding volumes.*

From **Fig. 5.17** it gets clear that the anisotropic lattice distortions appear to consist of two basic different kinds of changes located at the waveguiding and the damaged regions respectively. As previously stated, at the waveguiding volumes the lattice shows some anisotropic dilatation along the *xy*-plane which is defined by the O ions octahedron (see **Table 5.4**), and this dilatation is observed to be accompanied by both a clear blue-shift of the emission peaks (see **Fig. 5.16**), and an increment in the polarization ratio σ/π (see **Fig. 5.17**). These combined changes suggest that the Nd^{3+} ion sites (Li sites) have been very slightly distorted, in such a manner that the mean crystal field strength would be reduced and its symmetry slightly changed, inducing the observed spectral changes in the Nd^{3+} ions luminescence properties. The origins of the refractive index increase at the waveguide volume at the light of these measurements will be then discussed in the next section.

High-repetition rate DLW in $LiNbO_3$: Low-loss waveguide ultrafast fabrication

In the case of the waveguide written in the thermal regime the sample was not doped so that only micro-Raman experiments were performed. The experimental set-up and Raman configuration was the same as that previously described, and in this case a 0.75 NA 50x microscope objective was used focused at the sample surface. In this case two-dimensional (2D) maps were performed all along the waveguide mode and the observed different defect channels (see **Fig. 5.9**).

Figure 5.18 shows the results corresponding to the intensity, energy shift, and FWHM (damping) of the $A(TO_1)$, $A(TO_2)$, and $A(TO_4)$ phonon modes. No data could be obtained for the $A(TO_3)$ due to low acquisition times which were needed to perform the 2D mapping. Again as for the case of low-repetition rate DLW waveguides, both the intensity and FWHM of all modes present clear reductions and increments, respectively, at the previously assigned defect volumes Spots 1, 2, and 3. This indicating at the three Spots some different degrees of lattice disorder and amorphization has been induced. It is also observed that the spatial extension and position of each feature coincides very well with the waveguide morphology previously analyzed from the microscope transmission images, and with the assumption that the self-focusing and defocusing of the laser pulses has created the three damage channels. All the Raman features present at the defect zones are then equivalent to those previously observed in the case of low-repetition rate DLW waveguide, whereas the morphology of the damaged regions is clearly different.

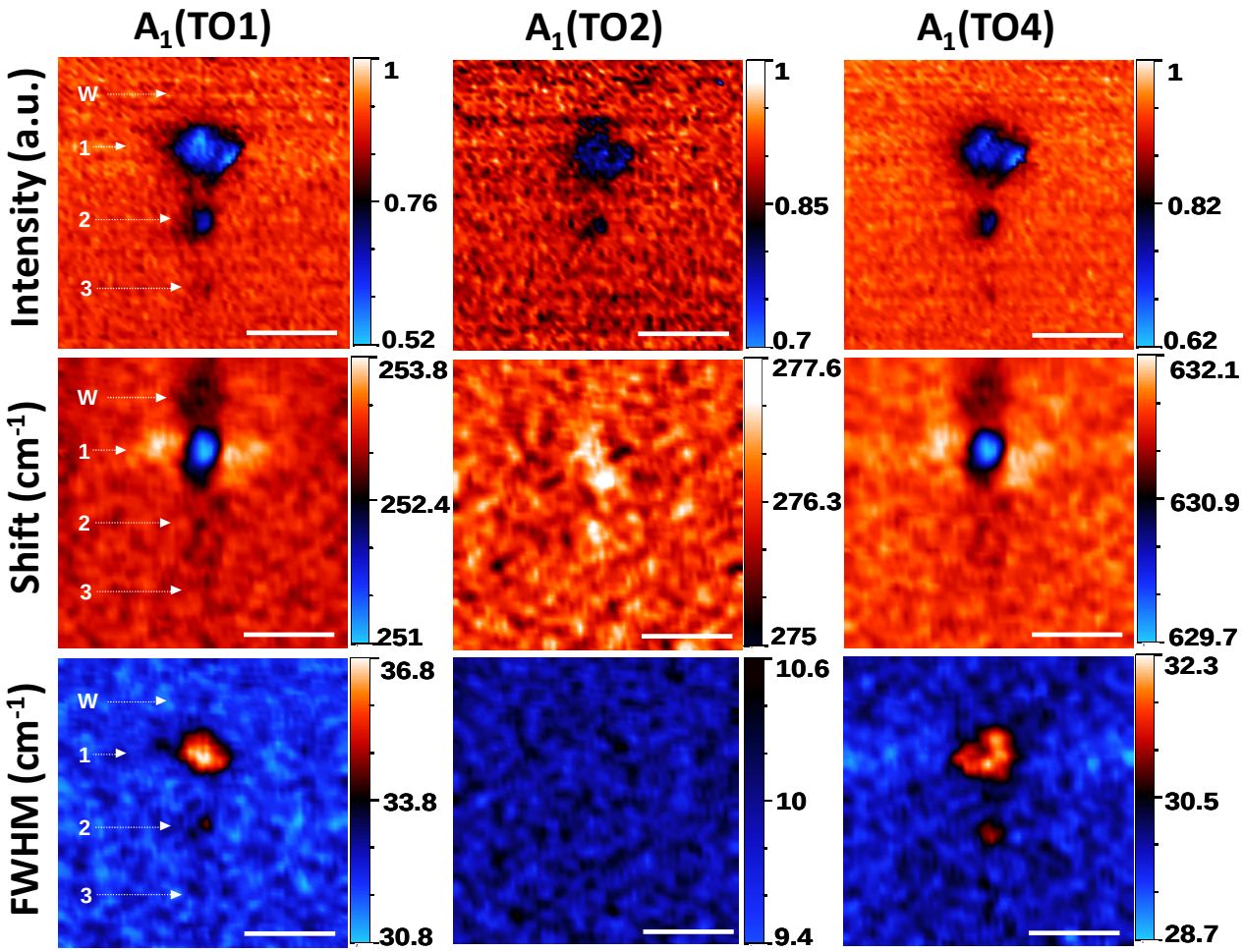

Figure 5.18. *Spatial distribution of the intensity, energy shift, and FWHM of the A(TO_1), A(TO_2), and A(TO_4) phonon modes. The waveguide volume is indicated by W and the different subsequent damage channels are labeled as Spots 1, 2, and 3. Scale bar is 10 µm in all images.*

Simultaneously to these variations in intensity and damping, at the defect volumes the vibration energy of the different Raman modes is also observed to vary. A strong decrease in the phonon energies of the A(TO_1) and A(TO_4) modes is observed, while a slight increase in the energy of the A(TO_2) takes place. As it was previously described (see the Raman introduction of **Section 5.3.4**), these changes imply that the main lattice distortion at the damaged zones is that of a dilatation of the O ion octahedron along the *xy*-plane, which in this case coincides with the plane normal to the laser propagation direction, and together with this dilatation, also a slight compression along the optical *c*-axis could be present, as the positive energy shift of the A(TO_2) mode indicates.

At both lateral sides of the central damage Spot 1, along the *y*-axis direction, it also appears clear that the A(TO_1) and A(TO_4) modes shift to higher vibration energies, this indicating that along this lattice direction a slight compression of the O octahedron has been reciprocally induced, adjacent to the expansion at the main laser focal volume (Spot 1). Whereas this compression could be causing a localized refractive-index increment, at these regions no waveguiding was reported by Amir et al., probably as a result of the close lying damage track, which would induce too high propagation losses. These regions are hereafter regarded as the surrounding regions to the central damaged Spot 1.

Finally, it is also worth noting how the spatial extension of Spot 1 is considerably different as seen on the intensity and damping variations, with respect to the modulation on the energy shifts of the A(TO_1) and A(TO_4) modes. In this sense, the spatial extension of lattice damage is about ~5.8 μm in diameter (as measured from the intensity and FWHM 2D maps), but that of lattice anisotropic dilatation is much smaller, and of about ~3.4 μm (as measured from the energy shift 2D maps). Thus, the lattice damage region can be considered as extending well outside the dilated central region, partially covering the compressed lateral regions.

At the waveguide volume, indicated as W in **Fig. 5.18**, no intensity reduction or FWHM increase was measured, and only some slight red-shift of the A(TO_1) and A(TO_4) modes was observed, while the A(TO_2) mode remained unaltered. Thus, it can be concluded that at the waveguide zone a similar dilatation of the O ion octahedron would cause the index change responsible for the refractive index increase.

This dilatation appears in a similar way to that observed in the case of the low-repetition rate double-line waveguides, which was previously analyzed. The origins of the refractive index increase at the waveguide volume and the observed polarization dependence of the waveguide modes at the light of these Raman measurements will be then discussed in the next section.

Table 5.5 summarizes the observed Raman changes at each modified region, as extracted from **Fig. 5.18**.

	Damage Core				Surrounding				Waveguide			
Mode	**$A(TO_1)$**	**$A(TO_2)$**	**$A(TO_3)$**	**$A(TO_4)$**	**$A(TO_1)$**	**$A(TO_2)$**	**$A(TO_3)$**	**$A(TO_4)$**	**$A(TO_1)$**	**$A(TO_2)$**	**$A(TO_3)$**	**$A(TO_4)$**
Intensity	0.52	0.7	-	0.62	0.76	0.91	-	0.82	**1**	**1**	-	**1**
FWHM	6	0	-	3.6	3	0	-	1.8	**0**	**0**	-	**0**
Energy Shift	-2.1	1.3	-	-1.8	+0.7	0	-	+0.6	**-0.7**	-	-	**-0.7**

Table 5.5. *Raman modes changes at the different zones: damaged, surroundings and waveguide region.*

From these data, a summary of the main lattice distortions and changes which have been induced at the irradiated volumes can be made. This summary is next presented in the **Table 5.6**. The regions have been divided between the main damage (Spot 1) area, which corresponds to the focal volume, the lateral surroundings to it (along *y*-axis), and the waveguiding zone.

REGION	Extension	Defects	Disorder	Compression	Dilatation
Damage Spot	~5.8 µm	general	A and O sites	Weak and along *c*-axis	Strong and along the *xy*-plane
Surrounding	~4.8 µm	Slight in A and O sites	Slight in A and O sites	Along the *xy*-plane	no
Waveguide	~4.8 µm	no	no	no	Along the *xy*-plane

Table 5.6. *Lattice changes at the different zones. The extension of damaged core and waveguide is the total lateral extension of these zones, and for the surrounding the lateral extension is indicated.*

With the goal of inspecting the periodic micrometric dark fringes which were previously observed by microscope transmission imaging, and which were aligned along the cleavage direction, a high resolution mapping was also done only at the main damage Spot 1. As the mean separation between fringes was measured to be around 1 µm, a high NA 1.4 objective (immersion oil 100x Olympus UPlanSApo), together with a reduced confocal aperture of minimum size acceptable in terms of signal to noise ratio and exposure time, were used in this case, in order to resolve the specific Raman features at these sub-micron volumes. In this case, although the origin of such fringes is still unexplained (and it is also out of the scope of this work), the phenomenon is enough curious to try understanding the lattice properties forming it. From this mapping, a general

reduction in all the Raman modes was detected, as it is exemplified in **Figure 5.19**, where the intensity modulation is shown only for the case of the $A(TO_4)$ mode.

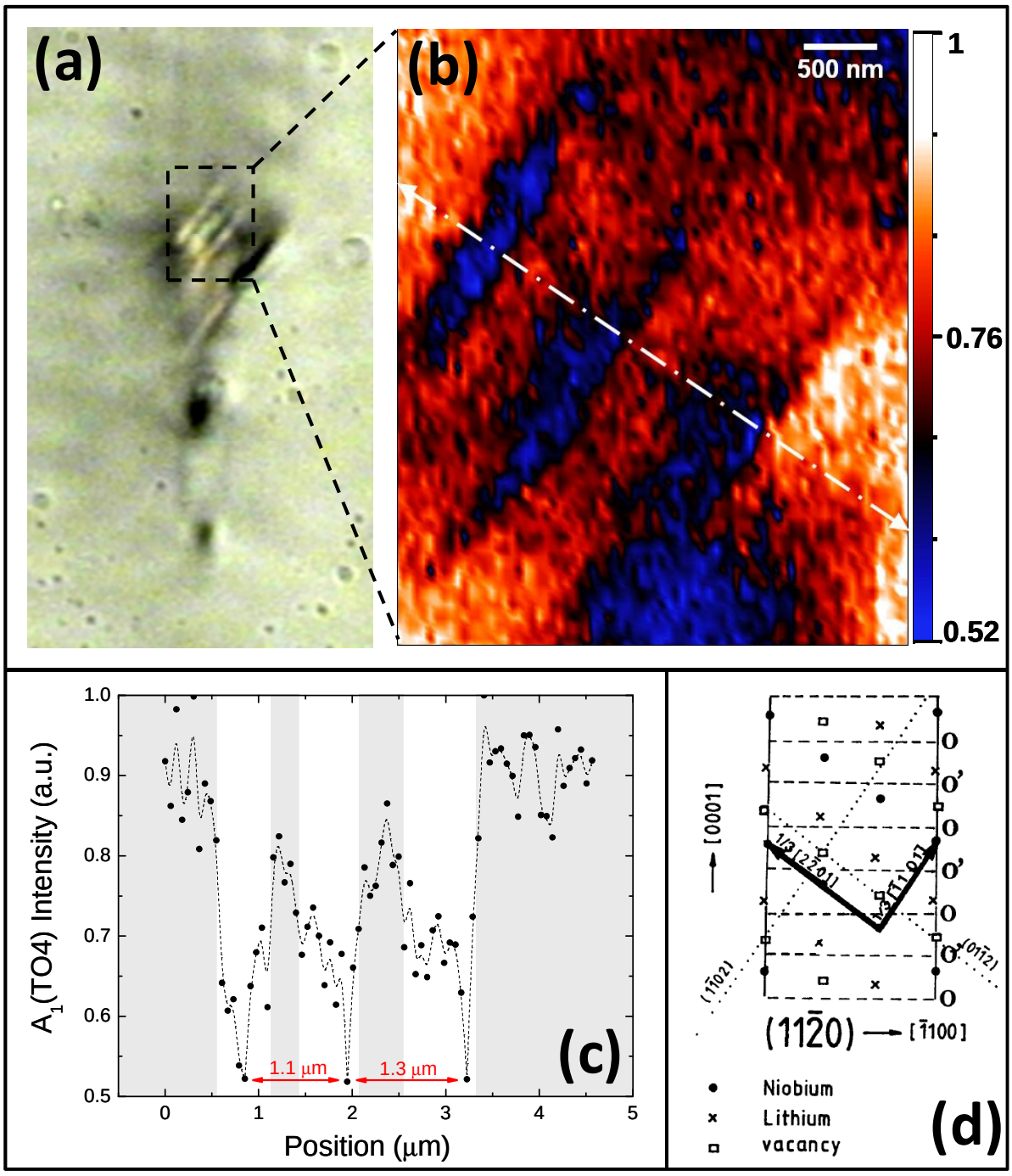

Figure 5.19. *Analysis of the laser induced fringes which appear located at the laser focal volume, as shown in **(a)**. The Raman $A(TO_4)$ phonon mode normalized intensity map **(b)**, and its cross section **(c)** -indicated by a white discontinuous line-. **(d)** Lattice arrangement in a prismatic plane showing the characteristic $(1\,\bar{1}\,0\,2)$ slip plane* [76].

No relevant contrast in the phonon energy shifts or damping was observable within the signal to noise ratio imposed by the small confocal aperture needed to resolve the sub-micrometric fringes. But nevertheless, the intensity modulation clearly reveals that the fringes consist on a strong periodic modification of the $LiNbO_3$ lattice properties. The fringes indeed appear extending along the 56º cleavage direction of the lattice, with an average distance between fringes of ~1.2 µm that matches the periodicity previously reported by Amir. et al. [23]. The observed alignment coincides in fact with the slip plane $(1\bar{1}02)$, along which plane gliding is well expected as a result of strain fields, which in the case of poly-domain samples can also correspond to twining and cracking during deformation [76], so that defect creation as well as defect propagation and nucleation are then more probable.

5.3.5. Refractive-index change mechanisms

As extracted from the µ-luminescence and µ-Raman measurements three different lattice change processes are present at the irradiated zones and surroundings, which are lattice defects and disorder at the focal regions, and anisotropic lattice distortions at its surroundings, matching with the observed waveguiding regions.

In the case of those zones in which a slight degree of amorphization has been induced it is well known that a refractive-index decrease will take place [77]. However, at the waveguiding zones, the index change mechanism must be of other nature.

To understand the refractive-index increase at the waveguiding zones it is important noting that neither lattice damage or disorder, nor compositional changes, has been observed at the refractive-index increased regions. Thus, only the observed lattice distortions, which would consist on unit cell volume changes, must be at the origin of the refractive-index increments. Any kind of lattice distortion or volume change would imply changes in the spontaneous polarizability and density of the crystalline lattice.

It is important to note that other index-change effects could also be taking place, such as an electro-optic index change produced by charge redistributions resulting from the laser induced photo-voltaic effect [78-81], but as no other measurements were performed to investigate this possibility, this effect cannot be taken into account here, unless the lattice distortions do not explain the index changes alone.

As discussed on **Chapter 3**, the refractive index depends on any pressure, temperature or volume changes of the medium, through both the density (ρ) and the lattice polarizability (α). That means that if a volume change is present, the index change can be separated into two components arising from (i) the change in the number of dispersion centers per unit volume, and (ii) the change in the lattice polarizability caused by the change in the inter-atomic distances and electronic bonds [82]. In general, an isotropic volume decrease induces a decrease in the density which reduces the refraction index, but it also induces an increase in the polarizability (in general, $d\alpha/d\rho<0$), so that the resulting change in the refractive index polarizability component opposes the effect of the volume decrease.

This competition between the different components of the refraction index is not well understood in the case that anisotropic crystal lattice distortions take place in the $LiNbO_3$ lattice, and so it is not easy to predict if the net refractive-index change will be in the case of anisotropic lattice distortion of the $LiNbO_3$ lattice.

At the light of the results of the previous sections, however, we know that the observed lattice micro-modifications in both kinds of ultrafast laser written waveguides mainly consist on anisotropic lattice dilatations (along the *xy*-plane in both cases). From this, the conclusion that a general volume increase (i.e. a decrease in the density) takes place at the waveguiding zones can be obtained (these conclusions were obtained at the light of the observed Raman red-shifts in the high-repetition rate waveguide, and from the combined Raman modes red-shifts and Nd^{3+} ions blue-shifts of the emission bands in the low-repetition rate case).

It can then be excluded the possibility that the refractive-index increase results from an increase in the lattice density, and thus, only a change in the spontaneous polarizability can explain the appearance of waveguiding volumes. That is, the positive refractive-index change, proven by the observation of waveguiding, must be due to changes in the lattice polarizability. The polarizability changes being produced by the observed anisotropic lattice distortions of the $LiNbO_3$ lattice.

Whatever are the exact microscopic mechanisms, the variation of the refractive indices of $LiNbO_3$ as a result of the observed laser induced strain fields can be calculated from the empirical piezo-optic coefficients (also called photoelastic effect) with the help of the well known relations:

$$\Delta n_i = -\frac{n_i^3}{2}\pi_{ij}\sigma_j ; (i,\ j = 1,...,6) \tag{5.8}$$

where Π_{ij} and σ_j are the piezo-optic and stress tensor elements, respectively (see **Chapter 2** for further details).

The stress elements for each waveguide can be obtained from the Raman mode shifts of **Table 5.3** and **5.5** for the low-repetition rate non-thermal and high-repetition rate thermal-regime DLW waveguide, respectively. In a first order approximation, the energy shift of the $A(TO_2)$ and $A(TO_4)$ modes can give us the main types of stress which is present at the waveguiding volumes of each waveguide type; the $A(TO_2)$ and $A(TO_4)$ modes are chosen as these two modes give the corresponding lattice compressions or dilatations along the lattice axes *z* and *x*/*y*, respectively. The hydrostatic pressure dependence of the $LiNbO_3$ Raman modes has been studied by Jarayaman et al. [60], and from these experimental data, only as a first order approximation, the corresponding stress can be extrapolated. These data is shown in **Table 5.7**.

ΔE (cm^{-1}) [σ(kbar)]	A(TO_2)	A(TO_4)
LOW REPETITION RATE	**+0.3 [0.47 Kbar]**	**-0.7 [-2.8 Kbar]**
HIGH REPETITION RATE	**0**	**-0.7 [-2.8 Kbar]**

Table 5.7. *Main Raman energy shifts and stress fields present on each type of waveguide.*

Using these data and **Eq. 5.8** we can then estimate, in a first order approximation, the stress field components at the waveguide volumes..

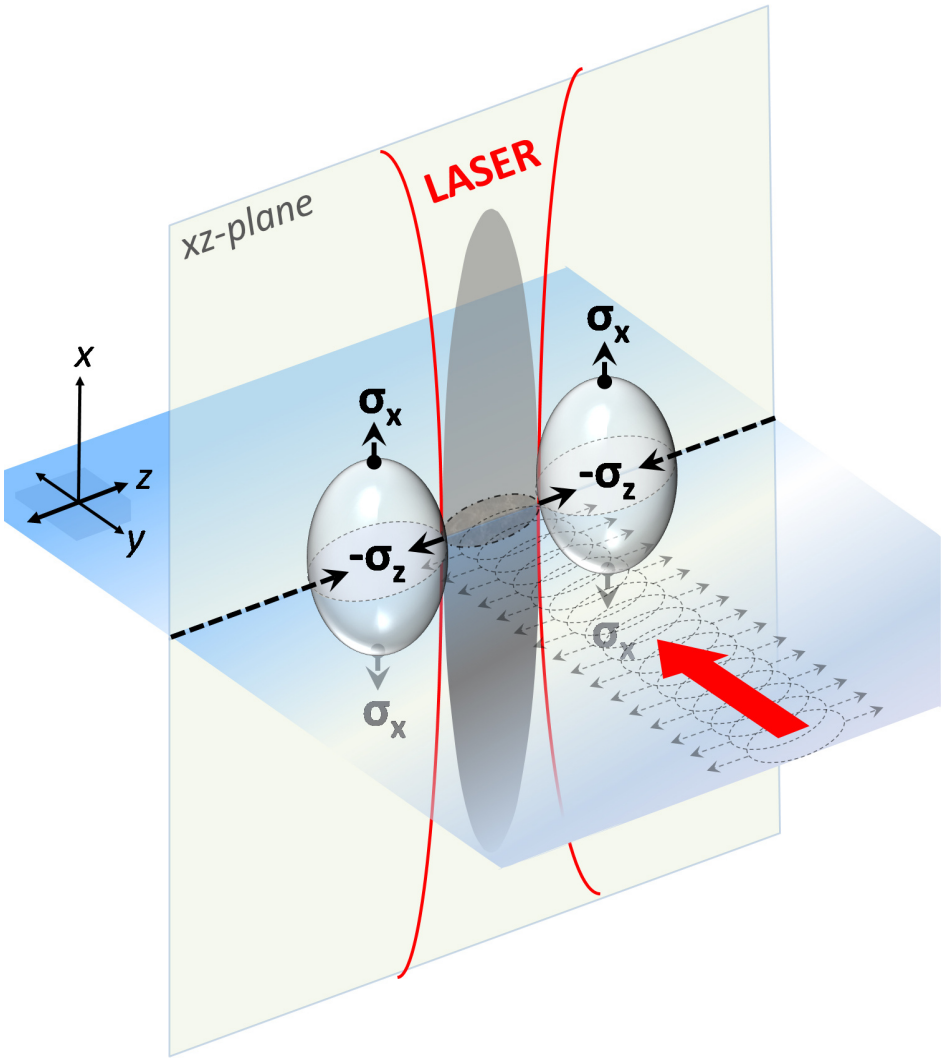

Figure 5.20. *Diagram of the DLW process in the low-repetition rate case, showing the defect track defect volume in grey, and the main induced stress fields which have been measured at the laterals of the tracks, contained in the xz-plane, and coinciding with the waveguide cross section plane.*

In the case of the low-repetition rate waveguide, the non-zero components would be $\sigma_1=\sigma_x=$ 2.8 Kbar, and $\sigma_3=-\sigma_z=-0.47$ Kbar (taking into account that the sign convention is that of positive components for tensile stress, and negative for compressive stress). So that the variation of the refractive indices (taking into account the refractive indices n_e=2.135 and n_o=2.21 at around 1.5 μm) can be calculated as:

$$\Delta n_x = -\frac{n_o^3}{2}\left[\pi_{11}\sigma_1+\pi_{13}\sigma_3\right] = -\frac{n_o^3}{2}\left[-0.030\times(2.8)+0.058\times(-0.47)\right]\times\left(10^{-3}\right)\cong +0.6\times10^{-3}$$

$$\Delta n_z = -\frac{n_e^3}{2}\left[\pi_{31}\sigma_1+\pi_{33}\sigma_3\right] = -\frac{n_e^3}{2}\left[0.075\times(2.8)-0.016\times(-0.47)\right]\times\left(10^{-3}\right)\cong -1.06\times10^{-3} \quad (5.9)$$

This analysis of the stress fields predicts that waveguiding resulting from the piezooptic effect should only be observed for TM polarization. Burghoff et al. have indeed previously anticipated this by numerical calculations [26]. In this case, however, waveguiding was observed to occur for both TE and TM polarizations. This means then that in this case a piezo-optic mechanism does not completely explain the waveguide origin, and some other mechanism must be responsible for the observed guiding at TE polarization.

As previously mentioned, another well known effect which can be taken into account in $LiNbO_3$ is the photovoltaic effect. As it has been studied by several authors [78-81], after the fs pulse laser irradiation is performed inside $LiNbO_3$ a space-charge field pattern can be generated via photovoltaic effect. If the laser beam is incident in the direction perpendicular to the *c*-axis then the photovoltaic current would be excited in the *c* direction, and a change in the extraordinary refractive index in the order of 10^{-3} would arise as a result of the space charge induced electric field. This effect has, in fact, been very recently observed in SBN crystals after 250 kHz fs pulse laser DLW of two-line type waveguides is performed [81]. In this case, waveguiding was observed to occur between tracks for TE polarization, coinciding with the *c*-axis.

Also some evidence that this photovoltaic process could in fact be taking place comes from the fact that Zhang et al. demonstrated that if these low-repetition rate double-line waveguides are fabricated on a *z*-cut sample, then waveguiding is only observed for TM polarization [43], being this consistent with the fact that the photovoltaic effect would no longer induce the TE guiding. As a result of this, we state here that it is possible that the origin of the waveguiding properties of these waveguides is not only of a strain-optic nature, but also of a ultrashort pulse laser induced photovoltaic nature.

In the case of the high-repetition rate waveguide, the non-zero component is only the $\sigma_2=\sigma_y=$ 2.8 Kbar. So that the variation of the refractive indices can be calculated as:

$$\begin{aligned}\Delta n_y &= -\frac{n_o^3}{2}[\pi_{22}\sigma_2] = -\frac{n_o^3}{2}[-0.030\times(2.8)]\times\left(10^{-3}\right) \cong +0.45\times10^{-3}\\ \Delta n_z &= -\frac{n_e^3}{2}[\pi_{32}\sigma_2] = -\frac{n_e^3}{2}[0.075\times(2.8)]\times\left(10^{-3}\right) \cong -1.02\times10^{-3}\end{aligned} \tag{5.10}$$

In this case waveguiding was observed to occur only for TE polarization, and piezo-optic calculations yield that a refractive-index increment occurs only for the ordinary index, i.e. for TE polarization. Thus, it can be concluded that in this case the piezo-optic effect explains very well the origin of the index changes and waveguiding. What is more, the fact that no extraordinary index increment is observed indicates that in this case a possible photovoltaic process cannot explain the observed TE guiding.

To conclude, some characteristic features of each kind of waveguide can be summarized:

In the case of the low-repetition rate waveguides, fabricated in the non-thermal regime, the main waveguiding zones appear at the sides of the tracks, as a result of the strain fields which are induced by the laser micro-modifications at the focal volume. This kind of TM waveguiding has been observed independently of the crystal orientation and is well predicted by the piezo-optic effect for all sample orientations, due to the fact that it comes determined from the compressive stress along

the perpendicular plane to the tracks, and the tensile stress along the direction parallel to the written lines and writing direction. It has also been observed that TE guiding can occur if the waveguide is fabricated with the laser beam incident in the direction perpendicular to the *c*-axis, and in this case the piezo-optic effect alone cannot explain the observed refractive-index increment for TE polarization, and thus a second contribution due to the electro-optic effect can be tentatively given, that could explain the extraordinary refractive index increments.

On the other hand, in the case of the high-repetition rate low-loss waveguides, the piezo-optic effect also explains very well the induced waveguiding, which is mainly produced as a result of the uniaxial tensile stress along the TE polarization direction, and no compressive stress has been found. The main laser interaction mechanism which appears then responsible for such strong differences is that of lattice dilatation in the pre-focal region as a result of the thermal annealing and heat diffusion processes characteristic of the thermal regime, this being in well agreement with the observed lattice distortions and waveguiding process.

5.4. Conclusions

The fs pulse DLW method for micro-fabricating optical waveguides in $LiNbO_3$ crystals has been reviewed, and a comparative study has been performed for two specific cases of buried waveguides: the low-repetition rate (1 KHz) non-thermal regime, and the high-repetition rate (700 KHz) thermal regime.

The main types of waveguides and physical processes involved in the formation of the high-refractive index regions have been discussed. The main physical processes involved in the creation of high-refractive index regions have been identified to be the piezo-optic effect resulting from the pressure shock waves originated at the laser pulse focal regions, or the electro-optic effect produced by the space charge fields which can be induced in the ferroelectric crystal as a result of the laser pulse ionization process.

A comparative study of all published works on DLW buried waveguides in $LiNbO_3$ crystals has been presented and qualitative differences have been presented so that critical fabrication parameters have been identified, these being the normalized pulse frequency and the laser pulse energy. The normalized frequencies vary for more than 5 orders of magnitude between different works, so that three main fabrication regimes can be identified: the non-thermal regime, the critical regime, and the thermal regime. The fabrication and micro-spectroscopy analysis of waveguides fabricated in the thermal and non-thermal regimes has been done, and some qualitative differences have been extracted:

1. The non-thermal regime, is that in which the time lapse between laser pulses is longer than the thermal diffusion time from the focal spot volume. Due to the absence of heat accumulation, the laser propagation and focusing conditions can be well explained by standard material parameters and the morphology of the material changes can be well predicted. The main processes responsible for a refractive-index increase in this case are the piezo-optic response of the material, or the electro-optic effect entailed by space charge distributions induced by the fs laser field through the photovoltaic effect. From the Raman and micro-luminescence changes the stress fields which are induced have been solved, so that it appears that compressive and tensile stresses are present on the horizontal and vertical waveguide cross sections. This biaxial stress can only explain one type of refractive index increase which corresponds to the TM polarization. To explain the observed TE guiding the photovoltaic effect appears as the most plausible process, although no evidence was extracted from the micro-spectroscopy analysis.

2. The thermal regime, is that in which the time lapse between pulses is shorter than the focal volume thermal diffusion time. In this regime heat diffusion, accumulation and annealing processes become important, and the morphology of the crystal modifications at the laser focal volume and surroundings becomes more unpredictable, due to the fact that the high temperature changes alter the lineal and non-lineal refractive indices of the material, and different focusing dynamics with respect to the non-thermal case are observed. In this case

no photovoltaic process has been previously reported by other authors, and no evidence has been either found that any electro-optic index change is present on the studied waveguides. From the Raman study in has been concluded that the main lattice strain present at the waveguide volume is that of a uniaxial tensile stress which well explains the observed TE guiding.

References

[1] R. L. Fork, B. I. Greene, and C. V. Shank, *Generation of optical pulses shorter than 0.1 psec by colliding pulse mode-locking*, Appl. Phys. Lett. **38**, 9, 671 (1981)

[2] R. L. Fork, O. E. Martínez, and J. P. Gordon, *Negative dispersion using pairs of prisms,* Opt. Lett. **9**, 5 (1984)

[3] J. H. Strickler, and W. W. Webb, *3-Dimensional optical-data storage in refractive media by 2-photon point excitation*, Opt. Lett. **16**, 22, 1780-1782 (1991)

[4] D. Du, X. Liu, G. Korn, J. Squier, and G. Mourou, *Laser-induced breakdown by impact ionization in SiO_2 with pulse widths from 7 ns to 150 fs*, Appl. Phys. Lett. **64**, 23, 3071-3073 (1994)

[5] K. M. Davis, K. Miura, N. Sugimoto, and K. Hirao, *Writing waveguides in glass with a femtosecond laser*, Opt. Lett. **21**, 21, 1729-1731 (1996)

[6] Y. Kawata, H. Ueki, Y. Hashimoto, and S. Kawata, *3-dimensional optical memory with a photorefractive crystal*, Appl. Opt. **34**, 20, 4105-4110 (1995)

[7] E. N. Glezer, M. Milosavljevic, L. Huang, R. J. Finlay, T.-H. Her, J. P. Callan, and E. Mazur, *Three-dimensional optical storage inside transparent materials*, Opt. Lett. **21**, 24, 2023-2025 (1996)

[8] Y. Sikorski, A. A. Said, P. Bado, R. Maynard, C. Florea, and K. A. Winick, *Optical waveguide amplifier in Nd-doped glass written with near-IR femtosecond laser pulses*, Electron. Lett. **36**, 226-227 (2000)

[9] J. Burghoff, C. Grebing, S. Nolte, and A. Tunnermann, *Efficient frequency doubling in femtosecond laser-written waveguides in lithium niobate*, Appl. Phys. Lett. **89**, 8 (2006)

[10] W. Watanabe, T. Asano, K. Yamada, and K. Itoh, *Wavelength division with three-dimensional couplers fabricated by filamentation of femtosecond laser pulses*, Opt. Lett. **28**, 24, 2491-2493 (2003)

[11] N. Takeshima, Y. Narita, S. Tanaka, Y. Kuroiwa, and K. Hirao, *Fabrication of high-efficiency diffraction gratings in glass*, Opt. Lett. **30**, 4, 352-354 (2005)

[12] Y. Chen, K. Sugioka, and K. Midoriwaka, *Microfluidic laser embedded in glass by three-dimensional femtosecond laser microprocessing*, Opt. Lett. **29**, 17, 2007 (2004)

[13] H. B. Sun, S. Matsuo, and H. Misawa, *Three-dimensional photonic crystal structures achieved with two-photon-absorption photopolymerization of resin*, Appl. Phys. Lett. **74**, 6, 786-788 (1999)

[14] M. Deubel, G. von Freymann, M. Wegener, S. Pereira, K. Busc, and C. M. Soukoulis, *Direct laser writing of three-dimensional photonic-crystal templates for telecommunications*, Nat. Mater. **3**, 444 (2004)

[15] G. Zhou, and M. Gu, *Direct optical fabrication of three-dimensional photonic crystals in a high refractive index $LiNbO_3$ crystal*, Opt. Lett. **31**, 18, 2783 (2006)

[16] H. Misawa, and S. Juodkazis, *3D Laser Microfabrication*, Wiley-VCH Verlag, Weinheim (2006)

[17] A. Ródenas, G. Zhou, D. Jaque, and M. Gu, *Rare-Earth Spontaneous Emission Control in Three-Dimensional Lithium Niobate Photonic Crystals*, Adv. Mater. **21**, 34, 3526 (2009)

[18] L. Kuna, A. Haase, C. Sommer, E. Zinterl, J. R. Krenn, F. P. Wenzl, P. Pachler, P. Hartmann, S. Tasch, and G. Leising, *Improvement of light extraction from high-power flip-chip light-emitting diodes by femtosecond laser direct structuring of the sapphire backside surface*, J. Appl. Phys. **104**, 074507 (2008)

[19] H. C. Tapalian, J. Langseth, Y. Chen, J. W. Anderegg, and J. Shinar, *Ultrafast laser direct-write actuable microstructures*, Appl. Phys. Lett. **93**, 243304 (2008)

[20] M. Kamata, M. Obara, R. R. Gattass, L. R. Cerami, and E. Mazur, *Optical vibration sensor fabricated by femtosecond laser micromachining*, Appl. Phys. Lett. **87**, 051106 (2005)

[21] T. Gorelik, M. Will, S. Nolte, A. Tuennermann, and U. Glatzel, *Transmission electron microscopy studies of femtosecond laser induced modifications in quartz*, Appl. Phys. A **76**, 309-311 (2003)

[22] A. H. Nejadmalayeri, and P. R. Herman, *Ultrafast laser waveguide writing: lithium niobate and the role of circular polarization and picosecond pulse width*, Opt. Lett. **31**, 2987-2989 (2006)

[23] A. H. Nejadmalayeri, and P. R. Herman, *Rapid thermal annealing in high repetition rate ultrafast laser waveguide writing in lithium niobate*, Opt. Express **15**, 10842-10854 (2007)

[24] L. Gui, B. X. Xu, and T. C. Chong, *Microstructure in lithium niobate by use of focused femtosecond laser pulses*, IEEE Photon. Technol. Lett. **16**, 1337-1339 (2004)

[25] R. R. Thomson, S. Campbell, I. J. Blewett, A. K. Kar, and D. T. Reid, *Optical waveguide fabrication in z-cut lithium niobate using femtosecond pulses in the low repetition rate regime*, Appl. Phys. Lett. **88**, 111109 (2006)

[26] J. Burghoff, S. Nolte, and A. Tünnermann, *Origins of waveguiding in femtosecond laser-structured $LiNbO_3$*, Appl. Phys. A **89**, 127-132 (2007)

[27] J. Burghoff, H. Hartung, S. Nolte, and A. Tünnermann, *Structural properties of femtosecond laser-induced modifications in $LiNbO_3$*, Appl. Phys. A **86**, 165-170 (2007)

[28] H. T. Bookey, P. R. Thomson, N. D. Psaila, A. K. Kar, N. Chiodo, R. Osellame, and G. Cerullo, *Femtosecond laser inscription of low insertion loss waveguides in Z-cut lithium niobate*, IEEE Photon. Technol. Lett. **19**, 892-894 (2007)

[29] R. Osellame, M. Lobino, N. Chiodo, M. Marangoni, G. Cerullo, R. Ramponi, H. T. Bookey, R. R. Thomson, N. D Psaila, and A. K. Kar, *Femtosecond laser writing in periodically poled lithium niobate preserving the nonlinear coefficient*, Appl. Phys. Lett. **90**, 241107 (2007)

[30] A. Ródenas, A. H. Nejadmalayeri, D. Jaque, and P. R. Herman, *Confocal Raman imaging of optical waveguides in $LiNbO_3$ fabricated by ultrafast high-repetition rate laser-writing*, Opt. Express **16**, 18, 13979 (2008)

[31] A. Ródenas, L. M. Maestro, M. O. Ramírez, G. A. Torchia, L. Roso, F. Chen, and D. Jaque, *Anisotropic lattice changes in femtosecond laser inscribed Nd^{3+}:MgO:$LiNbO_3$ optical waveguides*, J. Appl. Phys. **106**,1, 013110 (2009)

[32] A. Ródenas, J. A. Sanz García, D. Jaque, G. A. Torchia, C. Méndez, I. Arias, L. Roso, and F. Agulló-Rueda, *Optical investigation of femtosecond laser induced microstress in neodymium doped lithium niobate crystals*, J. Appl. Phys. **100**, 3, 033521 (2006)

[33] R. R. Thomson, A. K. Kar, and J. Allington-Smith, *Ultrafast laser inscription: an enabling technology for astrophotonics*, Opt. Express **17**, 3, 1963-1969 (2009)

[34] W. Yang, P. G. Kazansky, and Y. P. Sviro, *Non-reciprocal ultrafast laser writing*, Nature Photon. **2**, 99-104 (2008)

[35] C. Méndez, J. R. Vázquez de Aldana, G. A. Torchia, and L. Roso, *Optical waveguide arrays induced in fused silica by void-like defects using femtosecond laser pulses*, Appl. Phys. B **86**, 2, 343 (2007)

[36] A. M. Streltsov, and N. Borrelli, *Study of femtosecond-laser-written waveguides in glasses*, J. Opt. Soc. Am. B **19**, 2496 (2002)

[37] F. Vega, J. Armengol, V. Diez-Blanco, J. Siegel, J. Solis, B. Barcones, A. Pérez-Rodríguez, and L. Loza-Alvarez, *Mechanisms of refractive index modification during femtosecond laser writing of waveguides in alkaline lead-oxide silicate glass*, Appl. Phys. Lett. **87**, 2, 021109 (2005)

[38] J. Burghoff, C. Grebin, S. Nolte, and A. Tünnermann, *Waveguides in lithium niobate fabricated by focused ultrashort laser pulses*, Appl. Surf. Sci. **253**, 7899 (2007)

[39] R. Osellame, G. Della Valle, N. Chiodo, S. Tacheo, P. Laporta, O. Suelto, and G. Cerullo, *Lasing in femtosecond laser written optical waveguides*, Appl. Phys. A **93**, 1, 17-26 (2008)

[40] Y. L. Lee, N. E. Yu, C. Jung, B.-A. Yu, I.-B. Sohn, S.-C. Choi, Y.-C. Noh, D.-K. Ko, W.-S. Yang, H.-M. Lee, W.-K. Kim, and He.-Y. Lee, *Second-harmonic generation in periodically poled lithium niobate waveguides fabricated by femtosecond laser pulses*, Appl. Phys. Lett. **89**, 171103 (2006)

[41] H. Chen, X. Chen, Y. Zhang, and Y. Xia, *Polarization-dependent coupling in a 1 x 4 waveguide array in lithium niobate fabricated by femtosecond pulses*, Appl. Phys. B **89**, 25-28 (2007)

[42] J. Thomas, M. Heinrich, J. Burghoff, S. Nolte, A. Ancona, and A. Tünnermann, *Femtosecond laser-written quasi-phase-matched waveguides in lithium niobate*, Appl. Phys. Lett. **91**, 151108 (2007)

[43] S. Zhang, J. Yao, Q. Shi, Y. Liu, W. Liu, Z. Huang, F. Lu, and E. Li, *Fabrication and characterization of periodically poled lithium niobate waveguide using femtosecond laser pulses*, Appl. Phys. Lett. **92**, 231106 (2008)

[44] M. Heinrich, A. Szameit, F. Dreisow, S. Döring, J. Thomas, S. Nolte, A. Tünnermann, and A. Ancona, *Evanescent coupling in arrays of type II femtosecond laser-written waveguides in bulk x-cut lithium niobate*, Appl. Phys. Lett. **93**, 101111 (2008)

[45] B. McMillen, K. P. Chen, and D. Jaque, *Microstructural imaging of high repetition rate ultrafast laser written $LiTaO_3$ waveguides*, Appl. Phys. Lett. **94**, 081106 (2009)

[46] A. Ródenas, A. Benayas, D. Jaque, G. A. Torchia, C. Méndez, and L. Roso, *Femtosecond laser assisted micro-modifications in Nd:YAG ceramics for photonic applications*, COLA 2007, 9th International Conference on Laser Ablation, PMO-12.

[47] G. A. Torchia, P. F. Meilán, A. Ródenas, D. Jaque, C. Méndez, and L. Roso, *Femtosecond laser written surface waveguides fabricated in Nd:YAG ceramics*, Opt. Express **15**, 20, 13266 (2007)

[48] Image courtesy of G. A. Torchia.

[49] J. R. Vazquez de Aldana, C. Mendez, L. Roso, and P. Moreno, *Propagation of ablation channels with multiple femtosecond laser pulses in dielectrics: numerical simulations and experiments*, J. Phys. D: Appl. Opt. **38**, 2764-2768 (2005)

[50] J. R. Vazquez de Aldana, C. Mendez, and L. Roso, *Saturation of ablation channels micro-machined in fused silica with many femtosecond laser pulses*, Opt. Express **14**, 3, 1329-1338 (2006)

[51] S. Juodkazis, H. Misawa, and I. Maksimov, *Thermal accumulation effect in three-dimensional recording by picosecond pulses*, Appl. Phys. Lett. **85**, 22 (2004)

[52] G. A. Torchia, A. Ródenas, A. Benayas, E. Cantelar, L. Roso, and D. Jaque, *Highly efficient laser action in femtosecond-written Nd:yttrium aluminium garnet ceramic waveguides*, Appl. Phys. Lett. **92**, 111103 (2008)

[53] A. Ródenas, G. A. Torchia, G. Lifante, E. Cantelar, J. Lamela, F. Jaque, L. Roso, and D. Jaque, *Refractive index change mechanisms in femtosecond laser written ceramic Nd:YAG waveguides: micro-spectroscopy experiments and beam propagation calculations*, Appl. Phys. B **95**, 85-96 (2009)

[54] C. B. Schaffer, A. Brodeur, J. F. García, and E. Mazur, *Micromachining bulk glass by use of femtosecond laser pulses with nanojoule energy*, Opt. Lett. **26**, 2, 93 (2001)

[55] H. P. Li, C. H. Kam, Y. L. Lam, W. Ji, *Femtosecond Z-scan measurements of nonlinear refraction in nonlinear optical crystals*, Opt. Mat. **15**, 237-242 (2001)

[56] T. C. Damen, S. P. S. Porto, and B. Tell, *Raman effect in zinc oxide*, Phys. Rev. **142**, 570 (1966)

[57] F. Abdi, M. Aillerie, P. Bourson, M. D. Fontana, and K. Polgar, *Electro-optic properties in pure $LiNbO_3$ crystals from the congruent to the stochiometric composition*, J. Appl. Phys. **84**, 2251-2254 (1998)

[58] V. Caciuc, A. V. Postnikov and G. Borstel, *Ab initio structure and zone-center phonons in $LiNbO_3$*, Phys. Rev. B **61**, 8806-88013 (2000)

[59] Y. Zhang, L. Guibert, P. Bourson, K. Polgar, and D. Fontana, *Characterization of short range heterogeneities in sub-congruent lithium niobate by micro-Raman spectroscopy*, J. Phys. Cond. Matter. **18**, 957-963 (2006)

[60] A. Jayaraman, and A. A. Ballman, *Effect of pressure on the Raman modes in $LiNbO_3$ and $LiTaO_3$*, J. Appl. Phys. **60**, 1208-1212 (1986)

[61] I. Savova, I. Savatinova, and E. Liarokapis, *Phase composition of Z-cut protonated $LiNbO_3$: a Raman study*, Opt. Mater. **16**, 3, 353-360 (2001)

[62] S. M. Kostritskii, and P. Moretti, *Micro-Raman study of defect structure and phonon spectrum of He implanted $LiNbO_3$ waveguides*, Phys. Stat. Sol. (c) **11**, 3126-3129 (2004)

[63] I. P. Kaminow, *An introduction to Electro-Optics Devices*, Academic, New York (1974)

[64] C. C. Shih and A. Yariv, *A theoretical-model of the linear electrooptic effect*, J. Phys. C **15**, 4, 825-846 (1982)

[65] Gustavo R. Paz-Pujalt, and David D. Tuschel, *Depth profiling of proton exchanged $LiNbO_3$ waveguides by Micro-Raman spectroscopy*, Appl. Phys. Lett. **62** (26), 3411-3413 (1993)

[66] R. M. Roth, D. Djukic, Y. S. Lee, R. Osgood, S. Bakhru, B. Laulicht, K. Dunn, H. Bakhru, L. Wu, and M. Huang, *Compositional and structural changes in $LiNbO_3$ following deep He^+ ion implantation for film exfoliation*, Appl. Phys. Lett. **89**, 112906 (2006)

[67] R. Mouras, M. D. Fontana, P. Bourson, and A. V. Postnikov, *Lattice site of Mg ion in $LiNbO_3$ crystal determined by Raman spectroscopy*, J. Phys.: Condens. Matter **12**, 5053-5059 (2000)

[68] F. Abdi, M. Aillerie, P. Bourson, and M. D. Fontana, *Defect structure in Mg-doped $LiNbO_3$: Revisited study*, J. Appl. Phys. **106**, 033519 (2009)

[69] I. Horcas, R. Fernández, J. M. Gómez-Rodríguez, J. Colchero, J. Gómez-Herrero, and A. Baró, *WSXM: A software for scanning probe microscopy and a tool for nanotechnology*, Rev. Sci. Instrum. **78**, 1, 013705 (2007)

[70] D. Jaque, J. Capmany, J. A. Sanz García, A. Brenier, G. Boulon, and J. García Solé, *Nd^{3+} ion based self frequency doubling solid state lasers*, Opt. Mat. **13**, 147-157 (1999)

[71] U. R. Rodríguez Mendoza, A. Ródenas, D. Jaque, I. R. Martín, F. Lahoz, and V. Lavín, *High-pressure luminescence in Nd^{3+}-doped $MgO:LiNbO_3$*, High Press. Res. **26**, 341 (2006)

[72] J. O. Tocho, J. A. Sanz García, F. Jaque, and J. García Solé, *Fluorescence bands of Nd^{3+} sites in LiNbO:Nd,Mg laser system*, J. Appl. Phys. **70** (10), 5582-5586 (1991)

[73] H. Loro, M. Voda, F. Jaque, J. García Solé, and J. E. Muñoz Santiuste, *Polarized absorption of Nd^{3+} in $LiNbO_3$: Effect of MgO codoping*, J. Appl. Phys. **77** (11), 5929-5935 (1995)

[74] M. Sekita, M. Nakamura, A. Watanabe, S. Takekawa, and K. Kitamura, *Induced emission cross sections of near-stoichiometric $LiNbO_3$:Mg, Nd*, J. Appl. Phys. **100**, 103501 (2006)

[75] Y. Liu, M. Shimizu, B. Zhu, Y. Dai, B. Qian, J. Qiu, Y. Shimotsuma, K. Miura, and K. Hirao, *Micromodification of element distribution in glass using femtosecond laser irradiation*, Opt. Lett. **34**, 2 (2009)

[76] E. Fries, and A. Péter, *Plastic deformation of $LiNbO_3$ single crystals*, Revue Phys. Appl. **22**, 1353-1359 (1987)

[77] P. D. Townsend, P. J. Chandler, and L. Zhang, *Optical Effects of Ion Implantation*, Cambridge University Press, Cambridge (1994)

[78] O. Beyer, I. Breunig, F. Kalkum, and K. Buse, *Photorefractive effect in iron-doped lithium niobate crystals induced by femtosecond pulses of 1.5 μm wavelength*, Appl. Phys. Lett. **88**, 051120 (2006)

[79] S. Juodkazis, M. Sudzius, V. Mizeikis, H. Misawa, E. G. Gamaly, Y. Liu, O. A. Louchev, K. Kitamura, *Three-dimensional recording by tightly focused femtosecond pulses in $LiNbO_3$*, Appl. Phys. Lett. **89**, 062903 (2006)

[80] Y. J. Ying, C. E. Valdivia, C. L. Sones, R. W. Eason, and S. Mailis, *Latent light-assisted poling of $LiNbO_3$*, Opt. Express **17**, 21, 18681-18692 (2009)

[81] L. Maestro, A. Ródenas, D. Jaque, R. Thomson, D. Reid, N. Heifield, R. Ajoy, *Electro-optic reversible waveguides fabricated in SBN nonlinear crystals by femtosecond direct laser writing*, to be submitted to Appl. Phys. Lett.

[82] J. F. Nye, *Physical Properties of Crystals*, Clarendon Press, Oxford University Press, 1984.

Chapter 6

Direct laser writing of rare-earth doped $LiNbO_3$ three-dimensional photonic crystals

In this chapter we present the first measurements on modified spontaneous emission of active lithium niobate three-dimensional photonic crystals, at the important telecommunication wavelength of 1.5 μm. The microfabrication of three-dimensional photonic crystals in Er^{3+}:Yb^{3+}:MgO codoped $LiNbO_3$ crystals is described following the conclusions of Chapter 5, where the DLW technique was addressed for the case of lithium niobate crystals.

The chapter is divided into three sections: In the first, the microfabrication set up and fabrication issues concerning the inscription of photonic band gap structures by tightly focusing fs-laser pulses inside lithium niobate crystals is discussed. In the next, the fabricated structures are described and optically inspected. In the final section, the optical properties of the active lithium niobate photonic structures are analyzed; first by angle-resolved NIR light transmission for external light sources, and second, by angle-resolved micro-luminescence of the spontaneous emission of erbium ions.

6.1 3D laser microfabrication

The laser microfabrication set up is schematically drawn in **Figure 6.1**. The writing laser used was an 800 nm wavelength, linearly polarized, 100 fs pulse train at a repetition rate of 1 KHz. A chirped pulse amplifier (Spitfire, Spectra Physics) was seeded by a mode locked Tsunami Ti:sapphire, respectively pumped by a Millennia cw green laser. The laser energy was controlled by a pair of polarizer filters. After expanding the beam, the laser waist was made to fit the back aperture of an immersion-oil high numerical aperture (NA=1.4) PlanAPO 60X Olympus microscope objective. All the fabrication process was monitored by back-illuminating the sample with a white lamp. Both IR femtosecond laser radiation and white light were separated by a dichroic splitter, and the white light was focused on a charged coupled device (CCD) so that all the process can be monitored in real time. The sample holder was placed on a 3D piezoelectric nanopositioning stage, and the lithium niobate sample was fixed to it with its optical c-axis perpendicular to the writing direction (this crystal orientation is preferable in order to avoid unwanted axial birefringence aberration effects which take place in the focal region of the high numerical aperture objective. See **Chapter 3** for a further detailed study).

The synchronized 3D movement of the nanopositioning platform with respect to the laser shutter was done by means of a home made LabView program. In this way the exposure time at each lattice point (τ_{voxel}), the delay time between contiguous points (τ_{points}) and between each layer positioning (τ_{layer}), could be controlled. The usual set of writing parameters for fabricating structures were: τ_{voxel}= 10 ms, τ_{points}= 50 ms, τ_{layer}= 400 ms. A time exposure set to 10 ms per voxel implies that each voxel site is irradiated by 10 laser pulses. No apparent change in the voxel morphology was found when higher exposure times where used. Shorter delay times between each successive voxel were found to lead to a desynchronizing of the shutter with the moving platform. With this configuration each structure needed at least from 15-30 minutes to be completed, depending on the total size and number of layers.

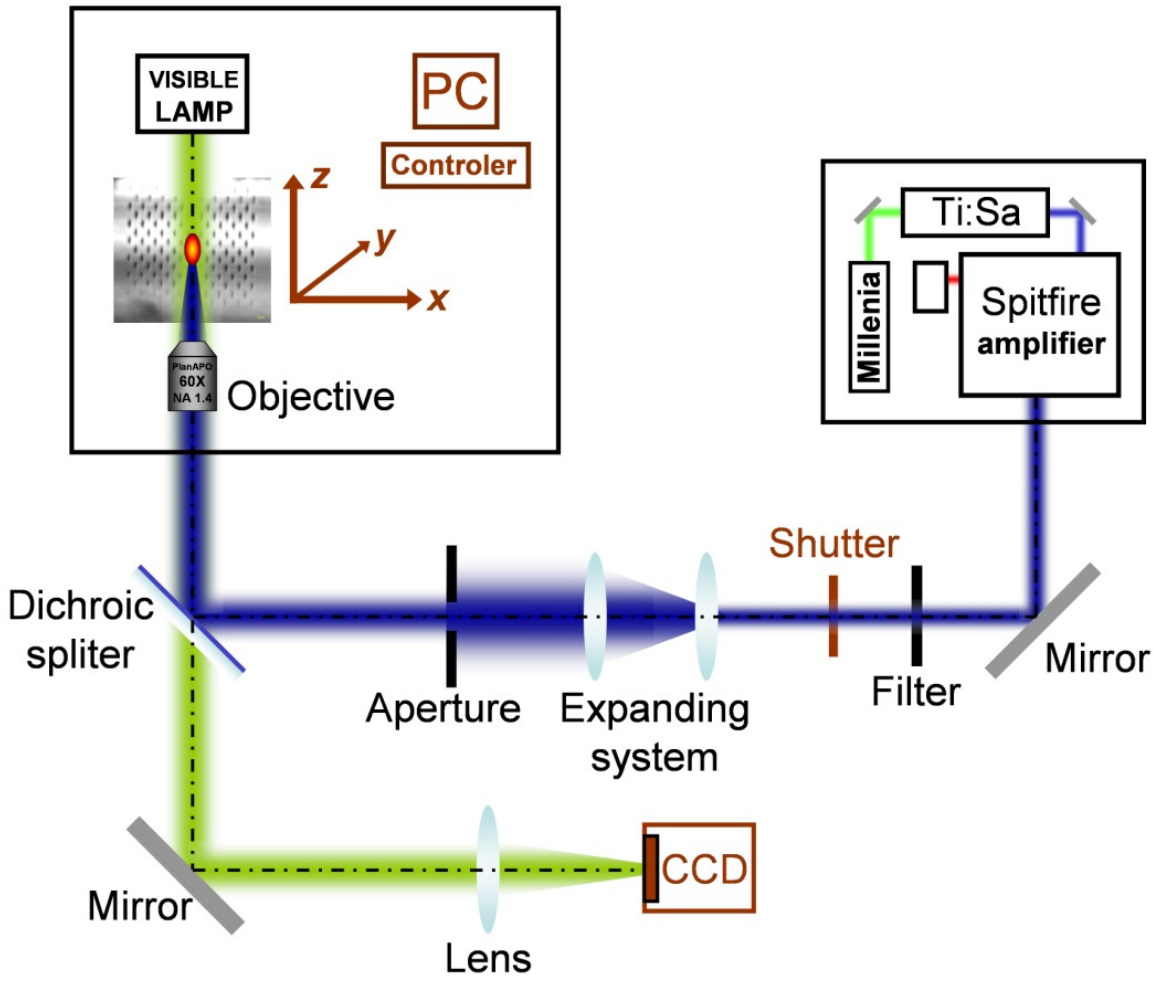

Fig. 6.1. *Schematic drawn of the 3D microfabrication laser set up. Fs pulse IR laser radiation is depicted in blue, while visible light from a white light lamp is shown in green. All elements which are computer controlled while microfabricating are also shown in brown (i.e. XYZ stage, laser shutter and CCD transmission image).*

The maximum size of the fabricated structures in the writing direction was also limited by the optical set up, due to the fact that it was not prepared to avoid the index mismatch between the high index of lithium niobate (n≈2.2) and that of the immersion oil (n≈1.56) of the high NA objective. Due to this index mismatch a characteristic spherical aberration is produced at the focal region. This distortion of the focal intensity distribution produces a decrease on the peak intensity which can only be counteracted by increasing the laser power but this at the extent of losing the small voxel size achievable in perfect conditions, which now becomes extremely broadened along the writing axis. Due to this limitation the maximum writing depths were limited to around 30 μm

from surface. The laser pulse energies for each different depth inside the sample (i.e. for each deeper lattice layer of the photonic crystals) were then needed to be adjusted during the fabrication to compensate the aberrated axial intensity distributions. The laser power was typically varied between 20 to 80 μW, for the minimum (~4 μm) to maximum depths (~30 μm) inside the lithium niobate sample. **Figure 6.2** shows a schematic map of different laser powers when writing at different depths inside a lithium niobate sample. The observed roughness of the sample border is due to the cut and polishing homemade process.

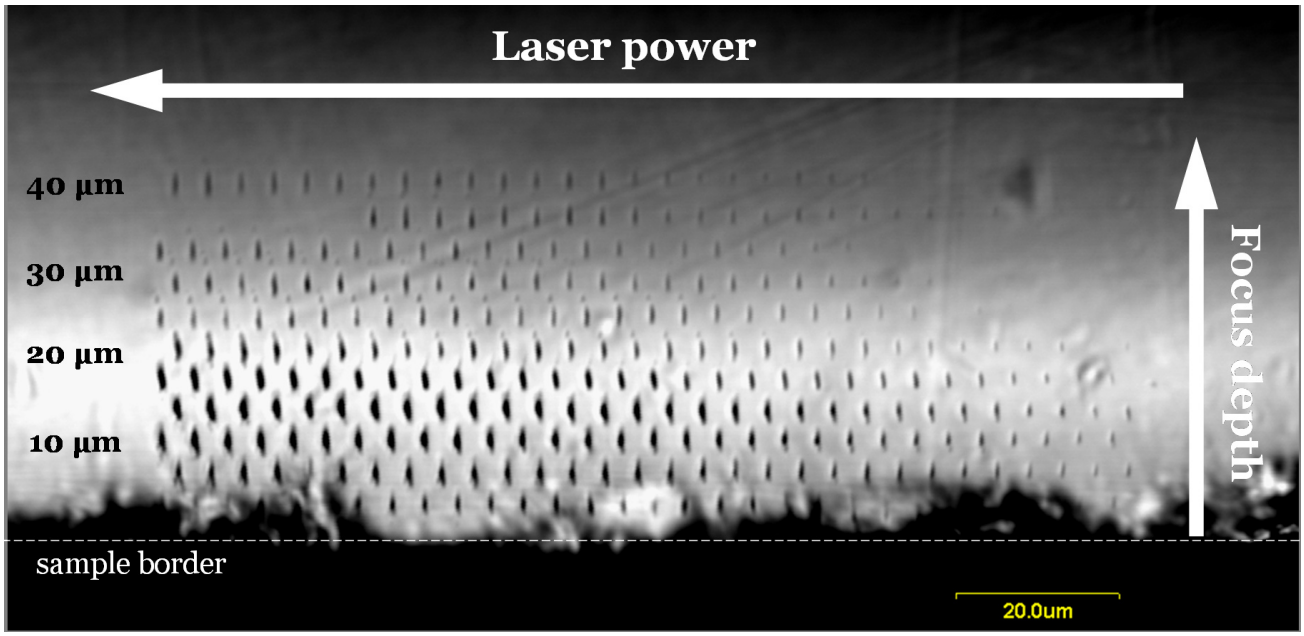

Fig. 6.2. Confocal Laser Scanning Microscope (CLSM) image of an area close to the sample border. An in-depth plane is laser written by gradually inscribing with different energies for each different depth in order to observe how the spherical aberration affects the voxel size.

Once this kind of previous analysis (**Fig. 6.2**) was performed, the voxel size for each depth and its laser power dependence could be roughly known and determined by observing the sample in a He-Ne laser confocal scanning microscope (CLSM). From that information different *writing routes* were then pre-designed[*]. This fabrication routes consisted on the set of laser powers to be used at each

[*] By *writing route* we mean here the specific settings of laser powers for the different layer depths inside the sample. The criteria followed simply consisted on selecting for each depth, the laser powers which led to a clear refraction index change and constant voxel size along all depths. From **Fig. 6.2** it can be observed that when writing beyond 20 microns deep inside the sample, the inscribed voxel size could by no means be kept constant due to spherical aberration. In the case that deeper layers were wanted higher laser powers were selected, in order to keep the index change but at the inevitable cost of altering the photonic crystal structure topology.

depth inside the sample. Examples of these power curves are summarized on **Figure 6.3**. From that figure it can be seen that the laser adjustment for structure fabrication always consisted on a gradual increment of laser power. The power increment with depth follows a nonlinear behaviour which was experimentally determined by measuring the voxel size from maps like the one in **Fig. 6.2**. The curves closer to the maximum dose limit (see **Fig. 6.3**) depict the maximum laser powers which would lead to an excessive accumulated stress load and a subsequent crystal breaking when the whole structure was fabricated. On the other hand, the curves closer to the lower dose limit were the ones which led to much lower refraction index changes (as seen by the image contrast obtained by using CLSM), which then do not produce any observable photonic stop gap.

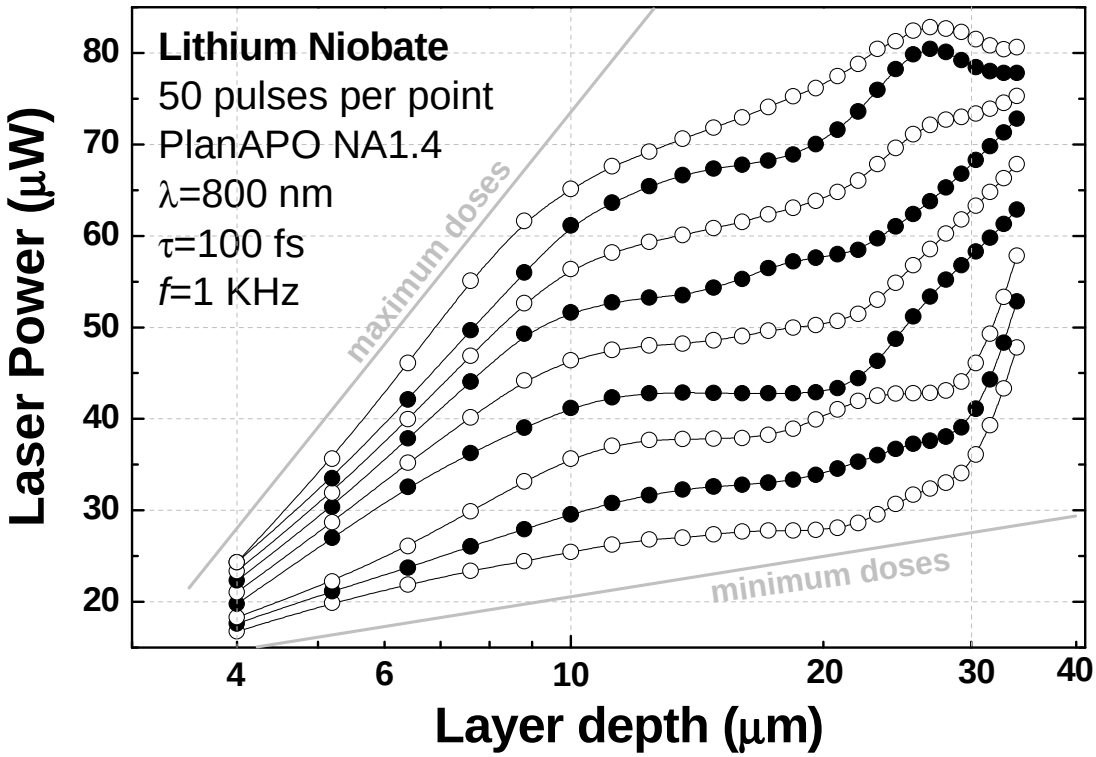

Fig. 6.3. E*xamples of the different laser powers used when writing at different depths inside the lithium niobate sample.*

Due to the spherical aberration effect not only the focal intensity distribution changes, but also its axial position, as measured from the sample/oil interface. This focal shift needs also to be calibrated in order to control the in-depth positioning of the laser focus; i.e. in order to fabricate controllably periodic structures along the in-depth direction. As shown in **Chapter 3** the shifted focal

positions can be fitted to a slope of 1.6, which is the ratio between the shifted and the linear focus of the objective. This means that for every 1 μm that the objective is moved towards the sample, the focus will move 1.6 μm due to the index-mismatch distortion. Precise calibration of this shift effect is thus a simple, but extremely important part of the fabrication process, as it gives the possibility to periodically write inside the sample. This calibration has to be done also whenever the transparent materials, or the kind of microscope objective, are changed. Once both the focus shift correction and the laser power curves were determined, structures could be written by following pre-defined routes.

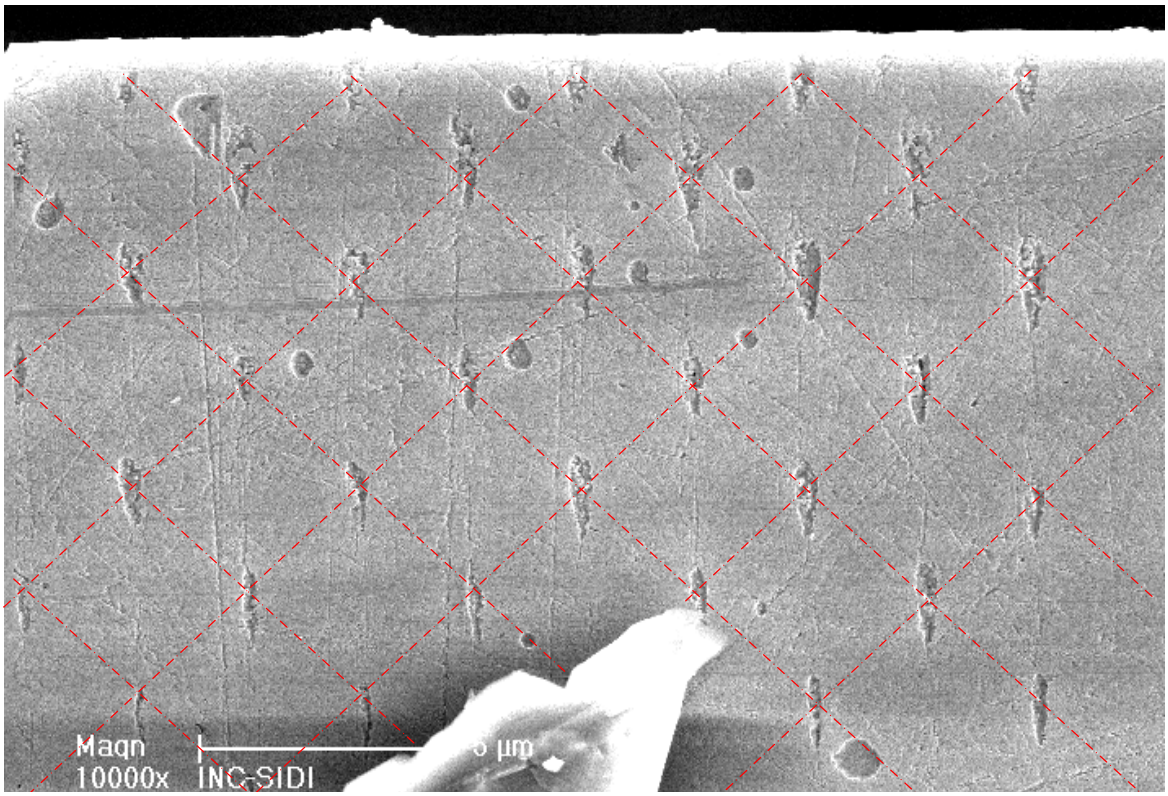

Fig. 6.4. *SEM image of a chemically revealed written structure.*

A further improving of this fabrication parameters can be performed by SEM inspecting a processed sample, so that the final resulting structures can be evaluated. To observe the written voxels the sample had to be cut and polished to the point where the voxels emerged to surface. Then, a HF:H_2O (1:2) chemical etching bath was performed for 5 minutes so that amorphous $LiNbO_3$ volumes constituting the voxels were removed with respect to surrounding crystalline regions.

Figure 6.4 shows such image where a vertical layer of periodically distributed voxels has been written and chemically revealed.

Two conclusions can be obtained by a first inspection of **Fig. 6.4**:

First, the voxels aspect ratio, as it appears after the polishing and chemical etching processes, has a very strong dispersion along the writing direction due to the unavoidable spherical aberration; and, in addition, voxels in a same horizontal layer (i.e. written at a same depth inside the sample), also feature an important size dispersion, which can be probably due to both surface defects affecting the laser power at focal position, or to slight power instabilities of the laser system.

Secondly, from **Fig. 6.4** it can also be observed that the voxel positions along the vertical writing direction seem to have a slight dispersion which should also be ascribed to the index-mismatch induced optical aberrations. This last effect translates into a slight dilatation of the photonic crystal lattice along the writing direction and means that the focal shift effect was not completely avoided. These two kinds of deviations of the fabricated structures from the ideal homogeneous ones are expected to cause a significant degrading of the photonic stop gaps; mainly a decrease in the transmission inhibition rates inside the gaps, and a broadening and shift of the stop gaps spectral shapes and positions.

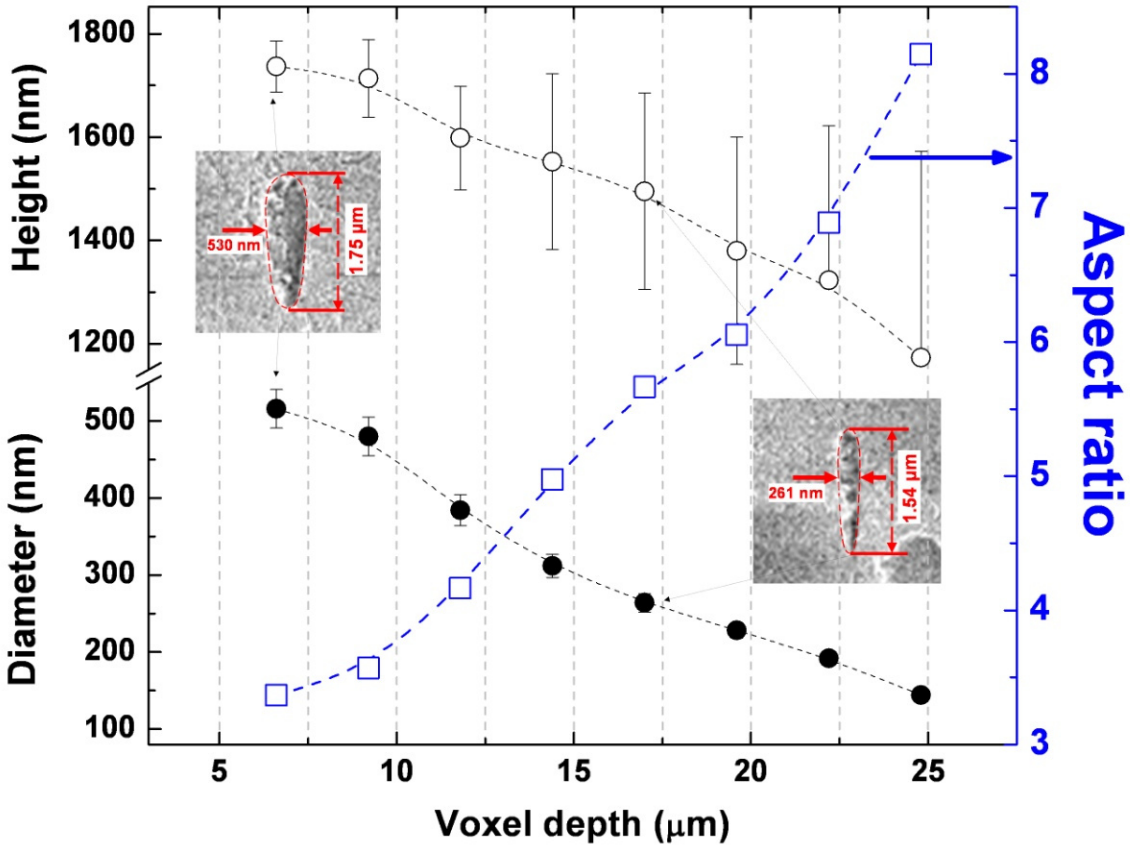

Fig. 6.5. *Height, diameter and aspect ratio of the voxels in a fabricated lithium niobate photonic band gap 3D structure.*

From SEM images like that of **Fig. 6.4** it is possible to determine with a much higher resolution than that of CLSM the different voxel sizes for each different depth and laser power. The characteristic shapes and aspect ratios were then obtained and analyzed. Results are shown on **Figure 6.5**. As it can be seen, when voxels are written close to surface and with a high laser power (4 μm / 25 μW) they are found to have a mean aspect ratio of 3.3, with a typical diameter of 530 nm, and 1.75 μm in height. Even in the case that the laser power was tailored with depth by following the previously designed correction curves (see **Fig. 6.3**), the aspect ratio is observed to further increase up to a value of 8 in the fabricated structures. Furthermore, the aspect ratio when writing at high depths is also observed to become more sensitive and dependent to laser power fluctuations.

These results depict two important factors to be improved in future fabrication works:

- The laser power needs to be controlled with a high accuracy. Ideally, in our experimental set-up conditions one would need a power resolution and stability <±0.5 μW, which was not our case due to instabilities of the pump Millenia laser. As already mentioned, the observed aspect ratio increase in **Fig. 6.5** is due to spherical aberration, but it is also found to be extremely sensitive to slight power variations of the femtosecond laser pulses, even though that the voxel inscription in our set up is performed in a multipulse regime. Vertical error bars of voxel heights in **Fig. 6.5** show the statistical size dispersion which can be observed when laser power is varied within a ± 5 μW range. As it can be seen, although the voxel diameter features little variations, the voxel height does vary in an increasing extent with depth, and especially when writing beyond a 15 μm depth.

- The laser power correction curves, which must be taken into account when varying the focusing depths, must be further improved with respect to that used in the present fabrication and included in **Fig. 6.3**. This effect is mainly due to the shape variations of the intensity point spread function (IPSF) at different focal depths inside sample (see **Chapter 3** for further details), which translate for example in a voxel diameter reduction to around 100 nm for the last lattice layers (i.e. deeper ones), which represents a fifth of that of the first layer value. This strong distortion of the photonic crystal lattice probably represents the most important disorder source in our fabricated structures. However, apart from trying to compensate it by changing (increasing) the laser power, the aberration effect could be completely corrected by implementing an aberration compensation scheme which would allow writing reproducible voxel shapes along much higher depths.

6.2 3D structure microfabrication

Before explaining the direct 3D laser microfabrication on lithium niobate one has to realize that voxels cannot be arranged in a closed packed manner in our fabrication approach, because of the strong stress fields which are induced on the crystalline surroundings of each voxel inside the lithium niobate lattice, as it would induce an excessive stress load and the subsequent crystal

breaking. Due to this, in our fabrication approach the 3D photonic band-gap lattices will necessarily have a low filling fraction (*ff*)[†], i.e. they will be rather sparse structures.

Taking into account an average voxel height of about ~1.6 µm (as previously determined), we can then expect that a layer separation of around *d*~2 µm would be enough to ensure the preservation of the crystal lattice integrity, as voxels would not overlap. So, once we know the rough dimensions of the lattice that we want to inscribe, we then need to know what will be the effective refraction-index value, which depends on the refraction-index values inside and outside the voxels. The real content inside a voxel is not yet precisely known, but it is expected to mainly consist on amorphous lithium niobate material. Amorphous lithium niobate is known to have an approximate refraction index of ~2, and crystalline lithium niobate of ~2.2. From these values it is then easy to calculate that the effective refraction index (n_{eff}) of, for instance, a face centred cubic (fcc) structure with a lattice separation of 2 µm, would be around 2.197. It can be also calculated that these structures will have a very low index-contrast of only δ=1.1, and a very low filling fraction of only *ff*=0.007 which make the fabricated structures extremely sparse. The n_{eff} can be also calculated for other face centred tetragonal (fct) or diamond structures, and it is observed to vary only within a 1% of the fcc value (for equal layer spacings of 2 µm). We can then state that neither the *ff*, nor the n_{eff} value, will significantly change for the diamond-like, fcc, or fct structures. This is so because of the very low *ff* value which is limited to avoid the stress-induced crystal cracking. However, whereas these parameters do not significantly change, these structures are known to have very different dispersion properties. For instance, fcc structures are known to show a cPBG between the 8th and 9th bands, and diamond-like ones to have it between the 2nd and 3rd bands. This property implies that, for a given desired stop-gap wavelength, diamond structures would require much smaller layer spacings than fcc ones.

Although among the various photonic crystal lattices diamond-like ones are considered as the clear "champions" [1], we can easily determine that a diamond structure will not fit our

[†] The filling fraction (*ff*) gives the relative volume of scattering material with respect to the total unit cell volume. All along this chapter different lattice parameters will be used, which define each structure and need to be known. These parameter definitions, along with quick overview over the photonic crystal properties and microfabrication issues, are included on the **Appendix** of this manuscript.

requirements: We know from previous experiments that a DLW voxel-based diamond-like structure of similar dimensions, written in a polymer (NOA 63), results on stop gaps of at least 3 μm in wavelength [2]. Thus, if the same structures were to be implemented in lithium niobate -which has a higher index of refraction than the polymer 2.2 >> 1.56, it can be easily calculated by using Bragg's law that the stop gaps would approximately fall far in the IR region ($\lambda_{gap} \geq 4$ μm), being this too far from the NIR region of interest (λ~1.5 μm). From data of ref. [2] and extrapolating to the lithium niobate refraction-index, it can be roughly calculated that unless a layer spacing lower than 400 nm was used, these stop gaps would not fall into the 1.5 μm wavelength region. Thus, diamond-structures can be disregarded at this point.

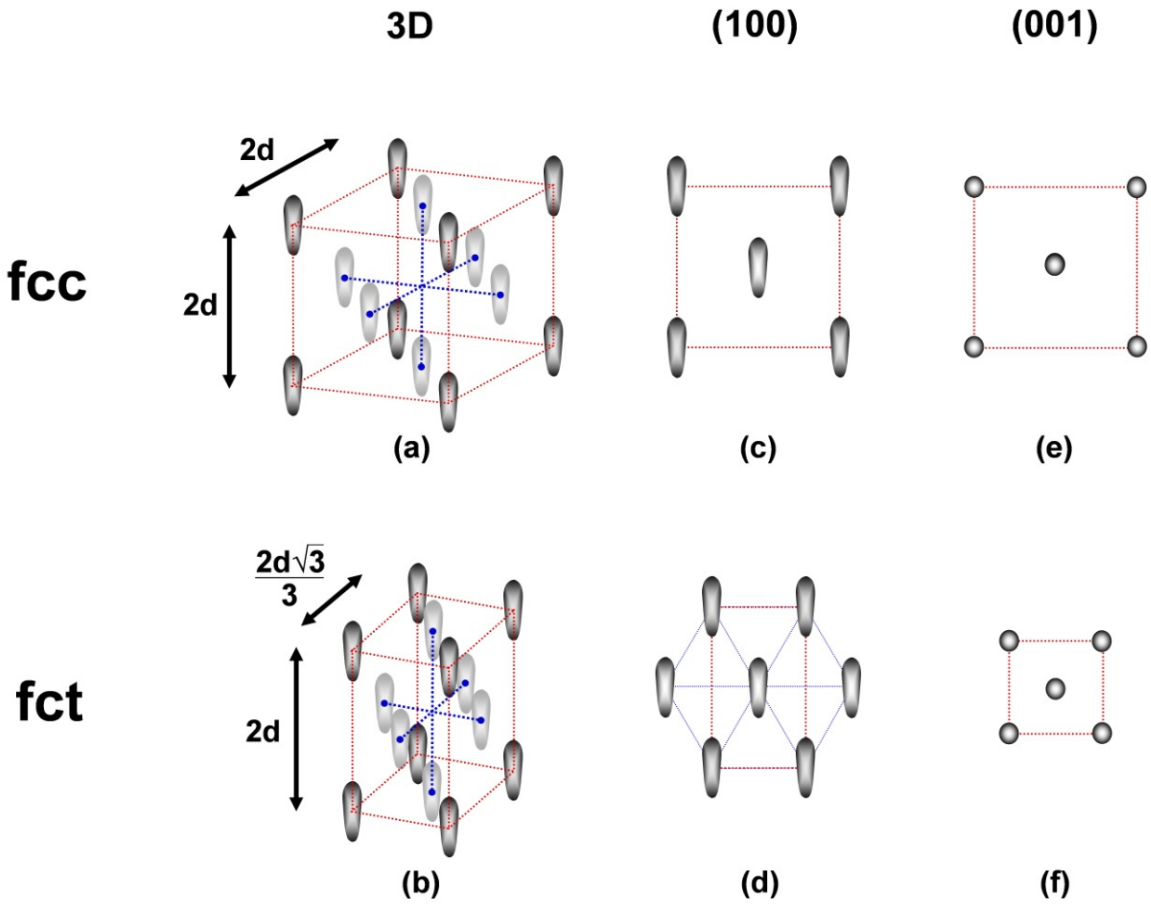

Fig. 6.6. *Schematic view of the two types of fabricated lattices.*

However, from Bragg's law (by using our previously established conditions of a layer spacing d=2 μm and n_{eff}=2.197) it can be roughly estimated that a sixth order photonic stop band could lie on the wavelength range of 1.5 μm[‡]. Due to this, fct and fcc structures could then be expected to feature the required stop-gap spectral overlap with the NIR emission from rare-earth ions. Following this, the fabricated structures consisted of fcc lattices, and an alternative fct configuration. The fabricated fct lattices have a six-fold symmetry along the in-plane layers, and a higher filling fraction than the fcc for equal layer spacing. Both types of structures are depicted on **Figure 6.6**, where the relative size of voxels (500 nm in diameter and 1750 nm in height) with respect to the layer spacing (d=2 μm) is maintained. **Figs. 6.6 (a)** and **(b)** show the 3D views of the fcc and fct structures, respectively.

The only structural variation between the fcc and fct structures is a contraction of the lattice along the perpendicular direction to laser fabrication, in such a way that the cubic cell becomes elongated in a similar way to that of voxels. These two tetragonal structures have then the same layer spacing d along the (001) direction, but different along the rest of directions (see **Fig. 6.6**). As we will see in the next section, this different lattice symmetry will considerably change the order of diffraction of the measured (001) stop gaps.

The structures are always fabricated with the highest possible laser powers which do not produce the cracking of the sample. This cracking is observed to be directly proportional to the lattice density of voxels. Consequently, as different structures are tried with different layer spacings, they have to be fabricated also with different DLW power routes (see **Fig. 6.3**). The more compact the structure is, the less the energy which can be deposited per layer in order to avoid excessive strain accumulation and crystal breaking. From now on, the different laser power routes, as those shown in **Fig. 6.3**, will be labelled E1, E2, E3, etc. for the higher to lower power curves.

[‡] Bragg law for photonic crystals reads: $m\lambda_{Bragg}=2n_{eff}d$, where m is de order of diffraction, λ_{Bragg} the diffracted wavelength, n_{eff} is the effective refraction index of the lattice, and d is the lattice layer spacing at normal incidence; see **Appendix** for further information concerning photonic crystals.

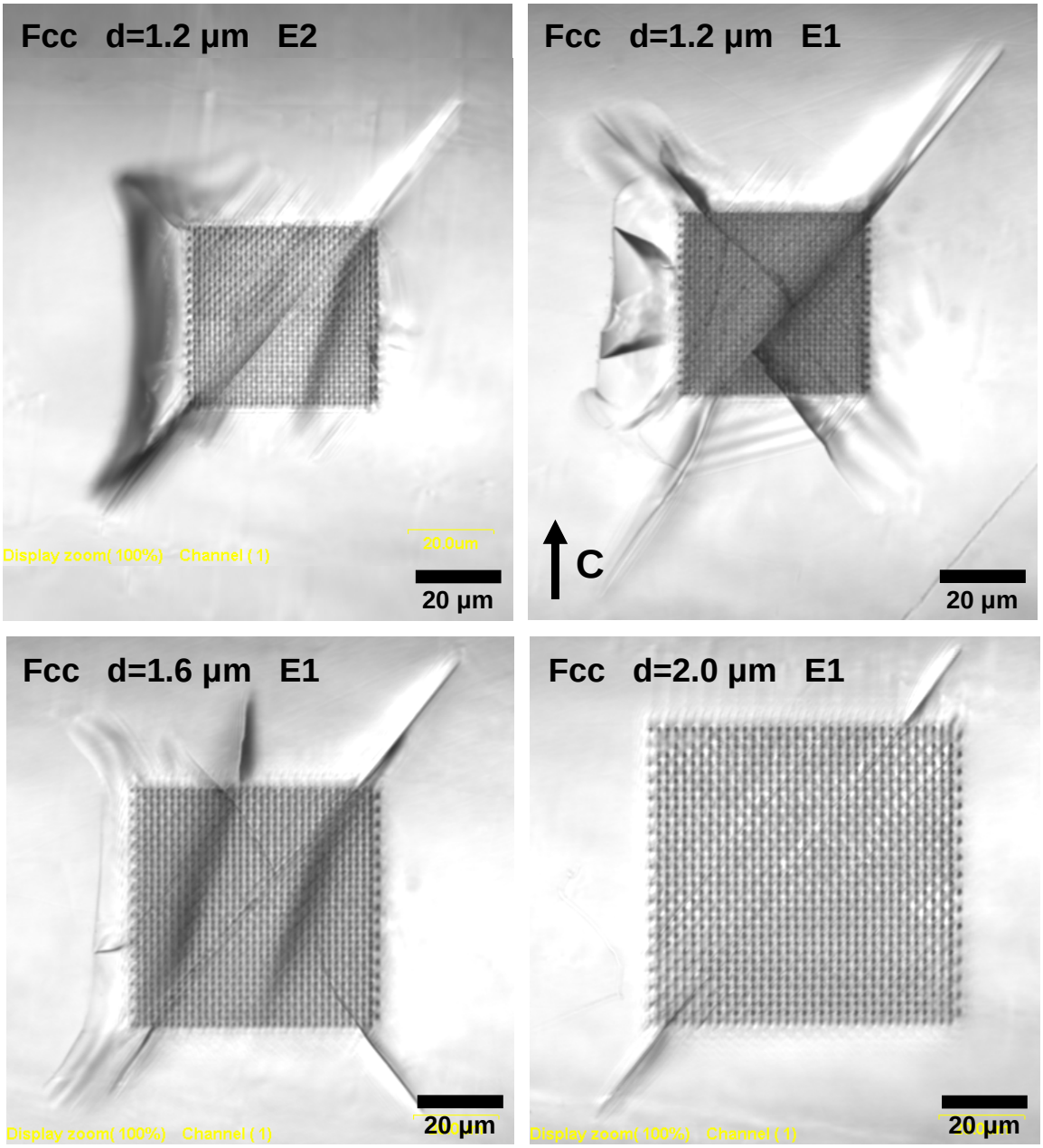

Fig. 6.7. *CLSM images of different fcc structures fabricated with a different layer spacing. The laser power routes used for each one are labelled as E1, E2, E3, etc. for the higher to lower power curves, respectively, as depicted in* ***Fig. 6.3****.*

After fabrication the structures where examined by CLSM to asses their quality and classify them. CLSM images of both the fcc and fct structures are shown in **Figures 6.7** and **6.8**, respectively. As it can be seen in **Fig. 6.7**, for fcc structures with layer spacings equal to 1.2 µm, an excessive stress load is induced which causes the crystal breaking along crystallographic planes[§]; while for

[§] This effect is expected since defect creation and propagation are more probable along the crystallographic planes.

both medium (E2) and high (E1) power routes crystal breaking occurred, for lower powers no cracks were observed. However, when no cracking occurred no stop gaps could be then observed probably due to the lower index change induced inside voxels or to the lower resulting *ff*. On the other hand, for fcc lattice spacings higher than 1.2 μm this lattice breakdown could be slightly avoided, by carefully tailoring the laser powers for each layer. Though even in that case, defect propagation from the corners of structures and along the crystallographic plane at ~52^o to the optical c-axis did never disappear. This axial cracking was observed even for structures with much higher lattice spacings, such as of 2.0 μm or 2.4 μm. As we will see in the next section, cracking of the photonic crystal causes light to dramatically scatter from the device so that its functionability is wiped away. However, if some cracking occurs only at certain parts of the sample and outside it, the stop gaps can still be easily observed, and are found to be stronger than in the case were the structure does not present any crack. The optimum DLW power routes were then the maximum ones which did not cause an excessive crack breaking, but were enough to induce a maximum index change.

For the case of fct structures with a higher voxel *ff*, due to the closer in-plane spacing of voxels the laser power had to be slightly reduced and the number of fabricated layers was also diminished in some cases to avoid excessive crystal breaking. **Figure 6.8** depicts different fabricated fct structures all with a medium layer spacing of 2 μm. For each structure the laser power writing route and the number of written layers are indicated (for example: E2 (16)).

In the fct case, if fabrication was performed with the highest (E1) power route, several cracking was observed close to the sample surface even when the structures were only fabricated to half is size, i.e. up to an approximate depth of 15 μm (see upper image on **Fig. 6.8**).

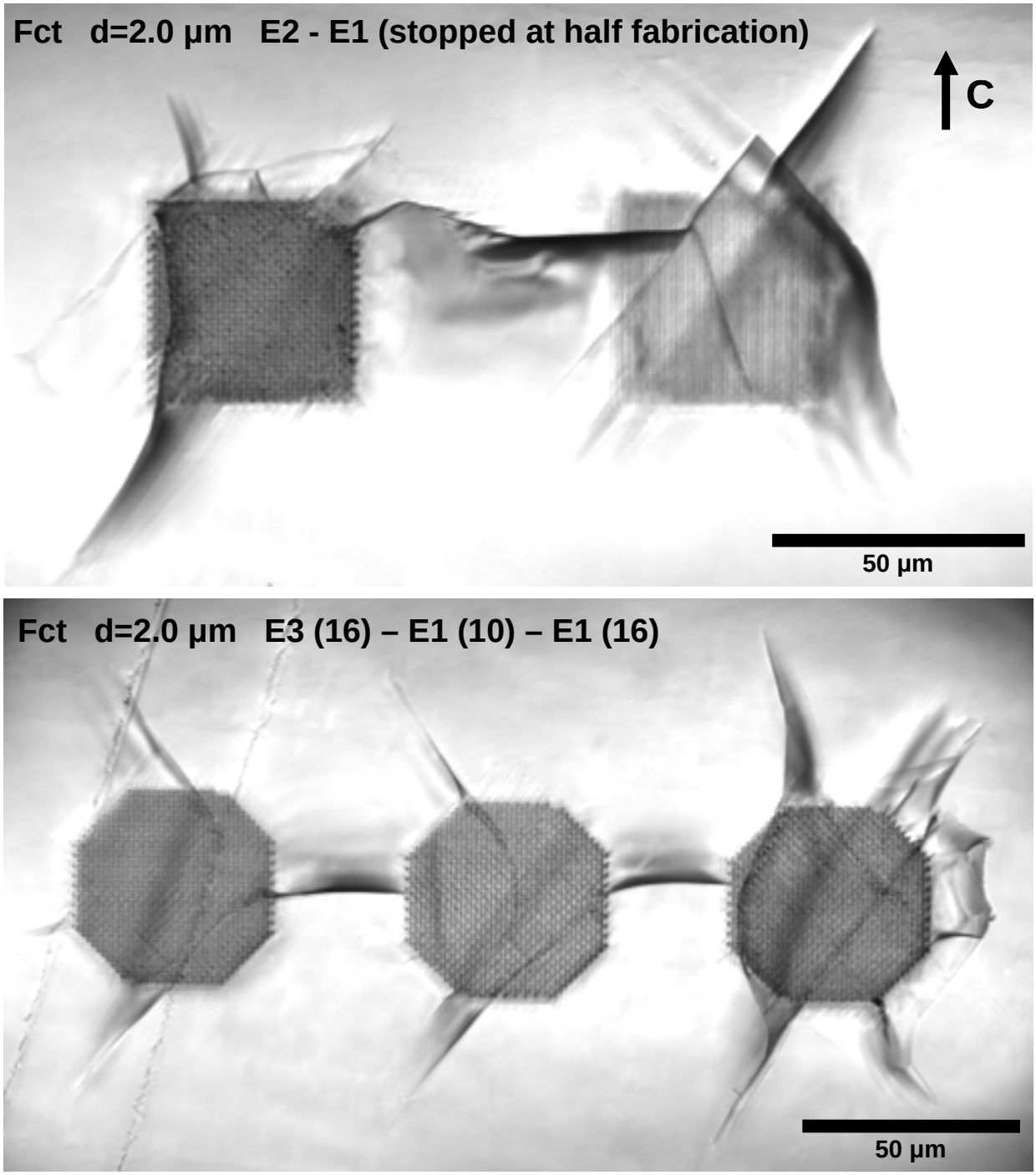

Fig. 6.8. *CLSM images of different fct structures with different layer spacing, number of layers, and laser powers.*

By lowering the power to E2, structures could be successfully fabricated with all its layers (up to the close to surface ones). Crystal break and defect propagation could however never be eluded. To further mitigate this, several structures where also worked out with a hexagonal shape so that

sharp corners where removed. And also the laser power for voxels positioned at the corners was specifically lowered in order to avoid strain accumulation at those positions. By performing these steps, complete structures could be fabricated with high power (E1) laser writing routes, although important breaking was still observed. Finally, only by further lowering of the laser power routes (E3), or by fabricating smaller structures with only 10 layers, these breaking could be reduced (for the case of d=2 μm the typical number of layers -limited by spherical aberration- was set to 16, and thus the structures are 32 μm in depth).

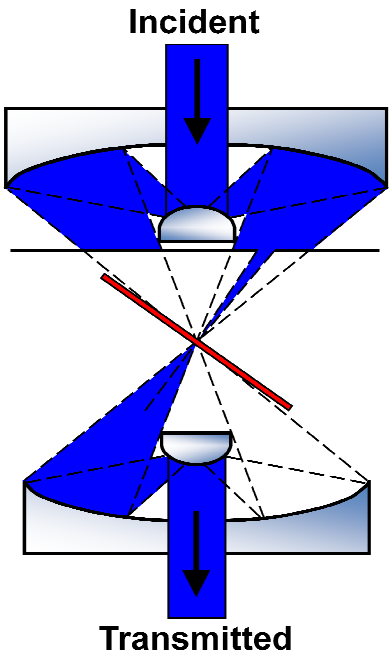

Fig.6.9. *Angle resolved transmission set up used in combination with a Reflechromat microscope objective and pinhole.*

6.3 Optical characterization

To optically characterize the photonic crystals both NIR transmission and luminescence rare earth ions emission spectra were studied. The following sections describe the results.

6.3.1 NIR transmission spectra

The transmission spectra of the fabricated lithium niobate photonic crystals were measured using a Fourier-transform IR spectrometer (Thermo Nicolet) in combination with an IR microscope (Contiuum). In order to focalize light from the whole NIR-IR range into the micrometric structures a Reflechromat objective (32x, NA=0.65) was used (see **Fig. 6.9**). To measure the transmission along the ΓX direction ([001]) a small pinhole was placed in front of the objective so that light was confined to a cone with a reduced half angle of about $\theta \sim 5^{o}$. The sample was tilted to have its normal direction matching the half angle of the microscope objective. The aim of such a tight angular restriction is that of providing the information from a single direction of propagation. Only in the case that the stop gaps were complete its use would not be necessary. Transmission spectra were routinely obtained by normalizing the spectra taken with the focus centred inside the structures to that taken from a point close behind the structures.

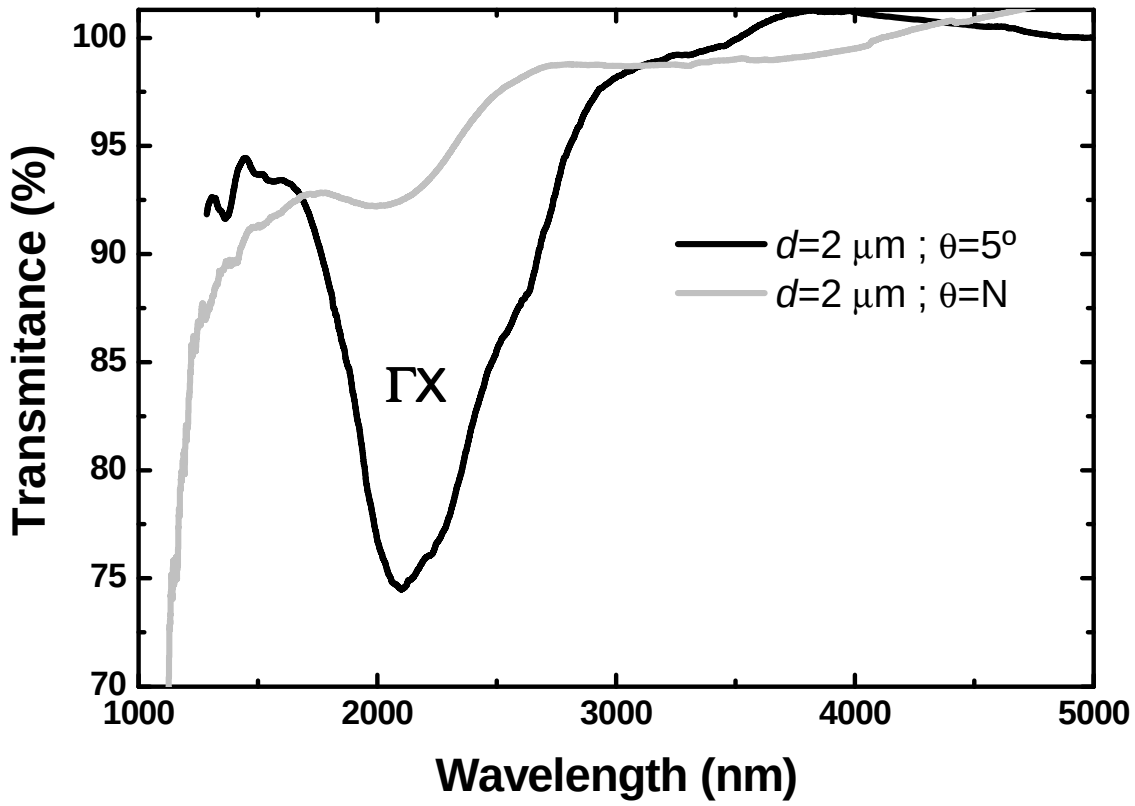

Fig. 6.10. *Example of the transmission spectra of an fct structure when it is measured with and without a pinhole in the set up.*

Figure 6.10 gives an example of one of the measurements performed on an fct structure (with layer spacing d=2 μm) with and without angular restriction (i.e. with and without pinhole). The use of a pinhole to limit the angular range of incident rays is compulsory, as the character of the obtained stop gaps is extremely angle dependant due to the fact that the structures have a very low index contrast and filling fraction, which implies a very weak stop gap generation for only certain specific angles. All transmission spectra were routinely measured with the pinhole restriction of the incoming light, and sample tilt adjusted to match the [001] direction.

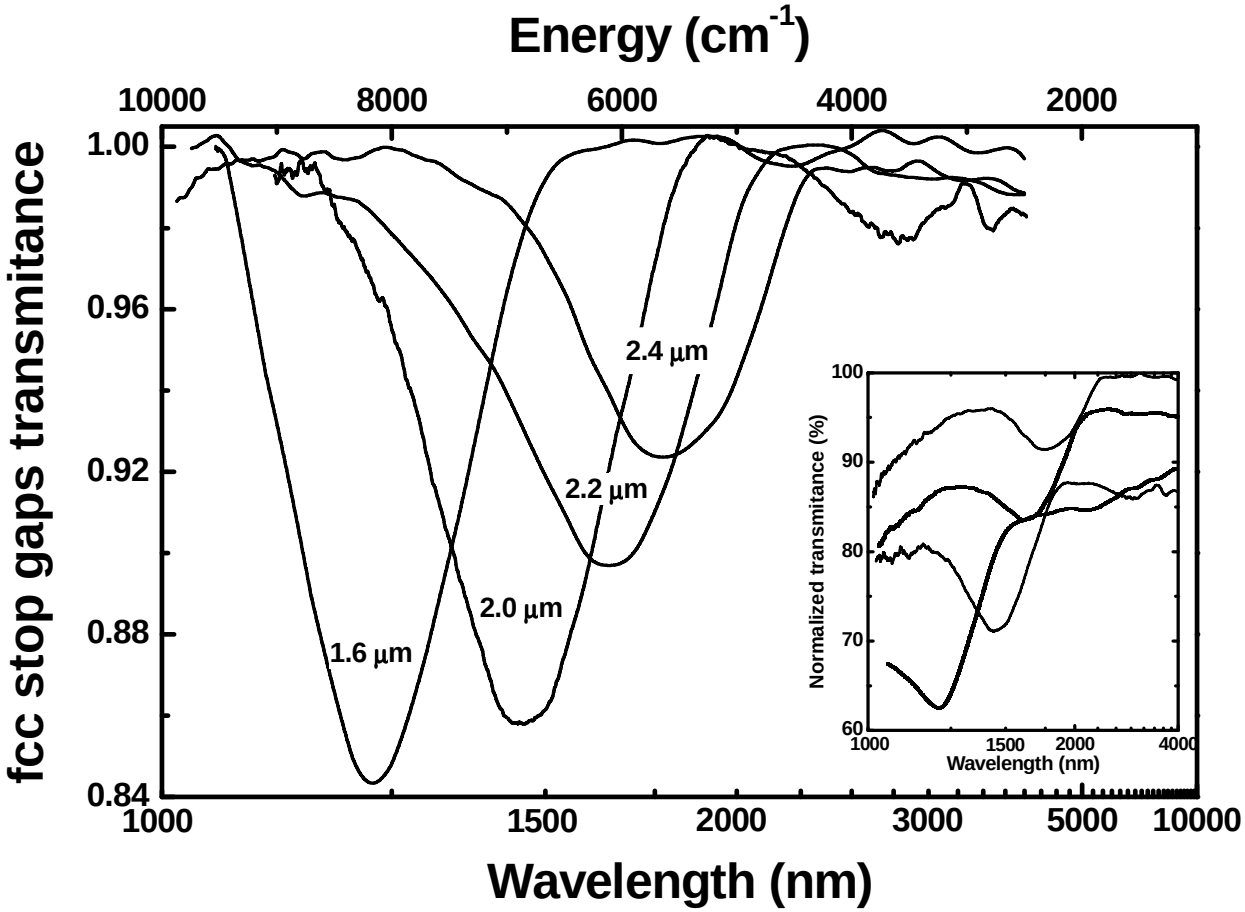

Fig. 6.11. *Normalized transmission spectra of fcc structures with different layer spacing. Inset shows non normalized as-measured spectra including the scattering effects.*

Results for the fcc lattices are first shown. For the fcc structures the minimum layer spacing achievable without excessive breaking of the crystal was found to be of 1.6 μm for our experimental

set up. Thus, **Figure 6.11** shows the transmission spectra for fcc structures with layer spacing ranging from 1.6 μm to 2.4 μm. The spectra are obtained after substracting a scattering baseline, so that both the stop gap position and inhibition rate can be compared.

The inset on **Fig. 6.11** also shows the as-measured spectra without any baseline correction. As it can be seen, the decreasing of layer spacing implies that the stop-gap transmission inhibition blue-shifts, and also becomes more abrupt. The stop-gap inhibition rate increases when reducing the layer spacing due to the fact that the filling ratio of voxels increases; although it is found to saturate for small layer spacings (of around 1.6 μm), probably due to the increment of lattice point defects which would smear the light coherent interference process inside the structure, thus limiting the performance. The dependence of stop gap spectral position with respect to layer spacing can be easily calculated by simple Bragg's Law. Taking into account the ellipsoidal shape of voxels, and its approximate mean size (voxel diameter, $d_{voxel} \approx 1600$nm, and voxel height, $h_{voxel} \approx 500$nm), the filling fraction (*ff*) can be calculated, and from it a measure of the effective refraction index can be obtained.

$$v_{voxel} = \frac{\pi}{6} d_{voxel}^2 \cdot h_{voxel} \approx 0.21 \mu m^3 \tag{6.1}$$

$$v_{d=2\mu m}^{fcc} = \left(2 d_{layer}\right)^3 \approx 64 \mu m^3 \tag{6.2}$$

$$ff_{fcc} = \frac{4 v_{voxel}}{v_{fcc}} \approx 0.0131 \tag{6.3}$$

$$n_{eff} = ff \cdot n_{2.0}^{voxel} + (1 - ff) \cdot n_{2.2}^{LiNbO_3} \approx 2.197 \tag{6.4}$$

From **Equation 6.4**, and taking into account the small value of the filling fraction ($ff \approx 0.0131$), it gets clear that the n_{eff} of our structures is almost independent from the value of the refraction index inside voxels. Thus, the effective refraction index is almost the same to that of the lithium niobate matrix. Even so, the structures indeed show significant stop-gaps (see **Fig. 6.11** and **6.13**). The expected stop-gap spectral position of the different structures can be calculated by Bragg's Law as:

$$\lambda_{gap} = \frac{2 d_{layer} n_{eff}}{m} \tag{6.5}$$

where *m* is the diffraction order.

With this relation, experimental data for the stop-gap centre wavelengths corresponding to different layer spacing structures can be analyzed. **Figure 6.12** shows the corresponding experimental results together with the fitted curve. In this figure, different points for a same layer spacing value indicate the different obtained values for structures fabricated with same layer spacing but with different laser powers or sizes. From the linear fit of all data an order of diffraction *m*=6 is obtained for all the observed fcc structures stop gaps.

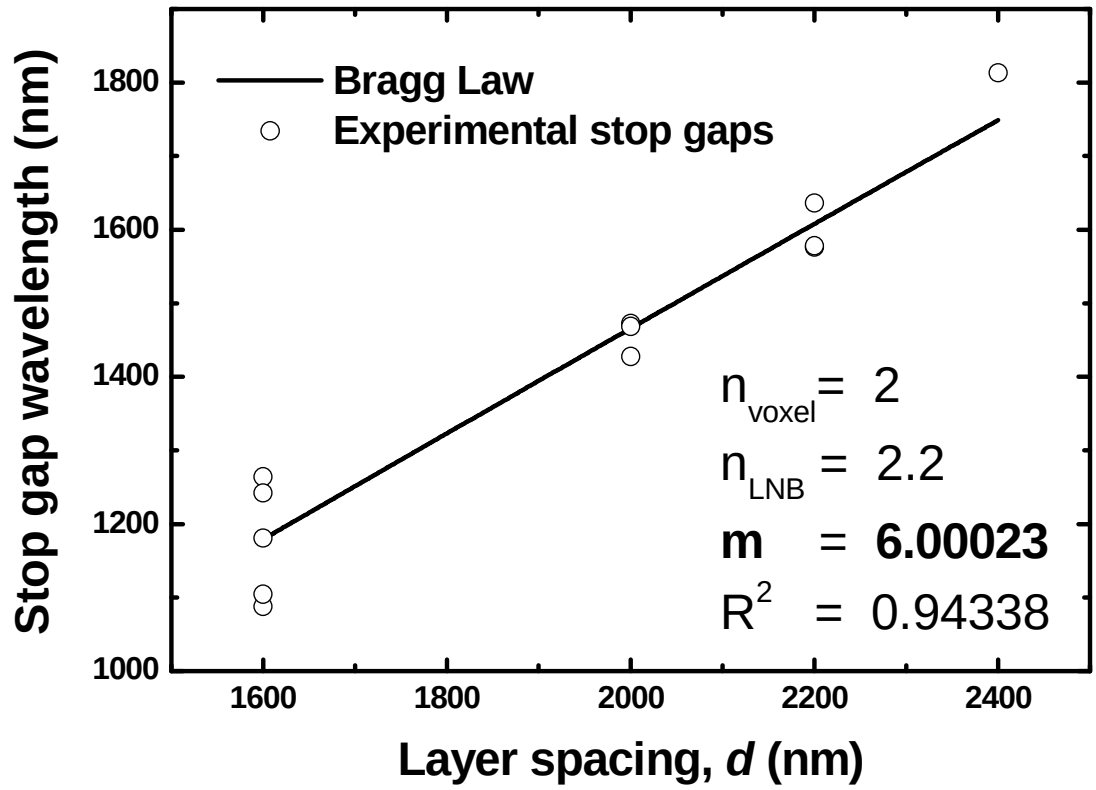

Fig. 6.12. *Linear fit over the experimental stop-gap centre wavelengths of different fcc structures fabricated with a choice of laser powers and lattice parameters. From the fitting, all these fcc stop-gaps can be assigned to a sixth order diffraction gap.*

For fct structures favourable results were more complicated to obtain due to its higher filling fraction, and to the fact that each written voxel involves a strain field to the surrounding lithium niobate lattice. It was found that for the required layer spacings (layer spacings lower than *d*=2 μm) the strong scattering inside the samples disguised the stop gaps. Fct structures were fabricated with layer spacings ranging from 1.2 to 2.0 μm, and neither of them showed measurable stop gaps. Nevertheless, for higher spacing structures, important transmission stop gaps could be measured ranging from λ~2μm to 2.4 μm, which are shown in **Figure 6.13**.

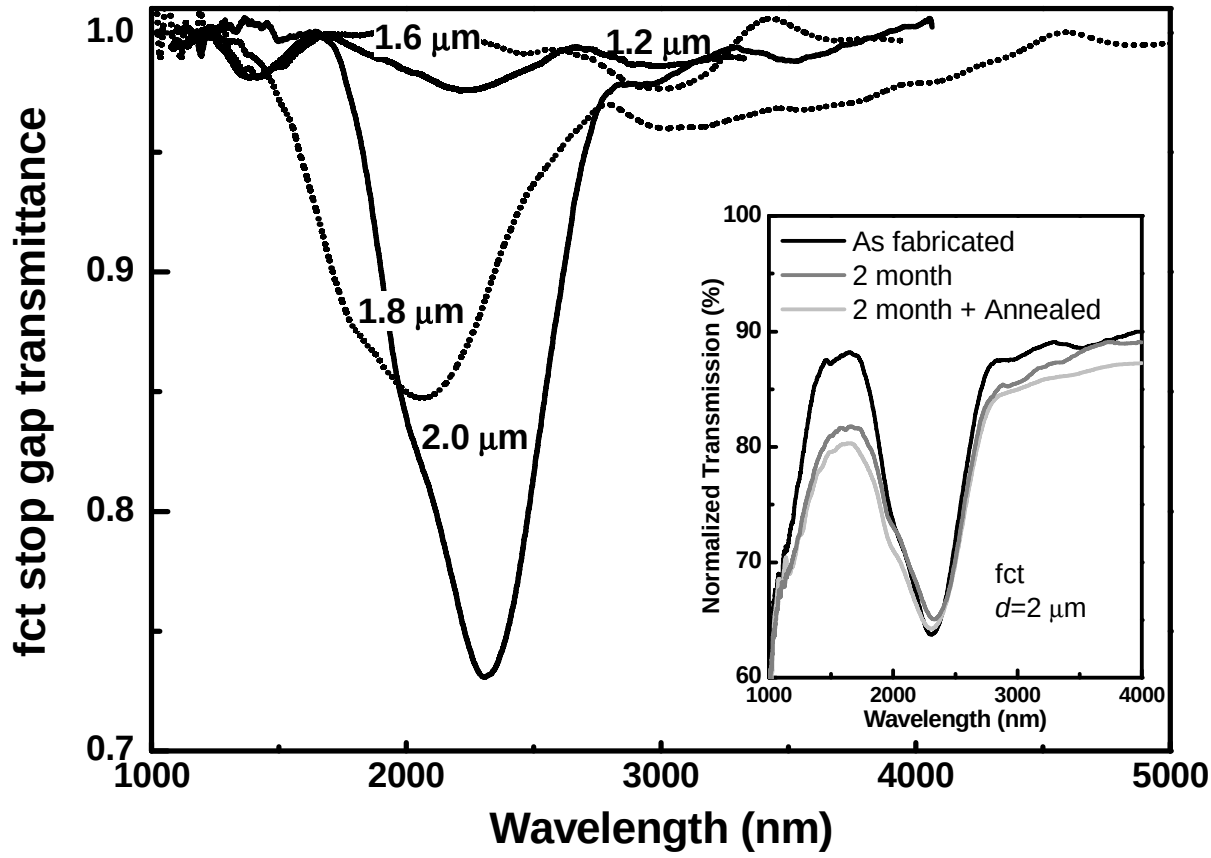

Fig. 6.13. *Measured transmission spectra for different fct fabricated structures. Inset shows transmission spectra of a same structure after thermal annealing and a two month period.*

In conclusion, although tetragonal symmetry lattices have promising properties (see the **Appendix**), when fabricated by the fs laser method in lithium niobate here described (and under our experimental set up), the limited crystal resistance to the induced stress leds to an inability to reach the required filling fractions needed for obtaining stop gaps at telecommunication wavelengths (1.5

μm). However, the obtained stop gaps are seen to be more strong and wide than that of fcc structures. By performing the same Bragg law calculations, these observed stop gaps arising from the tetragonal symmetry can be unequivocally related to 4^{th} order diffraction modes. Indeed, tetragonal structures are theoretically expected to feature stop gaps between the 4^{th} and 5^{th} energy bands [3].

The transmission properties of the structures were also checked after a period of two months following the fabrication, and further annealing processes were also performed to the samples in order to ensure their thermal and mechanical stability. Inset of **Fig. 6.13** shows the spectra of a fct lattice photonic crystal (see its image in **Fig. 6.8**, the top left structure fabricated with an E2 laser power route) immediately after fabrication, after a period of two months, and after a final annealing process at $700^{o}C$ for about 1 hour. The stop gaps were observed to be degraded after the two month period, retaining about an 80% of the original inhibition rate. The annealing process, however, was observed to not affect the transmission properties to any observable extent. From these observations the fabricated photonic crystals can be regarded as durable and resistant structures.

In conclusion, from the tailoring of the different laser fabrication parameters various structures were fabricated featuring significant stop gaps in the near infrared range from 1 μm to 2.4 μm wavelength. These data are summarized in **Figure 6.14**, where the stop-gap centre wavelengths have been plotted as a function of the layer spacing for both the fcc and fct type structures.

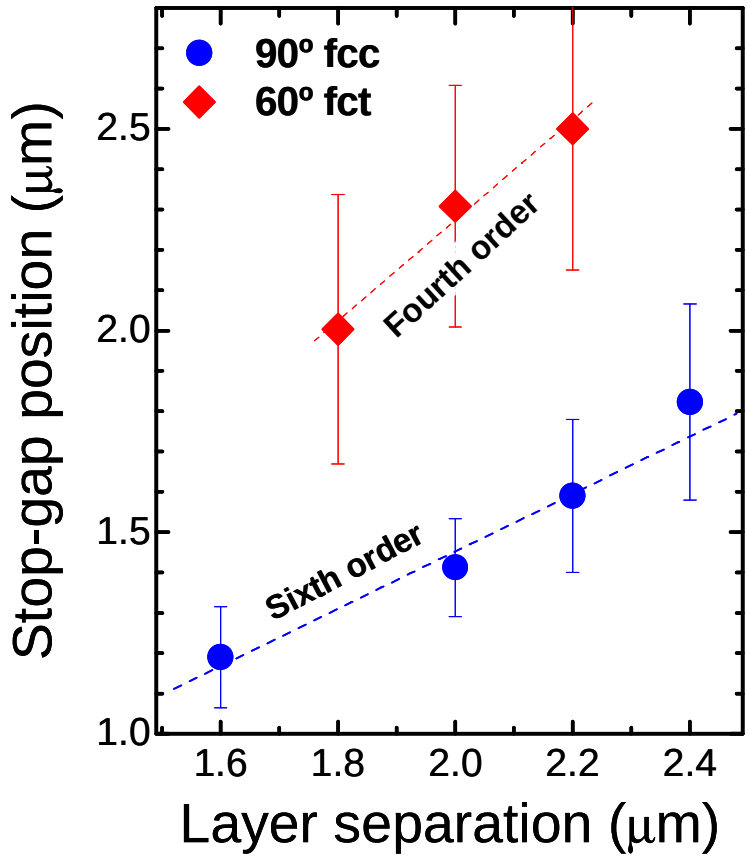

Fig. 6.14. *Variation of the stop-gap centre wavelength as a function of layer spacings for fcc and fct lattices.*

6.3.2 Rare-earth spontaneous emission modification

To assign the degree of modification of the local spontaneous emission (SE) from rare-earth ions inside irradiated material, the local luminescence at the submicron scale was first evaluated, which gives information on the intrinsic emission characteristics of material inside the structures, as a result of the lithium niobate lattice modification. This detailed information was then taken into account in the evaluation of the collective spontaneous emission modification due to photonic stop gap creation.

To evaluate the local luminescent properties inside the 3D structures, high resolution SE imaging experiments were performed by means of a high NA immersion oil microscope objective (Olympus 100X, UPlanSApo, NA 1.4), in combination with a confocal set-up (for more information on the

confocal set-up see **Chapter 5** of this thesis). The purpose of this study is to assign the degree of modification of the characteristic luminescence of rare-earth ions inside the inscribed voxels and at its surroundings.

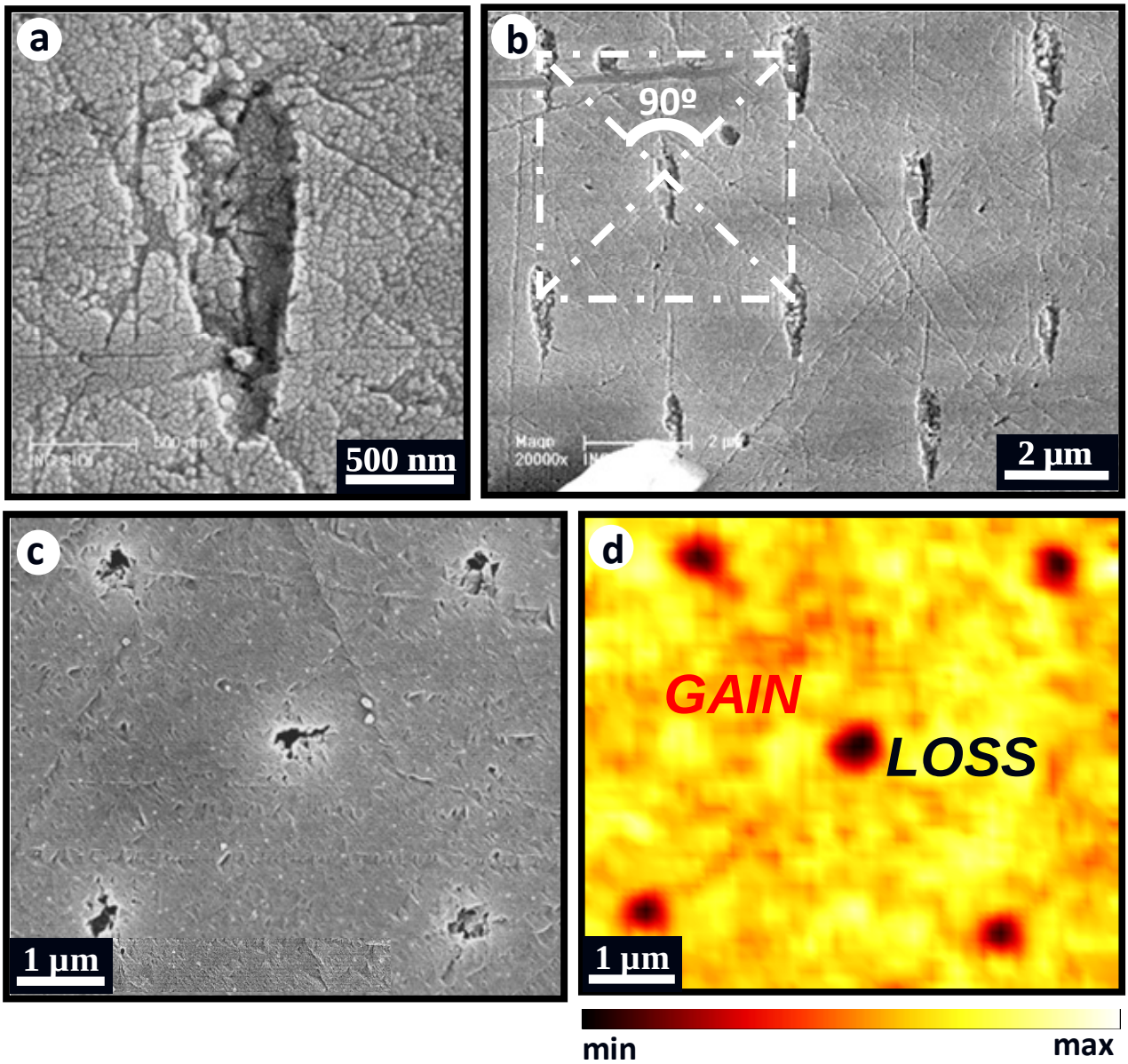

Fig. 6.15 (a)-(c) *SEM images of an fcc structure after the chemical-etching revealing of voxels from the lateral view ((a) and (b) and along the DLW direction (c).* **(d)** *Micro-luminescence intensity spatial distribution of the erbium ions visible emission bands as recorded for the same first layer voxels of (a) but before the polishing and wet etching processes.*

Figure 6.15 (d) shows this luminescence intensity spatial variation of the erbium ions visible emission bands, as recorded from the first photonic crystal layer (closest one to surface) and along

the [001] direction. The main observation in **Fig. 6.15** is that the SE is slightly reduced at voxels sites (~5%), this probably due to the laser induced amorphization process of the lithium niobate lattice. The intensity distribution inside the material perfectly matches the lattice periodicity, as shown for clarity in the SEM image of the revealed patterned area. The fact that the intensity reduction is of only a 5% is related to the fact that amorphized volumes are much smaller than the effective focal volume of the confocal system, which thus collect luminescence from the surrounding volume of crystalline material. Similar SE reductions are also observed for any other of the luminescence bands of the rare-earth ions, both on the visible and NIR ranges. The assumption that the SE intensity is inhibited at voxel positions well agrees with the assumption that tightly localized amorphization of the LN crystalline structure takes place inside voxels, as it has been previously observed in similar experiments on femtosecond DLW of rare-earth doped crystals [4]. **Fig. 6.15** also demonstrates that SE is preserved to a high extent in every region of the 3D photonic lattice. What is more, regions of higher/lower optical gain are expected at the high/low dielectric regions of the structures, respectively. This result provides an important aspect for laser action and light localization studies, as it opens the possibility of 3D tailoring at the sub-micrometer scale the SE properties of widely used solid state laser crystalline materials such as lithium niobate.

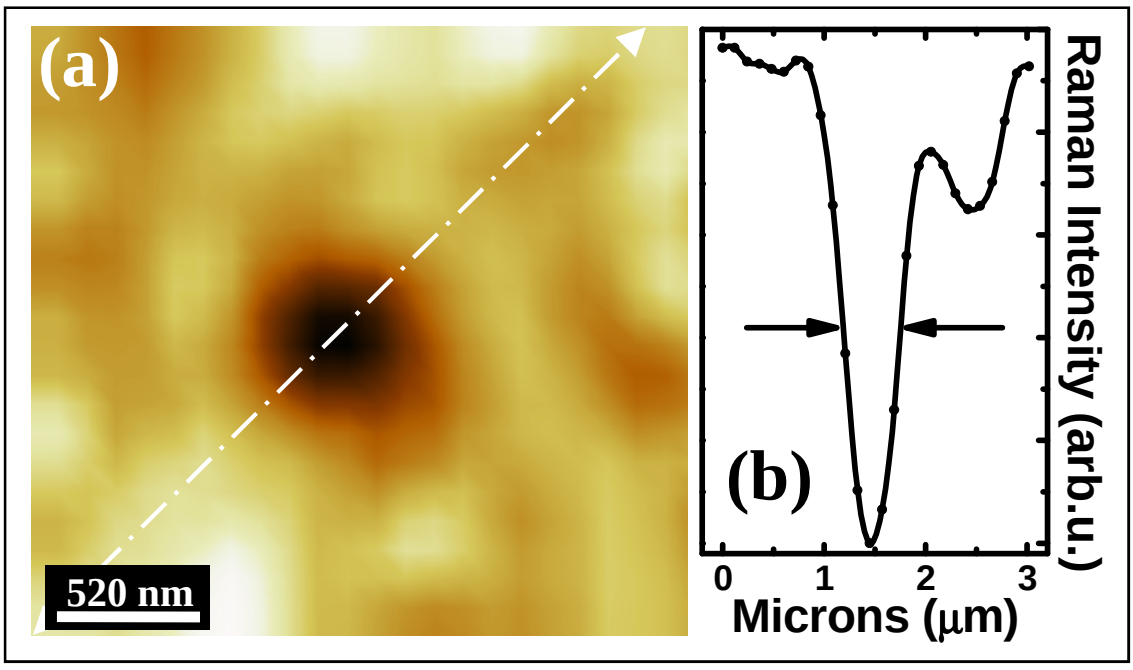

Fig. 6.16. *Raman integrated intensity* **(a)**, *and cross-section* **(b)**, *as measured at voxel position.*

Further proof of the amorphization process can be obtained from micro-Raman analysis. **Figure 6.16 (a)** shows a Raman intensity confocal image of a first layer voxel. Although the confocal optical set up does not completely resolve the details of each voxel, a clear intensity reduction can be observed which corresponds to an inscribed voxel position. This Raman intensity corresponds to the integrated emission of the whole Raman spectra. **Fig. 6.16 (b)** shows the corresponding image cross section (as depicted in **Fig. 6.16(a)**) with a FWHM of 560 nm, limited by the optical resolution of the confocal system.

From this evidence of the amorphous state of material inside voxels, the structures can be assigned to a Cermet-topology[**] fcc lattice of low refraction-index amorphous voxels surrounded by higher-index lithium niobate crystalline material.

Once the details on the local luminescent properties were known, the collective emission arising from inside the photonic band-gap structures could be analyzed. The study of the collective SE (as opposed to the spatially localized) that is generated from inside a luminescent three-dimensional photonic crystal structure is a matter of considerable interest due to the fact that active species inside the structure can preferentially couple to modes that are inaccessible from outside the structure. In fact, measuring the SE from inside photonic crystals has been proven to be a more reliable way of evaluating the existence of stop-bands, rather than plane-wave reflectance or transmission measurements.

The inhibition of SE in 3D photonic stop-band structures is also known to be highly sensitive to diffuse scattering from structural defects near the surface [5]. This effect appears when photons which are scattered to all directions from defects near the surface leave the sample and reach the detector from a direction that other wards would be forbidden by the stop-gap directionality. From these kinds of scattering effects, we can then expect the SE attenuation rate of the structure to be reduced with respect to the measured transmission for external sources.

[**] A *Cermet topology* is that where some of the higher or lower index regions of the lattice consist on isolated regions, in contrast with a *network topology*, where the different regions are all continuously interconnected. See **Appendix** for further details.

To evaluate the possibility of any SE inhibition as a result of stop-band creation inside our photonic crystal structures, the emitted intensity from erbium ions at 1.5 μm wavelength was measured at normal incidence ([001] direction) to the sample's surface, in the same way as for transmission spectra (see previous **Section 6.3.1**). Previously, a transmission attenuation rate at the 1.5 μm wavelength was only found for the fcc structures with layer spacings of 2.0 μm (see **Fig. 6.11**). The attenuation rate was found in that case to be around ~30%, due to both scattering and coherent Bragg diffraction, and ~15% when scattering was roughly subtracted. Due to this low percentage of transmission attenuation, and taking into account that even lower rates are expected for the SE inhibition, a smaller angular detection cone of ~1^o was set for measuring the SE from inside the structures. By decreasing the angular detection cone the transmission effects around the normal direction to surface should be enhanced. In these experiments, the size of the excitation spot was also enlarged (by using low N.A. optics) in order to collect luminescence that is generated from an active volume that covers several constituting layers of the three-dimensional photonic structure.

The evaluate the SE changes, the investigations were performed on structures with only a small difference in the lattice spacing, but fabricated all of them under the same experimental conditions. In this way, it was possible to analyze the SE in structures with a stop-gap overlapping the spectral position of SE band of erbium ions, or rather lying behind it. A representative NIR SE spectra of samples together with the measured transmission spectra for two structures with layer spacings *d*=2.0 μm and 1.6 μm, is shown on **Figure 8.17**, for comparison. This emission spectrum obeys to the 488 nm wavelength excitation ($^4I_{15/2}\rightarrow{}^4F_{7/2}$) or Er^{3+} ions. From the excited $^4F_{7/2}$ level, a fraction of the Er^{3+} ions relaxes non-radiatively to the $^4I_{11/2}$ level, from where either radiative and non-radiative intra-erbium relaxation or energy transfer to the $^2F_{5/2}$ level of Yb^{3+} ions occurs. Thus, the emission spectra in Fig. 8.17 corresponds to both the 1.5 μm ($^4I_{13/2}\rightarrow{}^4I_{15/2}$) emission band of Er^{3+} ions and to the 1.0 μm ($^4I_{11/2}\rightarrow{}^4I_{15/2}$ and $^2F_{5/2}\rightarrow{}^2F_{7/2}$) emission bands of Er^{3+} and Yb^{3+} ions, respectively.

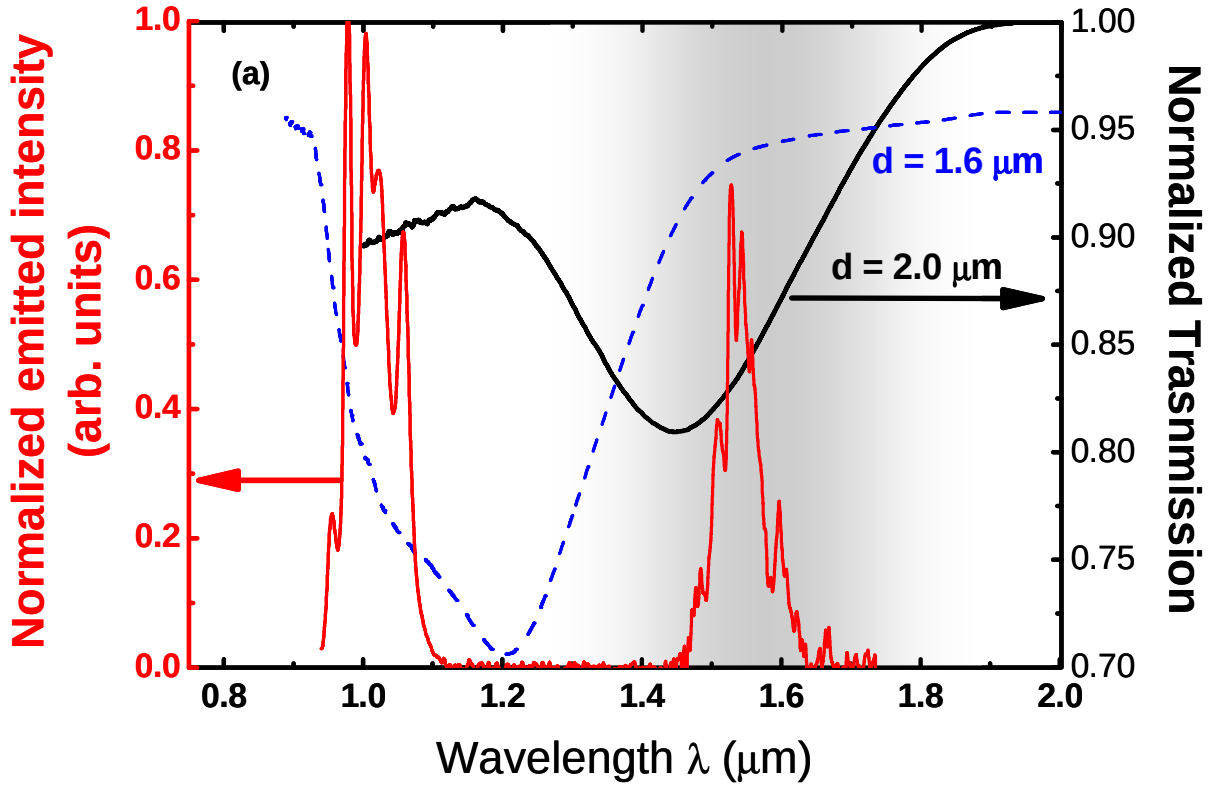

Fig. 6.17. *Typical NIR SE spectra of simples, together with the measured transmission spectra for structures with layer spacings of 2.0 μm and 1.6 μm.*

Comparison between these two structures represents the best possible reference system for quantitative experimental determination of any SE change at 1.5 μm resulting from stop gap creation. As defects and lattice order can vary along the [001] direction, the SE was surveyed while scanning the focal position inside the structures along the [001] direction. The integrated emitted intensity was obtained under constant pump power at 488 nm wavelength from an Ar laser, and compared between the two structures. **Figure 6.18 (a)**, **(b)** and **(c)** show the angle-resolved luminescence set up used for the SE measurements, the in-depth dependence of the 1.5 μm emission band integrated intensity of erbium ions for the two similar structures, and the SE ratio between both structures, respectively.

It is important to mention that the respective filling fractions of these two structures are *ff*≈0.01 and ≈0.02, for *d*=2.0 μm and 1.6 μm, respectively. Due to this very low filling fractions, the pump power distribution inside structures is expected to be almost equal, whereas for the *d*=1.6 μm (with higher *ff*) a slight pump power reduction with respect to the *d*=2.0 μm could be expected due to

scattering. For the collected emission comparison from each structure, this difference in the *ff* has to be also taken into account, as each voxel volume is known to emit approximately a 5% less (see **Fig. 6.15**). However, this effect only gives a negligible contribution (~0.0005) to the emitted intensity difference between both structures.

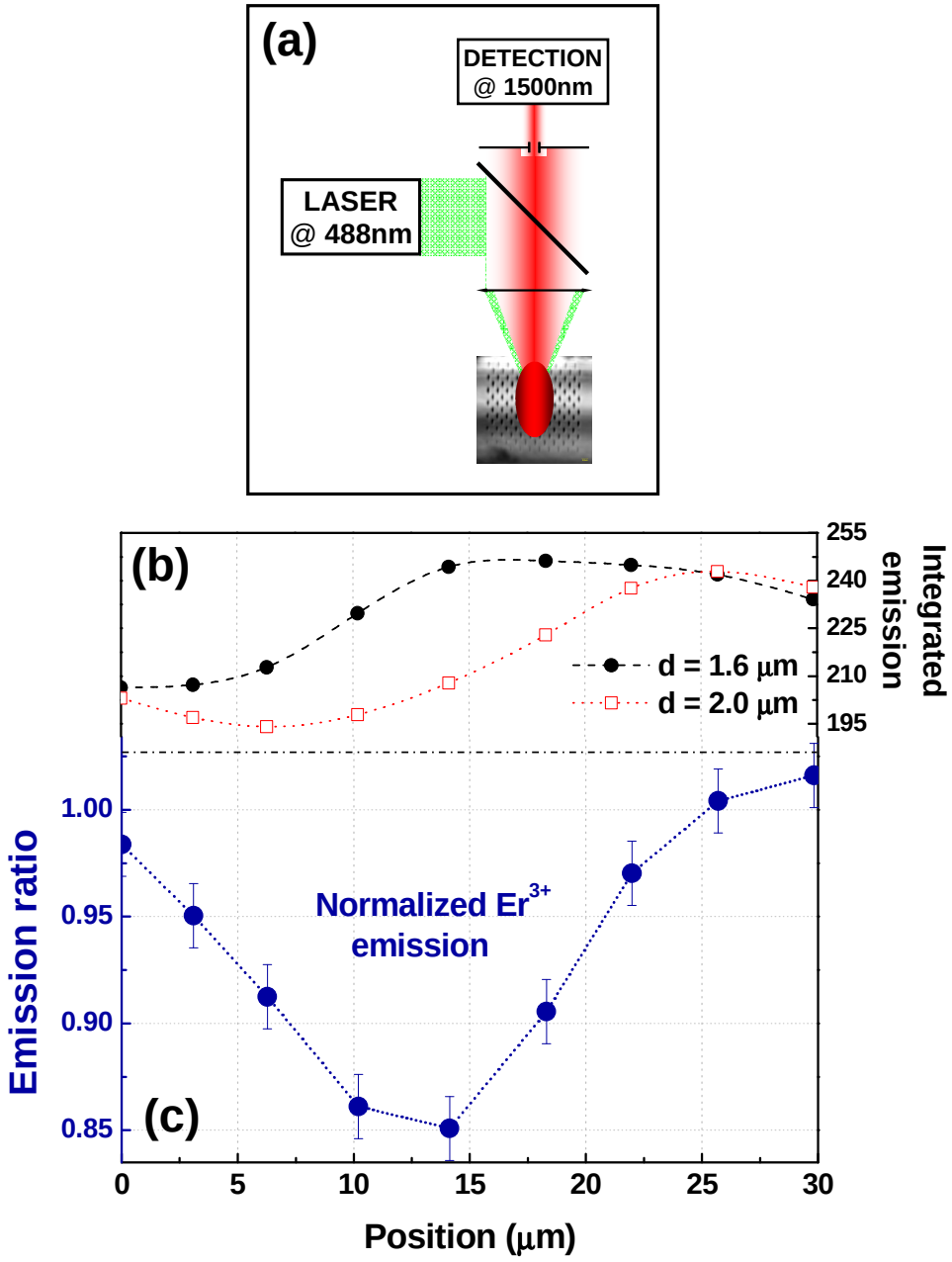

Figure 6.18. (a) *Schematic diagram of the angle-resolved luminescence set up.* **(b)** *In depth dependence of the 1.5 µm wavelength emission band of Er^{3+} ions for both structures with layer spacings of 2.0 µm and 1.6 µm.* **(c)** *SE ratio between both curves. Values below 1 indicate SE suppression inside the structure with layer spacing of 2.0 µm.*

In **Fig. 6.18 (c)** values below 1 represent suppression at the 1.5 μm spectral region inside the structure with a stop-gap matching the spectral range. From these observations it can be concluded that directional SE inhibition has been clearly induced due to stop gap creation. This observed inhibition accounts only for the [001] direction inside the structures, and cannot be expected for transversal directions where the structure topology is different. In fact, the observed 15% reduction would probably completely vanish if the total fluorescence over all directions was measured. Furthermore, as these photonic crystals only exhibit a very small refraction-index contrast, the inhibition effect can only be regarded as a Bragg reflection due to stop gap transmission attenuation, and not to a strict inhibition of the local density of states (LDOS). This implies that the observed SE inhibition does not correspond, as far as our experiments can demonstrate, to any reduction in the LDOS inside the photonic crystal. To evaluate this possibility further SE decay measurements should be performed which were not possible under the angular restrictions which we needed to impose.

6.4 Chapter conclusions

The direct laser microfabrication of three-dimensional photonic crystals in Er^{3+}:Yb^{3+} codoped MgO:$LiNbO_3$ crystals, in absence of any post fabrication step, is demonstrated. From the tailoring of laser fabrication parameters, different structures can be fabricated featuring significant stop gaps in the near infrared range from 1 μm to 2.4 μm wavelength.

The collected spontaneous emission from Er^{3+} ions in an fcc structure featuring a stop gap matching the emission wavelength (1.5 μm) is modified by a ~15% when compared to that of a reference structure featuring a stop gap at a slightly lower wavelength (1.2 μm). This modification is due to the change in the collected emission due to internal Bragg scattering in the structure. These measurements have not hitherto been reported, and constitute the first experimental demonstration of modified spontaneous emission from a three-dimensional active lithium niobate photonic crystal at the telecommunication wavelength of 1.5 μm.

References

[1] M. Maldovan, and E. L. Thomas, *Diamond-structure photonic crystals*, Nat. Mater. **3**, 593 (2004)

[2] G. Zhou, M. J. Ventura, M. R.Vanner, and M. Gu, *Use of ultrafast-laser-driven microexplosion for fabricating three-dimensional void-based diamond-lattice photonic crystals in a solid polymer material*, Opt. Lett. **29**, 19 (2004)

[3] O. Toader, M. Berciu, S. John, *Photonic Band Gaps Based on Tetragonal Lattices of Slatend Pores*, Phys. Rev. Lett. **90**, 23 (2003)

[4] A. Ródenas, D. Jaque, G. A. Torchia, C. Mendez, I. Arias, L. Roso, P. Moreno, and F. Agulló-Rueda, *Femtosecond laser induced micromodifications in Nd:SBN crystals: Amorphization and luminescence inhibition*, J. Appl. Phys. **100**, 113517 (2006)

[5] M. Megens, J. E. G. J. Wijnhoven, A. Lagendijk, and W. L. Vos, *Light sources inside photonic crystals*, J. Opt. Soc. Am. B **16**, 9, 1403-1408 (1999)

Chapter 7

Conclusions

- It has been demonstrated the possibility of micro-fabricating surface relief structures in $LiNbO_3$ crystals with features down to 80 nm width for the first time. The ablation rate curves have been characterized for both low-NA and high-NA optics, finding almost no difference in the ablation rates between rare-earth doped or undoped samples.

- Non-collinear laser propagation and laser gain in microstructured Nd^{3+}:MgO:$LiNbO_3$ samples has been demonstrated. A comparative study of the diffraction efficiency of one-dimensional (1D) and two-dimensional (2D) surface diffraction gratings has been presented. The laser efficiency was found to be not significantly altered from the introduction of the gratings when laser oscillation was produced. However, due to non-collinear propagating components of both pump and fundamental laser radiation losses are introduced, and an increasing of the laser thresholds depending on the diffraction efficiency of each grating.

- The main luminescence change and lattice distortions in buried waveguides fabricated with low- and high-repetition rate lasers has been characterized. The origin of the refractive-index increments responsible for guiding have been identified to be the piezo-optic effect resulting from the pressure shock waves originated at the laser focal regions. In the case of low-

repetition rate guiding in both TE and TM polarizations cannot be explained by the piezo-optic effect alone which arises from the observed biaxial stress field, and it is hypothesised that the electro-optic effect due to space charge fields induced at the ionization process could be the origin of the guiding for TE polarization. In the case of high-repetition rate guiding is observed only for TE polarization, which is well explained by the piezo-optic effect alone resulting from a uniaxial tensile stress.

- The three-dimensional (3) inscription of amorphous low-index sub-micrometer voxels inside Er^{3+}:Yb^{3+} doped $LiNbO_3$ has been investigated for the first time. Both the induced aberration due to birefringence and spherical aberration have been characterized. From this knowledge the direct laser microfabrication of 3D photonic crystals has been presented. By tailoring the lattice parameters significant stop gaps have been achieved in the near infrared range from 1 µm to 2.4 µm wavelengths.

- It has been demonstrated for the first time the possibility of modifying the spontaneous emission from Er^{3+} ions in a 3D fcc photonic crystal featuring a 6^{th} order stop gap at 1.5 µm wavelength. The modification consists on a 15% reduction in the collected emission due to the internal Bragg scattering of the photonic crystal structure.

Conclusiones

- Se ha demostrado por vez primera la posibilidad de realizar estrcturas superficiales en $LiNbO_3$ por debajo de los 100 nm de resolución. Para ello se han caracterizado las curvas de ablación mediante optica de baja y alta aperture numérica. No se han encontrado diferencias significativas entre el procesado de muestras dopadas con iones de tierras raras y muestras congruentes sin dopar.

- Se ha demostrado la posibilidad de inducir ganancia láser y la propagación no-colinear de la radiación fundamental en muestras de Nd^{3+}:MgO:$LiNbO_3$ microestructuradas. Para ello se ha llevado a cabo un estudio comparativo sobre la eficiencia de difracción de redes de superficiales uni-dimensionales y bi-dimensionales. Se ha mostrado que la eficiencia láser en cavidad no se ve modificada significativamente por la introducción de las redes de difracción, mientras que las pérdidas introducidas por la propagación no-colinear de los haces de bombeo y fundamental varía en función de la eficiencia difractiva de cada tipo de red.

- Se han caracterizado mediante técnicas de micro-espectroscopía óptica los cambios inducidos en la red de $LiNbO_3$ en guías de onda fabricadas mediante láseres de alta y baja repetición. Se ha identificado el orígen de los cambios de índice como un efecto dominante de tipo piezo-óptico, que resulta de la deformación de la red debido a la propagación de ondas de presión inducidas durante el proceso de excitación e ionización del material en el foco láser. En el caso de guías de onda fabricadas en el régimen no-térmico se ha observado guiado óptico para ambas polarizaciones TE y TM. El guiado en polarización TM puede ser explicado mediante un efecto de stress biaxial, mientras que el guiado TE no se explica mediante este efecto, pero se propone el efecto electro-óptico debido a la separación de cargas durante el proceso de excitación laser como explicación. Para el caso de guías de onda escritas en regimen térmico, se

observa guiado solo en polarización TE que puede ser explicado mediante un campo uniaxial de stress y debido al efecto piezo-óptico.

- Se ha investigado la creación de estructuras tri-dimensionales (3D) en el interior de cristales de Er^{3+}:Yb^{3+}:$LiNbO_3$. Las estructuras están compuestas por voxels sub-micrométricos con una estructura amorfa e índice de refracción inferior al del material en fase cristalina. Se han caracterizado dos tipos de aberración óptica que tienen lugar en este proceso: la aberración esférica y la aberración de tipo birefringente. A partir de esto se ha llevado a cabo la fabricación de cristales fotónicos 3D con diferentes estructuras de red y diferentes tamaños de red, que han mostrado bandas de menor transmitancia en el rango del infrarojo cercano entre 1 µm y 2.4 µm de longitud de onda.

- Se ha demostrado por vez primera la posibilidad de modificar la emisión espontanea mediante la incorporación de cristales fotónicos 3D con bandas de menor transmitancia en el canal de emisión de los iones de Er^{3+}. Estas estructuras presentan un bandgap de sexto orden que posibilita así la inhibición de la propagación en determinadas direcciones espaciales a la longitud de onda de 1.5 µm. La reducción obtenida es del orden del 15%, y es debida a la dispersion interna de tipo Bragg en las estructuras 3D.

Appendix

Introduction to Photonic Crystals

"If a three-dimensionally periodic dielectric structure has an electromagnetic band gap which overlaps the electronic band edge, then spontaneous emission can be rigorously forbidden"

Eli Yablonovitch, December 1986

"A strong Anderson localization of photons in carefully prepared disordered dielectric superlattices […] a frequency pseudogap of localized states arising from remnant geometric Bragg resonances"

Sajeev John, March 1987

A *Photonic Crystal*, also referred to as photonic band gap material, is a superlattice in which the dielectric function is spatially modulated on a length scale comparable to the wavelength of light ($0.1 \leq a/\lambda \leq 5$, where a is the lattice constant. See **Figure 1**)[*]. As it will be explained along this appendix, photonic crystals will serve us to overcome some of the inherent limitations in controlling light of conventional materials, e.g. manipulating and guiding light at the submicron scale, focusing it beyond the diffraction limit or dispersing it about 500 times stronger than in a normal prism; eliminating important radiant loses in thermovoltaic devices; or for instance, generating the so

[*] Some interesting discussion over the history, use and misuse of the term "*photonic crystal*" within the optical community can be found in the OSA OPN issue of March 2007, page 12, entitled *Photonic Crystals: What's in the name?*, by the progenitor of the term, Eli Yablonovitch.

called ‘slow photons’ and thus enhancing the efficiency and control over the different light-matter nonlinear interaction processes.

In analogy to the periodic potential for an electron in solid media, the optical properties of a photonic band gap material are determined by its spatially varying dielectric function. And it is due to this modulation in the dielectric function that the material will exhibit a strong interaction with the light which traverses it, generating a certain number of frequency ranges and directions for which the light propagation will be forbidden, or strongly altered in very different manners. This interaction can be understood by the unique optical dispersion properties of this new class of artificial materials, which in turn are defined by the specific dielectric spatial modulations.

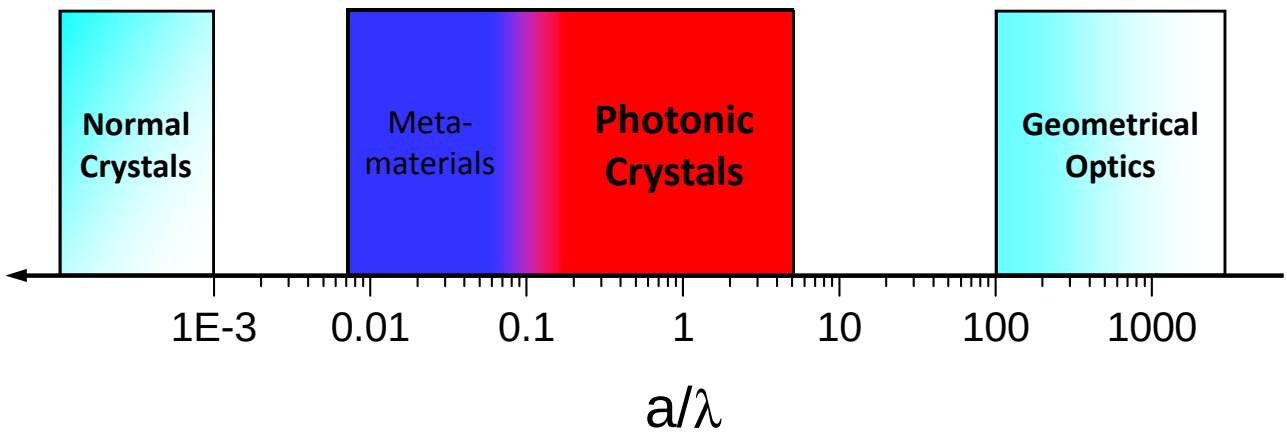

Fig. 1. *Scheme of different periodically ordered materials as a function of the relative lattice spacing with respect to optical wavelength of use.*

The aim of this appendix is to provide the background information for **Chapter 6** of this thesis, which is about the direct laser microfabrication of photonic crystals in lithium niobate laser crystals. The section gives a quick overview over the photonic crystal properties and microfabrication issues which will also serve to any interested reader who is not yet familiar with these concepts. A special effort has been done for briefly summarizing the different kinds of photonic crystal lattices and fabrication methods which have been developed up to date. Extensive scientific source bibliography is included up until the first months of the year 2009.

The appendix is organized as follows: First, a brief explanation of the concept of photonic band gap and its implications over light sources is given (see sections 1 and 2). Second, the main parameters which describe a photonic band-gap material and the different types of lattices and fabrication methods are given (sections 3, 4 and 5). Third, some further discussion over the specific dispersion properties of photonic crystals and their applications is also given (sections 6 and 7).

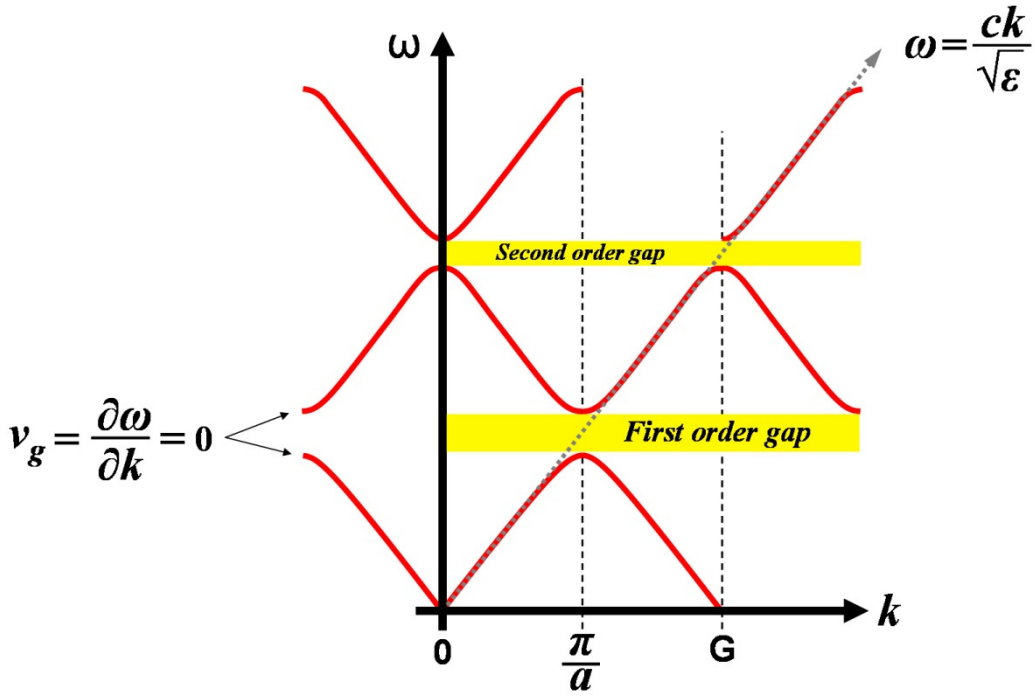

Fig. 1: *Scheme of photonic energy bands and Brillouin zones in a periodic band gap lattice*

1. Energy band gaps for light

The light that enters a photonic crystal will be scattered at the different dielectric regions. Ideally, a constructive interference condition will be met when the path difference between reflections from the lattice planes equals an integer times the wavelength of light, like in Bragg diffraction for X-rays [1]. For photonic crystals, the light wavelength over which a stop gap will be centred can be calculated according to:

$$m \cdot \lambda_{Bragg} = 2 \cdot n_{eff} \cdot a \cdot \cos\theta \quad (1)$$

where m is the order of the gap, a the layer spacing for the given direction, n_{eff} the average refractive index of the structure, and ϑ the angle of incident light with respect to the normal to lattice planes [2]. Although in this condition the order m represents only integer values, forbidden modes can also arise resulting in minor gaps of orders m-1/2 [3, 4].

As a rule of thumb, a stop gap gets broader as the difference between refractive indexes of the lattice increases. This can be easily understood by taking into account that the Bragg condition is actually met when the wave vector $k=2\pi/\lambda$ approaches $m\pi/a$ at the Brillouin zone border (see **Figure 2**). At these wavelengths the dispersion relation splits into two branches between which no solutions for propagation modes exist, and therefore a stop gap appears. These two counterpropagating waves are the only compatible modes with the symmetry of the lattice (at first order), and they will be concentrated at the high and low index material for the higher and lower light wavelengths, respectively. Therefore, as the refractive index contrast increases, the width of the stop gap $\Delta\omega_{gap}$ will increase.

A more strict explanation of stop gaps can also be obtained by recalling Bloch's theorem [5, 6], which states that the solutions to the Schrödinger equation for a periodic potential must consist on the product of a plane wave and a periodic function which has the period of the lattice. The solutions (or eigenfunctions) will actually have to satisfy a Hermitian eigenproblem. This implying that they must be orthogonal to each other; and moreover, that they will have to be concentrated on the different dielectric regions, thus having different frequencies. Any mode whose frequency lies between these two bands will then be forbidden, and the density of states (DOS) inside the gap will be said to be suppressed. Very interestingly, at the boundaries of the Brillouin zones these two modes will necessarily have zero group velocity; a condition which will be of paramount importance for enhancing nonlinear light-matter interaction phenomena.

There exists a certain ambiguity over the terms *photonic band gap* or *stop gap*. In general, whenever a gap arises only for certain lattice directions it is referred to as a *pseudogap*, indicating

the fact that a complete inhibition of light propagation will not be achieved only by its means (photons from inside the photonic crystal will be able to *"escape"* along any other propagation direction than that of the pseudogap). Conversely, if the gap opens for all directions and polarizations then it is called a *complete photonic band gap* (cPBG). The early history of photonic crystal research was about demonstrating that such an electromagnetic confining material was not a chimera, and then demonstrating it for optical frequencies. That scientific breakthrough took about 9 years of intense theoretical and experimental work to be first achieved (from its first concept postulation in 1987, to its first proof at optical wavelengths in 1996). However, even then the obtained structures presented some unavoidable fabrication defects that impeded the gaps from being strictly complete [7]. This fact demonstrates the extreme difficulty that such a precise microfabrication process was requiring. Fortunately, nowadays most of the potential applications of photonic crystal structures do not require a cPBG at all, but just a pseudogap working for a certain set of directions, and this relaxes to a very high extent the fabrication requirements.

An important parameter in photonic crystals is the so called *photonic strength*, *S*, which gives a measure of the interaction strength of photonic crystals with light [8, 9]. The photonic strength can be calculated experimentally by (see **Fig. 3**):

$$S = \frac{\Delta\omega_{gap}}{\omega_{gap}} \tag{2}$$

From the photonic strength a Bragg attenuation length L_B can be derived, which gives a measure of the distance travelled by light before decaying 1/e at λ_{gap} [8, 9]. The Bragg attenuation length L_B is equal to:

$$L_B = \frac{\lambda_{gap}}{\pi S} \tag{3}$$

In practice, the photonic strength has to be measured by the relative stop bandwidth in complete absence of disorder broadening, a condition which is difficult to reach under our direct

laser fabrication conditions. Thus, apart from simulated values, care must be taken before considering these parameters in our present fabricated structures.

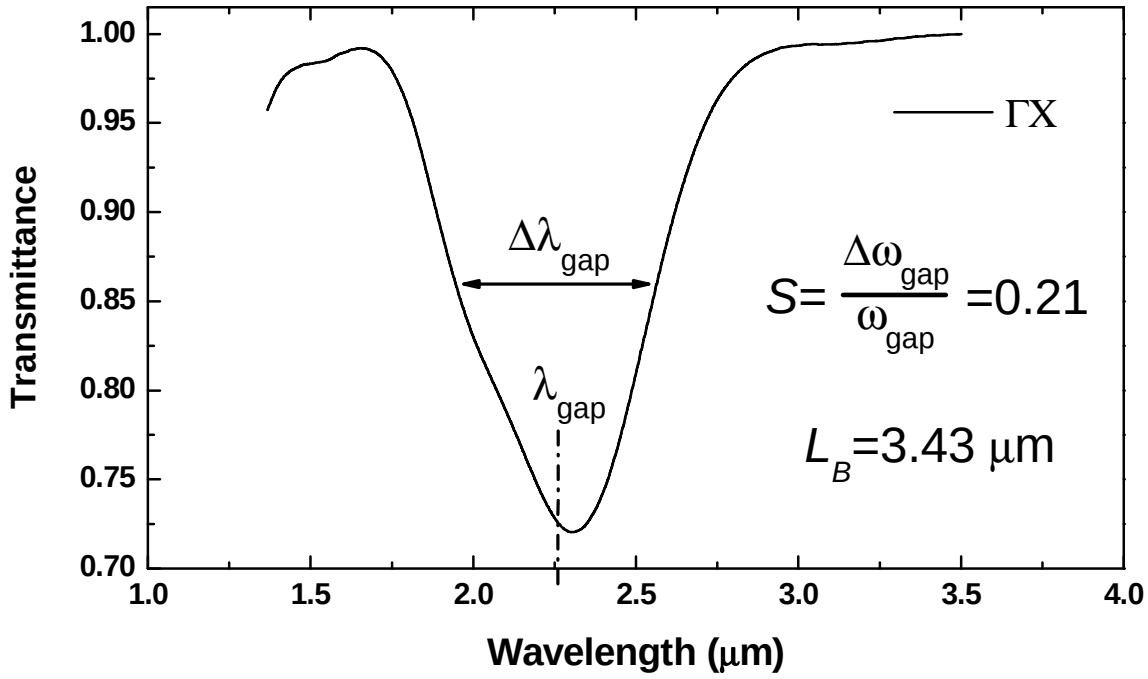

Fig. 2: *Example of a ΓX experimental transmission stop gap of a 3D face centred tetragonal lithium niobate photonic crystal.*

2. Light sources inside photonic crystals

The true significance of a cPBG can only be realized if one thinks of a light source inside the photonic structure. This was the idea inspiring the concept of photonic crystals in the original work of Eli Yablonovitch from 1987 [10]: "*If a three-dimensionally periodic dielectric structure has an electromagnetic band gap which overlaps the electronic band edge, then spontaneous emission can be rigorously forbidden*". And also simultaneously, a pioneering of Sajeev John was reflecting on a similar idea, but further taking into account the key concepts of disorder and light localization: a "*strong Anderson localization of photons in carefully prepared disordered dielectric superlattices*" was described, and a "*frequency pseudogap of localized states*" was expected to appear, as a result of "*remnant geometric Bragg resonances*" [11]. Since then, light localization (linked to the concepts

of cPBG ordered and disordered structures) has been a constant driving force in the development of photonic crystals. Still today, more than two decades later, most of the envisaged quantum devices continue being a daydream for scientists and optical engineers.

A detailed description of spontaneous emission phenomena inside photonic crystals completely exceeds the scope of this introduction [12, 13]. Thus, we will only summarize here some of the important effects that can be expected to happen in an optically active cPBG material. As previously mentioned, in such a system photons can be localized through a combination of the interference phenomena brought by the spatially periodic dielectric distribution (Bragg scattering) in one side, and by the local resonances of the individual scattering elements (Mie scattering) on the other. If an impurity or lattice defect is adequately introduced within the cPBG structure, a spatially localized EM state will be generated [10-11, 14-18]. The localized state must obviously be in the energy gap where no extended states (propagating modes) exist, that is, its frequency must not coincide with that of any Bloch mode so that its localized wavefunction does not mix with any of the extended Bloch wavefunctions.

From perturbation theory, the first order solution to a perturbation coupling with the states of a continuum spectrum gives the Fermi's Golden Rule [19]. With this result, considering the interaction between the atom and the electromagnetic field as a perturbation and assuming a dominant dipole interaction, the spontaneous emission rate of an atom inside the PBG media can be derived. The result is given by [13, 20]:

$$W_{i\to f} = \frac{\pi\omega_{i,f}}{\hbar\varepsilon(\vec{r})}\left|\langle f|\hat{\mu}|i\rangle\right|^2 \rho(\omega_i, f, \vec{r}) \tag{4}$$

with $\omega_{i,f}$ the transition frequency of the gap between the initial and final states, $\varepsilon(\vec{r})$ the spatially dependent dielectric function of the lattice, $\rho(\omega_i, f, \vec{r})$ the spatial and spectral dependent local photonic density of states (DOS), $|i\rangle$ and $|f\rangle$ the initial and final states electronic wave functions of the atom, and $\hat{\mu}$ the dipole operator. This result (**Eq. 4**) tells us that the radiative decay rate of the atom should be just the product of two terms: the dipole's intrinsic decay probability

(determined by the electronic wavefunctions of the atom), and the local DOS (which determines the available photonic states per unit volume for the atoms to decay into). As a result, depending on the lattice host (i.e. on the PBG structure) it should be possible that the dipole radiates at different rates. Or in other words, the lifetime of the atom is not a property of itself, but rather of its coupling to the radiation field. A complete control of the structure around the atom would then lead to the spatial and spectral control of the spontaneous emission from inside the photonic crystal, provided we are able to perform such a microscopic engineering task.

The spontaneous emission from inside a photonic crystal can then differ from that in a conventional laser. The fundamental difference here arises from the fact that spontaneous emission from the atoms or molecules present in the cavity could be completely inhibited, while the emission efficiency in a direction where optical modes were allowed to exist could be enhanced[†] [21-31]. It is convenient to recall here that the process of spontaneous emission is a quantum mechanical phenomenon which occurs even for an excited atom in vacuum[‡]. So only in the ideal situation that the DOS is suppressed (i.e. like inside a strong cPBG), vacuum fluctuations would be then suppressed too, and thus the atom would have to remain in its excited state with the emitted photon forming a bound state to the *dressed* atom [34]. These strong light-matter interactions are expected to have deep implications for laser and luminescence activity if implemented in an optically active solid state medium, such as a laser crystal or a semiconductor. It is believed that if such a coherent light localization [34-38] can be tailored, a new range of devices and quantum optical devices would be possible, such as integrated optical 3D circuits [39, 40] or highly efficient engineered micro-laser systems [41]. An important throwback appears however from the fact that disorder and multiple scattering effects are always present in real fabricated structures. The role of disorder in the light diffusion and extinction process in multiple-scattering media is relevant to the extent that effects such as the light localization and lasing activity can occur to change dramatically.

[†] This enhancement of spontaneous emission while the relaxation time is reduced was actually already intuited in 1946, by Nobel laureate E. M. Purcell, for nuclear magnetic moment transitions at radio frequencies [32], and the effect of controlling the spontaneous emission by tailoring the local DOS is therefore now frequently named as the *Purcell effect*.

[‡] The vacuum electromagnetic fluctuations are said to be the origin for the spontaneous deexcitation of the atom and the emission process [33]. Although in an EM vacuum there are no photons, when measuring the EM field one would obtain different non-zero values which vary randomly. In this way that the EM vacuum is also said to be subjected to zero-point fluctuations (ZPF).

For instance, as disorder is gradually increased in a photonic crystal structure, the lasing process can occur to change from being purely based on a photonic band-edge effect (in the ordered structure), to an *Anderson localization* process (in the mid-disordered one), and to completely disappear (in a highly disordered one) [42-44].

Finally, remarkable manipulations of the EM field can also arise from the fact that the resonant dipole-dipole interaction between atoms in a cPBG can lead to interesting low-threshold nonlinear effects, like optical bistability, or ultra-high speed optical switching [45-47]. And even more, based on an adequate combination of optically active medium with cPBG structure, different devices have been anticipated which would serve as a basis for a quantum computation [48-50]. In such systems, the cPBG would screen the spontaneous emission process and the dipole dephasing of the active species (such as rare-earth erbium ions) from damping effects; if achieved, this would provide the basis for performing qubit encoding and logic gating in a quantum computing device.

3. Photonic band gap lattice parameters

For any given photonic band gap material the following features and parameters need to be known:

- **Dimensionality:** Whether the lattice is in 1D, 2D or 3D.
- **Symmetry**: Obeying to translational symmetry there are 14 types of Bravais lattices in 3D [1], while simply obeying rotational symmetry and lacking from translational one, we have *quasicrystals*.
- **Topology**: For any given symmetry, a lattice can present infinite different topologies, which can be essentially classified as *network* or *Cermet* topology, depending on the *connectivity* of the different refractive index regions: Whenever the topology is constituted by continuous, interconnected regions of high index by one side and low index on another, the topology is referred to as network topology. On the other hand, if any of the different refractive index regions appears constituted by isolated units, then it will correspond to a Cermet topology [51, 52].

- **Lattice spacing**: This is the fundamental distance separating the different refractive index regions of the lattice for each direction. The range of wavelengths affected by the photonic lattice will depend on the scale of this parameter.
- **Effective refraction index**: It is usually calculated as the mean refractive index value per unit cell.
- **Filling fraction**: The relative volume of scattering material with respect to the total unit cell volume. It is calculated to determine the effective refraction index and is usually used to compare between the properties of different structures with the same symmetry and topology.
- **Refractive index contrast**: Defined as the ratio between the high and low indexes of the material, it offers a general idea of the scattering strength of the different dielectric regions. Together with the filling fraction it is the most important parameter to look after when optimizing a photonic crystal.

This set of parameters defines the dispersion properties of a photonic structure. As the Bragg condition indicates the two important parameters for determining the range of frequencies affected in a photonic band gap lattice are the lattice spacing and the effective refraction index. However, what really determines the limits and behaviour over which the dispersion properties will develop are the type of lattice symmetry and specific topology. It is thus important to remark that these subjects (lattice symmetry and topology) constitute the most important research issues in the field, along with the development of more precise and efficient microfabrication techniques.

In the two following sections some of the basic types of lattices and several of the most used fabrication techniques are described.

4. Three-dimensional photonic crystal lattices

Fabricating a photonic crystal for optical wavelengths implies sculpting structures on a submicron scale with nanometre resolution. In this way, the nanofabrication process is still the main bottleneck which prevents many of the anticipated optical devices from being practically attainable.

What is more, given a specific device requirement, i.e. on a specific material and with a specific optical functionality, the challenge usually comes in the form of obtaining the lattice structure which fits both the requirements of fabrication amenability in this material, and accomplishment of the required optical functions. This means that the problem is necessarily both theoretical (to predict the optical behaviour of a given lattice) and experimental (to find the microfabrication technique for a given lattice). In this sense, photonic crystal research clearly illustrates the absolute need for feedback between theoretical and experimental researchers, a fact which is particularly well exemplified in the lattice structure research issue.

From solid state physics we know that band gaps occur for wave vectors lying in the Brillouin zone boundary. Thus, for a cPBG to be achieved, one would like to have a sphere-like Brillouin zone in such a way that all pseudogaps would open at similar frequencies, and a cPBG would be easier to be achieved. Among the 3D Bravais lattices, the face centred cubic (fcc) presents the roundest Brillouin zone in the reciprocal space, and so it was the first one being proposed by John *et al.* in 1988 [53] to have a cPBG. Surprisingly, all the experimental efforts by Yablonovitch *et al.* following that work showed little agreement with John calculations [54] and only after two convulsive years[§] diamond-like structures were studied, and the first cPBG (for the microwave regime) was finally successfully reported [58][**].

Since those first years many more different 3D photonic crystal structures have been conceived. Some of the basic lattices are next summarized:

[§] In November 16th of 1990, Leung *et al.* and Zhang *et al.* both simultaneously published a fully vectorial Plane Wave Method (PWM) to calculate photonic energy bands [55, 56] which, agreeing with experiments, showed that the cPBG predicted by S. John [53] for fcc structures (between the 2nd and 3rd bands) did not exist. These findings led then J. Maddox, editor of the high impact journal 'Nature', to suitably assert the next month (December 6th, 1990) that "*Photonic Band-Gaps bite the dust*" [57]. However, only some days after Ho *et al.* publish again another work showing that fcc do not have a cPBG, but that diamond structures do possess one and with refractive-index contrasts as low as 2 [58]. Based on these and on experiments on new fcc structures with non-spherical 'atoms', three months later Yablonovitch and Leung were letting back all the previous disappointments answering to Maddox suggestions [59]. And one more year later improved calculations by Sözüer *et al.* finally showed that inverse fcc structures could feature cPBGs, but between the higher order 8th and 9th bands [60].

[**] It then took five more years to fabricate it with for optical wavelengths by chemically assisted ion beam etching through a triangular hole array mask, defined by electron beam lithography on GaAs [61].

- **Fcc structure**: Usually defined as constituted by spherical high-index dielectric voxels (usually artificial opals or colloidal particles), and surrounded by a low-index medium (see **Fig. 4a**). In that configuration it only shows pseudogaps[††], not cPBGs [60].
- **Inverse fcc structure**: Consists of low-index spherical voxels in a high index medium (see **Fig. 4b**), as opposed to the usual fcc one. Calculations show that in this case a cPBG can at least be opened between the high order 8^{th} and 9^{th} bands, for a minimum index contrast of $\delta \approx 2.8$ [60].
- **Simple cubic structures:** Whether composed of voxels, rods, or other topologies, these structures show robust cPBGs between the 5^{th} and 6^{th} bands, for a minimum index contrast of $\delta \approx 2.8$ [63, 64]. Interestingly, in the case of low-index voxels (i.e. inverse voxel-based simple cubic), calculations show that neither ellipsoidal deformation of the voxels nor tetragonal distortions of the cubic lattice, improve the cPBG [65].
- **Diamond-like structure**: Has been implemented in many different topologies each one arising from a different fabrication technique and was the first showing a cPBG [59]. Relevant examples are the so-called *woodpile* structures (see **Fig. 4d**) or the spiral-diamond (see **Fig. 4c**). It shows a cPBG between the 2^{nd} and 3^{rd} bands for index contrasts higher than $\delta \approx 2$ [58, 66].
- **Inverse diamond-like structure**: Exemplified by the inverse woodpile (see **Fig. 4e**), or by air-sphere diamond structures, it features cPBGs of higher theoretical photonic strength than their precursor (non inverted) diamond structures [67].
- **Quasicrystals**: These are lattices having a long-range rotational symmetry, while lacking from translational one (see **Fig. 4f**). They show promising experimental pseudogaps which can naively expected from the Bragg condition, which are expected to be more uniform or isotropic than that of translational periodic crystals, as they present more spherical Brillouin zones. Photonic quasicrystals

[††] Importantly, if non-spherical voxels are used, instead of spherical, degeneracy of the 2^{nd} and 3^{th} bands at the high symmetry point W breaks and a cPBG opens quite in the same way as for diamond lattices. And also the same occurs for bcc lattices, in which the symmetry induced degeneracy of the 2^{nd} and 3^{th} bands at points P and H is also removed and a cPBG arises. Both non-spherical voxel based fcc and bcc lattices can then be regarded as quasi-diamond like lattices in terms of their photonic band structure and symmetry. The difference between the two such structures resides, for instance, in that there exists a different favourable direction where the 2^{nd}-3^{th} cPBG opens. That is along the (111) and (210) directions for fcc and bcc distorted lattices, respectively [62].

are expected to have substantial cPBGs even for low dielectric contrasts, and are believed to play an important role in light diffusion and nonlinear optical properties of light in the near future [68].

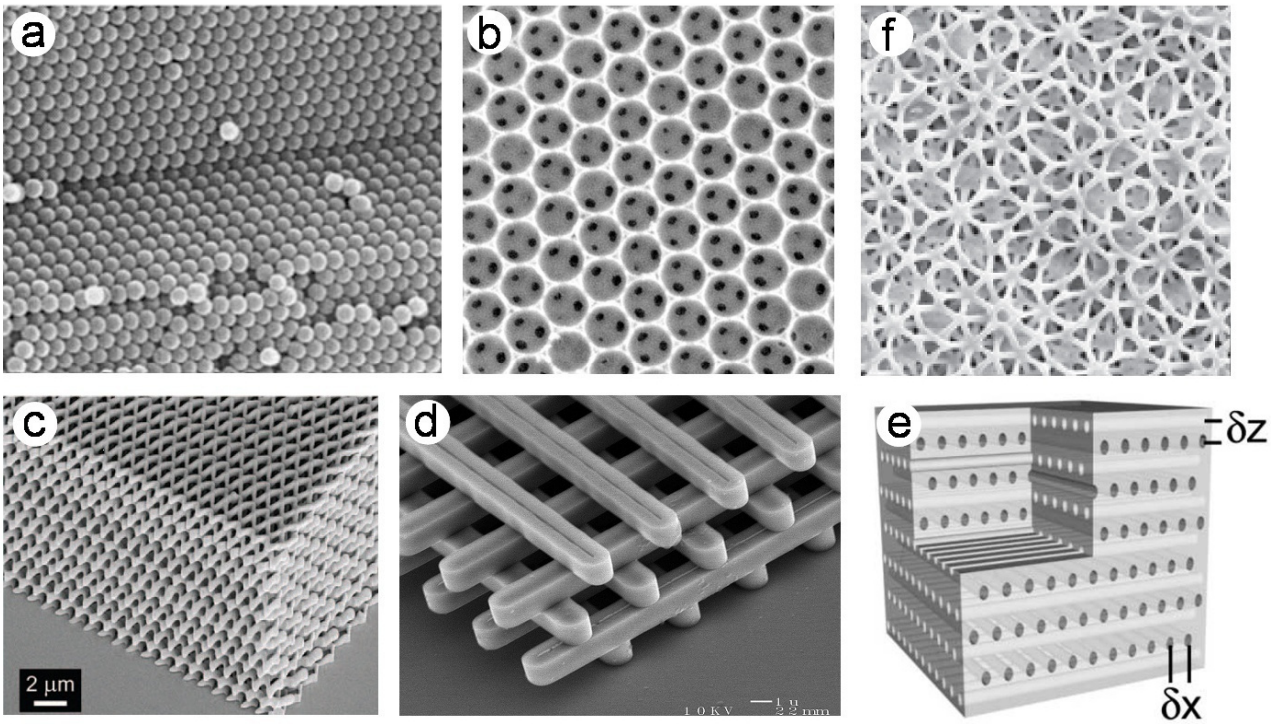

Fig. 3. *Basic kinds of photonic crystal structures:* **a)** *Opal self-assembled fcc structures.* **b)** *Inverse opal fcc structures.* **c)** *Spiral direct laser written structures.* **d)** *Woodpile structure.* **e)** *Inverse woodpile structure.* **f)** *Three-dimensional quasicrystal structures fabricated by silicon inversion of direct laser written templates.*

5. Fabrication methods

As previously mentioned, the microfabrication of photonic crystals has been the most challenging task since the first days when the idea was conceived [10, 11, 57, 59]. Even today, experimental methods for engineering and producing three-dimensional PBG devices capable of realizing most of the predicted optical functions are still lacking. This delay does not only reside on the difficulty of the high quality of miniaturization needed, but also on the complexity of achieving for the wide range of available dielectric, semiconductor and metallic media, each one having a dissimilar resistance to each nanofabrication technique. For instance, the standard techniques for

chemically structuring polymers may be of little use with dielectric crystals, the self-assembly techniques for dielectric or polymer opals may not serve if metallic opals are desired, or the usual laser techniques for structuring transparent dielectrics may be also of no use when working with opaque silicon based materials. Moreover, due to the high degree of perfection and optimization needed, microfabrication techniques are usually developed for one specific material of each kind. Nevertheless, everyday new experimental techniques are continuously being developed, which allow us to overcome some of the previous limitations. In a very brief description, some of the most frequently used approaches for photonic crystal fabrication are next summarized:

- **Multi-step lithography**: Lithographic techniques are widely used in the semiconductor industry, and very important advances have been achieved when applied for photonic structures, such as cPBGs at NIR frequencies with the option of including defects which can act as optical cavities. Unfortunately, it is in general an expensive procedure which inevitably consists of complex and time consuming multiple-step processes. Each of the diverse fabrication methods already developed consists on a cyclic combination of different steps such as: photo-lithography (see **Fig. 4d**) or electron-beam lithography, wafer-fusion, cleaving, stacking, laser alignment, chemical etchings and polishing sub-steps [61, 69-74].

- **Self-assembly**: Self-assembly of artificial opals has been one of the most successful and widely used techniques so far. It offers a cheap method available for many research laboratories, and has also led to important advances in the understanding of photonic crystals through achieving different breakthroughs. It usually consists on the amassing of colloidal spheres that self-organize in a crystal symmetry (see **Fig. 4a**). In order to obtain cPBGs, the low-index opals are usually infiltrated with some high-index material followed by removal of the original opals, obtaining in this manner inverse fcc structures of controllable filling ratio and index contrast (see **Fig. 4b**). Although large 3D crystals can be obtained, this technique usually leads to random defects and, what is more important, imposes strong restrictions over the available lattice symmetries and topologies.

However, very ingenious ways of controlling and improving the self-assembled lattices are being developed, such as using ellipsoidal particles whose aspect ratio can be tailored and which, after being magnetically activated, self-assemble into long-range superlattices under magnetic field control. All of these improved processes nonetheless at the expense of increasing the fabrication times to more than a day time [75-78].

- **Nano-manipulation**: Nano-manipulation has been used as a proof of concept of several 3D structures. It has been used, for instance, to obtain perfect diamond opal structures by means of stacking dielectric spheres, or to build up 3D woodpile structures by stacking sliced planar components [79-81]. While with this method one can obviously obtain personalized structures, the number of layers is usually limited to as much as 20, and the structural stability of the obtained samples is rather low. Although these direct methods are not intrinsically limited in resolution, neither on 3D positioning, it is still uncertain that will have industrial applicability.

- **Focus Ion Beam milling**: Interesting structures, such as the inverted woodpile, have been achieved in silicon by FIB milling in two orthogonal directions. Mounting, for example, the sample on a holder that can be tilted 45^{o} and aligning by using simple marks. Although the mechanical precision does not suppose an initial drawback, the milling technique still has limited capabilities compared to, for instance, wet or dry etching. Nevertheless, the FIB technique is nowadays being widely developed and studied as a promising technique for microstructuring both semiconductors and dielectrics for photonic applications [81, 82].

- **Interference or holographic techniques**: Multiple-beam holography, also known as holographic lithography, can be used to directly fabricate 3D structures in a photoresist. The technique offers a unique possibility for obtaining, in only one step, large ordered templates. An fcc lattice can be obtained, for example, by focusing four laser beams into a photoresist (with the help

of a specially designed prism) with the angles of the laser beams corresponding to a bcc reciprocal space lattice, which corresponds to a real-space fcc lattice in the photoresist. As the photonic structures are defined by the iso-intensity surfaces of the interference, the lattice symmetries achievable in this way (for example diamond-like lattices, or complicated quasicrystals) are not possible with other methods except with direct laser writing. The obtained templates can also be afterwards replicated or inverted in a higher index material, by a double-inversion process or a single-inversion one, respectively; obtaining very high quality high index contrast structures. Although the technique does not easily allow engineering structure geometries and creating defects, it is an extremely attractive method due to its ability to pattern large areas at considerably high speeds. DLW can be applied as a second fabrication step to engineer cavities on the obtained structures (see: Direct Laser Writing). Recent work with phase masks avoids some of its previous challenges concerning the delicate multi-laser alignments, thus allowing for large scale fabrication. Very recent works further improve the phase mask optics by means of a proximity field nanopatterning technique (PnP) [83]. A molded photopolymer can serve both as the optical phase mask and recording media for obtaining the 3D patterned structures by femtosecond two-photon polymerization. The molded relief produces various diffraction beams whose interference forms the 3D intensity distribution that defines the exposed geometry. The exposure is followed by a removal of unexposed regions and produces high quality 3D structures over large areas which are next inverted to silicon in a single step. Very importantly, the holographic technique can also offer a key additional advantage which is the possibility of using conventional CW lasers, such as an Argon laser, instead of ultrashort pico- or femtosecond pulse lasers. The holographic technique is nowadays being widely explored in laboratories all around the world and has been already claimed to be the first method for obtaining 3D PBG devices amenable for mass-production [84-89].

- **Direct Laser Writing (DLW)**: This is the technique studied in this thesis. In this fabrication scheme a laser pulse (usually with duration around ~100 fs to avoid thermal effects) is tightly focused inside a transparent material, to produce a highly localized irreversible change, usually referred to as a *voxel*. Depending on the material and on the laser wavelength, voxel creation is

mediated by a single photon or by a multi-photon absorption process, which is then followed by a transformation of the medium at only the focal volume. As a general rule, the higher the nonlinearity of the absorption process the smaller the written voxel. The most widely used DLW method for obtaining photonic crystals is that of two-photon polymerization of a photoresist, in such a way that an arbitrary 3D design is written inside the sample by computer controlling a nanopositioning stage. The directly written structure can then be obtained by easily removing the non-exposed, non-polymerized regions, and in the same way as for holographic lithography, the obtained polymer structures can then be replicated or inverted in a higher index material, by a double-inversion process or a single-inversion one, respectively (see **Fig. 4c** and **4f**). The DLW procedure was performed for the first time with the aim of obtaining a photonic crystal by H.-B. Sun, S. Matsuo and H. Misawa, in Japan in 1998 [90]. Since then, the method has been constantly improved, especially with respect to the template inversion processes, leading to several fundamental breakthroughs in the field, such as the first high-quality woodpile template at the NIR range [91] and subsequent silicon woodpile and inverse-woodpile structures [92, 93], the three of them by G. von Freymann, M. Wegener and co-workers. The structures obtained by DLW have in general the benefit of a complete design freedom and a very high degree of perfection [68]. These has allowed engineering and observing important features of PBG structures such as the presence and nature of high-order gaps [94], and tailored cavities performed during the DLW process or on a previously fabricated structure by other methods such as, for example, holographic lithography or self-assembled opals [95-97]. The DLW and holographic lithography are thus two completely compatible and complementary fabrication methods when applied to photo-polymerizable resins. When applied to dielectric materials such as glasses or crystals, the technique relies on the confined plasma generation at the tight laser focus (commonly named as dielectric or optical breakdown), which leaves an amorphous voxel of subwavelength lateral size, surrounded by a shell of slightly modified (strained) media (see **Chapter 3** for further details on DLW in dielectric media). So far, DLW photonic structures have been already created in glasses such as silica and chalcogenide glasses, and in laser crystals such as lithium niobate and Nd:YAG [98-103]. In general, this direct laser technique features an adequate combination of high structure-design freedom in a very wide material range, with high processing speeds and a cost-effective fabrication process.

6. Band dispersion effects

Now that we have introduced the basic concepts regarding photonic crystals: i.e. the propagation and emission properties governed by PBGs, the different 3D lattice symmetries and structures, and the different fabrication methods, we shall now introduce one of the aspects which attract more attention from photonic researchers: the nonlinear *slow-light* and *superprisms* effects.

According to the basic laws of refraction, if a plane electromagnetic wave falls on to a boundary between two homogeneous media of different refractive index it will change its propagation direction. The magnitude of this change being given by a constant magnitude, that is the ratio of refractive indices, or index contrast. Both the wave vectors components and energies must be conserved, and the dispersion relation will have a circular shape (spherical in 3D), $\omega = ck/n = c/n\sqrt{(k_{\perp}^2 + k_{ll}^2}$. In photonic crystals the energy bands depart from this behaviour and the effective refractive index must rather be taken as $n = c/(d\omega/dk)$, that is, as a function of the group velocity. This is nothing else but the usual description of a dispersive medium. Since at the centre and near the edges of stop gaps group velocities tend to zero (see **Fig. 2**), the time now taken for the plane wave to traverse the medium will be strongly increased, thus enhancing the interactions between the electromagnetic waves and the medium through the effect which is commonly named as *slow light effect*. The result of this dispersion phenomena is that the energy propagation (given by the group velocity $\vec{v}_g = \nabla_{\vec{k}}\omega$) will be strongly modified in direction by the rapidly varying equi-frequency surfaces of photonic crystals. For frequencies bellow a stop gap the equi-frequency surfaces are circular (spherical for 3D), increasing in size as the frequency increases ($\vec{v}_g$ points outwards as in a nondispersive medium), and if the frequency reaches a value laying in the pseudogap the surface will become discontinuous for those directions (we have forbidden modes for certain directions so there will be no value for the frequency of propagation). Conversely, for frequencies above the pseudogap the shape will be suddenly strongly modified. As the photonic bands now have an 'inverse' behaviour with direction (see **Fig. 2**) the surface will no longer be

spherical, and its size will decrease with frequency (therefore $\vec{v}_g$ will now point inwards). This non-circular shape of the equi-frequency surfaces expresses the fact that the refraction response of the medium is strongly anisotropic.

To illustrate this effect **Fig. 5** shows the refraction of two photons with same energy and incident direction at two equal 2D triangular-lattice lithium niobate photonic crystals of slightly different refraction index contrasts of 2.1 and 2.2. This illustration is made following the theoretical work of J. Amet *et al.* [104]. In the first case (**Fig. 5a**), the photon propagates through the crystal with a small angle change of 22.4^{o}, whereas if the index is slightly increased a 0.05% as in the second case, the propagating wave undergoes negative refraction. The main effect is that, for very similar refractive indices (or equivalently for very similar light wavelengths in the same index medium), the refracted waves propagate at drastically different directions. In the first case the incoming beam is only slightly refracted, while in the second one it exits along a lateral side of the photonic crystal. This effect is usually called *Superprism effect*, and is one the most interesting applications of photonic crystals on areas such as telecommunication technologies. As previously mentioned, it is important to emphasise here that this anomalous dispersion is thus completely independent from the existence or not of a cPBG. This means that the index contrast requirements for fabricating a superprism device are substantially much lower than that for creating a cPBG material.

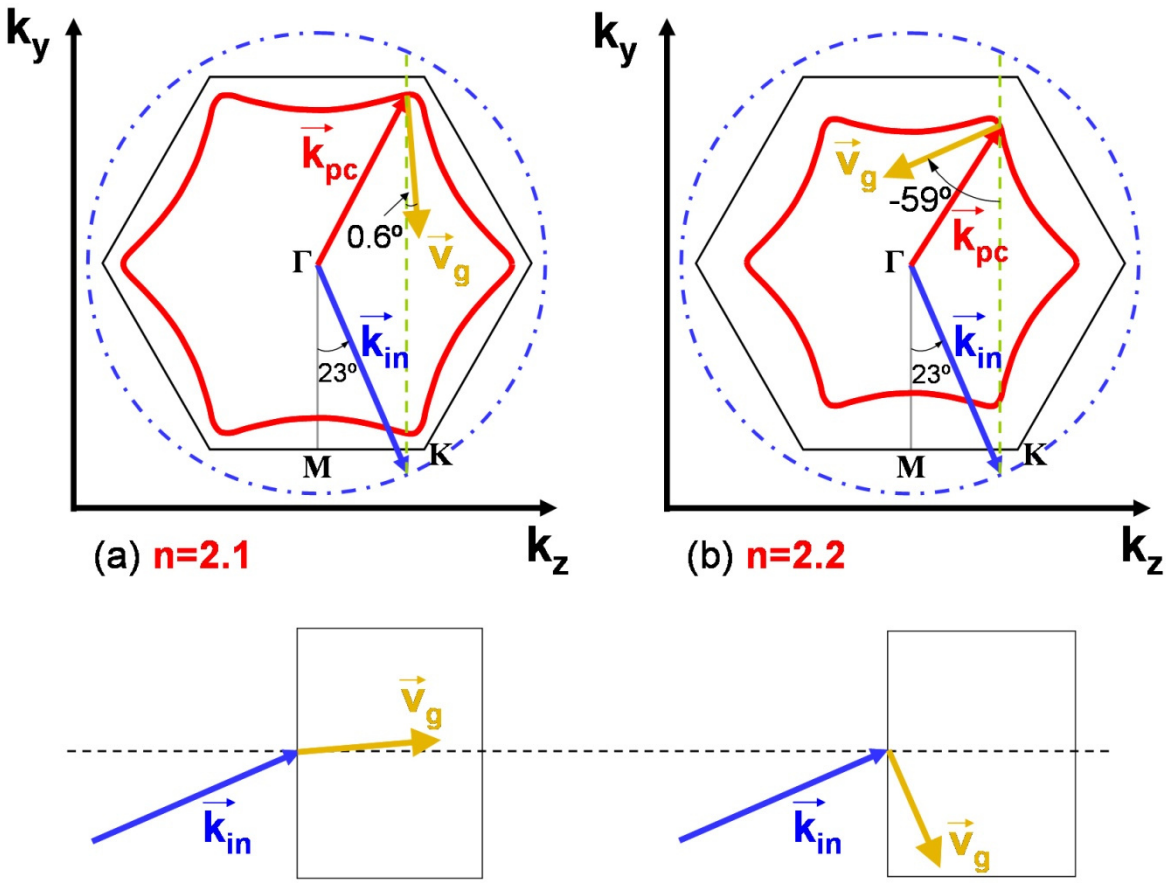

Fig. 5. *Equi-frequency dispersion surfaces for a 2D triangular lattice o fair holes in lithium niobate. In this example (adapted from [104]) it is shown how the light flow (i.e. the group velocity) inside the structure can be controlled in direction by electro-optically switching the index of refraction from 2.1 to 2.2.*

Although cPBGs have not yet been achieved in lithium niobate, very recently a 2D lithium niobate photonic crystal superprism device was successfully designed and fabricated for double demultiplexer applications [105]. While passive photonic crystals (not index tuneable) require the incident angle or wavelength to be varied externally to the device, the use of lithium niobate photonic crystals allows for a strong angular beam steering not only through passively tuning the wavelength, but also by controlling the enhanced non-linear effects due to slow light phenomenon. In that recent work researchers demonstrated a passive device exhibiting an angular dispersion of 1.5°/nm, while a value as high as 4.3°/nm was expected if the 2D PC design was further improved.

As a comparison with other previously fabricated superprisms, the stronger light deviation which has been experimentally reported corresponds to a value of 5^{o}/nm in a 3D PC [106].

7. Applications

As the field evolves and more breakthroughs are achieved new applications for photonic band gap devices are everyday realized. Now that optics is present on every part of our lives, photonic crystals hold the promise of engaging us into a higher level of technological development covering not only areas such as telecommunications and computing, but also as medicine, biology and renewable energies related ones.

The unusual dispersion in photonic crystals allows envisaging new optical systems such as *supercollimators*, *superlenses* and *superprisms*, which overcome the limitations of current lenses, filters, and prisms. For integrated optical circuits, a plethora of passive and active devices have already been designed and are continuously being improved by researchers. For instance, 2D photonic crystal waveguides (PCW) present numerous advantages with respect to the total internal reflection based ones, such as lossless sharp bends and enhanced functionality in a wide range of applications. To perform logical operations photonic transistors have also been predicted based on active 3D photonic crystals. The possibility of controlling quantum processes such as spontaneous emission also enables the opportunity of developing new optical quantum computing schemes, and low-threshold active devices such as microcavity lasers, chromatic switches or solar cells. These are only but a few of the most remarkable applications of the concept of *photonic crystal*.

References

[1] C. Kittel, *Introduction to Solid State Physics*, 8th edn. (Wiley, New York, 2005)

[2] T. Euser, *Ultrafast optical switching of photonic crystals,* PhD Thesis, FOM-COPS. Print Partners Ipskamp, Enschede, The Netherlands (2007). www.photonicbandgaps.com.

[3] M. Straub, M. Ventura, and M. Gu, *Multiple higher-order stop gaps in infrared polymer photonic crystals*, Phys. Rev. Lett. **91**, 4, 043901 (2003)

[4] A. Ródenas, G. Zhou, D. Jaque, and M. Gu, *Direct laser writing of three-dimensional photonic structures in Nd:yttrium aluminum garnet ceramics*, Appl. Phys. Lett. **93**, 151104 (2008)

[5] F. Bloch, *Über die quantenmechanik der electronen in kristallgittern*, Z. Physik **52**, 555-600 (1928)

[6] Steven G. Johnson, *Photonic Crystals: From theory to practice*, PhD. Thesis, Massachusetts Institute of Technology (2001)

[7] C. C. Cheng, V. Arbet-Engels, A. Scherer, and E. Yablonovitch, *Nanofabricated three dimensional photonic crystals operating at optical wavelengths*, Phys. Scripta. **T68**, 17-20 (1996)

[8] W. L. Vos, H. M. van Driel, M. Megens, A. F. Koenderik, and A. Imhof, *Photonic crystals and light localization in the 21st century*, edited by C. M. Soukoulis, Kluwer, Dordrecht (2001)

[9] A. F. Koenderik, *Emission and transport of light in Photonic Crystals*, PhD thesis, University of Amsterdam (2003)

[10] E. Yablonovitch, *Inhibited Spontaneous Emission in Solid-State Physics and Electronics*, Phys. Rev. Lett. **58**, 20 (1987)

[11] S. John, *Strong Localization of Photons in Certain Disordered Dielectric Superlattices*, Phys. Rev. Lett. **58**, 23 (1987)

[12] M. J. A. de Dood, *Silicon photonic crystals and spontaneous emission*, PhD thesis, FOM, The Netherlands (2002)

[13] J. Kalkman, *Controlled spontaneous emission in erbium-doped microphotonic materials*, PhD thesis, FOM, The Netherlands (2005)

[14] E. Yablonovitch, T. J. Gmitter, R. D. Meade, A. M. Rappe, K. D. Brommer, and J. D. Joannopoulos, *Donor and Acceptor Modes in Photonic Band Structure*, Phys. Rev. Lett. **67**, 24 (1991)

[15] J. D. Joannoupoulos, R. D. Meade, and J. N. Winn, *Photonic Crystals: Molding the Flow of Light*, Princeton, New York (1995)

[16] S. Fan, P. R. Villeneuve, and J. D. Joannopoulos, *Channel drop tunnelling through localized states*, Phys. Rev. Lett. **80**, 960-963 (1998)

[17] O. J. Painter *et al.*, *Two-dimensional photonic band-gap defect mode laser*, Science **284**, 1819-1821 (1999)

[18] S. Noda, A. Chutinan, and M. Imada, *Trapping and emission of photons by a single defect in a photonic bandgap structure*, Nature **407**, 5, 608-610 (2000)

[19] Claude Cohen-Tannoudji, Bernard Diu, and Franck Laloë, *Quantum Mechanics*, Vol. 2, (Wiley, 1977)

[20] E. Snoeks, A. Lagendijk, and A. Polman, *Measuring and modifying the spontaneous emission rate of erbium near an interface*, Phys. Rev. Lett. **74**, 13 (1995)

[21] M. Megens, J. E. G. J. Wijnhoven, A. Lagendijk, and W. L. Vos, *Light sources inside photonic crystals*, J. Opt. Soc. Am. B **16**, 9, 1403-1408 (1999)

[22] W. L. Vos, and A. Polman, *Optical probes inside photonic crystals*, MRS BULLETIN, 642-646, August 2001.

[23] N. Vats, S. John, and K. Busch, *Theory of fluorescence in photonic crystals*, Phys. Rev. A **65**, 043808 (2002)

[24] A. F. Koenderink, and W. L. Vos, *Light exiting from Real Photonic Band Gap Crystals is Diffuse and Strongly Directional*, Phys. Rev. Lett. **91**, 21 (2003)

[25] M. J. A. de Dood, A. Polman, and J. G. Fleming, *Modified spontaneous emission from erbium-doped photonic layer-by-layer crystals*, Phys. Rev. B **67**, 115106 (2003)

[26] P. Lodahl, A. F. van Driel, I. S. Nikolaev, A. Irman, K. Overgaag, D. Vanmaekelbergh, and W. L. Vos, *Controlling the dynamics of spontaneous emission from quantum dots by photonic crystals*, Nature **430**, 654-657 (2004)

[27] I. S. Nikolaev, P. Lodahl, and W. L. Vos, *Quantitative analysis of directional spontaneous emission spectra from light sources in photonic crystals*, Phys. Rev. A **71**, 053813 (2005)

[28] L. Bechger, P. Lodahl, and W. L. Vos, *Directional Fluorescence Spectra of Laser Dye in Opal and Inverse Opal Photonic Crystals*, J. Phys. Chem B **109**, 9980-9988 (2005)

[29] I. S. Nikolaev, P. Lodahl, A. F. van Driel, A. F. Koenderink, and W. L. Vos, *Strongly nonexponential time-resolved fluorescence of quantum-dot ensembles in three-dimensional photonic crystals*, Phys. Rev. B **75**, 115302 (2007)

[30] M. J. Ventura, and M. Gu, *Engineering Spontaneous Emission in a Quantum-Dot-Doped Polymer Nanocomposite with Three-Dimensional Photonic Crystals*, Adv. Mat. **20**, 1329-1332 (2008)

[31] A. Brzezinski, J-T Lee, J. D. Slinker, G. G. Malliaras, P. V. Braun, and P. Wiltzius, *Enhanced emission from fcc fluorescent photonic crystals*, Phys. Rev. B **77**, 233106 (2008)

[32] E. M. Purcell, *Spontaneous Emission Probabilities at Radio Frequencies*, from the Proceedings of the American Physical Society, Phys. Rev. **69**, 681 (1946)

[33] T. A. Welton, *Some observable effects of the quantum-mechanical fluctuations of the electromagnetic field*, Phys. Rev. **74**, 1157 (1948)

[34] S. John, and J. Wang, *Quantum Electrodynamics near a Photonic Band Gap: Photon Bound States and Dressed Atoms*, Phys. Rev. Lett. **64**, 20, 2418-2421 (1990)

[35] S. John, *Localization of Light*, Physics Today, May 1991, 32-40.

[36] S. John, and J. Wang, *Quantum optics of localized light in a photonic band gap*, Phys. Rev. B **43**, 16 (1991)

[37] S. John, and T. Quang, *Spontaneous emission near the edge of a photonic band gap*, Phys. Rev. A **50**, 2 (1994)

[38] S. John, and T. Quang, *Localization of Superradiance near a Photonic Band Gap*, Phys. Rev. Lett. **74**, 17 (1995)

[39] A. Chutinan, and S. John, *Light localization for broadband integrated optics in three dimensions*, Phys. Rev. B **72**, 161316(R) (2005)

[40] H. Takeda, A. Chutinan, and S. John, *Localized light orbitals: Basis states for three-dimensional photonic crystal microscale circuits*, Phys. Rev. B **74**, 195116 (2006)

[41] L. Florescu, K. Busch, and S. John, *Semiclassical theory of lasing in photonic crystals*, J. Opt. Soc. Am. B **19**, 9, 2215-2223 (2002)

[42] A. F. Koenderink, A. Lagendijk, and W. L. Vos, *Optical extinction due to intrinsic structural variations of photonic crystals*, Phys. Rev. B **72**, 153102 (2005)

[43] S. John, and G. Pang, *Theory of lasing in a multiple-scattering medium*, Phys. Rev. A **54**, 4 (1996)

[44] C. Conti, and A. Fratalocchi, *Dynamic light diffusion, three-dimensional Anderson localization and lasing in inverted opals*, Nat. Phys. **4**, 794-798 (2008)

[45] S. John, T. Quang, *Optical bistability and phase transitions in a doped photonic band-gap material*, Phys. Rev. A **54**, 5 (1996)

[46] Y. Liu, X. Hu, D. Zhang, B. Cheng, D. Zhang, and Q. Meng, *Subpicosecond optical switching in polystyrene opal*, Appl. Phys. Lett. **86**, 151102 (2005)

[47] T. G. Euser, H. Wei, J. Kalkman, Y. Jun, A. Polman, D. J. Norris, and W. L. Vos, *Ultrafast optical switching of three-dimensional Si inverse opal photonic band gap crystals*, J. Appl. Phys. **102**, 053111 (2007)

[48] T. Quang, M. Woldeyohannes, S. John, and G. S. Agarwal, *Coherent Control of Spontaneous Emission near a Photonic Band Edge: A Single-Atom Optical Memory Device*, Phys. Rev. Lett. **79**, 26 (1997)

[49] M. Woldeyohannes, S. John, *Coherent control of spontaneous emission near a photonic band edge: A qubit for quantum computing*, Phys. Rev. A **60**, 6 (1999)

[50] M. Woldeyohannes, and S. John, *Coherent control of spontaneous emission near a photonic band edge*, PhD Tutorial, J. Opt. B: Quantum Semiclass. Opt. **5**, R43-R82 (2003)

[51] E. N. Economou, and M. M. Sigalas, *Classical wave propagation in periodic structures: Cermet versus network topology*, Phys. Rev. B **48**, 18 (1993)

[52] S. John, *Localization of Light: Theory of Photonic Band Gap Materials*, page 587 on the book *Photonic Band Gap Materials*, edited by C. M. Soukoulis, which contains the papers presented at the NATO Advanced Study Institute 'Photonic Band Gap Materials' held in Crete, 1995.

[53] S. John, and R. Rangarajan, *Optimal structures for classical wave localization – an alternative to the Ioffe-Regel criterion*, Phys. Rev. B **38**, 10101 (1988)

[54] E. Yablonovitch, and T. J. Gmitter, *Photonic Band-Structure – the face-centered-cubic case*, Phys. Rev. Lett. **63**, 1950 (1989)

[55] K. M. Leung, and Y. F. Liu, *Full vector wave calculation of photonic band structures in face-centered-cubic dielectric media*, Phys. Rev. Lett. **65**, 2646 (1990)

[56] Z. Zhang, and S. Satpathy, *Electromagnetic-wave propagation in periodic structures – Bloch wave solution of Maxwell Equations*, Phys. Rev. Lett. **65**, 2650 (1990)

[57] J. Maddox, *Photonic Band-Gaps bite the dust*, Nature **348**, 481 (1990)

[58] K. M. Ho, C. T. Chan, and C. M. Soukoulis, *Existence of a Photonic Band Gap in Periodic Dielectric Structures*, Phys. Rev. Lett. **65**, 25, 3152-3155 (1990)

[59] E. Yablonovitch, and K. M. Leung, *Hope for Photonic Bandgaps*, Nature **351**, 278 (1991); E. Yablonovitch, T. J. Gmitter, and K. M. Leung, *Photonic Band Structure: The Face-Centered-Cubic Case Employing Nonspherical Atoms*, Phys. Rev. Lett. **67**, 17 (1991)

[60] H. S. Sözüer, J. W. Haus, and R. Inguva, *Photonic Bands – Convergence problems with the Plane-Wave Method*, Phys. Rev. B **45**, 13962 (1992)

[61] C. C. Cheng, V. Arbet-Engels, A. Scherer, and E. Yablonovitch, *Nanofabricated Three Dimensional Photonic Crystals Operating at Optical Wavelengths*, Physica Scripta. **T68**, 17-20 (1996)

[62] Z.-Y. Li, J. Wang, and B.Y. Gu, *Full Band Gap in Fcc and Bcc Photonic Band Gaps Structure: Non-Spherical Atom*, J. Phys. Soc. Jap. **67**, 9, 3288-3291 (1998)

[63] M. Maldovan, A. M. Urbas, N. Yufa, W. C. Carter, and E. L. Thomas, *Photonic properties of bicontinous cubic microphases*, Phys. Rev. B **65**, 165123 (2002)

[64] R. Biswas, M. M. Sigalas, K.-M. Ho, and S.-Y. Lin, *Three-dimensional photonic band gaps in modified simple cubic lattices*, Phys. Rev. B **65**, 205121 (2002)

[65] S. Matthias, R. Hillebrand, F. Müller, and U. Gösele, *Macroporous silicon: Homogeneity investigations and fabrication tolerances of a simple cubic three-dimensional photonic crystal*, J. Appl. Phys. **99**, 113102 (2006)

[66] M. Maldovan, and E. L. Thomas, *Diamond-structured photonic crystals*, Nat. Mater. **3**, 593-600 (2004)

[67] R. Hillebrand, S. Matthias, and F. Müller, *Theoretical study of a modulated pore approach to a photonic crystal of inverted diamond like type*, Phys. Rev. B **71**, 045125 (2005)

[68] A. Ledermann, L. Cademartiri, M. Hermatschweiler, C. Toninelli, G. A. Ozin, D. S. Wiersma, M. Wegener, and G. V. Freymann, *Three-dimensional silicon inverse photonic quasicrystals for infrared wavelengths*, Nat. Mater. BUSCAR REF.

[69] S.-Y. Lin, and J. G. Fleming, *A three-dimensional optical photonic crystal*, J. Light. Tech. **17**, 11 (1999)

[70] M. Qi, E. Lidorikis, P. T. Rakich, S. G. Johnson, J. D. Joannopoulos, E. P. Ippen, and H. I. Smith, *A three-dimensional optical photonic crystal with designed point defects*, Nat. **429**, 538-542 (2004)

[71] M. Imada, L. H. Lee, M. Okano, S. Kawashima, and S. Noda, *Development of three-dimensional photonic-crystal waveguides at optical-communication wavelengths*, Appl. Phys. Lett. **88**, 171107 (2006)

[72] J.-H. Lee, C.-H. Kim, Y.-S. Kim, K.-M. Ho, K. Constant, and C. H. Oh, *Three-dimensional metallic photonic crystals fabricated by soft lithography for midinfrared applications*, Appl. Phys. Lett. **88**, 181112 (2006)

[73] S. Takahashi, M. Okano, M. Imada, and S. Noda, *Three-dimensional photonic crystals based on double-angled etching and wafer-fusion techniques*, Appl. Phys. Lett. **89**, 123106 (2006)

[74] Y.-L. Yang, F.-J. Hou, S.-C. Wu, W.-H. Huang, M.-C. Lai, and Y.-T. Huang, *Fabrication and characterization of three-dimensional all metallic photonic crystals for near infrared applications*, Appl. Phys. Lett. **94**, 041122 (2009)

[75] J. E. G. J. Wijnhoven, and W. L. Vos, *Preparation of photonic crystals made of air spheres in titania*, Science **281**, 802-804 (1998)

[76] A. Blanco, E. Chomski, S. Grabtchak, M. Ibisate, S. John, S. W. Leonard, C. López, F. Meseguer, H. Miguez, J. P. Mondia, G. A. Ozin, O. Toader, and H. M. van Driel, *Large-scale synthesis of a silicon photonic crystal with a complete three-dimensional bandgap near 1.5 micrometres*, Nat. **405**, 437-440 (2000)

[77] B. Gates, and Y. Xia, *Fabrication and characterization of chirped 3D photonic crystals*, Adv. Mat. **12**, 18, 1329-1332 (2000)

[78] T. Ding, K. Song, K. Clays, and C.-H. Tung, *Fabrication of 3D photonic crystals of ellipsoids: Convective self-assembly in magnetic field*, Adv. Mat. **21**, 1-5 (2009)

[79] F. García-Santamaría, MIRAR AUTORES, *Nanorobotic manipulation of microspheres foro n-chip diamond architectures*, Adv. Mater. **14**, 1144 (2002)

[80] K. Aoki, MIRAR COAUTORES, *Microassembly of semiconductor three-dimensional photonic crystals*, Nat. Mater. **2**, 117 (2003)

[81] R. W. Tjerkstra, F. B. Segerink, J. J. Kelly, and W. L. Vos, *Fabrication of three-dimensional nanostructures by focused ion beam milling*, J. Vac. Sci. Technol. B **26**(3) (2008)

[82] *FIB for Photonics*, Proceedings of the First International Workshop on FIB for photonics, edited by R. M. de Ridder, F. Ay, and L. J. Kauppinen, Eindhoven, the Netherlands, 13-14 June (2008)

[83] D. Shir, E. C. Nelson, Y. C. Chen, A. Brzezinski, H. Liao, P. V. Braun, P. Wiltzius, K. H. A. Bogart, and J. A. Rogers, *Three dimensional silicon photonic crystals fabricated by two photon phase mask lithography*, Appl. Phys. Lett. **94**, 011101 (2009)

[84] Y. V. Miklyaev, D. C. Meisel, A. Blanco, G. Von Freymann, K. Busch, W. Koch, C. Enkrich, M. Deubel, and M. Wegener, *Three-dimensional face-centered-cubic photonic crystal templates by laser holography: fabrication, optical characterization, and band-structure calculations*, Appl. Phys. Lett. **82**, 8 (2003)

[85] Y. Lin, P. R. Hermann, and K. Darmawikarta, *Design and holographic fabrication of tetragonal and cubic photonic crystals with phase mask: towards the mass-production of three-dimensional photonic crystals*, Appl. Phys. Lett. **86**, 071117 (2005)

[86] X. Wang, J. Xu, J. C. W. Lee, Y. K. Pang, W. Y. Tam, C. T. Chan, and P. Sheng, *Realization of optical periodic quasicrystals using holographic lithography*, Appl. Phys. Lett. **88**, 051901 (2006)

[87] J. Chen, W. Jiang, X. Chen, L. Wang, S. Zhang, and R. T. Chen, *Holographic three-dimensional polymeric photonic crystals operating in the 1550 nm window*, Appl. Phys. Lett. **90**, 093102 (2007)

[88] W.-D. Mao, G.-Q. Liang, Y.-Y. Pung, H.-Z. Wang, and Z. Zeng, *Complicated three-dimensional photonic crystals fabricated by holographic lithography*, Appl. Phys. Lett. **91**, 261911 (2007)

[89] J.-H. Kang, J. H. Moon, S. K. Lee, S.-G. Park, S. G. Jang, S. Yang, and S.-M. Yang, *Thermoresponsive hydrogel photonic crystals by three-dimensional holographic lithography*, Adv. Mater. **20**, 3061-3065 (2008)

[90] H.-B. Sun, S. Matsuo, and H. Misawa, *Three-dimensional photonic crystal structures achieved with two-photon-absorption photopolymerization of resin*, Appl. Phys. Lett. **74**, 6 (1999)

[91] M. Deubel, G. von Freymann, M. Wegener, S. Pereira, K. Busch, and C. M. Soukoulis, *Direct laser writing of three-dimensional photonic-crystal templates for telecommunications*, Nat. Mater. **3**, 444 (2004)

[92] N. Tétreault, G. von Freymann, M. Deubel, M. Hermatschweiler, F. Pérez-Willard, S. John, M. Wegener, and G. A. Ozin, *New route to three-dimensional photonic bandgap materials: Silicon double inversion of polymer templates*, Adv. Mater. **18**, 457-460 (2006)

[93] M. Hermatschweiler, A. Ledermann, G. A. Ozin, M. Wegener, and G. von Freymann, *Fabrication of silicon inverse woodpile photonic crystals*, Adv. Funct. Mater. **17**, 2273-2277 (2007)

[94] M. Straub, M. Ventura, and M. Gu, *Multiple higher-order stop gaps in infrared polymer photonic crystals*, Phys. Rev. Lett. **91**, 4 (2003)

[95] H.-B. Sun, A. Nakamura, K. Kaneko, S. Shoji, and S. Kawata, *Direct laser writing defects in holographic lithography-created photonic lattices*, Opt. Lett. **30**, 8 (2005)

[96] S. A. Rinne, F. García-Santamaría, and P. V. Braun, *Embedded cavities and waveguides in three-dimensional silicon photonic crystals*, Nat. Photon. **2**, 52-56 (2008)

[97] T. Y. M. Chan, and S. John, *Circuits for light in holographically defined photonic-band-gap materials*, Phys. Rev. A **78**, 033812 (2008)

[98] S. Juodkazis, S. Matsuo, H. Misawa, V. Mizeikis, A. Marcinkevicius, H.-B. Sun, Y. Tokuda, M. Takahashi, T. Yoko, and J. Nishii, *Application of femtosecond laser pulses for microfabrication of transparent media*, Appl. Surf. Sci. **197-198**, 705-709 (2002)

[99] S. Wong, M. Deubel, F. Pérez-Willard, S. John, G. A. Ozin, M. Wegener, and G. von Freymann, *Direct laser writing of three-dimensional photonic crystals with a complete photonic bandgap in chalcogenide glasses*, Adv. Mater. **18**, 265-269 (2006)

[100] E. Nicoletti, G. Zhou, B. Jia, M. J. Ventura, D. Bulla, B. Luther-Davies, and M. Gu, *Observation of multiple higher-order stopgaps from three-dimensional chalcogenide glass photonic crystals*, Opt. Lett. **33**, 20 (2008)

[101] G. Zhou, and M. Gu, *Direct optical fabrication of three-dimensional photonic crystals in a high refractive index $LiNbO_3$ crystal*, Opt. Lett. **31**, 18 (2006)

[102] A. Ródenas, G. Zhou, D. Jaque, and M. Gu, *Rare-earth spontaneous emission control in lithium niobate three-dimensional photonic crystals*, Adv. Mater. **x**, x-x (2009)

[103] A. Ródenas, G. Zhou, D. Jaque, and M. Gu, *Direct laser writing of photonic structures in Nd:yttrium aluminum garnet laser crystals*, Appl. Phys. Lett. **93**, 151104 (2008)

[104] J. Amet, F. I. Baida, G. W. Burr, and P. M. Bernal, *The superprism effect in lithium niobate photonic crystals for ultra-fast, ultra-compact electro-optical switching*, Photonics and nanostructures – Fundamentals and Applications **6**, page 51 (2008)

[105] S. Diziain, J. Amet, F. I. Baida, and P. M. Bernal, *Optical far-field and near-field observations of the strong angular dispersion in a lithium niobate photonic crystal superprism designed for double (passive and active) demultiplexer applications*, Appl. Phys. Lett. **93**, 261103 (2008)

[106] H. Kosaka, T. Kawashima, A. Tomita, M. Notomi, T. Tamamura, T. Sato, and S. Kawakami, *Superprism phenomena in Photonic Crystals: Toward Microscale Lightwave Circuits*, J. Lightwave Technol. **17**, 11, 2032 (1999)